RESIDUAL STRESSES IN D/H DRILL BITS

C. G. JONKER

THE APPLICATION OF X-RAY DIFFRACTION AND FINITE ELEMENT ANALYSIS TO THE DETERMINATION OF RESIDUAL STRESSES AND STRAINS ON THE SURFACES OF BRAZED COMPOSITES OF STEEL AND SINTERED TUNGSTEN CARBIDE-COBALT COMPACTS

A thesis presented to the Faculty of Engineering, University of the Witwatersrand, in fulfilment of the requirements for the degree of Doctor of Philosophy

by

CHRISTIAAN GERRIT JONKER, B.Sc. (Hons.) (UKSW)

This work was carried out in the Department of Metallurgy, Faculty of Engineering, University of the Witwatersrand, under the supervision of

Prof. D.D. Bowat Ph.D. (Glas.)

and

Dr. F.P. Jochens Ph.D.(RAND)

U N D E R T A K I N G

I hereby certify that this is my own work and has not been submitted for a Doctor of Philosophy degree at any other University

C. G. JONKER

ACKNOWLEDGEMENTS

The work in this thesis has been sponsored by Dourt and Hard Metals (S.A.) Ltd. and I would like to thank Drs. N. Pope and B. Young for the opportunity and assistance given to me. I would furthermore like to thank Prof. D.D. Howat of the Department of Metallurgy for his supervision and willingness to give me his time for discussions.

Since the scope of this work fell partially outside the Metallurgy field, I have received considerable help from outside sources, and I would particularly like to thank Dr. Schöning from the Department of Physics, of this University and Mr. E. Stacey of the Rock Mechanics Department, C.S.I.R. Pretoria, for their invaluable comments and advice.

SYNOPSIS

The strains on the surface of the components of a cruciform 'down-the-hole' bit were investigated because of the importance of the surface condition under fatigue loading. X-ray diffraction was selected as the most suitable technique as it may be used to measure elastic strain separated from plastic strain and to determine stress gradients over small distances. Stress values calculated from X-ray line displacement measurements on the (211) d-spacing of hardened EN 10B steel were found to correlate directly with those obtained by strain gauge measurement.

X-ray diffraction peak profile analysis was employed to determine values of the elastic strains, line broadening as a result of plastic strains and the particle size of tungsten carbide grains on the surface of sintered tungsten carbide-cobalt compacts. The surface strains and particle size resulting from several different methods of surface finishing operations were determined. The annealing process implicit in the drill bit brazing operation was found to remove the greater part of the surface residual stresses.

Residual stresses in the drilling rim of a cruciform 'down-the-hole' drill bit were investigated using an inclusion, made of the same materials as the drill bit and having a similar geometry. The symmetry of the geometry of the cruciform bit permits the prediction of the residual stress pattern in the entire annular surface by finite element analysis using the annulus geometry, material constants and thermal history. The residual stress data calculated from X-ray diffraction measurements correspond with the residual stress pattern evaluated by finite element analysis.

This thesis / -6-

This stress pattern is presented for one sector of the analogue by loci defining the magnitude, type and direction of the principal and shear stresses. This close correspondence between the experimentally determined and finite element analysis residual stress pattern allows the use of the finite element analysis in estimating the residual stresses in the surface of the sintered carbide compacts and those generated prior to and after the martensitic transformation of the EN 30B steel.

TABLE OF CONTENTS

Table of Contents (continued)

/ - viii -

Table of Contents (continued)

LIST OF TABLES

1. Introduction

1.1 Residual Stresses in 'Down-the-Hole' Drill Bits

Residual, internal or locked-in stresses may be defined as the system of stresses which can exist in a body when it is free from external forces. These residual stresses are to be considered as purely elastic stresses. There are two distinct types of these stresses, a macro- and a micro-stress.

The macro-residual stresses, with which this project is concerned, vary continuously through the volume of the body and act over regions which are large compared with atomic dimensions.

Micro-stresses act over dimensions as small as several unit cells, although their effect may extend throughout most of a grain. A major contribution in this field was made by Laszlo and has been reviewed by Noyce[1]. He attributes these stresses to the failure of neighbouring grains to fit together, due to anisotropic thermal expansion. This is true for all crystal structures of low symmetry, in contrast with the high symmetrical cubic lattices, which behave isotropically during thermal expansion.

The residual stresses to be measured in this project occur in 'Down-the-Hole' drill bits, commonly abbreviated to D/H bits. The drilling machine is lowered into the drill hole with this drill, so that the drill bit is very compact. No extensions are required.

The main components of the D/H bit are a steel shaft and crown; in the crown four hard-metal cutting faces are located in cruciform positions (See Figure 1.1).

The basic function of the shank is as a connection with the drilling machine, and it is designed such that the power-drive can rotate the D/H bit in conjunction with the percussive motion. This motion is transmitted to the drill bit via splines machined on the shank, on which the power drive is located.

The crown tapers outward from the shank to the desired gauge width and consists of four wings separated by flutes. Each wing contains one radial slot to accommodate a hard metal insert. The smaller D/H bits have wings at angles of 90^{o} to each other, while the larger units are in the shape of a cross with an acute angle of 80^{o}. The flutes provide a cooling effect and allow the removal of grit from the drill faces. The hard metal inserts are located in the centre of each wing, radiating out from the central ferrule. The wings are tapered from the flutes towards the inserts, so that the latter occupy the extreme positions in the drill face and can act as cutting faces.

The steel body of the D/H bit is turned, drilled, milled and machined to the right dimensions prior to the brazing of the hard metal inserts into the wings. Depending upon the type of D/H bit, flushing channels are drilled into the body. These flushing channels consist of one central channel through the shank into the crown, where four other channels radiate out into the four flutes or the wing faces, providing internal cooling of the drill by air or water.

The complexity of construction of the crown, i.e., the presence of flutes and flushing channels in the steel, in addition to the hard metal inserts, which are brazed into the wings, indicates the existence of many variables which may influence the service life of a D/H bit.

The loading condition of a D/H bit during its service life consists of fatigue loading perpendicular to the face of the drill bit and a radial compressive stress acting on the sides of

the crown / - 3 -

the crown of the drill bit.

Fatigue failure is usually initiated at the surface of an object under load and hence the surface condition of the bit is of extreme importance. Notches present by virtue of the geometry of design, surface roughness and surface residual stresses may affect the fatigue life of the drill bit considerably. Surface roughness is frequently an adverse factor in a sample exposed to loading, as it introduces numerous physical defects which seriously reduce the fatigue strength by acting as stress raisers. Surface residual stresses, as introduced by shotpeening, grinding and quenching after heat-treatment can either contribute to or detract from the service life of a drill bit. Shotpeening usually introduces a favourable compressive residual stress pattern, but excessive shotpeening damages the surface, introducing localised stress raisers and reducing the fatigue performance. Tarasov, Dyler and Letner [2] have found that grinding of hardened steel can produce either tensile or compressive surface residual stresses, depending upon grinding conditions.

In most fatigue investigations, it has been recognised that compressive residual stresses in the surface are favourable factors for an increased fatigue life, hence it is very important to assess whether compression or tensile residual stresses are present in the surface of a drill bit. The final grinding of the cutting faces in the crown of a drill bit after the brazing operation will usually introduced compressive residual stresses. However it is possible to initiate subsurface fatigue failure if a very steep stress gradient exists leading towards a tensile residual stress below the surface. It is therefore extremely important to determine the residual stress pattern just below the drill bit surface underneath the stress pattern introduced by grinding. Any residual stress present not originating from these machining processes is due to thermal shrinkage effects between the hard metal inserts, brazed joints, and steel sections of the crown. These residual stresses are generated by

differential / - 4 -

differential thermal contraction of the components of the drill crown when cooled to room temperature from the brazing temperature.

During manufacture of cemented carbides from their chemical constituents in powder form, several restraints in the body of the compact generate residual stresses. These are the following:

1. Thermal stresses right throughout the body of the compact caused by the differential shrinkage of the cobalt binder and the tungsten carbide grains.
2. Mechanical stresses in the surface layers of the compact, caused by grinding and shot-blasting operation during manufacture. These latter stresses are partially relieved by heat-treatment during D/H bit assembly, but are of great importance in relation to the brazing characteristics of the hard metal compact.

After brazing of the inserts into the slots of the drill bit crown, further grinding stresses are introduced in the surfaces of the hard metal compacts by the final sharpening operation. These stresses will be present at the cutting surface only, and will modify any residual thermal stresses.

During the cooling cycle of the brazing operation the following series of events generate residual stresses near the tungsten carbide/braze metal and steel/braze metal interfaces.

a) The tungsten carbide inserts are brazed into the steel slots at a temperature of 670°C. The braze metal solidifies over the temperature range 650° - 630°C. When at 630°C all three different components of the crown are solid, interaction is expected to occur between them upon cooling to room temperature, due to their different specific thermal contractions. The macro-stresses so generated in the braze, the sintered carbide and the steel are only partially relieved by

plastic deformation of the relatively soft braze alloy.

b) The steel section of a D/H bit is made from EN 30B steel, which is an airhardening steel. After austenisation of the steel at 870°C, the brazing temperature, the steel is martempered, this heat-treatment being described in Section 3.1. The austenitic structure transforms to martensite and possibly some lower bainite, this transformation generating volume-stresses inside the steel, which are part of the residual stress pattern in the composite D/H drill.

A survey of the modes of failure of all drills returned over a period of four months indicates that more than sixty per cent of all failures were initiated at the braze-steel and braze-tungsten carbide interfaces and had propagated through either the steel wing or the sintered carbide insert. A smaller number of drills had failed by excessive shank and spline wear and failure of the braze metal itself.

It was therefore decided to select and establish a stress measurement technique with the intention of determining the magnitude, type and distribution of the residual stresses in the surface layers of the drillhead, with the ultimate aim of investigating the possible connection between residual stress and failure of the drill.

Macro residual stresses in the surface of a D/H bit with a right-angle cruciform geometry are generated during cooling from the brazing temperature, and are increased in addition by grinding and machining operations on the surfaces of the tungsten carbide-cobalt hard metal inserts and the steel crown of the drill bit respectively.

1.2 selection / - 6 -

1.2 Selection of Method of Stress Measurement

All stress measurement methods are based upon experimental measurement of the corresponding strains.

Several methods of measuring macro-residual stresses exist and these fall into three broad classes, i.e., mechanical-, deflection- and X-ray techniques.

Using mechanical methods the residual stresses are calculated from the measurements of strain that are obtained when the body is sectioned and the locked-in residual stresses are progressively released. These strains may either be measured by electrical resistance strain gauges or by a micrometer. This technique is rather laborious and therefore methods which are more rapid have been developed. These methods involve the mechanical slitting of the specimen and measurement of the deflection of the slit element.

The X-ray method was considered the most suitable for the present project and was selected for the following reasons:

a) The X-ray method is non-destructive. The extreme hardness of the sintered tungsten carbide compacts, and to a lesser degree of the austenitic steel, make mechanical and deflection methods extremely difficult to use. Furthermore, the values of strain measurements by either of these two methods will be the averages of strains over the whole steel-centered carbide specimen. This renders these methods useless, since the components of a H/B bit react to different extents to these techniques of stress relief.

b) The X-ray method can determine the residual stress over very small regions of approximately 5 square millimetres in area by reducing the cross-section of the X-ray beam to a circular beam approximately two millimetres in diameter.

This feature / - 7 -

This feature makes the technique particularly suitable for measurements of steep stress gradients extending over a limited region.

c) The X-ray method makes it possible to measure elastic strains directly and to measure line broadening of diffraction peaks yielding information on plastic straining.

1.3 Development of the X-ray Strain Measurement Technique

The underlying principle of the method is the determination of the change in interatomic spacing (Δ) of a particular set of crystallographic planes when the crystal or polycrystalline aggregate is strained in a homogeneous manner. These atomic strains are calculated from the diffraction data relating to the specific set of crystallographic planes. These diffraction data are obtained from X-ray diffraction peaks, which are a plot of diffracted X-ray intensities versus diffraction angle θ. Monochromatic X-radiation will yield a unique diffraction peak for each set of crystallographic planes and when the crystal is strained the angular shift of such a peak is a measure of the change in interatomic spacing (Δ).

The initial experimental work establishing this technique was performed using X-ray powder cameras, and the strains were measured from the displacement of the diffraction lines on the X-ray films with respect to the X-ray lines of unstressed material. This technique is only acceptable when the diffraction lines are sharp and well defined, which is not the case for hardened steels.

The development of a diffractometer technique by Christenson and Eastland [3] has promoted the X-ray technique of strain measurement on hardened steels to a practical tool. This method makes use of Geiger and other radiation counters to measure the intensity profiles of the diffraction peaks.

The relative / - 8 -

The relative merits of each technique have been reviewed previously [3,4]. The X-ray sub-committee of the Society of Automotive Engineers has also reviewed the diffractometer technique and has consolidated the fundamentals of X-ray strain measurements on hardened steels [5].

Initially most practical use of Christenson's and Rowland's contribution was made by the aircraft industry for the measurement of surface stresses in aluminium alloys and high tensile strength steel components [6,7]. Subsequently this technique was used on other steel and pure iron specimens [8,9].

Further sophistication, but no essential improvements, have been developed concerning computerisation of the X-ray diffraction data-collection and evaluation procedure [10].

One further step in the development of this technique was the measurement of stresses within a body, in contrast with the surface stresses considered up till now, and this has been described by several authors [5,11,12]. It necessitates the sectioning of the specimen but corrections have to be made for the stress relief caused by removal of layers of material [5].

Some experimental results of internal residual stresses corrected for layer removal stress relief, have been published [11,12], in particular the measurement of stresses in carburised metal surfaces [11].

2. X-ray Diffraction Technique - Theoretical Aspects

2.1 Principles of X-ray Diffraction Strain Measurement

The diffraction of X-rays from the atomic planes in a crystalline material is expressed by Bragg's Law

$$n\lambda = 2d \sin\theta \qquad (1)$$

where λ = wavelength of incident X-rays

n = order of reflection, which is always an integer

d = interplanar spacing of (hkl) planes which are diffracting

θ = Bragg angle of reflection

This derivation of this equation is described in all standard science textbooks.

Fundamentally the X-ray diffraction technique measures the elastic strain from the change in the average interplanar spacing (d) of a particular set of crystallographic planes (hkl). The plastic strain present is a function of the change in diffraction peak profile when stress is applied. The incident X-ray beam originates as the characteristic radiation of a pure chemical element excited by a high voltage, hence the wavelength, λ, lies in a narrow range. After diffracting from the specimen the beam is further monochromated by a metal filter with a suitable absorption edge wavelength, which filters out the K_β radiation plus most of the background radiation. The diffracted X-rays which finally ionise the gas molecules in the counter consist of K_α radiation, plus a background radiation of large wavelength range.

The wavelength K_α of the element is the value for λ used in Bragg's Law, i.e. λ is a constant, which simplifies this law to

$$d = \frac{k}{\sin\theta}$$

where k = constant.

This /

This relationship indicated that for a small variation in interplanar spacing (d) the diffraction angle θ will show the greatest variation for the higher order of (hkl) reflections, i.e., those which have large angles of diffraction. Christenson and Rowland [3] have shown that the X-ray diffraction technique is useful only when diffraction angles in the range $70^0 \leq \theta \leq 80^0$ are used. The maximum value, $\theta = 80^0$, which may be used is imposed by the mechanical limitations of the X-ray goniometer. The minimum value of $\theta = 70^0$ is chosen so that small changes in (d) may still be associated with appreciable change in diffraction angle θ.

Therefore a set of crystallographic planes and wavelength of radiation are chosen in such a way that the diffraction angles fall within the accepted range, on condition that the peak to background intensity ratio of the diffracted radiation is sufficiently high, i.e., at least of the order 2 : 1.

The X-ray method, for determining elastic strains only, is fundamentally a measurement of a set of interplanar spacings which are altered by elastic strains. The theory of elasticity assumes the material under state of stress is being measured to be elastic, homogeneous and isotropic. Assumptions which are usually true in the case of polycrystalline metals.

From the theory of elasticity the following X-ray stress-strain relationships can be derived [5],

$$\sigma_\phi = \frac{d_\phi - d_\perp}{d_\perp} \cdot \frac{E}{1+\nu} \cdot \frac{1}{\sin^2\psi} \qquad (2)$$

alternatively

$$\sigma_\phi = \frac{d_\phi - d_\perp}{d_\perp} \cdot \frac{1}{1+\nu} \cdot \frac{1}{\sin^2\psi} \qquad (2a)$$

and the corresponding strain

$$\varepsilon_\phi = \frac{d_\phi - d_\perp}{d_\perp} \cdot \frac{1}{\sin^2\psi} \qquad (3)$$

Where d_ψ and $d_\perp$ are the interatomic spacings of the planes (hkl), which respectively subtend angles $\psi \neq 0^\circ$ and $\psi = 0^\circ$ to the specimen surface and σ_ϕ and ϵ_ϕ are respectively the stress and strain in direction ϕ in the surface of the specimen.

Often, when X-ray diffractometers are used instead of cameras, it is convenient to express the stress in equation (2b) in terms of angle 2θ rather than interplanar spacing d.

To this end, differentiating Bragg's Law (equation 1) yields

$$\frac{\Delta d}{d} = - \cot \theta \, . \, \Delta \theta \qquad (4)$$

which is equivalent to

$$\frac{\Delta d}{d} = - \cot \theta \, . \, \frac{\Delta 2\theta}{2} \qquad (5)$$

Now $\frac{\Delta d}{d} = \frac{d_\psi - d_\perp}{d_\perp}$ and $\Delta 2\theta = 2\theta_\psi - 2\theta_\perp$

and substituting these relationships in equation (3) yields

$$\sigma_\phi = \frac{(2\theta_\perp - 2\theta_\psi) \, . \, \cot\theta}{2} \, . \, \frac{E}{1+\nu} \, . \, \frac{1}{\sin^2\psi} \qquad (6)$$

If the stress is measured on a hardened steel, and the same angle ψ is used in every measurement, then all the terms on the right hand side of equation (6) except those involving the θ angle, are constant, so that equation (6) may be written as

$$\sigma_\phi = K \cot\theta \, (2\theta_\perp - 2\theta_\psi) \qquad (7)$$

Where θ is expressed in radians.

Because the variation in θ for any one material is very small, $\cot\theta$ may also be considered a constant, hence

$$\sigma_\phi = K (2\theta_\perp - 2\theta_\psi) \qquad (8)$$

the constant K being the stress factor. It is convenient to determine this constant K during calibration experiments, so that the mechanical elastic constants E and ν do not have to be used when calculating stresses from X-ray strain measurements.

2.2 Mechanical Elastic Constants versus Stress Factor K

Any conventional (other than X-ray method) strain measurement method will yield values of strain averaged over all the grains and all the crystallographic planes in the direction of strain measurement. In contrast, the X-ray technique measures the strain on a unique set of crystallographic planes in grains with a specific orientation.

Therefore calculations of stress in a body from X-ray diffraction data using the stress factor K are only comparable with values of stress from conventional techniques using mechanical elastic constants like Young's Modulus, E, and Poisson's Ratio, ν, if the material under examination is completely isotropic. This is not the case for most crystalline materials. Iron for instance is anisotropic and its elastic properties vary with crystallographic direction.

Account may be taken of this anisotropic effect by calculating separate stress factors for specific crystallographic planes from a correlation of the interplanar spacing strain and the average stress as measured respectively by the X-ray method and a conventional technique using mechanical elastic constants.

2.3 The Angular Profile of Diffraction Data

Bragg's law (equation 1) predicts a unique diffraction angle for each set of crystallographic planes, when using monochromatic radiation. The deviation from this uniqueness as

observed /

observed for diffraction traces of a polycrystalline aggregate is due to the following factors:

a) The range of orientation of the grains in a polycrystalline aggregate causes a variable reaction to an applied stress from grain to grain, resulting in a range of diffraction angles.
Consider the unique set of crystallographic planes (hkl). A uniaxial stress imposed on the aggregate will cause strains on the (hkl) planes, which vary in a limited range from grain to grain, depending upon their orientation in the aggregate. A single crystal, elastically stressed in the annealed state, will yield a (hkl) diffraction line for a unique Bragg diffraction angle θ. The polycrystalline aggregate also elastically stressed in the annealed state, will diffract the X-ray beam over a small range of angles. This can be reproducted by a distribution curve of reflected intensity versus diffraction angle θ, commonly taken as either a Gaussian or Cauchy distribution curve. The specific diffraction angle associated with such a distribution and taken as representative of the (hkl) planes is the diffraction angle θ_p at the apex of the parabola which approximates the maximum intensity section of the distribution curve.

b) Very small crystallites have insufficient resolving power and tend to broaden a diffraction line. The extreme situation occurs when the crystallites are so fine that the aggregate can be considered amorphous and will not yield any defined diffraction lines. The broadening due to the particle size effect is completely symmetrical about the mean position of the line and can be detected by when the particle size is reduced to below about one thousand Angstroms.

c) The X-ray source used is never purely monochromatic, i.e. the beam emits envelopes values of the incident X-rays producing a small range of diffraction angles.

c) When / - 14 -

d) When a stress is imposed on a polycrystalline aggregate plastic deformation is present, associated with the elastic strain if the proportional limit is exceeded. This may be due to local stress concentrations, which, when an external stress is applied, can result in localised high stress levels resulting in plastic deformation. Plastic strain causes broadening of the base of the original sharp diffraction peak, and reduces its peak to background intensity ratio, while an elastic strain shifts the diffraction peak profile by interval $\Delta\theta$.

e) The austenite to martensite transformation is the main contributor to the line broadening phenomenon in the hardened steel. This can be ascribed to the microscopic residual stresses as well as the high dislocation content associated with the martensite transformation. This low temperature transformation reaction is a diffusionless process. The face centred cubic austenitic crystal structure transforms to a body centered structure, but since the amount of carbon present is one hundred times more than can be held in solid solution, this carbon super-saturated body centered cubic lattice is distorted to a tetragonal structure, characterised by severe lattice strain.

f) Instrumental broadening. .The response of the proportional counter and other electronic parts introduces deviation from unique diffraction angles.

3. X-ray Diffraction Technique - Practical Aspects

3.1 Location and Construction of Diffraction Peaks

The accuracy of the method depends upon the location and construction of diffraction peaks which is the fundamental step in the stress determination procedure. The work involved in subsequent steps is time-consuming, but basically mathematical.

Christenson and Rowland [3] and others [4,5,9,10] have demonstrated the superior accuracy of a diffractometer for the examination of diffuse diffraction lines. As the present work is concerned with the examination of diffuse diffraction peaks of hardened steel and tungsten carbide-cobalt compounds, the diffractometer was selected as the X-ray tool.

A diffractometer provides the facility for automatic construction of diffraction peaks on a recording chart during a continuous scan over a range of diffraction angles. This method is useful for the determination of the approximate location of a particular diffraction peak. The precision of the method, however, is low due to the time lag introduced by the components intermediate to and including the counter and the recording pen.

The more precise construction method used, is the following :

a) The specimen is irradiated and diffraction data are collected over the range of diffraction angles, $\theta_1 \longrightarrow \theta_2$ in which the apex of diffraction angle occurs as has been located by the graphical method.

b) The specimen is irradiated at angle θ_1 for a fixed period of time and the diffracted X-ray intensity is recorded as the number of pulses per unit time.

c) The diffraction angle is increased by a small increment $\Delta\theta$ and the procedure is repeated until intensity data for all angles in the range are obtained

By using extended periods of counting time accurate values of the intensities of the diffracted beam can be obtained for each diffraction point in the range $\theta_1 \longrightarrow \theta_2$, statistically this reduces the percentage error, as it is related to the number of pulses counted by the electronic circuit, and is inversely proportional to the square root of the total number of counts, $\sqrt{n}$.

The K radiation /- 16 -

The K_α radiation of the source has the two distinct wavelength components, K_{α_1} and K_{α_2} which for a well resolved diffraction trace will occur as two distinct peaks close to one another. The stresses present in the specimen, and particularly the line broadening due to the martensite transformation in steel cause the K_{α_1} and K_{α_2} peaks to merge in such a way that they cannot be resolved, except by algebraic means. Therefore the merged diffraction peaks are treated as one single diffraction peak of K_α radiation and for calculations the K_α wavelength, which is a composite value incorporating the K_{α_1} and K_{α_2} wavelengths, is used. The apex angle of this diffraction peak can be calculated algebraically by fitting to a hypothetical parabola the diffraction data for all intensities more than eighty per cent of the maximum intensity recorded [14,15]. (See Figure 2). Alternatively the apex angle may be constructed graphically by extrapolating the linear sections on each side of the peak and identifying the angle of intersection as the angle at the apex[1]

The latter method is very useful for sharp diffraction traces, as these exhibit peaks with linear sections of considerable length. The former parabola method is selected for hardened steel diffraction traces, as these exhibit no distinct linear sections.

For example (figure 2) for (a) the intensity data for the three double diffraction angles $2\theta_1$ $2\theta_2$ and $2\theta_3$ separated by equal intervals $\Delta 2\theta$ where $I_{2\theta_2}$ exhibits the highest intensity value and $I_{2\theta_1}$ and $I_{2\theta_3}$ have intensities which are at least 80 per cent of that of $I_{2\theta_2}$. Using these data the apex double-diffraction angle $2\theta_p$ is calculated from the following mathematical relation[2], assuming a parabolic diffraction profile.

$$2\theta_p = 2\theta_2 + \frac{\Delta 2\theta}{2} \left(\frac{I_{2\theta_3} - I_{2\theta_1}}{I_{2\theta_1} + I_{2\theta_3} - 2I_{2\theta_2}}\right) \qquad (9)$$

where / = 17 -

where a = intensity difference between $2\theta_1$ and $2\theta_2$
b = intensity difference between $2\theta_3$ and $2\theta_2$
c = $\Delta 2\theta$

The intensity values used are the periods of time required to accumulate the same number of counts for each angle 2θ.

At this stage it is important to point out that it is not essential to determine the true and absolute angular position of the apex. An arbitrary position may be used, as the strain is only calculated as the difference between two relative apex angles. Hence accuracy of the method will hinge on the precision of repeating apex-constructions and not on their absolute positions.

7.2 Corrections of diffraction peaks for intensity factors dependent upon θ

A certain amount of asymmetry is introduced into every diffraction line, because many θ dependent intensity factors are closely associated with the diffraction and measuring process.

These factors vary slightly with diffraction angle θ, but become significant in magnitude for sizable peaks, as these extend over a considerable $\Delta\theta$ (diffractometer angle) range. All intensity data must be corrected for these facts a prior to constructing the curve of best fit and the location of the apparent peak position.

These factors are now discussed in detail in standard texts[10p177] and are identified as the Lorentz polarization factor and the absorption factor. The first factor is a combination of several θ dependent factors, while the second is dependent upon the mean path length of the X-rays within the sample and is only a function of diffraction angle θ for all angles ψ other than 90°.

Volume / - 18 -

Values for these two factors are readily calculated and a combination of these two as a single correction factor was used in this project, as computed by Ricklefs and Shipley[5]. The mathematical expressions for these factors are as follows:

L.P. = Lorentz Polarisation Factor = $\frac{1}{8} \cdot \frac{1+\cos^2 2\theta}{\sin^2 \theta}$)
) (10)
A = Absorption Factor Relation = $1 - \tan\psi \cot\theta$)

Corrected Factor from Ricklefs and Shipley = $\frac{1}{A}$ (L.P.)(A). (11)

3.3 Focussing Implications of Varying the Angle ψ

For the normal diffractometer geometry, i.e. when $\psi=0^0$, the X-ray beam diffracted from the (hkl) planes, will always focus on the circumference of a circle, defined by the goniometer axis as centre, and the source to specimen-surface distance as radius (Figure 3a).

As soon as the specimen cutting plane is rotated about the goniometer axis independently of the receiving slit position, i.e. where $\psi \neq 0^0$, the rays diffract from the (hkl) planes which subtend the angle ψ to the specimen surface, and will focus at a distance either greater or smaller than the radius of the circle, for respectively clockwise and anticlockwise rotation of the specimen surface (Figure 3b). Hence the standard receiving slit assembly is not located at the focussing position and consequently has to be shifted radially to a different position S for every angle ψ .

The proper focussing distance of the receiving slit may be calculated from the following relation :

$$S = D \cdot \frac{\cos(\psi + \eta)}{\cos(\psi - \eta)} \qquad (12)$$

where $\eta = 90^0 - \theta$

D = source to specimen distance

S = required focussing distance

4. Apparatus

4.1 Philips Diffractometer

A standard Philips diffractometer with a long shield vertical anode tube and a vertical goniometer with a horizontal specimen rotation axis was used. The specimen rotation and the counter rotation were geared to a 1 to 2 ratio, i.e. the θ to 2θ relationship.

The counting tube used was a proportional counter, which has the advantage of a linear response between the ionisation in the gas chamber and the intensity of radiation for a considerable range of X-ray intensities. The voltage signals from the counter were fed through a voltage discrimination unit before reaching the electronic counting unit.

For steels, a chromium X-ray tube with Vanadium foil filter was selected, instead of the usual cobalt tube iron filter combination, because of the former's superior peak to background intensity ratio of the diffraction peaks of the specific crystallographic planes under examination. The wavelength range of the cobalt tube causes fluorescence of iron K radiation by the specimen, which increases the background radiation level.

For tungsten carbide diffraction, the cobalt tube was selected on the basis of obtaining a diffraction trace in the required range $116^{\circ} \leq 2\theta \leq 160^{\circ}$ having a satisfactory peak to background intensity ratio.

4.2 Alterations to the standard diffractometer

a) The divergent slit assembly was replaced by a pinpoint collimator of the usual Debye-Scherrer powder camera design. The Soller baffles in the divergent slit assembly, which are present for collimating purposes, were also removed.

The collimator [illegible]

The collimator reduced the beam cross section from a rectangle of approximately one hundred square millimetres to a circle with a diameter of approximately two and a half millimetres.

The collimator was used primarily to reduce the area from which diffraction data were obtained, and hence to improve the localisation of the strains measured, i.e., diffraction data could be obtained from areas right next to the braze metal, which were not just an average of the strain over the whole adjoining section.

b) The receiving slit assembly was replaced by a unit from which the Soller baffles were removed. This improved the intensity of the diffracted radiation which reached the counting tube. The pinpoint collimator reduced the intensity of the incident beam proportional to its reduction in cross-sectional area to a narrow circular beam. The Soller baffles in the receiving slit assembly were superfluous, as they were intended to collimate the rectangular diffracted beam.

c) Incident intensity and collimation of the beam were improved by changing the X-ray tube from line to point focus. This was achieved by rotating the central glass portion of the tube, containing the anode, through ninety degrees with respect to its housing. This meant that the X-ray beam from the source was identical with that of the standard Debye-Scherrer powder camera set-up, i.e. radiation from the X-ray tube emitted through the pinpoint collimator now emanated from the edge of the anode. This inverted collimation corresponds to the Debye-Scherrer collimator was designed for pinpoint radiation

6.3 Attachments - Goniometer Fit and Stress Attachment for the Vertical Pinpoint Goniometer

These two goniometer attachments, manufactured by the Atomic Energy Research Establishment, were

required / - 21 -

required to overcome the specimen-size problem and to alter the r. goniometer for stress determination work.

This metallurgical kit permitted the examination of relatively l rge specimens, by providing a spacious platform on which the specimen was mounted. This allowed a traverse to be made across the specimen in all directions. To cope with the platform, the goniometer was shifted by 50.8 mm away from the vertical plane of the incident and diffracted X-ray beams.

The stress attachment kit provided a dovetail slide for the proportional counter and receiving slit system, so that the optimum focussing conditions of the diffracted beam could be attained for most angles of rotation Ψ .

A four point bending stress attachment was also provided by which a specimen could be stressed in tension or compression while in position for X-ray diffraction. It was used to calibrate the strain as measured by X-ray diffraction against resistance strain gauge measurements.

This bending attachment was used (Chapter 5) to evaluate by X-ray diffraction the elastic constants and the X-ray stress constants of EN 30B steel. These constants were then compared with the elastic constants which were determined by conventional techniques on a macroscopic scale.

The goniometer axis assembly was also altered, to permit rotation of the specimen surface, through the range $-60^{\circ} \leq \Psi \leq +60^{\circ}$, independent of the counter tube and receiving slit rotation.

4.4 Alterations to the Metallurgical Kit and Stress Attachment

The present project required the handling of large specimens, often two to diameter as well as the accurate positioning of the specimen with respect to the incident radiation and the provision of the means to collect diffraction

with / - 22 -

data from identified positions in close proximity to one another. To achieve these aims a lightweight aluminium vice clamp with a maximum gap of 120 mm was used.

This vice clamp was constructed so that it could move along an aluminium dovetail slide and be locked in position. A vernier scale was attached to the vice and the slide to measure the vice movement and hence pinpoint the traverse of the specimen area under irradiation to 0.025 mm when the specimen is clamped in the vice.

The whole unit (see photograph) consisting of vice clamp, dovetail slide and vernier scale was bolted in position on the platform provided with the metallurgical kit.

3. Calibration Experiments on EN 30B Steel

3.1 Specimen Preparation

The surface condition of any specimen to be examined by X-ray diffraction is of paramount importance, because the incident X-ray beam will diffract only from the outermost surface layers. The depth of penetration of the X-rays may be calculated from the following relation [16]

$$I/I_o = e^{-(\mu/\rho)\cdot\rho x} \qquad (13)$$

where μ/ρ = mass absorption coefficient of the metal under examination

ρ = density of the material

x = depth of penetration

I/I_o = ratio of intensity I at depth x and intensity I_o of X-rays which strike the surface

For iron, as irradiated material, and chromium K_α as incident radiation, the following values are applicable [20]

μ/ρ = 134.0 $cm^2\ gms^{-1}$ and ρ = 7.9 $gms\ cm^{-3}$

Equation (13) / - 23 -

Equation (13) becomes

$$\ln \frac{I}{I_0} = - \frac{\mu}{\rho} \cdot \rho x$$

For a fifty per cent drop in intensity at depth X :

$$2.303 \log 0.5 = - 114.6(7.8)\, x \qquad x \approx 9 \mu m$$

Hence the diffraction pattern obtained is representative at the most of the first 9 μm in depth of the iron, as any X-rays which penetrate further upon diffraction from lower atomic planes will be absorbed completely before they emerge from the surface.

Most sectioning or mechanical polishing techniques will disrupt the [illegible] layer of material to such a depth, that the diffraction patterns obtained are indicative only of the disruption due to the method of specimen preparation and not of the original residual stress level.

The elimination of surface distortion due to sectioning and mechanical grinding methods was achieved by preparing the surface by a standard metallographic procedure, i.e., emery paper polishing with paper of increasingly finer particle size, diamond paste polishing including etch cycles, followed by extended periods of electropolishing (Appendix A).

The restoration of the (310) peak of a heavily deformed annealed EN [illegible] steel specimen to the shape of the (310) peak of the undeformed annealed reference specimen (Figure 3) indicates the satisfactory elimination of surface distortion associated with plastic deformation introduced by sectioning and grinding. The curve [illegible], in Figure 4, representing the (310) diffraction peak of the reference specimen of fully annealed EN 30B steel, i.e., in unstressed condition, is narrow sharp with a high peak to background intensity ratio. The surface metal layers of this specimen have not been disrupted at all after heat-treatment and therefore are free of stress and deformation.

The other diffraction traces, curves b, c, d and e in Figure 4, represent the same (310) diffraction peak after sectioning, grinding and polishing. Ultimately, using an electropolishing technique, the line broadening introduced by the sectioning and grinding operation was removed almost completely, as represented by curve f in Figure 4.

Therefore the outlined specimen preparation technique shows that the plastically deformed surface layers may be removed successfully.

The removal of the elastic strains by use of metallographic and electrolytic polishing techniques can be observed only from a comparison of the interatomic- or d-spacings of the atomic planes which incline at the angles $\psi = 0^{o}$ and $\psi \neq 0^{o}$ to the specimen surface, as discussed in Section 2.2.

These interatomic spacings were measured on several strips of IX 308 steel, which were heat-treated in a manner analogous to that of the actual final heat-treatment cycle of a 'Downstone-Hole' drill bit.

The heat-treatment of a D/H bit is as follows:

a) Austenitization of the steel at 870°C for 20-30 minutes. The actual D/H bit is immersed in a salt bath at this temperature for this period of time, to liquify the brass metal and to austenitize the steel shank and crown.

b) Quenching in a salt bath held at 350°C, during which the brass solidifies.

c) controlled cooling to room temperature in powdered vermiculite, which is initially kept at 200°C.

The last two steps are typical of a martempering procedure. The resultant microstructure of the steel is mainly martensitic, but some bainite may also be expected to be present. The

hardness / - 25 -

hardness level is in the range of 44 - 48 Rockwell C.

After heat-treatment, the surfaces of the hardened EN 30B steel strips were prepared as follows:

1. Wet emery paper grind, successively 220, 400 and 600 mesh particle size.
2. Diamond polish (4 - 8 micron) + 10 per cent nital etch
3. Diamond polish (0 - 1 micron) + 10 per cent nital etch
4. Electropolish, removing 0.075 mm from the surface.

Table 1. presents the data obtained from the four strips by X-ray diffraction. Strips 1 and 2 were prepared up to and including the second step, as outlined above. Strip 3 was prepared up to and including step 3. Strip 4 was prepared up to and including step 4. All strains were measured in the direction of the applied stress, along the longitudinal axis of the EN 30B specimen. The stress and strain values quoted in Table 1. were calculated from the double diffraction angle $2\theta_\psi$ using equations (1) and (2), viz:

$$n\lambda = 2d \sin\theta \qquad (1)$$

where λ = wave length of chromium K_α = 229.1 n m.

hence $$d = \frac{229.1}{2 \sin\theta} \qquad (2)$$

and $$\sigma_\phi = \frac{d_\phi - d_\perp}{d_\perp} \times \frac{E}{1+\nu} \times \frac{1}{\sin^2\psi} \qquad (20)$$

where $$\epsilon_\phi = \frac{d_\phi - d_\perp}{d_\perp} \times \frac{1}{\sin^2\phi}$$

ϵ_ϕ = the strain in the surface plane in direction ϕ.

$E = 207 \times 10^3$ MN/m^2

and $\nu = 0.27$ are the elastic constants used (20).

All residual stresses and strains in the EN 30B strips were found to be compressive and of the same order of magnitude as published by other authors (5).

Table 1. / - 26 -

Table 1. shows that only electropolishing removed the residual strain introduced by preceding methods of surface preparation. The residual strain left after electropolishing was very small and of the same order as the limits of experimental error $34MN/m^2$ as quoted by other authors[5].

A further FN 308 strip, heat-treated as the others, has been mechanically ground to evaluate the type and magnitude of grinding stresses. Actual D/H bit crowns are ground after brazing, and hence these grinding stresses add to any residual stress already present. The grinding operation disrupted the surface to a considerable extent as has been observed for the pearlite specimens (Figure 4) ; this prevented the measurement of the elastic strain. The peak to background intensity of the diffraction profile after grinding was reduced to near zero, i.e. the peak merged with the background radiation.

The evaluation of the stress σ_ϕ from the X-ray values of interplanar strain ε_ϕ using Young's Modulus E and Poisson's Ratio ν , is open to criticism. The justification for this procedure, i.e., the assumption that the strain as determined by X-ray diffraction had a 1 : 1 correlation with the average strain as measured by conventional techniques, is found in the next section.

5.2 Correlation between Electrical Resistance Strain Gauge Data and X-ray Diffraction Strain Data

The four point bending stress attachment, incorporated in the modified goniometer (section 4.3) was used to set up tension on the surface of a FN 308 specimen while subject to irradiation by X-rays (Figure 5). Between the two inner points of the bending unit an unstrung rectangle of 20 x 15 mm is available, to which a SR 4 type electrical resistance strain gauge was attached. The gauge next to the SR 4 type strain gauge is still part of the unstrung rectangle and is used to

obtain / = 27 -

obtain X-ray diffraction data. On this basis it was assumed that the strain values recorded by the SR 4 type strain gauge and those derived from X-ray diffraction are two measurements of the same strain. These strain values may differ as the SR 4 type strain gauge measured the average strain of the specimen, while the X-ray method measured only the strain on the d spacings of a particular set of crystallographic planes. Hence anisotropy of the crystal lattice may cause a variation in strain with crystallographic direction, which can become apparent as a different strain value when measured from the unique set of planes used in diffraction. As is shown next, this proved not to be the case for the specific set of crystallographic planes selected.

For hardened EN 30B specimens the (211) d spacing was selected, which diffracted at approximately $2\theta_B = 153^0$, when using chromium K_α radiation; this is well within the required $140^0 \leq 2\theta \leq 160^0$ range.

SR 4 type strain gauges were attached to the four EN 30B strips used for experimentation in the previous section and these strips were stressed progressively in tension. At every increment the strain on the specimen was measured by a Huggenberg strainmeter. X-ray diffraction strain values were also recorded at every strain increment. The relationship between the strain gauge measurements and the X-ray diffraction strain values are presented in Figure 6.

It should be noted that the strain measurements from the SR 4 type strain gauges yielded values, which are indicative of the externally applied strain only. The residual strain present was not measured by the SR 4 type strain gauge, and this strain level is actually the arbitrary zero reference from which the externally induced tensile strains were measured. In contrast with this, the X-ray strain measurements at any stage represent the total strain level in the specimen, measuring the sum of the imposed residual strain and the strain induced by the externally applied stress. Any residual strain present

before / - 28 -

before applying the external tension was revealed as a discrepency in magnitude of the d spacin t the (211) planes which subtend different angles to the specimen surface.

The increments of strain between two levels of applied tension measured by either technique are both a measure of the same change in tension. Therefore it was necessary to determine a correlation between these two types of strain measurement.

Table II. presents the data from which the graphs in Figure 6 were constructed. The relationships between the strains as measured by X-ray and SR 4 type strain gauges, depicted by these graphs, are linear and have slopes of 45°, i.e., for each increment of applied external tension, the X-ray- and strain gauge-measured strains vary by an identical amount. This indicates that the correlation between the two types of measurement is not only linear, but has a one to one correspondence, i.e., the proportionality constant necessary to equate the two strain measurements is unity.

The $\Sigma\varepsilon$ values quoted in Table II. represent the total strain in the specimen surface introduced by the preparation techniques and correspond with the intercepts of the linear graphs of Figure 6 with the ordinates. These values are the sum of the residual strains present in the specimen before applying an external strain.

The range in the values of $\Sigma\varepsilon$ for each external strain level applied to a specimen is evident for specimen 3 and equals $\Delta\varepsilon = .0001$. This strain value range $\Delta\varepsilon$ corresponds with a double theta angle range of $\Delta 2\theta = .02^{\circ}$. Hence this value limits the precision of the method; similar magnitudes of precision have been published by several investigators [5].

The dispersion of X-ray strain values could be due to local inhomogeneous straining inherent in the crystal structure,

but it is / = 20 -

but it is far more probable that it is due to the surface preparation. When electropolishing, it was impossible to attain a perfectly level surface free of etch pits.

The graphical relations of Figure 6 again point out the removal of residual surface strain by electropolishing. Specimens 1, 2 and 3 have undergone a final diamond polishing finish and nital etch treatment only, while specimen 4 has undergone an extensive electropolishing treatment, which had removed the strained surface layers.

From the data in Table II. and the graphs in Figure 5, it is concluded that the strains calculated from the X-ray data relating to the (211) interplanar spacings are in close agreement with the values of average strain as measured by SR 4 type strain gauges. It would appear therefore that the displacement of these (211) d spacings as measured by X-ray diffraction, is representative of the strain in the whole specimen. Therefore anisotropy and lack of homogeneity, characteristic of polycrystalline materials, do not appear to exert a significant influence on the particular (211) d-spacings selected from X-ray stress measurement.

Furthermore, this direct correlation justifies the use of mechanically determined values for Young's Modulus E and Poisson's Ratio ν in evaluating the residual stresses from residual strains as measured by X-ray diffraction.

5.3 Measurements of Poisson's Ratio ν

A further indication of agreement between the SR 4 type strain gauge measurements and the (211) d-spacing diffractometer measurements is the close agreement in the Values of Poisson's Ratio as calculated from both sets of data.

a) Three specimens were milled to tensile test specification from EN 30B strips and heat-treated in identical manner to the EN 30B strips as used in four point bending (Section 5.1.).
The lateral positioning of SR 4 type strain gauges on the tensile specimens yielded stress-strain data, from which Poisson's Ratio ν could be calculated and it was found that $\nu = 0.27$.

b) Poisson's Ratio was also calculated from (211) $\underline{d}$ spacings as measured by X-ray diffraction. To this end the relationship between d_1 and d_ϕ from equation (2a) was used, substituting $d_1 = d_o\left(1 - \frac{\nu\sigma_\phi}{E}\right)$:

$$d_\phi = \left(\frac{1+\nu}{E} \cdot d_o \cdot \sigma_\phi\right)\sin^2\Psi + d_o\left(1 - \frac{\nu\sigma_\phi}{E}\right) \quad (14)$$

where d_ϕ = interplanar spacing $\underline{d}$ of (211) planes at angle ϕ to the specimen surface
d_o = unstressed interplanar spacing $\underline{d}$ of (211) planes
ν = Poisson's Ratio
E = Young's Modulus = 0.2×10^6 MN/m^2
σ_ϕ = unidirectional stress on the surface at angle ϕ to a reference line on surface

The interplanar spacing $\underline{d}$ of the set of (211) planes is calculated from X-ray diffraction data obtained at various levels of externally applied bending stress. The graphical relation of $\underline{d}$ and $\sin^2\Psi$ yields a set of linear graphs (Figure 7) which have a unique point of intersection. The value of $\sin^2\Psi$ at this point of intersection is related to the value of Poisson's Ratio only, and the associated $\underline{d}$ spacing is the unstressed $\underline{d}$ spacing d_o . That angle Ψ is a unique angle, chosen such that the negative component of strain transverse to the direction of applied compression (the positive strain in the direction of stress)

Therefore Poisson's Ratio could be calculated from equation (14)

When $d_\psi = d_\alpha$, equation (14) yields the following relation

$$\sin^2\psi = \frac{\nu}{1+\nu}$$

From Figure 7, $\sin^2\psi = \frac{\nu}{1+\nu} = 0.22$ Hence $\nu = 0.28$

The two values of Poisson's Ratio as calculated in Section (a) and (b) respectively $\nu = 0.27$ and $\nu = 0.28$, agree very well with the average engineering value quoted for steels, which is $\nu = 0.29$. This agreement also enhances the acceptability of the (211) d spacing as a gauge length representative of the whole EN 30B specimen.

5.4 Measurement of stress Constant K of the (211) d-spacing for Hardened EN 30B Steel

From equation (2) the stress constant K of the (211) d-spacing for hardened EN 30B steel can be calculated. Consider two stresses $(\sigma_\phi)_1$ and $(\sigma_\phi)_2$ of different magnitudes acting in the same direction. The corresponding strains produced are e_1 and e_2, with respective diffraction angles $(\theta_\perp, \theta_\psi)_1$ and $(\theta_\perp, \theta_\psi)_2$.

Now substituting equation (3)

$$e_\phi = \frac{d_\psi - d_\perp}{d_\perp} = \frac{1}{\sin^2\psi}$$

in (2) yields

$$\sigma_\phi = e_\phi \cdot \frac{E}{1+\nu} \qquad (15)$$

Hence using equation (2)

$$K = \frac{(\sigma_\phi)_1}{(2\theta_\perp - 2\theta_\psi)_1} = \frac{(\sigma_\phi)_2}{(2\theta_\perp - 2\theta_\psi)_2} = \frac{(\sigma_\phi)_1 - (\sigma_\phi)_2}{(2\theta_\perp - 2\theta_\psi)_1 - (2\theta_\perp - 2\theta_\psi)_2}$$

Substituting σ_ϕ of equation (15), this yields

$$K = \frac{(e_1 - e_2)\cdot\frac{E}{1+\nu}}{(2\theta_\perp - 2\theta_\psi)_1 - (2\theta_\perp - 2\theta_\psi)_2} \qquad (16)$$

Using the data in Table II, K was calculated by equation (16) by substituting values for strain measured by the X type strain gauge

$$K = 1217 \text{ MN/m}^{-2} / \text{unit } \theta$$

Using mechanical values of $E = 20.64 \times 10^4$ MN/m^{-2} and $\nu = 0.29$, the stress factor K is calculated, without using the data obtained by the SR 4 type strain gauges.

Substituting σ_ϕ of equation (6) into equation (8) yields the following relation for stress factor K

$$K = \frac{\alpha E \theta}{2} \cdot \frac{1}{1 + \nu} \cdot \frac{1}{\sin^2 \Psi} \qquad (17)$$

This equation yields a value for K, the stress factor, without using X-ray data of the diffraction peak shifts

$$K = 12.1 \quad \text{MN/m}^{-2} / .01^0\theta$$

Considering these two values of K it is seen that the precision of K from experimental and theoretical calculations is $\pm$ 5 %, which is within the experimental X-ray diffraction error $\Delta 2\theta$. This is expected from the previous correlation between SR 4 type strain gauge measurements and X-ray diffraction strain measurements.

5.5 Summary

1. The profile of the (311) diffraction peak of the pearlite in 308 steel specimens, using chromium K_α radiation, is used to demonstrate the satisfactory removal by mechanical and electrolytic polishing of non-homogeneous plastic deformation which causes diffraction peak broadening.
The same polishing technique does also remove grinding, sectioning and other plastic stresses in the surface of hardened EN 8D steel specimens.
2. The calibration of the X-ray strain data of the (211) d-spacing of hardened EN 8D steel and SR 4 type electrical resistance strain gauge data show a correlation coefficient of unity for these two types of strain measurement.
Therefore the measurement of the elastic strain on the

(211) d-spacing - 33 -

(211) d-spacing of hardened EN 30B steel is directly representative of the elastic strain in the specimen, and the use of mechanically determined values for Young's Modulus E and Poisson's Ratio ν is justified.

3. X-ray and mechanical measurement of Poisson's Ratio ν for hardened EN 30B steel yield values of 0.27 and 0.28 respectively. These agree with the average engineering value quoted for steels, which is $\nu = 0.29$.

4. The stress constant K for EN 30B hardened steel is calculated from X-ray data and electrical resistance strain gauge data, the average value being:

$$K = 12.4 \text{ MN/m}^{-2} / .01^{\circ}\theta \quad .$$

6. Determination of Strains in Tungsten Carbide Sintered Compacts

6.1 General Characteristics of Sintered WC-Co Compacts

The cutting tools or D/H dies are sintered compacts of tungsten carbide grains in cobalt binder, also known as hard metal compacts. Cobalt and tungsten carbide, both as powders, are mixed and then ball-milled to the required particle size. All the iron group elements are suitable as binding agents, but cobalt has been used for a long time because cold working by milling causes the metal to change to the hexagonal structure, and the transformation facilitates the breakdown of particles. Lewthwaite's experiments[16] indicated that cobalt can be milled to about 0.01 μm compared with 0.1 μm for nickel and iron. In the subsequent sintering process, shrinkage of the WC-Co compact becomes noticeable at about 800°C which coincides with the effective sintering temperature of pure cobalt. The shrinkage increases with rise in temperature, and reaches a maximum between 1300°C and 1350°C. The decrease in porosity noted at these temperatures is associated with the presence of a considerable amount of liquid which binder cobalt. It is generally thought that the densification of WC-Co compacts takes place by

a re-arrangement of the carbide particles under the influence of the surface tension forces of the binder [18].

The structure of a WC-Co compact is dependent upon the actual cobalt content. It was concluded from the data of severa authors that for compacts with a low cobalt content, i.e., 3 volume per cent cobalt, the carbides form a continuous skeleton, while for compacts with a high cobalt content, i.e., 20 - 25 volume per cent, the structure is a cobalt-base matrix with more or less large carbide clusters embedded in it [18].

The structure of a 10 volume per cent cobalt-tungsten carbide compact, as used for D/H bits, is thought to consist of interlocking skeletons of tungsten carbide and cobalt[18].

The strength of WC-Co composite exceeds that of the pure cobalt binder phase many times, and this is thought to be due to several factors, namely :

a) The severe restraint exerted by the carbide particles on the binder.

b) The presence after cooling of residual stresses explained by the difference in coefficients of thermal expansion of both components.

c) The fact that some tungsten carbide remains in solution in cobalt at room temperature, which results in solution hardening.

A fourth point suggested to contribute to the strength of the binder, is the allotropic transformation of cobalt from a face centered cubic to a close packed hexagonal structure with its associated volume change[18]. This point is very powerful, as a large proportion of all the cobalt in the matrix at room temperature is in the high temperature f.c.c. form, even though it is thermodynamically unstable. The result allotropic transformation is sluggish, due to the very low free energy change associated

with it / - 35 -

with it, and hence the presence of f.c.c. cobalt at room temperature is very feasible. The presence of cobalt binder as a f.c.c. structure at room temperature is generally used as an industrial criterion of a satisfactory sintering technique.

The coefficients of thermal expansion of cobalt and tungsten carbide are in the ratio of three to one. The cobalt therefore will contract more than the tungsten carbide upon cooling: this sets up a tension in the cobalt and compression in the tungsten carbide grains. A mechanism explaining how these cooling stresses occur was proposed by Schröring [19] and is outlined below.

As a result of the differential thermal shrinkage of the constituents of the composite, two mechanisms of contraction may take place. When cooling starts, the tungsten carbide grains can still move freely with respect to each other, hence the cobalt binder, which contracts at a faster rate, can draw the tungsten carbide grains closer together. The overall shrinkage of the compact is consequently greater than that of the individual tungsten carbide grains. This mechanism can only operate so long as the tungsten carbide grains are free to move in the cobalt matrix. After the grains have made contact with each other, the compact will shrink further at the same rate as the tungsten carbide grains. The cobalt matrix is now bound to the WC grains, and hence cannot contract freely. This interaction sets up hydrostatic tensile stresses in the cobalt binder and hydrostatic compressive stresses in the tungsten carbide grains.

The final operations in the manufacture of WC-Co hard metal consists of several mechanical treatments to achieve a satisfactory cutting tools. These include tumbling, sand blasting, alumina blasting, and vapour blasting. These processes place the outer skin of the composite under compression, for more severely than the compression of WC grains due to thermal

contraction / - 36 -

contraction. Measurements of these strains are reported in the next section and yield an indication of the severity of each surface treatment operation.

6.2 Measurement of Strain in WC Grains Introduced by Surface Finishing Operations on Sintered WC-Co Compacts

The radiation selected for the diffraction of sintered 10 per cent cobalt-WC specimens was cobalt K_α, with an iron K_β radiation filter. The (hkl) reflection in the desired range $140^\circ \leq 2\theta \leq 160^\circ$ for strain measurement is that of the (202) planes of WC; their peak position is approximately $2\theta_F = 153^\circ$.

To measure the strain in the surface WC grains of a hard metal compact as induced by various finishing operations, diffraction measurements were made of the as-sintered and surface treated compacts. To measure the actual strain present, no polishing or other metallographic surface-preparation was applied. On the majority of the samples the surface even under different conditions of preparation is sufficiently smooth to permit successful X-ray diffraction measurements to be made.

The data in Table III indicate the residual strain levels in the surface WC grains representative of a maximum depth of 3 μm. The strain level of the sintered compact is negligible, unlike the remaining surface treated specimens. These were subjected to surface preparation operations, like grit blasting, vapour blasting, rotating, mechanical grinding and vibratory tumbling and exhibited very high levels of surface distortions. Electrolytic grinding proved to be the surface treatment which introduces minimum straining of the WC grains in the compact.

Some measurement of the severity of grit blasting and polishing with diamond paste were published also by French[23,24]

His parameter / - 37 -

His parameter for measuring the X-ray strain was the (212) d spacing using chromium K_α radiation.

The limits of precision of the elastic stress measurement are again a function of the strain measurement and are $\pm$ 69 MN/m^2 for the tungsten carbide - cobalt.

All data on the vapour blasted specimens indicate that, despite the difference in preliminary steps of preparation, the common final operation of vapour blasting was so severe that it established its own strain level eliminating any evidence of the prior level of deformation.

It has to be noted that the values of elastic strain quoted in Table III. are representative only of the tungsten carbide grains. No data are included relating to the elastic straining of the cobalt binder. Therefore, according to Schöning's model of contractional events during cooling, the strain measured in the tungsten carbide grains is only a part of the total strain imposed on the hard metal compact. This was in agreement with the findings of Koshanovska, Evans and Marsak[21], who estimated that the X-ray method yielded results which were 40 per cent less than those calculated from other techniques, which measured the combined strain in WC grains and cobalt binder both groups of investigators attributed this discrepancy to the presence of the cobalt matrix.

This explanation is not wholly satisfactory, considering the value these investigators used for Young's Modulus when calculating the stresses. The value used in their calculations $E = 0.46 \times 10^6$ MN/m^2 is considerably lower than that used to calculate the stresses quoted in Table III. This value taken from Smithells data[20] $E = 0.71 \times 10^6$ MN/m^2 - is 35 per cent greater than that used by Koshanovska and co-workers. D.K. Ferrel[22,23] determined the X-ray value for Young's Modulus from measurements of the (212) d spacings using chromium K_α radiation, and found this to be $E = 0.72 \times 10^6$ MN/m^2, in full agreement with the value as quoted by Smithell[20]. Hence

the 40 per cent discrepancy between X-ray stress values and stress values from other techniques, as observed by Kochanovska and co-workers, could be due to an unfortunate selection of the value of the modulus of elasticity E .

The diffraction peak shape for most of the sintered hard metal compacts was investigated for low and high angles of diffraction. The comparison of these peaks with those of an unstressed specimen has yielded information on the inhomogeneous straining and particle size which resulted in the phenomenon of peak-broadening.

To evaluate this inhomogeneous straining the diffraction peaks of atomic planes with Miller Indices (001),(100), (101), (201), and (112) were investigated. The first three planes diffracted in the angular range $35^{0} < 2\theta < 60^{0}$ and in the free condition had a narrow base with a very high peak to background intensity. Diffraction of the last two planes (201, 112) occured within the range $100^{0} < 2\theta < 120^{0}$, and even in the unstrained condition these peaks were relatively broad at the base, with lower ratios of peak to background intensity. The profiles of the diffraction peaks are required to calculate the magnitude of the inhomogeneous straining and the diffracting crystal size.

All reflection traces were recorded on the diffractometer charts, both for a forward and a reverse scan. The interpolation of the forward and reverse traverses was assumed to be the most reliable representation of a particular diffraction peak, as it eliminates the inertial lag of the recording unit. These interpolated peaks are represented in Figures 8, 9, 10, 11 and 12.

The diffracting crystal size of the WC grains is dependent upon the deformation of the surface, or imposed stress

will fragment / - 39 -

will fragment the WC particles into a mosaic structure with smaller areas of crystal perfection. Only crystallites smaller than 10 μm will give rise to peak broadening.

In all diffraction peak profile analyses, the actual profiles are assumed to follow either a Gaussian or Cauchy distribution curve. These profiles are defined as follows :

Gauss profile : $I_G = I_o \exp (- k^2 x^2)$

Cauchy profile : $I_C = I_o / (1 + k^2 x^2)$

This assumption constitutes an inherent weakness of these calculations as the shape of the experimental diffraction peak profile is generally intermediate between these two. In the next calculation it is assumed that both the non-homogeneous plastic deformation and the mosaic particle size independently give rise to peak broadening.

Stokes [64] expressed the diffraction peak profiles for broadened lines and reference lines of annealed samples as a Fourier series to obtain line width values for deformation and particle size only. In this project the $K_{\alpha_1 \alpha_2}$ doublet, as presented by the K_α profiles in Figures 8 to 12, was separated by the graphical method of Rachinger [65]. After this separation the breadths of the α_1 peaks for the reference specimen of annealed WC powder and the sintered compacts were calculated as the quotient of the area, $A\ \alpha_1$, under the α_1 peak (which has been corrected for background intensity) and the maximum intensity, $I\ \alpha_1$, of the α_1 peak. Next the integral breadth, β, of a broadened peak, i.e. the difference in peak breadth between the broadened peak and the reference specimen peak, is calculated from the following relationships:

Gauss : $\beta = B - b$

Cauchy : $\beta = B - b$

where β = integral peak breadth

B = peak breadth of a specimen with peak broadening

b = peak breadth of annealed WC powder

If the / - 40 -

If the diffraction peak profiles are assumed to be of the Cauchy type intensity distribution, then the following relation[26] has been derived

$$\left(\frac{\beta \cos\theta}{\lambda}\right)^2 = \left(\frac{1}{D}\right)^2 + \frac{16\varepsilon^2 \sin^2\theta}{\lambda^2} \qquad (18)$$

where D = size of diffracting crystal ite
ε = a measure of strain
λ = wavelength in μm

Table IV. contains the values for integral breadth, β, particle size, D, and strain, ε, as derived from the diffraction peak profiles and equation (18).

Using the Rachinger α_1 α_2 doublet separation construction the subsequent calculation of D and ε is given in Appendix B. Values for $(\frac{1}{D})^2$ and ε^2 are obtained from the intercept and slope respectively of the linear relationship between $(\frac{\beta \cos\theta}{\lambda})^2$ and $\frac{16 \sin^2\theta}{\lambda^2}$ as presented in Figure 13. It has been possible to calculate D and ε only for the tumbled, electrolytically ground and grit blasted sintered compacts. The (201) and (112) diffraction peak profiles of the other specimens are not easily distinguishabl from the background radiation, due to the extremely low ratio of peak to background intensity. Hence only the β values for the (001), (100) and (101) diffraction peaks were obtained for these compacts, and this lack of data prohibits the construction of the linear relationship of $(\frac{\beta \cos\theta}{\lambda})^2$ versus $\frac{16 \sin^2\theta}{\lambda^2}$

Values of ε in Table IV. indicate that the electrolytically ground and tumbled compacts have the lowest value for non-homogeneous plastic strain. Finishing operations based on physical erosion, e.g. grinding and surface blasting by several media, introduce a far greater degree of plastic deformation of the WC grains in the sintered compact surface.

The surface / - 41 -

The surface roughness of the specimens can also contribute to the reduction in ratio of peak to background intensity and this is discussed in the next section. However, surface roughness measurements across the surfaces of the specimens, of which the strain data are quoted in Tables III. and IV. indicated similar roughness profiles for all specimens. Therefore, we may attribute the reduction of the intensity ratio to the surface strain alone.

The three low angle reflections of the fresh tungsten carbide powder (Figures 8,9 and 10) have well defined narrow peaks with very high ratios of peak to background intensity. This powder is almost completely strain free, as confirmed by the fact that the high angle (201) and (112) reflections show well resolved α_1 and α_2 peaks. (See Figures 11 and 12). The slightest strain would destroy this resolution and merge the particular α_1 and α_2 peaks into the usual compound α peak. Hence the tungsten carbide powder data can be used as a reference, representing material with virtually zero strain.

The diffraction peaks of the sintered only compacts show even better definition than the fresh powder peaks, having a narrower base and higher ratio of peak to background intensity. This is most probably due to grain growth of the tungsten carbide particles during the sintering process; large particles will always yield sharper diffraction lines than small particles even of similar crystal perfection. From values of B in Table IV., compared with those of the reference W powder, it is concluded that the sintering process does not introduce strain on the surface layers of the compacts.

The diffraction peaks of all the other compacts, which have undergone one of the surface treatments, as outlined in Table IV., showed increased broadening of the peak and also a reduced ratio of peak to background intensity.

The difference / - 42 -

The difference in surface distortion between the virtually stress free sintered only compacts and the compacts subjected to various surface treatments is clearly shown by the diffraction profiles in figures 11 and 12. All the surface treated compacts exhibit diffraction profiles for the (201) and (112) crystal planes with a composite K_α diffraction peak, in contrast with the well resolved K_{α_1} and K_{α_2} peaks of the sintered only compact. Besides this phenomenon a marked drop occurs in maximum peak intensity for the surface treated specimens. These high angle diffraction peaks have limited use, as a small strain tends to affect the profiles drastically, preventing the obtaining of any information on the relative differences in surface distortion between the surface treated compacts. This phenomenon is explained by Bragg's Law (equation 1), which shows that the relationship between interplanar spacing d and diffraction angle θ is a sinusoidal function, i.e., for a small variation in d, the diffraction angle will show maximum variation for crystallographic planes having large angle reflections. The low angle reflections of crystallographic planes as shown in figures 8,9 and 10 do indicate the differences in diffraction peak profile for most of the surface treated compacts. It is evident that the largest amount of distortion occurs in the ground and vapour blasted compacts. The ratio of peak to background intensity for these diffraction profiles is reduced to a value of two to one, which indicates extremely severe distortion of the surface layers.

The data quoted in Table III, for the same compacts indicate similarly large levels of residual stress for all the surface treated compacts, except for the electrolytically ground compacts. The diffraction profile distortion data in Table IV, do however indicate that the plastic deformation associated with the respective surface treatments differs considerably, e.g., the tumbled and grit blasted specimens show a considerably lower level of surface distortion than the mechanically ground and vapour blasted specimens.

6.3 Surface / - 43 -

6.3 Surface Roughness introduced by Surface Preparation of Sintered WC-Co Composts

The successful measurement of residual strain by X-ray diffraction is dependent upon the condition of the surface of the specimen.

A high level of surface roughness indicates the presence of a large number of high peaks and deep valleys in the surface of the composite. This physical phenomenon causes a wide scatter of the reflected X-ray beam, which diffracts from the crystallographic planes in the surface. As the scatter increases with increasing surface roughness, the diffraction peak maximum intensity decreases until it merges with the background radiation. At a certain degree of surface roughness no satisfactory strain measurements can be made due to the large error involved in locating the peak position of a very small diffraction peak profile.

Nevertheless it is important to know these levels of surface roughness, as the surfaces will comprise numerous stress raisers introduced by abrasion or other surface finishing processes. The presence of these stress raisers may lead to early fatigue failure and hence detract from the service life of the compact. Microcracks presumably present in the hard metal surface in contact with the braze metal may reduce the life of the braze/sintered compact bond, by early failure of the WC grains adjacent to the braze.

Surface distortion of the specimens examined and reported on in Table V, was such that it was impossible to evaluate the plastic deformation from line-broadening, as the diffraction peak profiles had always been completely eliminated. It is therefore helpful to consider the surface roughness levels as indicators of the surface distortion introduced by finishing operations.

The physical / - 44 -

The physical profile of a surface is measured by a surface roughness tester, which yields values for surface roughness in terms of the number of peaks and troughs on the surface and their height or depth with respect to an intermediate reference line.

The surfaces of identical sintered compacts were abraded by blasting them with a variety of media for different periods of time.

Table V. includes the values of X-ray strain measurement on those particular specimens. These data show a level of surface roughness for Samples 5,6 and 7 which is so high that no strain data could be calculated. The amount of material removed from these three specimens was also far greater than that of the first four specimens: this factor and the surface roughness level are probably interrelated.

Specimens 8 and 9 represent two identical sintered WC compacts which have had the conventional surface treatment. The levels of surface strain of these two reference specimens and the first four specimens are of a similar magnitude and also of the same order as the values quoted in Table III, for the shotblasted sintered specimens.

The only comparable specimen used by Friend [18,33] was a grit blasted sintered compact which had a residual stress of $-1331\ MN/m^2$. This stress level is of the same order as those quoted in Tables V. and VI. These values are comparable but cannot be equated, because of possible differences in compositions of the sintered carbide, in gritblasting conditions and in strain value as measured from the two different sets of crystallographic planes due to anisotropy of the hexagonal crystal lattice.

6.4 The Effect of Heat-Treatment on the Surface Strain of Sintered WC-Co Compacts

During the brazing cycle in the D/B bit fabrication the tungsten carbide compacts are heat-treated as described in Section 5.1. and this may have a beneficial effect in lowering the surface stress level.

Several chiselbit tungsten carbide compacts which had undergone normal surface treatment operations and exhibited a high level of surface stress were annealed in a hydrogen atmosphere at different temperatures. The levels of stress before and after heat-treatment were measured and are quoted in Table VI.

Specimen No. 1. in Table VI. indicates the residual stress of the compact prior to any heat treatment and may be taken as representative of the stress introduced by the normal surface treatment operation.

Increasing reduction in the stress level of the WC grains in the surface of the compacts is achieved by annealing at increasingly higher temperatures. Annealing the compacts for 1 hour at 900°C in a hydrogen atmosphere caused the stress level to drop off to very low values, i.e., +110 to +160 MN/m^2. This is only slightly higher than the limit of precision of stress-measurement on WC by X-ray diffraction which is ± 70 MN/m^2. This startling reduction in stress was not observed by Finch[22] when heat-treating compacts of similar composition, the lowest stress level present in these compacts as reported by him was still +447 MN/m^2.

The reduction of the stress level by sub-critical annealing procedure indicates that during the brazing cycle in the fabrication of a D/B bit, the greater part of the residual stresses, introduced into the sintered compact surface by abrasive finishing operations, are relieved. Surface defects present in

the material / - 46 -

the sintered compact surface are also expected to have been removed by this heat-treatment.

6.5 Summary

The previous results show that different finishing operations introduce various degrees of surface damage and various levels of residual stress in the surfaces of the compacts.

1. An analysis of the (001), (100), (101), (201) and (113) WC diffraction peak profiles yields information on the relative surface distortion introduced by the various surface finishing operations.
2. Electrolytic grinding, which is an electrochemical erosive process, imposes a far lower level of residual stress and non-homogeneous plastic deformation in the skin of the sintered composite than any of the other mechanical finishing treatments.
3. Diffraction data on various specimens indicate that at high levels of surface roughness the physical condition of the surface causes the diffraction peak to merge with the background radiation, so preventing any stress measurement.
4. Heat-treatment of abraded sintered compacts indicates that a large decrease in residual stress does occur during the bonding of the inserts in a drill bit crown. Annealing temperatures of 700°C and 900°C, which are respectively below and above the normal brazing temperature, reduce the residual stress levels considerably.

(7. Residual / c.A) -

7. Residual Stress Pattern in the Surface of a D/H bit Analogue

7.1 X-ray Measurement of Residual Strains in the Analogue Surface

A D/H bit (Figure 1) is too large and heavy to be accommodated on the specimen platform of the modified goniometer. To circumvent these problems and to simplify the surface geometry of a D/H bit, an analogue (Figure 24) was constructed, differing from the D/H bit as outlined below.

1. The analogue has no steel shank but is of a form corresponding with a D/H bit sectioned at right angles to its axis on a plane just below the sintered tungsten carbide compacts and fracule position.
2. The surfaces of the steel wings and the sintered tungsten carbide compacts all lie in one plane, unlike a D/H bit, where the cutting faces of the sintered compacts occupy the extreme positions in the four roof shaped wings.
3. The surfaces of the steel wings of a D/H bit subtend an acute angle to the plane, while the wing surfaces of the analogue are at right angles to the equivalent plane.

The analogue was constructed from the same materials as a D/H bit and by the same production-scale brazing techniques, as described in Section 5.1. The Easyflo brazing alloy used for D/H bit and analogue brazing liquifies over the temperature range 634° – 656°C and upon cooling from brazing it is assumed, that the brass metal is completely solidified at 634°C, disregarding possible solidus temperature fluctuations due to diffusion of alloying elements from the steel and tungsten carbide compacts into the braze. Therefore thermal stresses are only generated between the fully solid phases in the analogue at temperatures below 634°C.

The D/H bit / – 48 –

The D/H bit analogue, as in the case of a D/H bit, possesses a high degree of symmetry, which directly influences the stress pattern produced by thermal shrinkage. Figure 14 is a diagram of the analogue, showing that it consists of four equivalent steel sectors, bounded by four equivalent hard metal inserts. No individual characteristic distinguishes one sector from the next and with such a symmetrical construction, each sector will have a stress pattern equivalent to the next. Obviously it is only necessary to know the stress pattern in one sector to construct the stress pattern in the whole analogue.

Consider the top right hand sector BCD in Figure 14; close examination of the geometry reveals the existence of further symmetry elements within the sector. The line bisecting angle afe, i.e. the bisector fm, is obviously the two-fold axis of symmetry of the sector. The geometrical position of any point P(x,y) in the sector is symmetrical with the point P(y,x) in the sector. This means that the strain measurements taken in the area a'fm of the sector will yield a stress pattern in this area, which is symmetrical with the stress pattern generated in the opposite area of a'fm of the sector. Hence measurements made in area a'fm can be cross-checked by measurements in area a'fm. Upon cooling the body of the analogue contracts about its geometric center, which lies upon the axis cc (Figure 14).

Considering solely the surface plane of the analogue, it will contract equally about point C (Figure 14), but the hard metal segments will contract to a far lesser extent about their respective geometric centres and hence stresses are generated at the bonded joint in the steel and the hard metal segments.

The variation and extent of the residual stresses introduced in the surface layers of sintered tungsten carbide-

cobalt / - 49 -

cobalt compacts, as used in 'Down-the-Hole' drill bits, are described and discussed in Section 6.2. Any stresses introduced prior to the brazing operation are reduced to very low levels by the annealing operation implicit in the brazing cycle (Section 6.4., Table VI.).

Residual stresses introduced in the surface of the steel section of the D/H bit crown prior to brazing are also removed during brazing, as the EN 30B steel is austenitised during this process.

Post brazing grinding of the crown surface introduces considerable stresses in the surface, which are extremely difficult to assess quantitatively but experimental work described earlier has revealed that the residual stresses associated with the preparation of the hardened steel surface by emery paper and diamond polishing are 414 MN/m^2 in compression (Table I. Section 5.1.).

Grinding stresses in the hard metal compacts of the same magnitude have been reported by D.N. French [22] at approximately -393 MN/m^2. The reason for the unsuccessful measurement of grinding stresses in hardened EN 30B steels in these tests in contrast with French's successful measurements is that the diffraction peaks of the hard metal compacts in the as-sintered condition are clearly defined with an excellent peak to background intensity ratio, while the diffraction peaks of hardened steel, prior to any externally imposed stress, are already very broad and have low ratios of peak to background intensity. This is due to the distortion of the lattice of the steel matrix following hardening.

As a consequence, the grinding stresses nearly obliterate the broad martensite diffraction peaks but not the sharp, well defined tungsten carbide diffraction peaks.

In order to / - 50 -

In order to measure the thermal residual stress pattern in the surface of the D/H bit analogue, this specimen was prepared by the polishing technique described in Section 5.1. The analogue has four identical sectors of which one was selected and electrolytically polished. The X-ray results obtained from this sector are considered to be representative of all four sectors. The analogue situated in position for X-ray diffraction of the electropolished surface can be observed on the photograph on the next page.

Because of the size limitations of the electrolytic polisher, three adjoining areas on the sector surface had to be polished. The boundaries between these three polished areas present problems in strain-measurement, as they exist as uneven edges of metal between the polished areas. This is in contrast with the greater centre part of the polished areas, which has a smooth bright surface. The positions of the electro-polished areas on the analogue sector surface are shown in Figure 15. From this diagram it is noted that the unevenly electro-polished areas are represented by the shaded areas A and B.

X-ray data were collected for a grid of positions in the surface of the analogue sector, as depicted in Figures 16 (a), (b) and (c). Figure 16 (a) shows the positions of the strain data taken in the x-direction; Figure 16 (b) shows the positions of the strain data taken in the 45° direction, i.e., 45° with respect to the x- and y-axes in the direction normal to the bisector of (Figure 14); Figure 16(c) shows the positions of all strain data taken in the y-direction.

The calculated strain values for each position in the respective three directions are tabulated in Tables VII, VIII and IX. A sample calculation of strain-data from X-ray diffraction data is given in - Table X. Figures 17 to 19 represent the total strain-data measured in the x-direction over the x-traverses across the sector surface, i.e., data

from / - 51 -

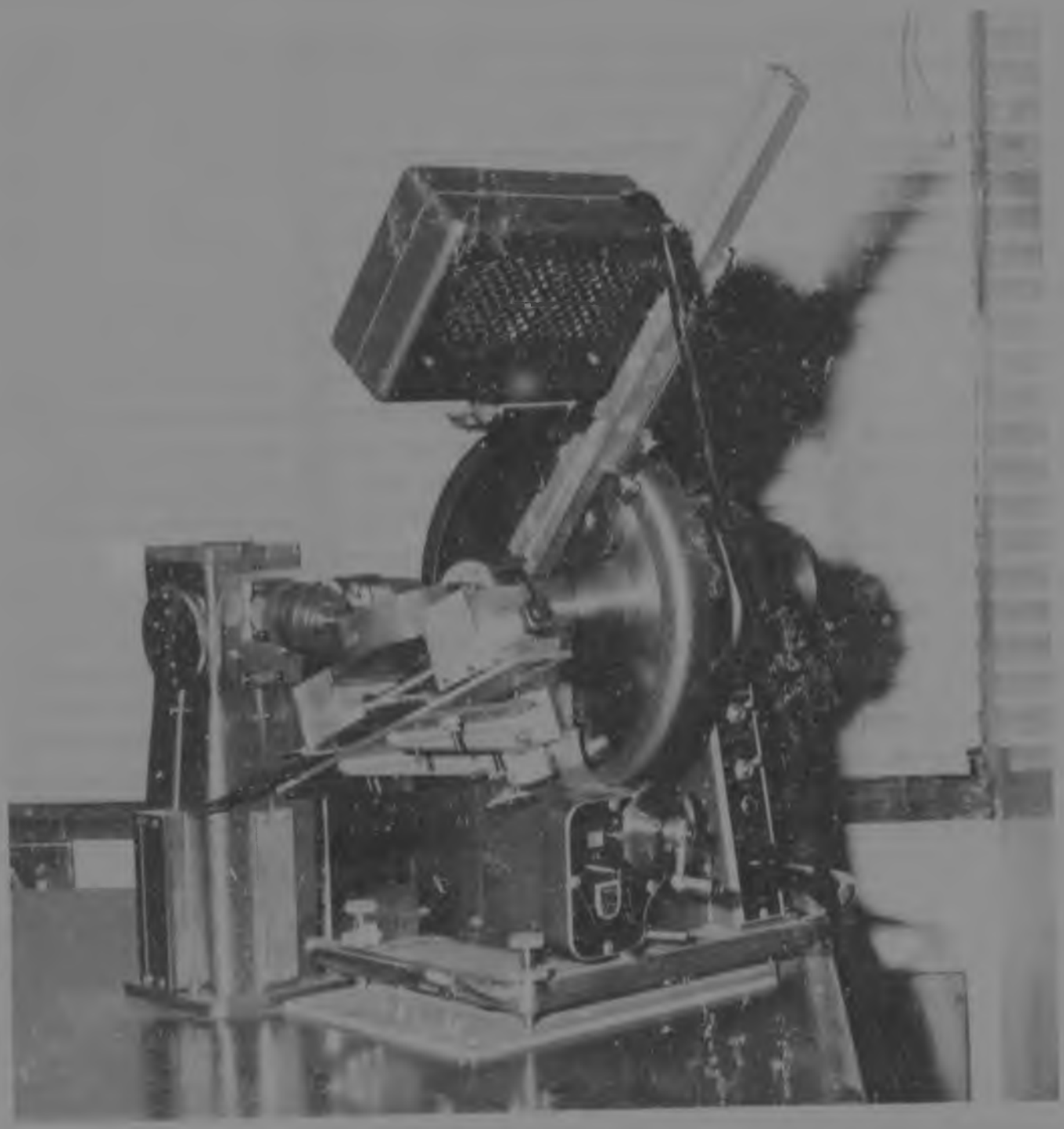

PHOTOGRAPH I The modified X-ray unit used for the measurement of residual stresses in the drill-bit analogue.

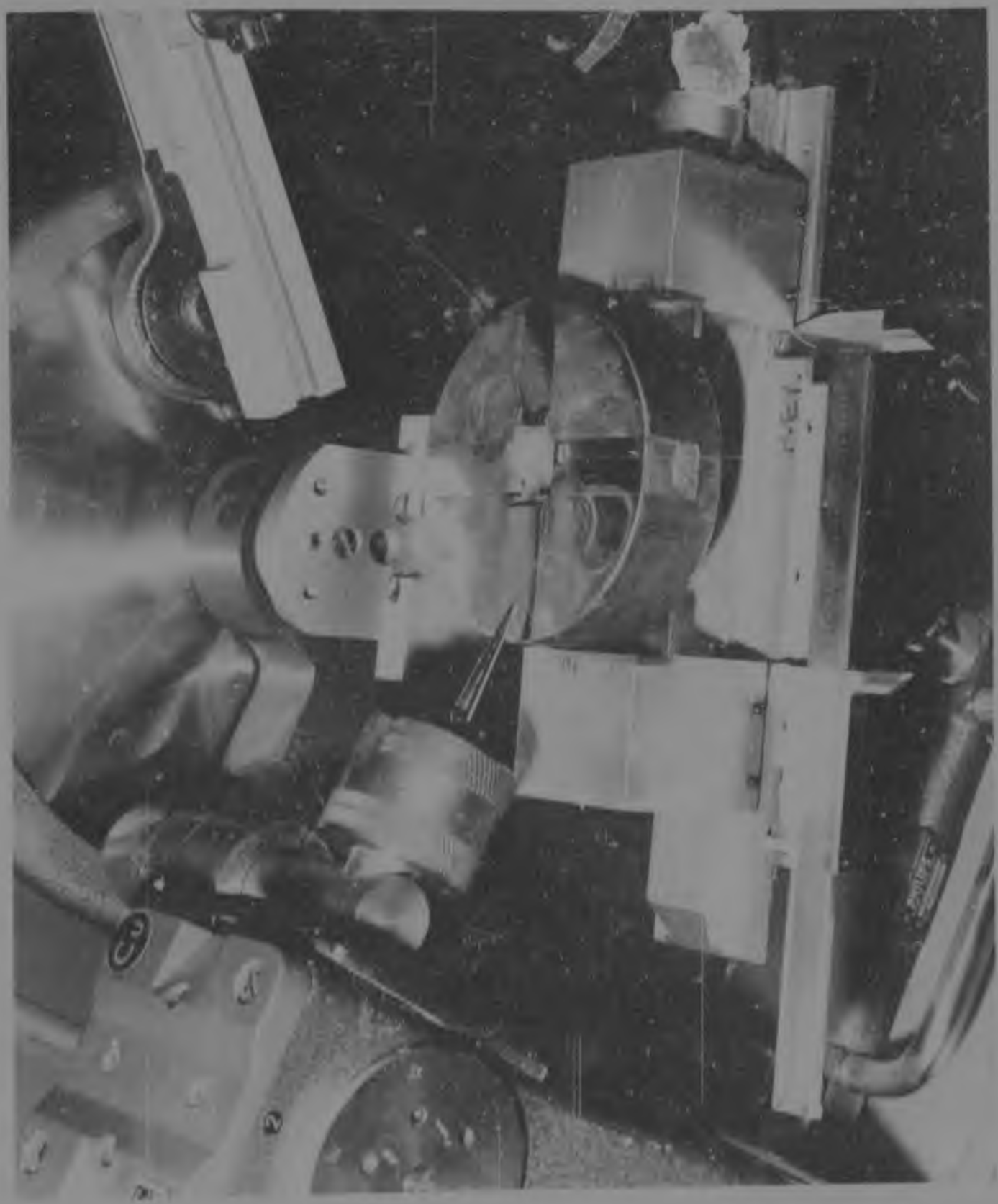

PHOTOGRAPH II.4 The modified X-ray unit used for the measurement of residual stresses in the drill-bit analogue - close-up view.

from Table VII. Figures 26 to 34 represent the X-ray strain-data measured in the 45^0 direction along the 45^0 traverses, i.e., data from Table VIII. Finally Figures 35 to 43 represent the X-ray strain-data measured in the y-direction along the y-traverses, i.e., data from Table IX.

All the data of these Figures 17 to 43 are plotted as strain versus distance along the respective traverse. Each calculated strain value is an average of the strain across the width (2.5 mm) of the X-ray beam and is plotted along the respective traverses at the respective co-ordinate of the centre point of the X-ray beam. Next the curves or lines of best fit were constructed to fit these data points.

Figures 17 to 25 and 35 to 43, the x- and y-strain traverses respectively, indicate the decay of strain with distance from the x = 0 and y = 0 interfaces respectively. Figures 26 to 34, representing the 45^0 traverses do not indicate any similar strain decay as these traverses start and end at the two stress initiating interfaces, i.e., the two interfaces fe' and fa'.

From Figures 26 to 34 it may be seen that the strain-distance relationship for each traverse varies over a small range of strain values only. The decay of strain for the 45^0 traverses can only be observed when comparing the mean value of the lines of best fit for each traverse. This value decreases for each successive 45^0 traverse, whose distance s from point f increases. S is measured as the length of the normal from point f onto the 45^0 traverse, i.e., along the line fm (Figure 16 (b)).

It may be observed that the difference between the maximum and minimum values of measured strains is greater for the x- and y-traverses in Figures 17, 18, 20 and 35 to 38 than for the x- and y-traverse strain relationships in Figures 21 to 25 and 39 to 43. Therefore the precision of strain measurement

has a percentage smaller effect on the precision of the curves of best fit of Figures 17, 18, 20 and 35 to 38 than on the curves or lines of best fit of Figures 21 to 25 and 39 to 43. Consequently the curves of best fit through the data points of Figures 17, 18, 20 and 35 to 38 have a higher coefficient of correlation than the lines or curves of best fit through the data points of the Figures 21 to 25 and 39 to 43.

This decrease in correlation between the data and the curves or lines of best fit is important, as these lines and curves are used next to evaluate the strain data in directions x, y and 45° for each point P(x,y) in the sector surface.

It is impossible to ascertain, if the strain data in Figure 19 exhibit the same trend as those in Figures 17, 18, 20 and 35 to 38, because the length of traverse along which strains were measured was restricted by the presence of etch pits in the steel caused by uneven electrolytic polishing. It is however very likely to be similar, because the trend exists along strain measurement traverses on either side of the traverse in Figure 19, as shown by Figures 18 and 20, as well as by the approximately equivalent y-traverses of Figures 36 and 37.

The precision of the strain data along the traverses of Figures 22 to 25, 30 to 34 and 40 to 43 approaches the magnitude of the measured strains along these traverses. Hence this reduces the importance of these strain traverses with respect to the overall strain distribution in the sector, as the percentage error in position of the lines of best fit is greatly increased.

It may be concluded that the x- and y-traverse strain relationships initiated at edges Fa and Fe within a radius of 10 mm from point F (Figures 17 to 21, 35 to 37) as well as the 45° traverse strain relationships within a distance y = 10 mm from point F along Fa (Figures 26 to 29) have

the higher degree of precision and hence are the more important for the following calculations of the residual stress pattern.

7.2 Derivation of the Residual Stress Pattern in the Analogue Surface from X-ray Strain Data

Because of experimental difficulties in locating the area to be irradiated, the three grids of e_x, e_y and e_{45} strain data do not superimpose. For any given point P on the surface it is required to know strain data in three directions to permit evaluation of the principal stresses and their direction. It was there ore essential to derive a method which validly interpolated strain data in three directions for any point P on the surface. The graphical method used is discussed in Appendix D and its application to the strain data of tables VII, VIII and IX yields values for the strain in directions x, y and 45°, i.e., e_x, e_{45} and e_y, for each point P(x,y) in the surface of the sector. These strain values have been determined from two separate graphical interpretations of the experimental X-ray data for the three grids. These two separate interpretations of the same data make it possible to determine the strains in the areas of the sector for which one or the other has no equivalent values. To elucidate this matter it is necessary to consider the x- and y-traverses of Figures 16(a) and (c). Consider the e_x x-traverse of Figure 16(a); obviously the e_y and e_{45} x-traverses straddle the same positions on the sector surface. These exclude any strain values whatsoever across the gap 13.7 mm $< x <$ 23 mm as no experimental x-traverses were obtained in this gap, because it contains the uneven area A, which is the overlap of the two superimposished areas 1 and 2 of Figure 15.

The y-traverse of e_x, e_{45} and e_y data do however yield strain values near this area from the curve of best fit through the data points. No actual measurements are made in the above gap, but the presence of strain values before and after the gap, warrant the extrapolation of the curve of best fit to cover the gap between the two sets of data points (as shown in Figures 35 to 43), yielding valuable strain data in this area.

However / - 54 -

However these y-traverses of ε_y, ε_{45} and ε_x data do not yield any strain data across the gap 13 mm $< x <$ 23 mm, corresponding to the uniform area B, the overlap of the two electropolished areas 1 and 3 of Figure 15. The x-traverses of ε_x, ε_{45} and ε_y data however do yield strain data in this area for reasons similar to those discussed for the y-traverses across area A (Figure 15).

Hence the two parallel calculations serve to confirm one another and yield complementary data.

The calculation of the state of stress at any point P(x,y) in the analogue sector was performed using data from the ε_x, ε_{45} and ε_y loci of the x- and y-traverses and is presented in Tables X and XI respectively. All strain data of the Tables X and XI are used in an algebraic evaluation of Mohr's circle of strain (see Appendix I), results of which are recorded in the same tables.

Tables X and XI yield values for the principal strain, and also for corresponding principal stresses, the angular relationship α of principal strains to the x-axis, the sum of the principal stresses and the difference of the principal stresses.

From the data of Tables X and XI the following relationships are plotted on a diagram of the sector source of the analogue for example to obtain the state of stress in the sector.

1. The σ_1 and σ_2 isobars, which constitute the loci of points having equal values of principal stress σ_1 and σ_2 (Figures 61 to 64).
2. The isoclinics, which are the loci of points, tangents to which represent the principal directions of stresses at the point of tangency (Figures 65,66).
3. The isomachics, which are the loci of points having equal values of ($\sigma_1 + \sigma_2$) (Figures 67, 68).

4. The isoclinics/-55-

4. The isoclinics, which are the loci of points having the same principal directions of stress (Figures 69, 70).
5. The isochromatics, which are the loci of points, having equal values of (σ_1 - σ_2) i.e., these curves represent twice the magnitude of the shear stress on the surface of the sector (Figures 71, 72).
6. Maximum shear trajectories, which are the loci of points, tangents to which represent the directions of the maximum shear stresses at the points of tangency (Figures 73, 74).

Using the loci as described in above paragraphs 1 to 6 the state of stress at any point P(x,y) in the steel sector surface is described completely. At this stage of the discussion it is important to consider a further variable in the accommodation of strain, viz., the effects of the observed variations in the widths of braze along the x- and y-interfaces. Appendix G quotes the data on the respective braze widths; examination by microscope showed that the width of the layer of braze in the x-direction is approximately thirty three per cent larger than the braze width in the y-direction, the respective figures being 0.36 ± 0.03 mm and 0.27 ± 0.03 mm. Therefore a larger proportion of the differential thermal contraction between hard metal and steel can be accommodated by the larger volume of braze along the x-axis. Consequently the stresses near points 0 and x should remain comparable in magnitude, but a faster decrease in the magnitude of this stress is anticipated along the y-axis, and the tensile stress generated parallel to this interface should be of a lower magnitude than that parallel with the y-direction brazed interface.

The difference in braze width, with the associated difference in magnitude of stress along the brazed interfaces, should disrupt the predicted x- and y-direction symmetry to a certain extent. Of the previously described stress pattern loci those defining the magnitude of the principal and shear stresses present in the sector surface should be noticeably affected by the difference in braze width.

1. Isobars

The isobar diagrams of Figures 63 and 64 depict the distribution of the principal stress (σ_2) across the surface of the analogue sector. The maximum compressive stress values occur at the unbraced edges of and of (Figure 14) and equal 195 to 237 MN/m^2.

The compressive stress decays with increasing distance along the x- and y-braced interfaces as well as with increasing distance towards the centre of the steel sector surface.

As anticipated from the difference in brace widths, the principal stress σ_2 decays more rapidly along the y-axis than the x-axis. As a result, at approximately 20.3 mm along the x- and y-axis, the discrepancy between the $(\sigma_2)_x$ and $(\sigma_2)_y$ stresses has widened to 40 MN/m^2. Therefore the isobars are not completely symmetric about the bisector to .

The distribution of the complementary principal stress σ_1 across the sector surface is presented in Figures 61 and 62. This principal stress σ_1 is also compressive in character at the unbraced edges of and of, but is of a lower magnitude than σ_2; the maximum value for σ_1 being 55 to 72 MN/m^2. With distance from the centre and along the braced interface, viz., ou' and ou'', σ_1 decreases to zero and then changes sign reaching a tensile stress of approximately 70 MN/m^2. Moving towards the centre of the steel sector, σ_1 decreases to zero.

Again the differing brace widths along the x- and y-axis affect the magnitude of the principal stress. At distances of 20.3 mm along the x- and y-interfaces the discrepancy in the magnitude of the principal stress σ_1 is approximately 35 MN/m^2. This value is similar to the quoted precision in relative stress measurements and hence is not significant. However a definite trend towards lower magnitudes exists along

the y-axis and therefore this can be attributed to the differing braze widths.

The data in all four diagrams (Figures 61 to 64) are symmetrical about the bisector fm within a sector of 10 mm radius from point f. However the variation in strain accommodation by the braze is reflected in a disruption of the symmetry of the isobars about bisector fm beyond this 10 mm radius.

The following anomalies occur : In the vicinity of x = 12,7 mm and y = 12,7 mm in Figures 63 and 64, i.e., towards the centre of the steel sector, the values of σ_2 are larger than at adjacent positions closer to the brazed interfaces.

Furthermore the σ_1 values in the vicinity of the braze from x = 22 to 32 mm along the y-axis (Figures 61 and 62) also show discrepancies. The σ_1 stress value along the y-axis increases in magnitude normal to the brazed interface.

These differences are further highlighted by the graphs of the resultants (Figures 69 and 70), which show a considerable discrepancy in the magnitude of angle α between the above mentioned positions with anomalous stress data and the adjacent positions.

2. Isoclines

The isoclines in Figures 65 and 66 give additional information about the principal stresses. These diagrams show the direction in which σ_1 and σ_2 act in the surface of the steel sector. The tangent to the curves on the diagram at the point P(x,y) represents the direction in which the respective principal stress acts.

At positions close to point f in the sector the stress initiated at the two mutually perpendicular brazed joints have an equal effect on the resultant stress so that σ_1 and σ_2 act in directions which

act in directions which subtend angles of 45^0 to the x- and y-axes.

Along the x-axis, the effect of the stress initiated at the insert No. 3. becomes important, and the effect of the stresses generated at insert No. 1. (the y-axis) becomes negligible. Hence the principal stresses in this region act in directions parallel and normal to the brazed interface of insert No. 3. as is indicated in Figures 65 and 66. Similarly along the y-axis the principal stresses rotate from 45^0 to directions parallel and normal to the brazed interface of insert No. 1. Still further along the y-axis the direction of the principal stresses rotate away from these angles. Furthermore, in the area defined by x = 10 to 15 mm, y = 10 to 13 mm the directions in which the principal stresses act are erratic. These two anomalies are associated with those mentioned previously for the σ_z isobars and are discussed later in this section.

3. Isopachics

Figures 67 and 68 represent the isopachics in the surface of the primary sector. These figures show the magnitude of the sum of the principal stresses ($\sigma_1 + \sigma_2$), and indicate the areas of tension and compression in the steel sector surface. Near point 1, where the two compressive stresses generated at the two brazed joints are superposing, the steel sector is in considerable compression, $(\sigma_1 + \sigma_2) = -272\ MN/m^2$. Away from this area the compression is reduced as the stresses decay with distance from their points of initiation and the tensile stress initiated parallel to the brazed interfaces becomes significant in magnitude. In some isolated areas, particularly along the y-axis, are normally expected to exist. In the area defined by x = 0 to 6 mm and y = 27 to 32 mm a slight tension exists adjacent to the braze gap in the steel, which subsequently increases in magnitude with increasing y.

The zero $\sigma_z = 50$ c

The zero stress region extends over a considerable distance along σ'1 and σ'2, indicating that the tension generated parallel and adjacent to the brazed interfaces has a compressive counterpart of equal magnitude normal to these interfaces.

The effect of the different braze width is again apparent when considering stress data adjacent to the brazed interfaces. Along the x-axis the ($\sigma_1 + \sigma_2$) stress values decay more quickly and eventually reach tensile values in contrast with the slower decay along the y-axis, where the ($\sigma_1 + \sigma_2$) values only approach zero-stress. The difference in magnitude is again approximately 35 MN/m^2; this phenomenon is of course expected as it is directly related to the differences in magnitude of principal stresses along the x- and y-axes.

Again the x- and y-symmetry of stress distribution is disrupted along the brazed interfaces, in contrast with the continued symmetry between the unbrazed axes ox and oy. The fact that symmetry along ox and oy is unaffected, in contrast with the disruption of the brazed interfaces, again points to the difference in braze width as the likely cause of disruption of symmetry of stress patterns.

4. Isoclinics

Figures 19 and 20 show the positions of the isoclinics in the sector quarter. These are the loci of points in the stressed model, which have the same directions of principal stresses. The angle α represents the inclination of the principal stress with respect to the x- axis. Along the line Oc, bisecting the right angle xOy, in model of symmetry, i.e. α = 45°. Any angle β in area c'Oc greater than 45°, e.g. the isoclinic of α = 70°, has a corresponding angle 1 in area a'Oc, with which it should be symmetric, e.g. isoclinic α = 20° in this

case. Symmetry about the bisector fm is apparent, particularly in the area close to the unbrazed edges ei and af. However along the x-axis and y-axis, beyond x = 15 mm and y = 15 mm respectively, symmetry between these two axes is less apparent. Along the x-axis there exists a large area of $\alpha = 0^{\circ}$, while along the y-axis α decreases to zero and then changes even further to negative values. A consideration of the precision involved clarifies this anomaly which is associated with the euqally anomalous principal stress values in this area and the different brazewidths. The precision of strain measurement, e = .0001, determines the precision of the angle α at high and low values of stress. Near point f, in the steel sector, where both principal stresses are large and compressive, this precision is $\delta\alpha = 16^{\circ}$ (Appendix F). Along the y-axis at lower values of stress, this precision in the determination of α deteriorates to $\delta\alpha = 23^{\circ}$. Consequently most of the negative values for angle α along the y-axis are within the limits of precision of the calculation, assuming the true angle α to be zero degrees. Therefore, due to the large possible error in angle α at distances along the x- and y-axes, the isoclinics in these areas lose most of their significance.

A similar reasoning explains the erratic values of angle α at positions beyond point 1 along the line fm. Here the directions of the principal stresses vary widely, which may be due to the previously discussed low precision, which is associated with areas of low residual stress.

5. Isochromatics

The shear stresses associated with the stresses generated along the x- and y axes, are calculated from the principal stresses. The isochromatics in Figures 71 and 72 depict the distribution of double the maximum shear stress - $2\tau_{max} = (\sigma_1 - \sigma_2)$, in the surface of the steel sector.

The shear stress τ_{max} attains high numerical values of $\tau = 100\ MN/m^2$ when the principal stresses σ_1 and σ_2 have large numerical values but are of opposite sign. Hence near point I in the sector, where both σ_1 and σ_2 are large, but of equal sign, the highest values of τ_{max} are not found. At 7.5 mm from I along either the x- or y-axis, the principal stress σ_1 changes sign and becomes tensile, while σ_2 remains compressive (Figures 61 to 64). At the above noted two positions the highest values of τ_{max} occur as shown in Figures 71 and 72. Again in the areas 19 to 32 mm along the x- and y-axes, the symmetry between these two axes is disrupted. This is expected, as the shear stresses are calculated from the σ_1 and σ_2 principal stresses, which showed a discrepancy in magnitude over the same areas (Figures 61 to 64). The difference in average τ_{max} between the positions adjacent to the two brazed interfaces away from point I is approximately 35 MN/m^2 which is again attributed to the variation in strain accomodation by the braze due to the different braze widths.

6. Maximum Shear Stress Trajectories

The maximum shear stress occurs in directions which subtend angles of 45° to the direction of the principal stresses. Therefore the maximum shear stress trajectories, indicating the direction of the maximum shear stress at any position in the sector surface, are calculated from the values of angle α in Tables 3 and 4 and the isoclinics in Figures 69 and 70.

These maximum shear stress trajectories are presented in Figures 73 and 74. Again analogous to the isoclinics, the angles of maximum shear stress direction are calculated with respect to the axis of symmetry of the sector, the bisector at an angle of 45° (Figure 75). The trajectories of Figures 73 and 74 show that the direction of the maximum shear stress changes from parallel to the x- and y-axes near point I to angles of 45° with intersecting distance along the x- and y-axes. At these

angles see / - 62 -

angles are calculated from the isoclinics of Figures 69 and 70 similar erratic angles are present in the area beyond point 1 along the line fm. Here, near the line fm, the maximum shear stress directions deviate from the pattern observed in the remainder of the analogue sector.

All the previously discussed loci of Figures 61 to 74 have been calculated from the same experimental data and hence will show similar anomalies. The anomalies have been observed in areas 19 to 32 mm along the x- and y-axes and beyond point 1 along the bisector fm (Figure 14). At these positions in the steel sector, the observed residual stresses are far smaller than in the area close to point f, and hence the precision of relative stress measurement, being 34.5 MN/m^2, will introduce a larger percentage error in these results. This is particularly important with regard to the calculation of the direction of the principal stresses and maximum shear stresses. The precision of measurement of angle α decreases from 16^0 near point f to 23^0 along the x- and y-axis.

Therefore the trends of the loci discussed in the area close to point f, i.e., the sector surface within radius 10 mm from point f, have the higher precision and are more significant.

Summarising the residual stress pattern as measured in the surface of the steel sector and presented by Figures 61 to 74, the following description emerges:

1. Both principal stresses are large and compressive near point f and similar principal stresses are present near the inner intersections a_1' and a_2', where σ_1 becomes tensile and σ_2 remains compressive but decreases in magnitude. This symmetry is disrupted at x > 10 mm and y > 5 mm due to the variation in strain concentration of the different fringe orientations.
2. The stress pattern is symmetric about the bisector fm.

(The Maximum ... 63 >

3. The maximum shear stresses occur at a position adjacent to the brazed interfaces at $x = 5$ to 8 mm and $y = 5$ to 8 mm.

4. The state of stress near point 1 is compressive, but decreases to zero and turns tensile adjacent to the brazed interfaces for $x > 10$ mm and $y > 10$ mm.

7.3 Finite element analysis of the analogue surface plane

A structural analysis of the analogue surface plane was attempted using finite element analysis. This method permits the calculation of stresses and displacements in two- and three-dimensional structures of any shape or size. The analysis consists of three parts, first a structural idealisation by division of the specimen into discrete elements, secondly an evaluation of the element properties and lastly a structural analysis of the element assemblage. The theoretical background and application to engineering structures have been developed over the last ten years and an excellent review of the basic principles and its applications to various structures is provided by Zienkiewicz [28].

A summary of the analysis is as follows. The two-dimensional body is subdivided into discrete elements, which are assumed to be interconnected only at the corners, which are the nodal points. It is very important to make the right subdivision, because the analysis is actually performed on this structure and the results are only valid as long as the behaviour of the substitute structure closely approximates that of the actual structure. Obviously, when under load, neighbouring elements would deform independently except at the nodal points, if they were connected at the nodal points only. It is required that each element deforms similarly to the deformations developed in the corresponding region of the continuum. Therefore the elements have to be reduced small enough to approach this condition.

The stress-strain/-che-

The stress-strain characteristics of an element are represented by the relationship between forces applied to the nodal points and displacement of these nodal points, resulting from these forces. This relationship may be expressed by the flexibility or stiffness matrix of the element. The stiffness matrix of a nodal point is derived from the element stiffness matrices of those elements that share that nodal point. The equilibrium of the set of elements can be expressed by the following matrix equation

$$[F] = [K] . [r]$$

where $[F]$ is the matrix of all nodal point force component matrices

$[K]$ is the matrix of all nodal point stiffness matrices

$[r]$ is the matrix of all nodal point displacement component matrices.

The above matrix equation is divided into a series of simultaneous equations, one for each nodal point, and these equations are then solved by an iterative techn que using a computer program.

The structural idealisation of the analogue surface is presented in Figure 84. Triangular elements were selected and the size of the smallest elements was determined by the thickness, 0.3 mm, of the brazed joint between the sintered carbide insert and the steel. The element size across the length of the brazed joint remains constant and a row of the same size elements was selected for the immediately adjoining sintered carbide and steel. At the location, where the thermal stresses are generated, i.e. at the braze, it is very important to have a very small element size, because the smaller the element size the more accurate the analysis is. With distance away from the braze into the steel and the sintered carbide, the element size is less critical and was increased to reduce the total number of elements in the whole structural assemblage.

this reduces / - 65 -

This reduces the computing time required to complete the analysis; without materially affecting the accuracy of the results.

The program used to evaluate the structural analysis was adapted from an existing program [29], which computes thermal stresses from the material properties of the elements, the temperature interval of cooling and the co-ordinates of the nodal points.

The critical steps in this finite element analysis are the selection of the element size and the assumptions required to allow for the three dimensional analysis. Even though the X-ray strain measurements are of a plane stress system, these stresses had been generated by the thermal contraction of the three dimensional analogue and the positive volume change of the steel during the austenite to martensite transformation reaction. The finite element analysis is two-dimensional by selection and therefore fundamentally disregards the three-dimensional origin of the thermal stresses and corrections to the analysis were therefore made. Due to the limiting influence of the braze thickness on the selection of the smallest element size, a three-dimensional finite element analysis of the analogue was not attempted, because the computing time required is prohibitive.

Residual stresses in the analogue are only generated [illegible] the braze solidification temperature. Over the first few degrees of cooling below this temperature, the elastic limit of the braze is extremely small in magnitude and any stress [illegible] is relieved by plastic flow of the braze metal. In the finite element analysis it was assumed that the stresses generated over the first one hundred degrees centigrade below the braze solidification temperature are largely relieved by plastic flow and hence have negligible magnitude. A temperature [illegible] was therefore assumed to be the temperature below which significant residual stress generation would result in appreciable

residual

residual stress. Since no data of the magnitude of the elastic modulus of the ferric brass could be found, and since diffusion effects between the brass, steel and sintered carbide create new intermetallic phases which change the elastic modulus of the pure brass metal, the magnitude of the elastic modulus was estimated from the elastic moduli of the brass components and assumed to be $E = 100000\ MN/m^2$. Values for the coefficient of thermal expansion and Poisson's ratio were estimated from a consideration of the brass constituents and taken as $\alpha = 20 \times 10^{-6}\ /^{o}C$ and $\nu = 0.35$.

The austenite to martensite transformation of the EN30B steel has the following characteristic temperatures [30], $M_s = 290^{o}C$ and $M_{90} = 150^{o}C$ and the volume change associated with this reaction is represented by the positive linear change of 36×10^{-4} inch/inch as determined dilatometrically by Russell and Macrocordis[31].

Bearing the above consideration in mind, four phases are distinguished over the temperature interval $534^{o}C$ (brazing solidification temperature) to room temperature.

1. Temperature interval $534^{o}C$ to $534^{o}C$. This latter temperature represents a hypothetical point during the cooling cycle, above which temperature a negligible amount of residual stresses are generated, because of the ductile plasticity of the brass metal above $534^{o}C$, just below its solidification temperature.

2. Temperature interval $534^{o}C$ to $290^{o}C$. Over this temperature interval the steel is austenitic and hence has the coefficient of thermal expansion $\alpha = 21 \times 10^{-6}\ /^{o}C$. The elastic modulus of the brass is assumed to average $E_{534-290} = \frac{1 + 100000}{2} = 50000\ MN/m^2$, which allows for the reduction in magnitude of the elastic modulus at elevated temperatures.

3. Temperature interval 290°C to 170°C. Over this interval the steel increases in volume, the linear expansion is taken to be 56 x 10^{-4} inch/inch as discussed previously. Hence the average coefficient of thermal expansion of the steel is

$$\alpha = \frac{-56 \times 10^{-4}}{120} = -46.7 \times 10^{-6} /^{\circ}C$$

This is the nett result of the positive volume change associated with martensite formation and the negative volume change due to shrinkage upon cooling. The martensitic reaction is estimated to have $M_f = 170^{\circ}C$. The elastic modulus of the brass is assumed to average

$$E_{290-170} = \frac{2\ E\ brass}{3} = 33333\ MN/m^2$$

This decrease in magnitude allows for the still present, but reduced temperature effect on the magnitude of the elastic modulus.

4. Temperature interval 170°C to room temperature. Over this temperature interval the steel is completely martensitic and contracts according to the coefficient of thermal expansion for ferrite, $\alpha = 12 \times 10^{-6}/^{\circ}C$. Over this temperature range the elastic modulus approaches its value of $E_{brass} = 100\ 000\ MN/m^2$. The temperature effect is far less pronounced on the steel and sintered carbide components, as the cooling interval is considerably below their respective solidification temperatures.

Values used over the whole interval are

$E_{steel} = 199500\ MN/m^2$; $\nu_{steel} = 0.29$

$\alpha_{WC-Co} = 5.4 \times 10^{-6}/^{\circ}C$; $\nu_{brass} = 0.36$

$E_{WC-Co} = 579000\ MN/m^2$; $\nu_{WC-Co} = 0.22$

$\alpha_{brass} = 20 \times 10^{-6}/^{\circ}C$.

The finite element construction of the surface plate of the analogue specimen was limited to a 1/8" sector, the sector [illegible] in Figure 16. Because of the obvious symmetry of the four sectors and the symmetry of each sector with respect to its

symmetry / − 68 −

bisector, the line Cfm in Figure 14 which is a twofold axis of symmetry, each 45^{o} sector is equivalent to the next and the finite element analysis may therefore be restricted to the one 45^{o} sector.

The centre of the analogue surface plane is a void and is located in between the four sintered carbide inserts (Figure 14). Therefore a structural analysis of the 45^{o} sector does not incorporate the fact that the analogue is a steel continuum in the volume below the sintered carbides and the central void. This presence of the steel continuum will influence the dimensional contraction of the central void.

It was attempted to incorporate the indirect effect of the steel continuum on the shrinkage of the surface plane by including elements in the surface sector of the central void, area Cfed (Figure 14), with material constants

$$\alpha = \alpha_{steel}, \quad \nu = \nu_{steel}, \quad E = \frac{E_{steel}}{10}$$

The latter reduced modulus of elasticity was so selected that the contraction of the steel continuum affects the central void and surrounding material in a reduced manner, i.e. a specific strain in the steel continuum would in the surface plane generate only one tenth of the stress it would generate in the plane of the steel continuum.

The boundary conditions of the analysis, i.e. the nodal points, which have zero or one degree of freedom are the following.

1. Point C (Figure 14) is taken as the origin of the coordinate system and is defined to be fixed in both the x and y directions, i.e. it has zero degrees of freedom. In actual cooling events, C is the geometric centre of the surface plane about which the analogue surface contracts and hence has no degree of freedom.
2. The nodal points on the line Cd have one degree of

freedom / - 69 -

freedom and may move in the x-direction only.

3. The nodal points on the line Cfm are defined to move only along the line Cfm.

Both the nodal points of points 2) and 3) above, lie on a diameter of the analogue surface plane circle and hence, by definition, can only move along this diameter. The finite element analysis program, incorporating the above conditions and prerequisites, yielded values of principal stress σ_1, and σ_2 from which the σ_1 isobars of figure 80, the σ_2 isobars of figure 81, the ($\sigma_1 - \sigma_2$) isochromatics of figure 82 and the directions of the principal stress in figure 83 were plotted.

7.4 Finite element analysis versus the X-ray diffraction residual stress pattern

Before comparing the finite element analysis of the differential thermal contraction of the analogue with the residual stress pattern as presented in figures 61 to 74 and determined by X-ray diffraction measurements, the following fundamental differences between the two approaches should be realised.

1. The X-ray technique has measured the strains in a plane stress situation, which is the result of three dimensional differential contraction in the body of the analogue.
2. The finite element technique however is a plane stress analysis which assumes the differential contraction to be a two dimensional phenomenon in the surface plane of the analogue.

A small correction for the three dimensional origin of the plane stress situation was included by introducing a set of finite elements in the central void. These elements were allotted a reduced value of the modulus of elasticity of steel to allow numerically for the indirect effect of the steel continuum below the void. This modification hardly alters the

two dimensionality of the analysis however. The σ_1 isobars of figure 80, determined by finite element analysis, indicate the presence of stresses of compressive character near point P in the steel surface. These stresses change to tensile values with increasing values of s , i.e. towards the circumference of the sector. The similarity between the σ_1 isobars from this finite element analysis and the X-ray strain measurements, Figures 81 and 81, is pronounced in distribution and magnitude. The only difference in magnitude is the slightly higher level of tensile stresses near the circumference as computed by finite element analysis, i.e. + 150 MN/m^2 versus 70 MN/m^2 for the experimental work.

The maximum principal stress σ_1 in the sintered carbide surface is concentrated at either end of the insert, reaching values up to 200 MN/m^2 in tension.

The σ_2 isobars of figure 84 in the steel surface are compressive in character and reach maximum value of 700 MN/m^2 close to point P , but not at this point, its magnitude increases rapidly along line 1e and the solidification reaching zero-stress values circumferentially. The correspondence between the isobars in figure 81 and those determined experimentally (Figure 61, 62) is less close than for the σ_1 isobars. The decrease in magnitude near transition P is noted for the isobars in figure 81, which reach zero values in contrast to the isobars in figure 83 in which do not reach zero stress values. The σ_3 isobars of figure 85 in the sintered carbide surface are completely compressive with a stress concentration occuring parallel and adjacent to the brazed seal with a maximum value of 1 near point P (figure 10).

The maximum shear stresses from the finite element analysis are presented in figure 86 as the isocontours and show a distribution in the steel surface which is similar to those experimentally determined and presented in figures 71 and 72. There is a difference in magnitude with the finite element analysis values having a maximum of $\tau_{max} = 150$ MN/m^2 in contrast to the maximum value of $\tau_{max} = 90$ MN/m^2 in figures 71 and 72. The corresponding maximum shear stress in the

sintered carbide surface are concentrated parallel and adjacent to the brazed joint, having a value of 100 MN/m^2. In the centre of the carbide insert, the magnitude has decreased to 50 MN/m^2.

Figure 83 presents the directions of the maximum principal stress in the analogue surface. The second principal stress acts in a direction of 90^o to the arrows in Figure 83, as per definition of this principal stress. From this diagram it appears as if the tensile σ_1 stresses act mainly in the width direction of the sintered carbide; the σ_2 stresses tend to act in a direction along the length of sintered carbide.

The overall residual stress pattern determined by finite element analysis of the analogue at room temperature, appears closely similar to the experimentally determined one.

The residual stresses in the sintered carbide, which have not been determined experimentally on the analogue surface, are found to have maximum tensile stresses near the 2 edges across the width of the sintered carbide, complemented by a concentration of compressive stresses adjacent to the brazed joint. These stresses are maximally σ_1 = 200 MN/m^2 and σ_2 = - 300 MN/m^2. The maximum shear stresses are also concentrated adjacent to the braze over the length of the sintered carbide and have a maximum value of τ_{max} = 100 MN/m^2.

Because the finite element analysis was performed in four discreet cooling steps over separate temperature intervals the stress pattern at the end of each step was plotted to analyse the change in stress distribution associated with each contraction or expansion over each temperature interval.

The residual stresses generated over the first temperature interval, 634^oC to 534^oC, were assumed to be negligible and Figure 76 and 77 present the finite element analysis of the stresses in the analogue at 290^oC, the end of the temperature-

interval / - 72 -

interval 334°C to 290°C, during which the steel is completely austenitic. The σ_1 and σ_2 isobars (Figures 76 and 77) are found to be distributed similarly to those in Figures 80 and 81, the magnitude of the isobars in Figures 76 and 77 are however found to be far in excess of those in Figures 80 and 81, with maximum values of $\sigma_1 = 600\ MN/m^2$ and $\sigma_2 = -1200\ MN/m^2$.

Figures 78 and 79 present the σ_1 and σ_2 isobars of the residual stress pattern from the finite element analysis of the analogue after cooling to 170°C, at which temperature almost all the austenite is transformed to martensite and as a result the steel over the temperature-interval 290°C to 170°C has a positive volume change, which first cancels the residual stresses present at 290°C and at 170°C has its nett resultant residual stresses. This cancellation and new stress pattern imposition is shown by the fact that the σ_1 isobars of Figure 78 have a similar distribution to the σ_2 isobars of Figure 77 and the σ_2 isobars of Figure 79 have a distribution similar to that of the σ_1 isobars of Figure 76.

For all three residual stress patterns at room temperature, 170°C and 290°C respectively, the directions in which the principal stresses act were found to be very similar and Figure 83 is valid for all three stress patterns. The only difference is, as expected, that the arrows indicate directions of principal stress σ_1 for the stress patterns at 290°C and room temperature, but indicate directions of principal stress σ_2 for the stress pattern at 170°C.

A summary of events generating the residual stresses during the cooling interval from brazing temperature to room temperature appears to be as follows:

In the initially hot brazing temperature, the differential thermal contraction between tool, braze and sintered carbide is absorbed by plastic deformation of the braze

which is / - 73

which is extremely plastic at these tempera[illegible].

2. At lower temperatures down to 290°C, the austenitic steel, braze metal and sintered carbide contract differentially, which removes the stress distribution as described in figures 76, 77 and 83. Very large stresses are so generated, greater in magnitude than those of the stress pattern at room temperature.

3. From the M_s temperature, 290°C, to 170°C the steel transforms to martensite with an associated volume increase, while the braze and sintered carbide continue to contract. This causes the cancellation of the stresses previously generated by the contraction of the austenite, and this is followed by the establishment of a second stress distribution which is in effect the inverse of the former, with σ_1 isobars resembling the former σ_3 isobars etc. The magnitude of these stresses are also in excess of those present at room temperature. This stress pattern after the austenite to martensite positive volume change has a tensile state of stress near point P and affects a large area of the steel sector. This is quite apparent from the two graphs 78 and 79, where the tensile stress at the greater in magnitude than the compressive stress at the same position within a radius of 10 millimetres from point P in the st[illegible]. Hence the state of stress defined as the (σ_1 [illegible]) isoperibre is extremely tensile in character in nature as to the compressive state of stress for the stress pat[illegible] at 290°C and room temperature.

4. From 170°C to room temperature the steel again contracts as does the braze and the sintered carbide. This results initially in the amelioration of the stresses set up by the martensitic transformation, and is followed by the establishment of its own specific stress pattern defined by the compression of all three constants. As a result the stress pattern at room temperature resembles that at 290°C but is of a lower order of magnitude.

7.5 Discussion

Even though the finite element analysis does not allow for the three-dimensional origin of the residual stress in the analogue surface, the analysis results in a stress pattern closely similar to the experimentally determined stress pattern. This has the following implications and uses:

1. The computer output yielding a hypothetical residual stress pattern from finite element analysis may be considered to approximate the experimentally determined residual stress pattern in the steel surface of the analogue and hence save laborious experimental procedures.
2. The residual stress pattern in the sintered carbide inserts which could not be determined using the X-ray diffraction technique, may be assumed to resemble the residual stress pattern in these sintered carbide inserts from the finite element analysis.
3. The residual stress pattern in the analogue surface at elevated temperatures may be assumed to resemble the stress pattern obtained from the finite element analysis of the analogue differential thermal contraction at these temperatures.

During cooling from brazing temperature the behaviour of the steel matrix causes three successive residual stress patterns to be established.

Over the temperature interval 170°C to room temperature the residual stress pattern present at 170°C is cancelled by the contraction of the martensite, which opposes the volume increase from the austenite to martensite transformation which established the residual stress pattern present at 170°C.

It is proposed that at some temperature between room temperature and 170°C the analogue surface is almost completely free from any residual stresses due to differential thermal

contraction / - 75 -

contraction effects between the sintered carbide compact and the steel, and that the only residual stresses present are those generated by differential thermal contraction effects between the braze metal and the adjoining steel and the sintered carbide respectively. This latter stress pattern will be of comparatively negligible magnitude in the steel and the sintered carbide, because any differential thermal contraction is mainly absorbed by the braze, as it has the lower modulus of elasticity and hence absorbs the greater amount of the strain generated.

It is further proposed that the residual stresses as determined for the analogue surface will be very similar to the residual stress pattern in a plane normal to the longitudinal axis of a down-the-hole drill bit and intersecting the sintered carbide inserts through their upper portion below the cutting faces. The absence of flutes will introduce a less steep stress gradient in the steel of the analogue, but the stresses at the brazed interfaces should be similar because the finite element analysis indicated that these are purely a function of the cruciform geometry, the temperature-interval of cooling and the material constants. Similarly the absence of steel stock underneath the sintered carbide segments in the analogue will only affect the stress distribution at the circumference, but not at the brazed interfaces.

Therefore the residual stress pattern in the analogue surface directly adjacent to the brazed interfaces are thought to be very similar to the stresses in similar positions in a down-the-hole drill bit. The stresses at the circumference may differ between the analogue and the drill bit, due to more pronounced stress relief in the analogue steel by bending, which in the case of the drill bit is opposed by the rigidity of a long bar shaft of drill steel.

The reduction / - 76 -

The reduction in the magnitude of the residual stress pattern with an increase in temperature above room temperature can occur in practice, when under drilling conditions the drill head heats up. If the temperature of the drill head increases considerably during drilling the compressive nature of the residual stresses at the centre, near point f , may change to a tensile nature. This type of stress distribution is not favourable for fatigue loading conditions, which are present during drilling, and hence elevated temperatures during drilling should be avoided to prolong the working life of a drill.

7.6 Summary

1. It is anticipated that machining stresses in the steel surface of the drill-crown, introduced prior to brazing, are substantially removed by the austenitisation of the EN 30B steel during brazing.
2. Grinding stresses of considerable compressive magnitude are imposed on the drill crown surface after brazing. These stresses destroy the thermal residual stress pattern in the surface layers of the drill crown. This thermal residual stress pattern is generated during the cooling period from the brazing temperature and is present in the surface layers underneath the post-brazing grinding stresses.
3. The bisector of the blindly drilled angle between the two steel edges subtending the braze interfaces is a two-fold axis of symmetry in the mirror surface. This may be deduced from geometric considerations and is substantiated by the X-ray strain data. Symmetry of the residual stress pattern is not evident about this line but is probably disrupted by unequal stress relaxation in the braze associated with the different braze widths. Toward the geometric centre of the analogue the precision of the measurement of the strains is highest and hence the

text in this

loci in this area are the more significant indicators of the stress pattern.

a. The principal stresses in the steel are compressive and at a maximum near the centre of the analogue, the value being σ_1 = - 70 MN/m^2 and σ_2 = - 237 MN/m^2.

b. In the steel, away from the centre of the analogue and parallel to the two brazed interfaces, the principal stress σ_1 is tensile, the maximum value being σ_1 = + 90 MN/m^2. Normal to the brazed interfaces the principal stress σ_2 remains compressive, decreasing in magnitude towards the circumference of the analogue.

c. The principal stresses in the steel area adjacent to the two-fold axis of symmetry are parallel to this line. These directions change to 45° to the bisector, i.e. normal and parallel to the brazed interfaces, in positions further away from the axis of symmetry.

d. The state of stress in the steel sector area varies from compression to stress free, as indicated by the $(\sigma_1 + \sigma_2)$ sequence.

e. The direction of the maximum shear stress in the steel sector varies from parallel to the brazed interfaces, at the two-fold axis of symmetry, i.e. parallel with the brazed interfaces, with increasing distance from the bisector.

The maximum shear stress exists adjacent to the brazed interfaces at positions x = 5.4 to 12.7 mm along the x-interfaces and y = 5.4 to 12.7 mm along the y-interfaces. The maximum value of shear stress determined is τ_{max} = 83 MN/m^2.

4. A finite element analysis is used to calculate the thermal residual stress pattern from the specimen geometry and the material constants of the analogue components. This structural analysis yields a stress pattern, which is closely similar to the as measured stress pattern of

point 3.

5. The principal stresses in the surface of the hard metal inserts, balancing the residual stresses in the steel sector across the brazed interfaces, are assumed to be similar to those calculated by the finite element analysis. This assumption is made on the strength of the similarity between the stress patterns in the steel as determined from X-ray strain data and from finite element analysis.
The maximum stresses in the sintered carbide are respectively σ_1 = 200 MN/m^2 , σ_2 = - 300 MN/m^2 , τ_{max} 160 MN/m^2. Stress σ_1 is concentrated at the two edges of the carbide across its width, σ_2 is concentrated parallel and adjacent to the brazed joint, τ_{max} is also concentrated parallel and adjacent to the brazed joint.

6. The residual stress distribution in the analogue surface at elevated temperatures is thought to be similar to those calculated by finite element analysis on the strength of the correspondence between the two stress distributions, experimental and from finite element analysis, at room temperature.

8. Conclusions

1. A reliable X-ray method for residual strain measurement has been developed for EN 30B hardened steel. The measurements were calibrated by experiments using electrical resistance strain-gauges. Using this X-ray method, strains were measured over small circular areas of approximately 5.0 square millimetres which permits the experimental construction of residual stress gradient over small distances.

2. / comparative / -79-

2. A comparative investigation of the various surface treatment processes, which are or may be used during the final stages of production of sintered tungsten carbide composite, indicates that mechanical grinding, tumbling and shot and vapour blasting techniques introduce very high residual stresses in and considerable plastic deformation of the surface layers of the sintered compacts. A non-physical erosion finishing operation, viz., an electrolytic grinding process, was found to introduce minimal residual stress in and least plastic deformation of the surface layers.

   The greater proportion of all the residual stresses was found to be removed by the annealing process implicit in the brazing operation.

3. The close correspondence between the residual stress patterns in the analogue steel surface as constructed from X-ray experimental data and from finite element analysis has the following implications :
   a. The laborious experimental technique has validated the finite element analysis of cooling events in the analogue, so that the latter may be used for further residual stress problems under similar circumstances.
   b. The residual stress pattern at elevated temperatures may be estimated using the finite element analysis.
   c. Residual stresses in the sintered carbide compacts may be assumed to be similar to those determined by finite element analysis.

4. The residual stress pattern resulting from grinding and brazing in the surface layers of a percussion drill bit is complex. The extreme surface layers are in considerable compression, the magnitude and distribution of this state of stress being dependent on the geometry of the cruciform section and be caused by the large stresses

introduced / - 80 -

introduced during the post-brazing grinding. Underneath these grinding stresses, the residual stress pattern, generated by the differential thermal contraction, persists. An increase in operating temperature of the drill is thought to decrease the magnitude of the latter type of stress pattern, changing it to a tensile character. This could be detrimental to drill performance, as a tensile type of stress pattern is generally not beneficial under fatigue-loading conditions present during drilling.

REFERENCES

1. Laszlo, [illegible]. "Symposium on Internal Stresses in Metals and Alloys". Page 61.

2. L.P. Tarasov, W.S. Hyler and H.R. Letner. Proc. ASTM, vol. 57, pp. 601 - 622, 1957.

3. Christenson, A. and Rowland, E. Trans. A.S.M., 1953, vol. 45, p. 638.

4. Taira, S. and Arima, J. JSME Bulletin, 1964, vol. 7, No. 25, pp. 1 - 10.

5. SAE report TR 182.

6. Hawkes, G.A. Brit. J. Appl. Phys., June 1957, vol. 8, pp. 229 - 232.

7. Bolstad, A. Davis, R.E., Quist, W.E., Roberts, E.C. Metal Progress, July 1963, vol. 84, pp. 88 - 92, 118, 120, 122, 124.

8. Garrod, R.I. and Hawkes, G.A. Brit. J. Appl. Phys., 1963, vol. 14, pp. 422 - 428.

9. Ruud, K.F. Proc. ASTM, 1957, vol. 57, pp. 1282 - 1289.

10. Borel, G. and Hu, L.Y. Norelco Reporter, XI (3), July-September 1964.

11. Bond, W.B. Norelco Reporter, XIII (1), January-March 1966.

12. [illegible], [illegible]. Archiv für das Eisenh. Febr. 1964, vol. 35, pp. 133 - 140.

13. Timoshenko. "Strength of Materials", p. 210.

14. [illegible] and [illegible] A.S.M. Preprint 103, 1957, p. 14.

15. Ogilvie, R.E. "Stress measurement with X-ray spectrometer". M.S. Thesis, M.I.T., 1952.

16. Barrett, C.S. "The Structure of Metals", Mc Graw-Hill, New York, 1966.

17. Cullity, B.D. "Elements of X-ray diffraction". Addison-Wesley, London 1967.

18. Cobalt Monograph, Centre d'Information du Cobalt, Brussels, 1960.

/ - 2 -

References

19. Schöning, F.R.L. Internal Report. Physics Faculty, University of the Witwatersrand, South Africa.

20. Smithells, C.J. "Metals Reference Book". Butterworths, London 1967.

21. Kochanovska, Kronk and Mareak. Czeck J. Phys. vol. 13, p. 418, 1963.

22. French, D.N. J. Am. Ceram. Soc., May 1969, vol. 52, No. 5, p. 267.

23. French, D.N. J.Am. Ceram. Soc., May 1969, vol. 52, No. 5, p. 272.

24. Stokes, A.R. Proc. Phys. Soc., 1948, vol. 61, pp. 382 - 391.

25. Rachinger, W.A. J. Sci. Instr., vol. 25, p. 254, 1948.

26. Gillies, D.C. and Lewis, D. Powder Met., 11, vol. 22, p. 400, 1968.

27. Dieter, G.E. "Mechanical Metallurgy". p. 33. Mc Graw-Hill, New York, 1961.

28. Zienkiewicz, O.C. "The Finite Element Method in Engineering Science". Mc Graw-Hill. London.

29. C.S.I.R. Report MEG 614, Pretoria, South Africa, September 1969.

30. "Transformation Characteristics of Direct Hardening Nickel Alloy Steels". The International Nickel Corporation (Mond) Ltd. London, S.W.1, 1958.

31. Russell, T.F. and Mavrocordatos, C. J.I.S.I. May 1949. "Experiences in the Study of Isothermal Transformation".

APPENDIX 'A'

ELECTROPOLISHING OF HARDENED EN 30B STEEL

a / Electrolyte used :-

5.0 volume per cent H_2O
18.5 volume per cent $HClO_4$ 70 per cent
76.5 volume per cent $(CH_3CO)_2O$

Current density on surface of approximately 600 mm^2 :-

3.9 - 5.4 $m\backslash mp/mm^2$

APPENDIX 'B'

The Calculation of Particle Size D and lattice Strain of an Electrolytically Ground Sintered Compact

The K_α profiles of (001), (100), (101), (201) and (112) diffraction peaks are used to calculate the lattice-strain ε and particle size D .

The values for β are taken from Table IV. The following are the data required to evaluate graphically the Cauchy relationship.

$$\left(\frac{\beta \cos\theta}{\lambda}\right)^2 = \left(\frac{1}{D}\right)^2 + \frac{16\,\varepsilon^2 \sin^2\theta}{\lambda^2} \qquad (1)$$

(hkl)	$\frac{16 \sin^2\theta}{\lambda^2}$	$\left(\frac{\beta\cos\theta}{\lambda}\right)^2$
001	49.6	.018
100	63.1	.100
101	112.4	.181
201	302.0	.233
112	388.5	.177

The linear relationship of the equation (1) is defined by the data in above table. The construction of the locus is presented as line (1) in Figure 16, which has

slope $= \frac{0.10}{300} = 0.00033 = \varepsilon^2 \longrightarrow \varepsilon = 0.018$

intercept $= 0.08\mu m^{-2} = \left(\frac{1}{D}\right)^2 \longrightarrow D = 3.5\ \mu m.$

APPENDIX 'C'

Sample Calculation of Strain ϵ_ϕ from X-ray Data in Direction ϕ in a Steel Surface

X-ray intensity data measured for specimen surface angles $\psi = 0^0$ and $\psi = 45^0$ in direction ϕ are the following:

$\psi = 0^0$ / $2\theta^0$	Number of Pulses from counter	Time I secs	Time II secs	Time III secs	$I_o/_I$
$2\theta_1 = 154.7$	63548	2000	2520	2406	0.785
$2\theta_2 = 155.7$	[illegible]38	2000	1970	1388	1.000
$2\theta_3 = 156.7$	60613	2000	2540	2538	0.744

$\psi = 45^0$ / $2\theta^0$	Number of Pulses from counter	Time I secs	Time II secs	Time III secs	$I_o/_I$
$2\theta_1 = 154.8$	53000	1200	1631	1210	0.757
$2\theta_2 = 155.8$	70960	1200	1238	916	1.000
$2\theta_3 = 156.8$	57636	1200	1500	1146	0.800

The above data yields intensity as number of pulses from the proportional counter, received by the electronic counting circuit. The time column (I) is the time period over which pulses are counted. Column time (II) represents the number of seconds required to reach an intensity count of 60000 and 70000 pulses respectively for each angular setting $2\theta_1$, 2θ and $2\theta_3$.

Note in / - 2 -

Appendix 'C'

Data in Column Time (III) are the same time periods as recorded in Column Time (II), divided by the θ-dependent correction factors of Nicholls and Shipley [4], which correct the absorption dependent asymmetry of the diffraction peaks.

The last Column, $I_{o/I}$ represents the intensity ratios of the $2\theta_1$ and $2\theta_3$ positions relative to the $2\theta_2$ position, which is taken to be I_o. These intensity ratios are next used in the algebraic evaluations of the parabola equation to obtain the peak position $2\theta_p$.

$$2\theta_p = 2\theta_1 - \frac{c}{2}\left(\frac{3a + b}{a + b}\right)$$

where for $\psi = 0^o$

$a = 0.215 \quad b = 0.256 \quad c = 1.0^o \quad 2\theta$

hence $(2\theta_p)_0 = 154.7 + \frac{1.0}{2}\left(\frac{0.645 + 0.256}{0.215 + 0.256}\right) = \underline{155.656^o}$

and for $\psi = 45^o$

$a = 0.243 \quad b = 0.260 \quad c = 1.0^o \quad 2\theta$

hence $(2\theta_p)_{45} = \underline{155.849^o}$

Calculate ε_ϕ from equation (3) and equation (1)

$$\varepsilon_\phi = \frac{d_\psi - d_\perp}{d_\perp} \cdot \frac{1}{\sin^2\psi} \qquad (3)$$

$$n\lambda = 2d \sin\theta \qquad (1)$$

hence $d_\psi = \frac{n\lambda}{2 \sin\theta_\phi}$

and $d_\perp = \frac{\lambda}{2 \sin\theta_\perp}$

with this $\varepsilon_\phi = \frac{1/\sin\theta_\psi - 1/\sin\theta_\perp}{1/\sin\theta_\perp} \cdot \frac{1}{\sin^2\psi}$

for $\psi = 0^o$, $\sin\theta_\perp = \sin 77.828^o = .9775$

$\psi = 45^o$, $\sin\theta_\psi = \sin 77.925^o = .9779$

$\varepsilon_\phi = \left(\frac{1}{.9779} - \frac{1}{.9775}\right)(1.9775) = (1.02250 - 1.02302)(.9775)$

$= -.00041$ i.e., a compressive strain.

APPENDIX 'D'

Construction of Strain Values in Directions x, 45° and y for each point P(x,y) in the Steel Sector

To obtain the required strain data for each point P(x,y), the following constructions and calculations are carried out :

1. Using the respective strain data from the curves or lines of best fit of Figures 35 to 43, the x-direction traverse of the strain data in the y-direction, ε_y, is constructed, i.e. from each line or curve of best fit one strain value at a specific position y_1 (distance from insert No. 2) is obtained and all these strain values are used to construct the graph of ε_y versus distance along the x-direction traverse, which is the line parallel to the x-axis (insert No. 2) at distance y_1.
2. Similarly the x-direction traverse of all the strain data in the 45° direction, ε_{45}, from Figures 26 to 34 is constructed along the line $y = y_1$.
3. Using the x-direction traverses of ε_y and ε_{45} and the original x-direction strain data, ε_x, for the x-direction traverse the strain distribution at all points $P(x_1,y)$ along this x-direction traverse is calculated.

Analogous calculations and constructions are performed for the ε_x and ε_{45} values required for all x-direction traverses along lines $y = y_n$ together with the x-direction traverses of ε_y values. Hence the strain distribution for all points $P(x_n, y_n)$ in the analogue sector surface is known.

Analogously to the transposition of the ε_y and ε_{45} data along the y-direction traverses, the ε_x and ε_{45} data are also transposed along the x-direction traverses.

At this point / - 2 -

Appendix D'

At this point it is necessary to comment that the transposition of the strain data as described above introduces new errors. Besides the experimental error, due to equipment and surface preparation, the subsequent use of the curves of best fit through the transposed strain data may introduce an additional error.

Example - Construction of x-direction Traverse of y-direction Strain Data

The following construction is an example of the X-ray strain data transpositions.
Consider the y = 1.27 mm. traverse, i.e. the traverse of x-direction strain data (Figure 17) along the traverse y = 1.27 mm.

It is the aim to construct the loci of the y-direction and 45°-direction strain data along the same y = 1.27 mm traverse. To construct these two traverses, the y-direction and 45°-direction strain data at $\Delta y = 1.270$ mm. of curves in Figures 35 to 43 and Figures 26 to 34 respectively are acquired and plotted versus their respective Δx values along the y = 1.27 mm. traverse. Hence now for this traverse there exist three curves of strain in x, 45° and y-direction respectively versus distance in the x-direction. The data acquired from Figures 26 to 43 are quoted below.

Appendix 'b'

Δx mm	Δy mm	ε_y	Δx mm	Δy mm	a mm	b mm	ε_{45}
2.54	1.27	-.00090	0.53	1.27	1.27	0.75	-.00155
3.81	1.27	-.00100	2.33	1.27	2.54	3.30	-.00134
6.99	1.27	-.00068	6.32	1.27	5.71	8.25	-.00084
10.16	1.27	-.00056	11.33	1.27	8.90	16.00	-.00043
13.32	1.27	-.00039	14.00	1.27	10.79	19.82	-.00030
22.84	1.27	-.00038	16.70	1.27	12.70	22.88	-.00020
26.18	1.27	-.00040	27.87	1.27	17.78	33.76	+.00007
31.78	1.27	-.00038	30.60	1.27	22.56	43.92	+.00016
36.83	1.27	-.00045	36.43	1.27	26.66	51.54	-.00007

The two transposed x-traverses for ε_y and ε_{45° along $\Delta y = 1.27$ mm. can now be constructed. The y- and 45°-direction strain lines, ε_y and ε_{45° of figures 35 to 43 and 26 to 34 respectively are transposed in an analogous manner to the x-direction traverses over the range $5.82 \leq y \leq 11.75$ mm yielding analogous transposed x-traverses.

The x-traverses for all ε_y and ε_{45} data are presented in Figures 44 to 51.

The x-traverses for all ε_x and ε_{45} data are presented in figures 52 to 60.

APPENDIX 'C'

Mohr's Circle of Strain

Ref. p. 33-35 G.E. Dieter Mechanical Metallurgy
McGraw Hill 1961

The above reference describes the graphical evaluation of principal strain e_1 and e_2, shear strain γ and direction θ of principal strains with respect to the extraction from experimental values of the strains e_x, e_{45} and e_y.

These three strain data e_x, e_{45} and e_y completely define the Mohr circle and a computer program was written to circumvent the laborious graphical method of construction.

This computer program is based upon the following relationships

Mohr circle : Centre (x_{11}, y_{11}) , radius r
Principal strains are

$$e_1 = \varepsilon_{11} - r$$

$$e_2 = \varepsilon_{11} + r$$

$$x_{11} = \frac{e_x + e_y}{2}$$

$$r = \sqrt{\frac{(e_x - e_{45})^2 + (e_y - e_{45})^2}{2}}$$

$$2\theta = \cos^{-1}\left(\frac{e_x - \varepsilon_{11}}{r}\right)$$

Angle θ is determined with respect to the x-direction and is always positive except for the case

$e_x < e_{45} < e_y$, when $|e_x - e_{45}| > |e_y - e_{45}|$.

EXAMPLES

1. $e_x = -.00078$, $e_{45} = -.00010$, $e_y = +.00052$

then $x_{11} = -.00055$

and $s = \sqrt{\frac{(.00068)^2 + (.00022)^2}{2}} = .000505.$

and $2\alpha = \cos^{-1}\left(\frac{-.00078 + .00033}{.000505}\right) = 62.9^\circ,$

hence $\alpha = 31^\circ.$ $e_1 = -.00106,$ $e_2 = -.00005.$

2. $e_x = -.00040$, $e_{45} = 0$, $e_y = +.00020$

then $x_{11} = -.00010$

and $s = \sqrt{\frac{(.0004)^2 + (.0002)^2}{2}} = 0.000316$

hence $2\alpha = \cos^{-1}\left(\frac{-.00040 + .00010}{.000316}\right) = 18.5^\circ.$

and $\alpha = 9^\circ$, as $|e_x - e_{45}| > |e_y - e_{45}|$

and $e_x < e_{45} < e_y.$

$e_1 = -.00050$, $e_2 = +.00022$

APPENDIX 'F'

Calculation of Error $\Delta\alpha$ Associated with Angle α for Low and High Levels of Residual Strain

The precision of angle α for any set of strain data is a function of the magnitude of those strain data and its precision $\delta\varepsilon = \pm 1\mu\text{m/m}$.

From Appendix E the relationship between angle α and strain data x_1, x_2, and x_3 is

$$2\alpha = \tan^{-1}\cdot\frac{\frac{\varepsilon_x - \varepsilon_y}{2}}{\sqrt{\frac{(\varepsilon_x - \varepsilon_{45})^2 + (\varepsilon_y - \varepsilon_{45})^2}{2}}}$$

The maximum variation in angle 2α is

$$(2\alpha \pm \delta 2\alpha) = \cos^{-1}\left[\frac{\frac{(x_1 + x) - (x_3 - x)}{2}}{\sqrt{\frac{(x_3 - x - x_2 - x)^2 + (x_3 - x - x_2 - x)^2}{2}}}\right]$$

$$= \cos^{-1}\left[\frac{\frac{(x_1 - x_3) + 2x}{2}}{\sqrt{\frac{(x_1 - x_2)^2 + (x_1 - x_2)^2}{2} - 8x(2x_1 - 4x_2 + 2x_3) + 48x^2}}\right]$$

where $\varepsilon_x = x_1 \quad \varepsilon_{45} = x_2 \quad \varepsilon_y = x_3$

1. Low level of strain

e.g. $x_1 = -.000701 \quad x_2 = +.000086 \quad x_3 = +.000522$

$\therefore \alpha = 20^\circ \quad \text{or} \quad \alpha = 70^\circ$

$(\alpha + \delta\alpha) = 60^\circ \quad \text{or} \quad (\alpha + \delta\alpha) = 35^\circ$

Hence precision $\delta\alpha = 25^\circ$.

/ - 2 -

Appendix III

7. High Level of Strain

Given: $\lambda_1 = -.00110$ $\lambda_2 = -.00745$ $\lambda_3 = -.00122$

$\Sigma \alpha = 78^0 \longrightarrow \alpha = 39^0$.

$(\Sigma \alpha + \Sigma \delta\alpha) = 96^0 \longrightarrow (\alpha + \delta\alpha) = 23^0$.

Hence Twinning: $\delta\alpha = 16^0$.

Appendix 5a1

Widths of Braze between Blind Bottom and Hard Metal Insert No. 1 and 2 of the Analogue

Microscopic measurements at intervals of 1.0 mm. along the brazed welded run following data :

1. Braze seal to hard metal insert (1): 0.32 mm ⟷ 0.40 mm
Average : 0.35 mm.

2. Braze seal to hard metal insert (2): 0.29 mm ⟷ 0.35 mm.
Average : 0.325 mm.

However, on one part of the length of this braze gap less within the limits

0.24 mm ⟷ 0.29 mm.

Average : 0.263 mm.

TABLE 1.

DIFFRACTION DATA AND DERIVED RESIDUAL STRAIN AND STRESS VALUES ON EN 30B STEEL AFTER METALLOGRAPHIC POLISHING AND GRINDING

Specimen Preparation	$^{\circ}\psi$	$^{\circ}2\theta_p$	$\sin\theta_p$	$\frac{d_\phi - d_\perp}{d_\perp}$	STRAIN e_ϕ	STRESS σ_ϕ MN/m^2
1						
Emery Paper Grind and Diamond Polish	0	155.176	.97665	-.00128	-.0026	-414
	45	155.877	.97790			
2						
As above	0	155.335	.97691	-.00126	-.0025	-393
	45	156.019	.97814			
3						
As above	0	155.343	.97691	-.00108	-.0022	-345
	45	155.914	.97798			
4						
As above and Electropolish	0	155.965	.97804	-.00006	-.0001*	- 14*
	45	155.990	.97810		-.0002	- 34

* A tensile strain of .0001 was placed on Specimen 4 to enable it to remain in position in the goniometer; with no external strain it had a tendency to slip. Hence the measured results of $e_\phi = -.0001$ and $\sigma_\phi = -14$ MN/m^2 are not the actual residual strain and stress.

The true residual strain and stress are also quoted in Table 1 and are

$$e_\phi = -.0002 \; ; \; \sigma_\phi = -34 \text{ MN/m}^2.$$

TABLE II.

A COMPARISON OF STRAIN AS MEASURED BY SR 4 STRAIN GAUGES AND X-RAY DIFFRACTION

	ϵ_{SR4}	$\psi = 0^\circ$ $2\theta^\circ$	$\psi = 45^\circ$ $2\theta^\circ$	X-ray strain ϵ_x	$\Sigma\epsilon$
SPECIMEN 1	0	155.34	155.91	+.0022	-.0022
Emery paper	+.0006	155.43	155.82	+.0018	-.0024
grind and	+.0012	155.46	155.74	+.0012	-.0024
Diamond	+.0020	155.55	155.93	+.0005	-.0025
polish	+.0024	155.59	155.60	+.0001	-.0025
SPECIMEN 2	0	155.18	155.88	+.0026	-.0026
	+.0009	155.28	155.73	+.0018	-.0027
As above	+.0018	155.37	155.61	+.0009	-.0027
	+.0027	155.49	155.48	+.0001	-.0026
SPECIMEN 3	0	155.34	156.02	+.0025	-.0025
	+.0003	155.22	155.84	+.0023	-.0026
As above	+.0006	155.32	155.82	+.0022	-.0028
	+.0009	155.33	155.75	+.0016	-.0025
	+.0018	155.39	155.61	+.0009	-.0027
	+.0027	155.46	155.50	+.0001	-.0026
SPECIMEN 4	+.0001	155.97	155.99	+.0001	-.0000
	+.0006	156.02	155.91	+.0003	-.0003
As above -	+.0012	156.07	155.83	+.0008	-.0004
Electropolish	+.0018	156.14	155.75	+.0015	-.0003
	+.0024	156.24	155.68	+.0021	-.0003

ϵ_{SR4} = uniaxial strain imposed on specimen by 4-point bending and measured by SR 4 strain gauges.

X-ray strain ϵ_x = total elastic strain present in specimen as measured by X-ray diffraction.

$$\Sigma\epsilon = \epsilon_x - \epsilon_{SR4}$$

N.B. The SR 4 resistance strain gauges and the X-ray apparatus were both aligned to measure in the direction of the applied strain, i.e. along the longitudinal axis of the 4% strip.

TABLE III.

X-RAY MEASURED ELASTIC STRAINS AND THEIR CORRESPONDING STRESSES IN THE SURFACE OF SINTERED WC-Co COMPACTS

Specimen	e Compressive	Compression σ MN/m^2
1. As sintered	.0001	55
2. Tumbled	.0014	770
3. Grit blasted	.0015	825
4. Electrolytically Ground	.0004	220
5. Mechanically Ground	.0012	660
6. Vapour blasted	.0014	770
7. Alundum and Vapour blasted	.0014	770
8. Tumbled and Vapour blasted	.0014	770
9. Vibratory tumbled (1)	.0014	770
Vibratory tumbled (2)	.0017	935
10. Sintered and Gritblasted (D.N. French)		1311

The value of Young's Modulus used was obtained from Smithells[10] $E = 0.70 \times 10^6$ MN/m^2

TABLE IV.

STRAIN VALUES AND PARTICLE SIZES DETERMINED FROM THE INTEGRAL BREADTHS β OF DIFFRACTION PEAK PROFILES

Specimen description	DIFFRACTION PEAKS (001)		(100)		(101)		(201)		(112)		D μm	ε
	B	β	B	β	B	β	B	β	B	β		
1. WC powder	.22		.22		.20		.35		.40			
2. Sintered only	.13		.15		.15		.29		.36			
3. Electrolytically ground	.30	.08	.41	.19	.49	.29	.78	.43	.90	.50	3.5	.0182
4. Tumbled	.41	.19	.44	.22	.45	.25	.83	.48	1.14	.74	3.8	.0277
5. Gritblasted	.56	.34	.59	.37	.68	.48	1.38	1.03			2.2	.0535
6. Ground	.32	.10	.67	.45	.73	.53						
7. Vapour blasted	.32	.10	.67	.45	.73	.53						
8. Aluminium and vapour blasted	.32	.10	.67	.45	.73	.53						
9. Tumbled and vapour blasted	.32	.10	.67	.45	.73	.53						

$$B = \frac{A_{\alpha 1}}{I_{\alpha 1}} = \frac{\text{Area under } K\alpha_1 \text{ diffraction peak}}{\text{Max. intensity of } K\alpha_1 \text{ peak}}$$

$\beta_{(hkl)} = B_{(hkl)}$ broadened $- B_{(hkl)}$ WC powder

N.B. Specimens 2 to 9 inclusive are sintered compacts

TABLE V.

X-RAY MEASUREMENT ON THE SURFACE OF WC-Co SINTERED COMPACTS HAVING DIFFERENT LEVELS OF SURFACE ROUGHNESS

Abrasive	Pressure kN/m^2	Process Time (seconds)	Surface Roughness Before µm	Surface Roughness After µm	Thickness Before mm	Thickness After mm	Compressive Strain e	(Compression) σ MN/m^2
1. 400 mesh bauxite	586	30	.305	.889	11.02	11.01	.0023	1256
2. 400 mesh bauxite	586	30	.432	.889	11.02	11.01	.0020	1092
3. 400 mesh bauxite	586	30	.432	.889	11.01	10.99	.0022	1201
4. 45/75 Vacu-beads	586	30	.432	.559	11.01	11.01	.0019	1037
5. 80/20 Al.Oxide	586	30	.432	1.905	10.99	10.95	Measurement not possible because of extreme roughness of surface.	
6. 80/20 Al.Oxide	586	30	.406	2.032	11.00	10.93		
7. 50/20 Al.Oxide	586	30	.432	2.032	11.00	10.81		
8. Standard Hard Metals blasting (South Africa)							.0021	1147
9. Standard Hard Metals blasting (South Africa)							.0021	1147
10. D.N. French. Sintered and Gritblasted								1311

VALUES FOR STRESS WERE CALCULATED AS FOR TABLE III.

TABLE VI.

EFFECT OF HEAT TREATMENT ON THE LEVEL OF RESIDUAL STRESS IN SINTERED CARBIDE SURFACES

All specimens were acquired from Boart and Hard Metals (S.A.) Limited and had been processed with the normal surface blasting technique.

No.	Heat Treatment			Compressive Strain	Compressive Stress σ
	Temperature	Time	Atmosphere	e	MN / m^2
1	-	-	-	.0026	1430
2	520°C	1 hour	H_2	.0011	605
3	520°C	1 hour	H_2	.0014	770
4	700°C	1 hour	H_2	.0005	275
5	700°C	1 hour	H_2	.0005	275
6	900°C	1 hour	H_2	.0003	165
7	900°C	1 hour	H_2	.0002	110

Stress σ was calculated as for values in Table III.

TABLE VII.

RESIDUAL STRAINS IN X-DIRECTION ACROSS THE STEEL SECTOR SURFACE CALCULATED FROM X-RAY DIFFRACTION PEAK SHIFTS

The relevant X-ray data are quoted as the double diffraction angles $2\theta_p$ for the two angles of specimen surface rotation

$\psi = 0^0$ and $\psi = 45^0$

dx = distance from point f along insert (2).

dy = distance from f along insert (1).

POSITION dx mm	dy mm	$\psi = 0^0$ $2\theta^0_p$	$\psi = 45^0$ $2\theta^0_p$	$(2\theta_0 - 2\theta_{45})^0$ $\Delta 2\theta_p$	STRAIN e_x
0.64	1.27	155.597	155.814	-0.217	-.00085
1.27	1.27	155.606	155.860	-0.254	-.00099
1.91	1.27	155.544	155.793	-0.249	-.00097
3.28	1.27	155.642	155.743	-0.101	-.00039
4.45	1.27	155.663	155.741	-0.078	-.00030
5.82	1.27	155.666	155.778	-0.112	-.00044
8.36	1.27	155.725	155.790	-0.065	-.00025
10.90	1.27	155.759	155.739	+0.020	+.00008
13.44	1.27	155.789	155.691	+0.098	+.00038
15.98	1.27	155.839	155.714	+0.125	+.00049
24.14	1.27	155.774	155.660	+0.114	+.00045
26.00	1.27	155.714	155.653	+0.061	+.00024
27.96	1.27	155.750	155.654	+0.096	+.00037
29.82	1.27	155.764	155.659	+0.105	+.00041
31.75	1.27	155.738	155.682	+0.056	+.00022
33.64	1.27	155.727	155.630	+0.097	+.00038
35.58	1.27	155.726	155.647	+0.079	+.00031
1.27	3.81	155.654	155.871	-0.217	-.00085
1.91	3.81	155.733	155.815	-0.082	-.00032
3.28	3.81	155.633	155.774	-0.141	-.00055
4.45	3.81	155.673	155.734	-0.061	-.00024
5.82	3.81	155.720	155.730	-0.010	-.00004
8.36	3.81	155.719	155.673	+0.046	+.00018
10.90	3.81	155.808	155.693	+0.115	+.00045
13.44	3.81	155.747	155.684	+0.063	+.00025
15.98	3.81	155.781	155.724	+0.057	+.00022
24.14	3.81	155.735	155.700	+0.035	+.00014
26.00	3.81	155.780	155.724	+0.056	+.00021
27.96	3.81	155.711	155.660	+0.051	+.00020
29.82	3.81	155.795	155.710	+0.085	+.00033
31.75	3.81	155.726	155.661	+0.065	+.00025
33.64	3.8	155.677	155.657	+0.020	+.00008
35.58	3.81	155.698	155.645	+0.053	+.00020

continued ..

TABLE VII.
(continued)

POSITION dx mm	POSITION dy mm	$\psi = 0^\circ$ $2\theta^\circ_p$	$\psi = 45^\circ$ $2\theta^\circ_p$	$(2\theta^\circ_o - 2\theta_{45})$ $\Delta 2\theta^\circ_p$	STRAIN e_x
1.91	5.82	155.811	155.851	-0.04	-.00016
3.28	5.82	155.662	155.776	-0.116	-.00045
4.45	5.82	155.709	155.830	-0.121	-.00047
5.82	5.82	155.721	155.777	-0.056	-.00022
8.36	5.82	155.698	155.752	-0.054	-.00021
10.90	5.82	155.733	155.736	-0.003	-.00001
13.44	5.82	155.780	155.750	+0.030	+.00012
15.98	5.82	155.798	155.700	+0.098	+.00038
0.64	8.00	155.852	155.952	-0.100	-.00039
1.91	8.00	155.693	155.810	-0.117	-.00046
3.28	8.00	155.677	155.768	-0.091	-.00036
4.45	8.00	155.653	155.853	-0.200	-.00078
5.82	8.00	155.712	155.790	-0.078	-.00030
8.36	8.00	155.724	155.772	-0.048	-.00019
10.90	8.00	155.743	155.771	-0.028	-.00011
13.44	8.00	155.725	155.726	-0.001	.00000
15.98	8.00	155.801	155.689	+0.112	+.00044
21.60	8.00	155.827	155.731	+0.096	+.00037
24.15	8.00	155.747	155.652	+0.095	+.00037
26.68	8.00	155.783	155.723	+0.060	+.00023
29.20	8.00	155.782	155.740	+0.042	+.00016
31.70	8.00	155.751	155.720	+0.031	+.00012
34.30	8.00	155.725	155.746	-0.021	-.00008
0.64	9.53	155.754	155.860	-0.106	-.00041
1.91	9.53	155.751	155.849	-0.098	-.00038
3.28	9.53	155.718	155.894	-0.176	-.00069
4.45	9.53	155.724	155.890	-0.165	-.00065
5.82	9.53	155.808	155.851	-0.043	-.00017
8.36	9.53	155.763	155.819	-0.056	-.00022
10.90	9.53	155.710	155.842	-0.132	-.00052
13.44	9.53	155.683	155.799	-0.116	-.00045
15.98	9.53	155.776	155.838	-0.062	-.00024

continued ...

TABLE VII.
(continued)

POSITION dx mm	POSITION dy mm	$\psi = 0^\circ$ $2\theta^\circ_p$	$\psi = 45^\circ$ $2\theta^\circ_p$	$(2\theta_o - 2\theta_{45})$ $\Delta 2\theta^\circ_p$	STRAIN e_x
0.64	12.70	155.753	155.772	-0.019	-.00007
1.91	12.70	155.769	155.852	-0.083	-.00032
3.28	12.70	155.741	155.846	-0.105	-.00041
4.45	12.70	155.767	155.787	-0.020	-.00008
5.82	12.70	155.764	155.780	-0.016	-.00006
8.36	12.70	155.757	155.793	-0.036	-.00014
10.90	12.70	155.776	155.763	+0.013	+.00005
13.44	12.70	155.693	155.829	-0.136	-.00053
14.60	12.70	155.757	155.811	-0.054	-.00021
0.64	22.86	155.733	155.754	-0.021	-.00008
1.91	22.86	155.735	155.766	-0.031	-.00012
3.28	22.86	155.728	155.748	-0.020	-.00008
5.82	22.86	155.728	155.733	-0.005	-.00002
8.36	22.86	155.737	155.746	-0.009	-.00004
10.90	22.86	155.738	155.771	-0.033	-.00013
13.44	22.86	155.745	155.728	+0.017	+.00007
15.24	22.86	155.753	155.720	+0.033	+.00013
0.64	27.94	155.689	155.754	-0.065	-.00025
3.28	27.94	155.689	155.802	-0.113	-.00044
5.82	27.94	155.748	155.745	+0.003	+.00001
8.36	27.94	155.770	155.743	+0.027	+.00011
10.90	27.94	155.723	155.739	-0.016	-.00006
13.44	27.94	155.709	155.711	-0.002	-.00001
15.24	27.94	155.720	155.684	+0.036	+.00014
0.64	31.75	155.730	155.783	-0.053	-.00021
1.91	31.75	155.725	155.753	-0.028	-.00011
3.28	31.75	155.708	155.815	-0.107	-.00042
5.82	31.75	155.729	155.794	-0.065	-.00025
8.36	31.75	155.718	155.763	-0.045	-.00018
10.90	31.75	155.700	155.735	-0.035	-.00014
13.44	31.75	155.724	155.741	-0.017	-.00007

TABLE VIII.

RESIDUAL STRAINS IN THE 45° DIRECTION ACROSS THE STEEL SECTOR SURFACE CALCULATED FROM X-RAY DIFFRACTION PEAK SHIFTS

The relevant X-ray data are quoted as the double diffraction angle $2\theta_p$ for the two angles of specimen surface rotation

$\psi = 0^\circ$ and $\psi = 45^\circ$

b - distance along 45° traverse, measured from the y-axis

s - distance of 45° traverse line from point f, measured along the normal fm

POSITION s mm	b mm	dx mm	dy mm	$\psi = 0^\circ$ $2\theta^\circ_p$	$\psi = 45^\circ$ $2\theta^\circ_p$	$\Delta 2\theta^\circ_p$ $(2\theta_o - 2\theta_{45})$	STRAIN e_{45}
1.27	0	0	1.90	155.520	155.965	-0.455	-.00174
1.27	1.27	0.95	0.95	155.604	155.972	-0.368	-.00144
1.27	2.54	1.90	0	155.535	155.999	-0.464	-.00181
2.54	0	0	3.81	155.593	155.883	-0.290	-.00113
2.54	1.27	0.95	2.86	155.602	155.825	-0.223	-.00087
2.54	2.54	1.90	1.90	155.610	155.940	-0.330	-.00129
2.54	3.81	2.86	0.95	155.592	155.949	-0.357	-.00139
2.54	5.08	3.81	0	155.597	155.874	-0.277	-.00108
5.71	0.64	0.51	7.62	155.637	155.804	-0.167	-.00065
5.71	3.28	2.28	5.84	155.623	155.853	-0.230	-.00090
5.71	5.72	4.06	4.06	155.670	155.929	-0.259	-.00101
5.71	8.26	5.84	2.28	155.670	155.875	-0.205	-.00080
5.71	10.80	7.62	0.51	155.610	155.821	-0.211	-.00082
8.90	0	0	12.70	155.724	155.848	-0.124	-.00048
8.90	2.54	1.78	10.63	155.684	155.760	-0.142	-.00055
8.90	5.08	3.56	8.90	155.721	155.792	-0.071	-.00028
8.90	7.62	5.34	7.11	155.730	155.858	-0.122	-.00048
8.90	10.16	7.11	5.34	155.656	155.854	-0.198	-.00077
8.90	12.70	8.90	3.56	155.678	155.848	-0.170	-.00066
8.90	15.24	10.68	1.78	155.692	155.823	-0.131	-.00051
8.90	17.78	12.70	0	155.712	155.795	-0.083	-.00032

continued ....

TABLE VIII.

(continued)

POSITION s mm	b mm	dx mm	dy mm	$\psi = 0^\circ$ $2\theta^\circ_p$	$\psi = 45^\circ$ $2\theta^\circ_p$	$\Delta 2\theta^\circ_p$ $(2\theta_o - 2\theta_{45})$	STRAIN ϵ_{45}
10.79	0	0	15.87	155.763	155.715	+0.048	+.00019
10.79	2.54	1.78	14.35	155.696	155.760	-0.064	-.00025
10.79	5.08	3.56	12.58	155.693	155.790	-0.097	-.00038
10.79	7.62	5.34	10.80	155.732	155.796	-0.064	-.00025
10.79	12.70	8.90	8.90	155.700	155.816	-0.116	-.00045
10.79	15.24	10.80	5.39	155.679	155.794	-0.115	-.00045
10.79	17.78	12.58	3.56	155.693	155.782	-0.089	-.00035
10.79	20.32	14.35	1.78	155.672	155.786	-0.114	-.00045
10.79	21.59	15.87	0	155.729	155.757	-0.028	-.00011
12.70	0.64	0.64	18.40	155.712	155.747	-0.035	-.00017
12.70	3.18	2.28	16.63	155.738	155.697	+0.041	+.00016
12.70	5.72	4.06	14.86	155.758	155.742	+0.016	+.00006
12.70	8.26	5.84	13.08	155.721	155.778	-0.057	-.00022
12.70	13.33	9.40	9.40	155.720	155.831	-0.111	-.00043
12.70	18.40	13.08	5.84	155.700	155.812	-0.112	-.00044
12.70	20.96	14.86	4.06	155.710	155.802	-0.092	-.00036
12.70	23.48	16.63	2.28	155.760	155.811	-0.051	-.00020
12.70	24.79	18.40	0.64	155.729	155.756	-0.027	-.00011
17.78	0	0	25.40	155.683	155.689	-0.006	-.00002
17.78	2.54	1.78	23.38	155.769	155.691	+0.078	+.00030
17.78	5.08	3.56	21.60	155.734	155.723	+0.011	+.00004
17.78	7.62	5.34	19.80	155.696	155.745	-0.049	-.00019
17.78	12.70	8.90	16.12	155.749	155.751	-0.002	-.00001
17.78	17.78	12.57	12.57	155.693	155.760	-0.067	-.00026
17.78	22.86	16.12	8.90	155.717	155.773	-0.056	-.00022
17.78	27.94	19.80	5.34	155.742	155.712	+0.030	+.00012
17.78	30.48	21.60	3.56	155.760	155.718	+0.042	+.00016
17.78	33.02	23.38	1.78	155.723	155.700	+0.023	+.00009
17.78	35.56	25.40	0	155.700	155.708	-0.008	-.00003

continued ..

TABLE VIII.
(continued)

POSITION s mm	b mm	dx mm	dv mm	$\psi = 0^\circ$ $2\theta^\circ_p$	$\psi = 45^\circ$ $2\theta^\circ_p$	$\Delta 2\theta^\circ_p$ $(2\theta_o - 2\theta_{45})$	STRAIN e_{45}
22.56	0	0	31.76	155.687	155.569	+0.118	+.00046
22.56	2.54	1.78	30.46	155.659	155.603	+0.056	+.00022
22.56	5.08	3.56	28.70	155.665	155.634	+0.031	+.00012
22.56	7.62	5.34	26.92	155.731	155.634	+0.097	+.00038
22.56	12.70	8.90	23.00	155.749	155.681	+0.068	+.00027
22.56	17.78	12.57	19.30	155.774	155.704	+0.070	+.00027
22.56	24.13	17.00	14.86	155.713	155.726	-0.013	-.00005
22.56	30.48	21.46	10.29	155.753	155.732	+0.021	+.00008
22.56	35.56	24.79	6.73	155.734	155.725	0.009	+.00004
22.56	38.10	26.92	4.95	155.709	155.714	-0.005	-.00002
22.56	40.64	28.70	3.18	155.752	155.678	+0.074	+.00029
22.56	43.18	30.46	1.40	155.713	155.673	+0.040	+.00016
22.56	45.10	31.76	0	155.690	155.669	+0.021	+.00008
26.66	0	0	38.10	155.739	155.648	+0.091	+.00036
26.66	2.54	1.78	36.10	155.686	155.640	+0.046	+.00018
26.66	5.08	3.56	34.18	155.700	155.682	+0.018	+.00007
26.66	7.62	5.34	32.40	155.726	155.666	+0.060	+.00023
26.66	12.70	8.90	28.80	155.683	155.753	-0.070	-.00027
26.66	17.78	12.57	25.16	155.744	155.730	+0.014	+.00005
26.66	27.94	19.80	18.02	155.737	155.738	-0.001	0
26.66	35.56	25.16	12.51	155.743	155.741	+0.002	+.00001
26.66	40.64	28.80	8.90	155.733	155.721	+0.012	+.00005
26.66	45.72	32.40	5.34	155.713	155.748	-0.035	-.00014
26.66	48.26	34.18	3.56	155.739	155.748	-0.009	-.00004
26.66	50.80	36.10	1.78	155.695	155.756	-0.061	-.00024
26.66	53.34	38.10	0	155.683	155.678	+0.005	+.00002

TABLE IX.

RESIDUAL STRAINS IN THE Y-DIRECTION ACROSS THE STEEL SECTOR SURFACE, CALCULATED FROM X-RAY DIFFRACTION PEAK-SHIFTS

The relevant X-ray data are quoted as the double diffraction angle $2\theta_p$ for the two angles of specimen surface rotation

$\psi = 0^\circ$ and $\psi = 45^\circ$

dx = distance from point f along insert (2)

dy = distance from f along insert (1)

POSITION dx mm	dy mm	$\psi = 0^\circ$ $2\theta^\circ_p$	$\psi = 45^\circ$ $2\theta^\circ_p$	$\Delta 2\theta^\circ_p$ $(2\theta_o - 2\theta_{45})$	STRAIN e_y
2.54	0.64	155.571	155.847	-0.276	-.00108
2.54	1.27	155.602	155.819	-0.217	-.00085
2.54	2.54	155.635	155.794	-0.159	-.00062
2.54	3.81	155.652	155.784	-0.132	-.00052
2.54	5.35	155.741	155.768	-0.027	-.00011
2.54	8.89	155.767	155.733	+0.034	+.00013
2.54	11.43	155.783	155.736	+0.047	+.00018
2.54	13.97	155.753	155.712	+0.041	+.00016
2.54	24.79	155.738	155.686	+0.052	+.00020
2.54	27.30	155.722	155.688	+0.034	+.00013
2.54	29.82	155.702	155.625	+0.077	+.00030
2.54	32.40	155.737	155.673	+0.064	+.00025
3.18	0.64	155.638	155.902	-0.264	-.00103
3.18	1.27	155.634	155.908	-0.274	-.00107
3.18	2.54	155.616	155.839	-0.223	-.00087
3.18	3.81	155.690	155.864	-0.174	-.00068
3.18	5.08	155.714	155.852	-0.138	-.00054
3.18	6.35	155.746	155.822	-0.076	-.00030
3.18	8.89	155.763	155.763	0	0
3.18	11.43	155.793	155.742	+0.051	+.00020
3.18	13.97	155.770	155.725	+0.045	+.00018
3.18	16.50	155.793	155.732	+0.061	+.00024
3.18	27.30	155.784	155.717	+0.067	+.00026
3.18	32.40	155.766	155.672	+0.094	+.00037
3.18	34.90	155.743	155.645	+0.098	+.00038
3.1	37.45	155.767	155.646	+0.121	+.00047

continued ..

TABLE IX.
(continued)

POSITION dx mm	POSITION dy mm	$\psi = 0^\circ$ $2\theta^\circ_p$	$\psi = 45^\circ$ $2\theta^\circ_p$	$\Delta 2\theta^\circ_p$ $(2\theta_o - 2\theta_{45})$	STRAIN e_y
6.98	0.64	155.690	155.828	-0.138	-.00054
6.98	1.27	155.651	155.852	-0.201	-.00078
6.98	2.54	155.660	155.832	-0.172	-.00067
6.98	3.81	155.706	155.785	-0.079	-.00031
6.98	5.08	155.677	155.807	-0.130	-.00051
6.98	6.35	155.671	155.847	-0.176	-.00069
6.98	7.62	155.710	155.775	-0.065	-.00025
6.98	8.89	155.727	155.788	-0.061	-.00024
6.98	11.43	155.782	155.741	+0.041	+.00016
6.98	13.97	155.790	155.728	+0.062	+ 00024
6.98	16.51	155.789	155.680	+0.109	+.00043
6.98	24.79	155.787	155.660	+0.127	+.00050
6.98	26.00	155.7	155.677	+0.120	+.00047
6.98	27.30	155.800	155.673	+0.127	+.00050
6.98	29.82	155.853	155.717	+0.136	+.00053
6.98	32.40	155.778	155.672	+0.106	+.00041
6.98	34.90	155.751	155.647	+0.104	+.00041
6.98	37.45	155.775	155.680	+0.095	+.00037
10.16	0.64	155.711	155.818	-0.107	-.00042
10.16	1.27	155.686	155.867	-0.181	-.00071
10.16	1.91	155.723	155.854	-0.131	-.00051
10.16	2.54	155.717	155.840	-0.123	-.00048
10.16	3.81	155.733	155.863	-0.130	-.00051
10.16	5.08	155.762	155.833	-0.071	-.00028
10.16	6.35	155.742	155.846	-0.104	-.00041
10.16	7.62	155.753	155.815	-0.062	-.00024
10.16	8.89	155.751	155 779	-0.048	-.00019
10.16	10.16	155.763	155.720	+0.043	+.00017
10.16	11.43	155.774	155.751	+0.023	+.00009
10.16	12.70	155.800	155.750	+0.050	+.00020
10.16	13.97	155.807	155.743	+0.064	+.00025
10.16	17.78	155.822	155.708	+0.114	+.00044

continued ...

TABLE IX.
(continued)

POSITION dx mm	POSITION dy mm	$\psi = 0^\circ$ $2\theta^\circ_p$	$\psi = 45^\circ$ $2\theta^\circ_p$	$\Delta 2\theta^\circ_p$ $(2\theta_0 - 2\theta_{45})$	STRAIN e_y
13.32	0.64	155.777	155.866	-0.089	-.00035
13.32	1.27	155.766	155.875	-0.109	-.00043
13.32	2.54	155.772	155.867	-0.095	-.00037
13.32	3.81	155.722	155.838	-0.116	-.00045
13.32	6.35	155.754	155.876	-0.122	-.00048
13.32	8.89	155.681	155.835	-0.154	-.00060
13.32	11.43	155.708	155.820	-0.112	-.00044
13.32	13.97	155.740	155.750	+0.010	+.00004
13.32	16.51	155.825	155.772	+0.053	+.00021
22.86	0.64	155.731	155.843	-0.112	-.00044
22.86	1.91	155.711	155.794	-0.083	-.00032
22.86	3.28	155.714	155.795	-0.081	-.00032
22.86	5.82	155.708	155.755	-0.047	-.00018
22.86	8.36	155.718	155.748	-0.030	-.00012
22.86	10.90	155.723	155.738	-0.015	-.00006
22.86	13.44	155.731	155.726	+0.005	+.00002
22.86	13.98	155.705	155.732	-0.027	-.00011
26.18	0.64	155.655	155.805	-0.150	-.00059
26.18	1.91	155.710	155.768	-0.058	-.00023
26.18	3.28	155.671	155.773	-0.102	-.00040
26.18	5.82	155.702	155.745	-0.043	-.00017
26.18	8.36	155.688	155.721	-0.033	-.00013
26.18	10.90	155.681	155.743	-0.062	-.00024
26.18	13.44	155.703	155.730	-0.027	-.00011
26.18	15.98	155.719	155.720	-0.001	0
26.18	18.40	155.697	155.702	-0.005	-.00002
31.76	0.64	155.705	155.775	-0.070	-.00027
31.76	1.91	155.673	155.800	-0.127	-.00050
31.76	3.28	155.706	155.763	-0.057	-.00022
31.76	5.82	155.694	155.744	-0.050	-.00020
31.76	8.36	155.720	155.715	+0.005	+.00002
31.76	10.90	155.731	155.760	-0.029	-.00011
31.76	13.44	155.721	155.720	+0.001	0
31.76	15.98	155.685	155.666	+0.019	+.00007

continued ...

TABLE IX.
(Continued)

POSITION dx mm	POSITION dy mm	$\psi = 0^{\circ}$ $2\theta^{\circ}_{p}$	$\psi = 45^{\circ}$ $2\theta^{\circ}_{p}$	$\Delta 2\theta^{\circ}_{p}$ $(2\theta_{0} - 2\theta_{45})$	STRAIN e_y
34.98	0.64	155.667	155.802	-0.135	-.00053
34.98	1.91	155.691	155.791	-0.100	-.00039
34.98	3.28	155.655	155.826	-0.171	-.00067
34.98	5.52	155.678	155.761	-0.083	-.00032
34.98	8.36	155.698	155.741	-0.043	-.00017
34.98	10.98	155.678	155.682	-0.004	-.00002

TABLE X.

PRINCIPAL STRESSES AND ASSOCIATED STRESS LOCI, DERIVED FROM MOHR'S CIRCLE OF STRAIN CALCULATIONS USING X-RAY DATA

Δx	Δy	e_x	e_{45}	e_y	e_2	e_1	α^p	σ_1 MN/m^2	σ_2 MN/m^2	$\sigma_1+\sigma_2$ MN/m^2	$\sigma_1-\sigma_2$ MN/m^2
1.27	1.27	-.00080	-.00147	-.00070	-.00147	-.00003	43	- 5	-237	-242	232
2.54	1.27	-.00068	-.00132	-.00050	-.00123	-.00025	51	-40	-198	-238	158
3.81	1.27	-.00055	-.00116	-.00101	-.00122	-.00034	61	-55	-197	-252	142
5.08	1.27	-.00043	-.00102	-.00089	-.00109	-.00023	61	-37	-176	-213	139
6.35	1.27	-.00030	-.00088	-.00075	-.00094	-.00010	61	-16	-151	-167	135
7.62	1.27	-.00018	-.00076	-.00066	-.00084	0	63	0	-135	-135	135
10.16	1.27	+.00007	-.00055	-.00052	-.00066	.00021	66	34	-106	- 72	140
12.70	1.27	+.00031	-.00037	-.00042	-.00054	.00043	70	69	- 87	- 18	156
15.24	1.27	+.00047	-.00029	-.00040	-.00045	.00055	74	89	- 77	12	164
20.32	1.27	+.00063	-.00006	-.00040	-.00041	.00045	85	72	- 66	6	138
25.40	1.27	+.00038	+.00016	-.00040	-.00042	.00030	98	64	- 68	- 4	132
30.48	1.27	-.00033	+.00016	-.00040	-.00045	.00038	104	61	- 72	- 11	133
35.56	1.27	+.00028	-.00002	-.00040	-.00046	.00028	87	43	- 61	- 19	109
2.54	3.81	-.00050	-.00106	-.00049	-.00111	.00007	45	+11	-179	-168	190
3.81	3.81	-.00035	-.00087	-.00066	-.00109	-.00001	54	- 2	-161	-163	159
5.08	3.81	-.00020	-.00088	-.00064	-.00093	.00019	56	14	-150	-136	164
6.35	3.81	-.00006	-.00080	-.00059	-.00087	.00022	60	31	-140	-105	175
7.62	3.81	+.00009	-.00072	-.00055	-.00082	.00036	62	58	-132	- 74	190
10.16	3.81	+.00028	-.00055	-.00047	-.00068	.00040	65	79	-109	- 30	188

TABLE X.

PRINCIPAL STRESSES AND ASSOCIATED STRESS LOCI, DERIVED FROM MOHR'S CIRCLE OF STRAIN

CALCULATIONS USING X-RAY DATA

Δx	Δy	e_x	e_{45}	e_y	e_2	e_1	σ_x	σ_1 MN/m^2	σ_2	$\sigma_1+\sigma_2$	$\sigma_1-\sigma_2$
12.70	3.81	+.00028	-.00039	-.00042	-.00054	.00040	70	64	- 87	- 23	151
17.78	3.81	+.00026	-.00006	-.00034	-.00034	.00026	88	42	- 55	- 13	97
22.86	3.81	+.00024	+.00020	-.00038	-.00038	-.00032	110	52	- 61	- 9	113
27.94	3.81	+.00022	+.00020	-.00038	-.00039	.00031	111	50	- 64	- 13	113
33.02	3.81	+.00020	+.00019	-.00030	-.00040	.00030	112	48	- 64	- 16	112
2.54	5.71	-.00038	-.00089	-.00020	-.00090	.00034	41	+55	-145	- 90	200
3.81	5.71	-.00031	-.00082	-.00042	-.00082	.00006	48	10	-132	-122	142
5.08	5.71	-.00031	-.00075	-.00047	-.00072	-.00002	51	- 3	-122	-125	119
6.35	5.71	-.00027	-.00068	-.00048	-.00070	-.00005	54	- 8	-113	-121	105
7.62	5.71	-.00022	-.00060	-.00046	-.00063	-.00005	57	- 8	-101	-109	93
10.16	5.71	-.00009	-.00045	-.00040	-.00050	.00001	64	2	- 81	- 79	83
12.70	5.71	+.00008	-.00030	-.00035	-.00041	.00014	71	23	- 66	- 43	89
15.24	5.71	+.00030	-.00019	-.00031	-.00036	.00033	79	36	- 58	- 2	116

TABLE X.

PRINCIPAL STRESSES AND ASSOCIATED STRESS LOCI, DERIVED FROM MOHR'S CIRCLE OF STRAIN

CALCULATIONS USING X-RAY DATA

Δx	Δy	e_x	e_{45}	e_y	e_2	e_1	a°_x	σ_1 MN/m^2	σ_2	$\sigma_1+\sigma_2$	$\sigma_1-\sigma_2$
2.54	8.00	-.00040	-.00058	+.00005	-.00064	.00039	30	47	-103	- 56	150
3.81	8.00	-.00035	-.00054	-.00013	-.00056	.00006	35	10	- 90	- 80	100
5.08	8.00	-.00031	-.00050	-.00024	-.00050	-.00003	41	- 8	- 81	- 89	73
6.35	8.00	-.00026	-.00046	-.00028	-.00046	-.00008	46	-12	- 74	- 86	62
7.62	8.00	-.00022	-.00042	-.00026	-.00042	-.00006	48	-10	- [illegible]	- 75	38
10.16	8.00	-.00013	-.00034	-.00020	-.00034	.00001	51	2	- 55	- 53	57
12.70	8.00	.00000	-.00026	-.00017	-.00028	.00011	58	18	- 45	- 27	63
15.24	8.00	+.00027	-.00019	-.00016	-.00027	.00038	66	61	- 43	18	104
20.32	8.00	+.00040	-.00003	-.00015	-.00019	.00044	75	71	- 31	40	102
25.40	8.00	+.00032	+.00004	-.00015	-.00015	.00032	85	52	- 24	28	76
30.48	8.00	+.00016	-.00007	-.00015	-.00017	.00018	77	29	- 27	2	56
2.54	9.53	-.00066	-.00051	+.00015	-.00070	.00025	19	40	-113	- 73	153
3.81	9.53	-.00068	-.00041	+.00005	-.00069	.00006	7	10	-111	-101	121
5.08	9.53	-.00066	-.00071	+.00001	-.00069	.00004	14	6	- 79	- 73	85
6.35	9.53	-.00017	-.00033	-.00003	-.00033	.00013	36	21	- 53	- 32	74
7.62	9.53	-.00017	-.00032	-.00005	-.00033	.00011	37	18	- 53	- 35	71
10.16	9.53	-.00043	-.00029	-.00008	-.00043	-.00007	6	-11	- 69	- 80	58
12.70	9.53	-.00048	-.00026	-.00009	-.00048	-.00007	- 4	-14	- 77	- 91	63
15.24	9.53	-.00031	-.00022	-.00010	-.00031	-.00010	½	-16	- 50	- 66	34

TABLE X.

PRINCIPAL STRESSES AND ASSOCIATED STRESS LOCI, DERIVED FROM MOHR'S CIRCLE OF STRAIN

CALCULATIONS USING X-RAY DATA

Δx	Δy	e_x	e_{45}	e_y	e_z	σ_1	α_x^o	σ_1 MN/m^2	σ_2 MN/m^2	$\sigma_1+\sigma_2$ MN/m^2	$\sigma_1-\sigma_2$ MN/m^2
2.34	12.70	-.00038	-.00018	+.00020	-.00033	.00021	0	34	- 63	- 29	97
1.81	12.70	-.00032	-.00015	+.00020	-.00034	.00022	10	35	- 35	- 20	90
5.08	12.70	-.00006	-.00014	+.00020	-.00018	.00032	29	52	- 29	23	81
6.35	12.70	-.00007	-.00016	+.00020	-.00020	.00033	30	53	- 32	21	85
7.62	12.70	-.00010	-.00018	+.00020	-.00022	.00032	28	52	- 35	17	87
10.16	12.70	-.00003	-.00023	+.00020	-.00025	.00044	36	71	- 40	31	111
12.70	12.70	-.00000	-.00022	+.00017	-.00042	.00019	10	34	- 68	- 37	99
15.24	12.70	-.00010	-.00011	+.00012	-.00015	.00017	24	27	- 24	3	51
2.34	22.86	-.00011	+.00010	+.00018	-.00012	.00019	-12	31	- 19	14	50
3.81	22.86	-.00009	+.00014	+.00027	-.00010	.00028	- 8	43	- 16	29	61
5.08	22.86	-.00006	+.00016	+.00033	-.00006	.00033	- 2	56	- 10	46	66
6.35	22.86	-.00004	+.00018	+.00043	-.00004	.00043	2	69	- 6	63	75
7.62	22.86	-.00002	+.00020	+.00051	-.00002	.00050	5	82	- 3	79	85
3.81	27.94	-.00018	+.00027	+.00028	-.00027	.00037	-22	60	- 43	17	103
5.08	27.94	-.00007	+.00022	+.00035	-.00008	.00036	-10	58	- 13	45	71
6.35	27.94	+.00001	+.00016	+.00043	0	.00044	8	71	0	71	71
7.62	27.94	+.00003	+.00011	+.00050	-.00002	.00055	17	89	- 3	86	92

TABLE X.

PRINCIPAL STRESSES AND ASSOCIATED STRESS LOCI, DERIVED FROM MOHR'S CIRCLE OF STRAIN CALCULATIONS USING X-RAY DATA

Δx	Δy	e_x	e_{45}	e_y	e_2	e_1	α°_x	σ_1 MN/m^2	σ_2 MN/m^2	$\sigma_1+\sigma_2$ MN/m^2	$\sigma_1-\sigma_2$ MN/m^2
1.27	31.75	-.00012	+.00031	+.00020	-.00027	.00035	-30	56	- 43	13	99
2.34	31.75	-.00014	+.00025	+.00026	-.00022	.00034	-22	55	- 35	20	90
3.81	31.75	-.00015	+.00018	+.00032	-.00017	.00024	-11	39	- 27	12	66
5.08	31.75	-.00016	+.00012	+.00038	-.00016	.00058	- 1	61	- 26	35	87

TABLE XI.

PRINCIPAL STRESSES AND ASSOCIATED STRESS LOCI, DERIVED FROM MOHR'S CIRCLE OF STRAIN CALCULATIONS USING X-RAY DATA

Δx	Δy	e_x	e_{45}	e_y	e_2	e_1	α°_x	σ_1 MN/m^2	σ_2 MN/m^2	$\sigma_1+\sigma_2$ MN/m^2	$\sigma_1-\sigma_2$ MN/m^2
3.81	1.27	-.00056	-.00103	-.00101	-.00112	-.00045	66	- 72	-289	-252	108
3.81	2.54	-.00049	-.00101	-.00084	-.00105	-.00026	58	- 42	-169	-211	127
3.81	3.81	-.00043	-.00098	-.00067	-.00100	-.00013	53	- 16	-161	-177	145
3.81	5.08	-.00039	-.00092	-.00051	-.00092	.00002	49	3	-148	-145	151
3.81	6.35	-.00035	-.00084	-.00036	-.00084	.00013	45	21	-135	-114	156
3.81	7.62	-.00032	-.00075	-.00019	-.00075	.00024	41	39	-121	- 82	160
3.81	10.16	-.00027	-.00057	+.00012	-.00061	.00046	34	74	- 98	- 24	172
3.81	12.70	-.00022	-.00039	+.00019	-.00044	.00047	31	66	- 71	- 5	137
3.81	15.24	-.00018	-.00023	+.00026	-.00030	.00032	26	52	- 48	4	100
3.81	20.32	-.00015	+.00009	+.00023	-.00019	.00024	- 9	39	- 31	8	70
3.81	25.40	-.00018	+.00018	+.00026	-.00022	.00030	-16	48	- 35	13	83
3.81	30.48	-.00018	+.00005	+.00032	-.00018	.00032	2	52	- 29	23	81
2.54	1.27	-.00068	-.00120	-.00088	-.00121	-.00035	52	- 55	-195	-251	139
2.54	2.54	-.00060	-.00111	-.00066	-.00111	-.00015	47	- 24	-179	-203	155
2.54	3.81	-.00050	-.00102	-.00046	-.00102	.00006	44	10	-164	-154	174
2.54	5.08	-.00043	-.00093	-.00028	-.00093	.00022	41	35	-150	-115	185
2.54	6.35	-.00040	-.00084	-.00010	-.00086	.00034	38	55	-138	- 83	193
2.54	7.62	-.00040	-.00075	-.00002	-.00078	.00036	35	58	-126	- 68	184

TABLE XI.

PRINCIPAL STRESSES AND ASSOCIATED STRESS LOCI, DERIVED FROM MOHR'S CIRCLE OF STRAIN CALCULATIONS USING X-RAY DATA

Δx	Δy	e_x	e_{45}	e_y	e_2	e_1	a^o_x	σ_1	σ_2	$\sigma_1+\sigma_2$	$\sigma_1-\sigma_2$
								MN/m^2			
2.54	10.16	-.00038	-.00055	+.00017	-.00063	.00042	29	68	-101	- 33	169
2.54	12.70	-.00034	-.00037	+.00018	-.00047	.00031	24	50	- 76	- 24	126
2.54	15.24	-.00030	-.00027	+.00019	-.00038	.00027	21	43	- 61	- 18	104
2.54	20.32	-.00018	+.00002	+.00020	-.00028	.00020	- 1	32	- 29	3	61
2.54	25.40	-.00022	+.00017	+.00021	-.00028	.00027	-20	43	- 45	- 2	88
2.54	30.48	-.00026	+.00009	+.00022	-.00028	.00024	-12	39	- 45	- 6	84
6.99	1.27	-.00017	-.00075	-.00068	-.00084	-.00001	64	- 2	-135	-137	133
6.99	2.54	-.00017	-.00072	-.00064	-.00080	-.00001	63	- 2	-129	-131	127
6.99	5.08	-.00017	-.00061	-.00050	-.00066	-.00001	60	- 2	-105	-108	104
6.99	7.62	-.00017	-.00050	-.00031	-.00051	.00003	53	5	- 82	- 77	87
6.99	10.16	-.00014	-.00038	-.00002	-.00039	.00023	39	37	- 63	- 26	100
6.99	15.24	-.00003	-.00016	+.00036	-.00032	.00053	28	85	- 35	50	120
6.99	25.32	-.00004	0	+.00048	-.00012	.00056	20	90	- 19	71	109
6.99	25.40	-.00001	+.00004	+.00050	-.00008	.00057	19	92	- 13	79	105
6.99	30.48	-.00013	-.00004	+.00047	-.00020	.00054	17	89	- 32	57	121

TABLE XI.

PRINCIPAL STRESSES AND ASSOCIATED STRESS LOCI, DERIVED FROM MOHR'S CIRCLE OF STRAIN CALCULATIONS USING X-RAY DATA

Δx	Δy	e_x	e_{45}	e_y	e_2	e_1	α°_x	σ_1 MN/m.^{2}	σ_2 MN/m.^{2}	$\sigma_1+\sigma_2$ MN/m.^{2}	$\sigma_1-\sigma_2$ MN/m.^{2}
10.16	1.27	+.00010	-.00049	-.00057	-.00066	.00019	71	31	-106	- 75	137
10.16	2.54	+.00007	-.00043	-.00052	-.00058	.00013	73	21	- 93	- 72	114
10.16	5.08	+.00001	-.00030	-.00039	-.00042	.00004	76	6	- 68	- 62	74
10.16	7.62	-.00002	-.00030	-.00023	-.00033	.00008	60	13	- 53	- 40	66
10.16	10.16	-.00004	-.00029	+.00005	-.00028	.00029	4	47	- 4	2	92
10.16	12.70	-.00004	-.00027	+.00022	-.00029	.00047	35	76	- 47	29	123
10.16	15.24	-.00004	-.00021	+.00032	-.00025	.00053	31	85	- 46	45	125
10.16	17.78	-.00002	-.00008	+.00044	-.00016	.00058	26	93	- 26	67	119
13.33	1.27	+.00034	-.00018	-.00039	-.00042	.00037	79	60	- 68	- 8	128
13.33	3.81	+.00023	-.00010	-.00044	-.00044	.00023	90	37	- 71	- 34	118
13.33	6.35	+.00014	-.00013	-.00050	-.00050	.00014	94	23	- 81	- 58	104
13.33	8.89	+.00007	-.00018	-.00057	-.00058	.00008	96	13	- 93	- 80	106
13.33	11.43	+.00004	-.00025	-.00039	-.00046	.00005	80	8	- 64	- 56	72
13.33	13.97	+.00002	-.00016	-.00001	-.00016	.00017	47	27	- 26	1	53
13.33	16.51	+.00003	-.00002	+.00022	-.00005	.00030	28	48	- 8	40	56

TABLE XI.

PRINCIPAL STRESSES AND ASSOCIATED STRESS LOCI, DERIVED FROM MOHR'S CIRCLE OF STRAIN CALCULATIONS USING X-RAY DATA

Δx	Δy	e_x	e_{45}	e_y	e_2	e_1	α°_x	σ_1 MN/m^2	σ_2 MN/m^2	$\sigma_1+\sigma_2$ MN/m^2	$\sigma_1-\sigma_2$ MN/m^2
22.86	1.27	+.00041	+.00009	-.00038	-.00059	.00042	85	68	- 63	5	131
22.86	2.54	+.00032	+.00011	-.00033	-.00035	.00034	80	55	- 56	- 1	111
22.86	5.08	+.00028	+.00016	-.00022	-.00025	.00031	76	50	- 40	10	90
22.86	7.62	+.00026	+.00020	-.00015	-.00020	.00031	72	50	- 32	18	82
26.16	5.08	+.00025	+.00022	-.00028	-.00041	.00038	114	61	- 66	- 5	127
26.16	7.62	+.00030	+.00017	-.00021	-.00024	.00033	77	53	- 39	14	92
31.75	1.27	+.00030	+.00029	-.00038	-.00051	.00043	68	69	- 82	- 13	151
31.75	2.54	+.00026	+.00024	-.00030	-.00040	.00036	69	58	- 64	- 6	122
31.75	5.08	+.00019	+.00011	-.00017	-.00020	.00022	75	35	- 32	3	67

FIGURE 1

DIAGRAM OF A DRILL BIT

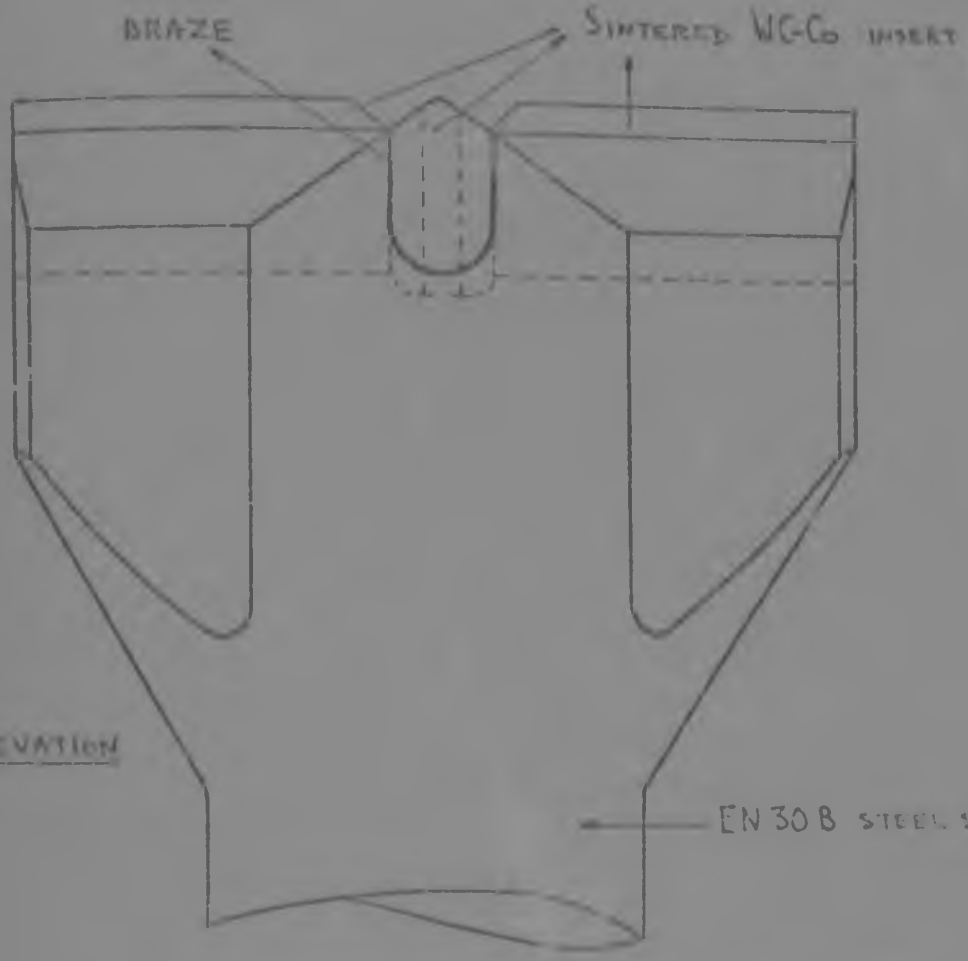

ELEVATION

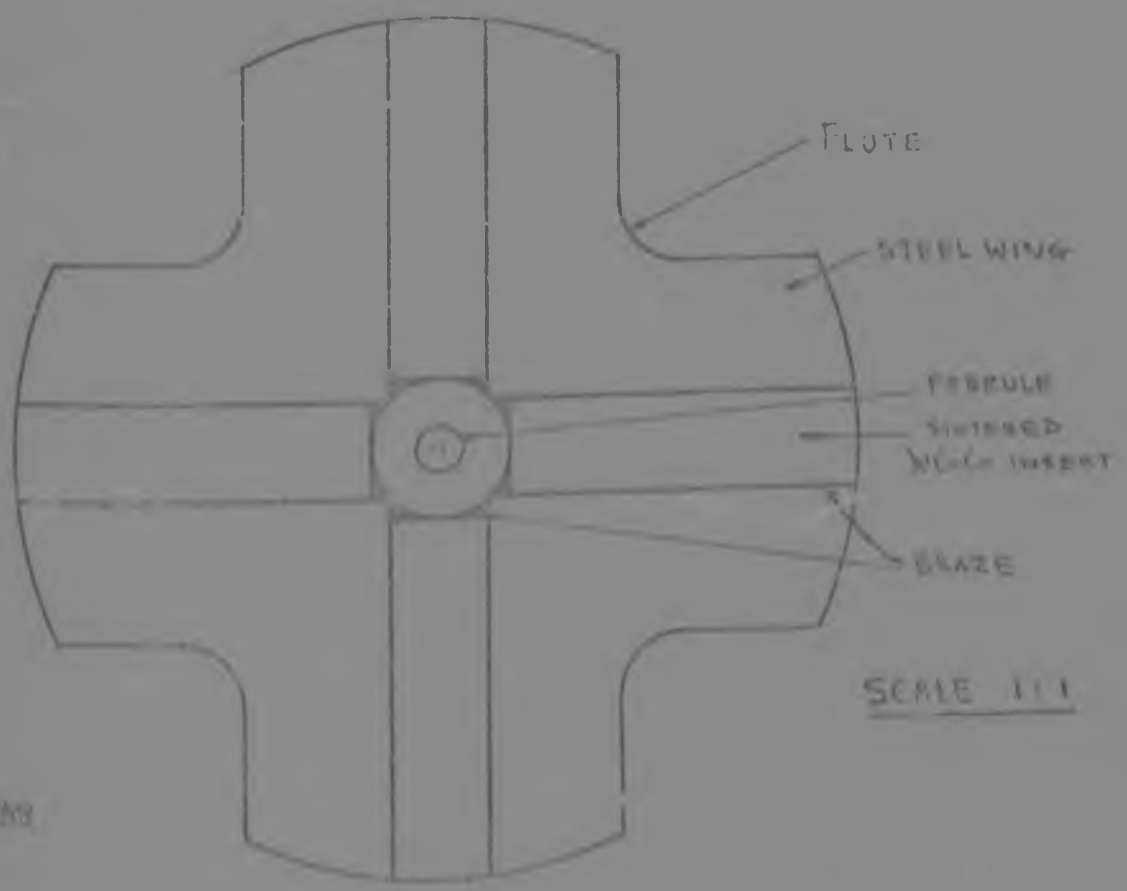

SCALE 1:1

PLAN

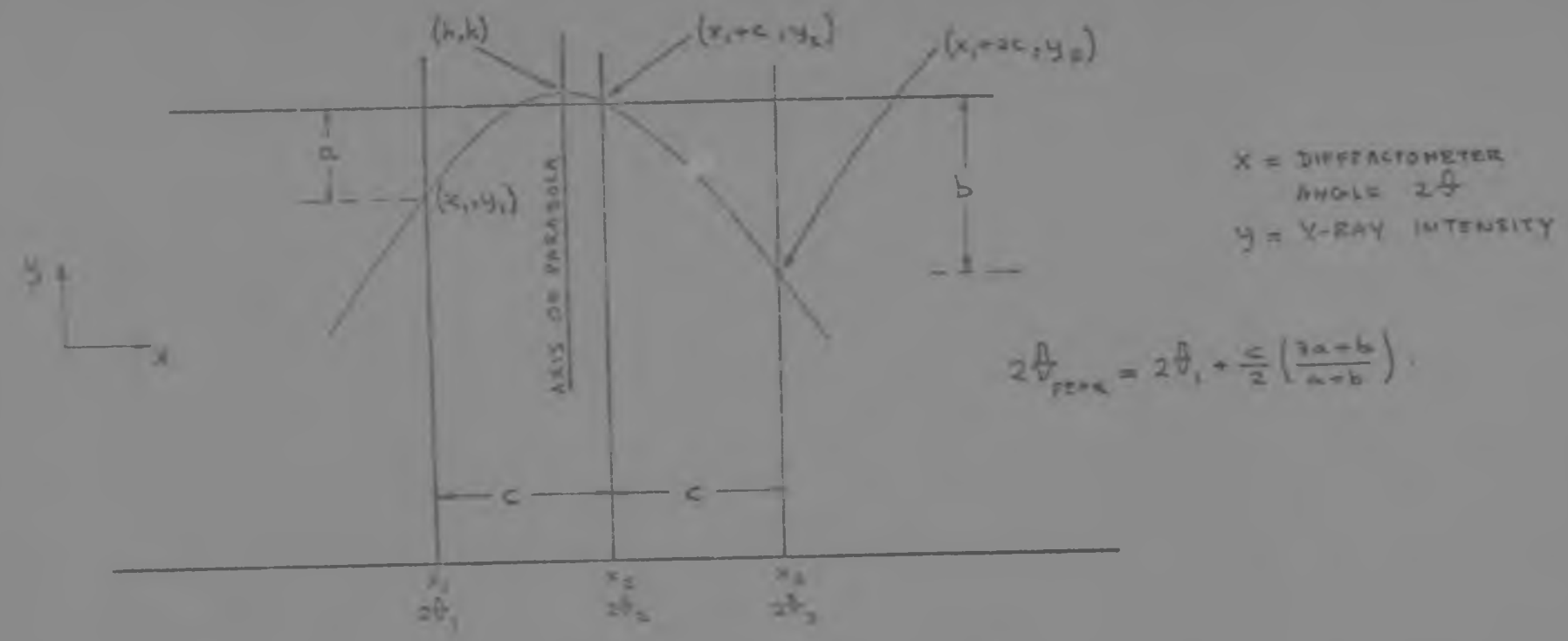

X = DIFFRACTOMETER ANGLE 2θ

Y = X-RAY INTENSITY

$$2\theta_{PEAK} = 2\theta_1 + \frac{c}{2}\left(\frac{3a-b}{a+b}\right)$$

FIGURE 2.

PARABOLA FITTED TO THREE X-RAY INTENSITY DATA (REF. 5)

Figure 3a/

Diffractometer focusing conditions with sample in normal position, $\psi = 0°$.

Figure 3b/

Diffractometer focusing conditions with sample rotated by ψ degrees (anti-clockwise) from normal position.

Figure 4. THE EFFECT OF SECTIONING AND METALLOGRAPHIC PREPARATION ON THE (310) DIFFRACTION PEAK OF PEARLITE

Notes: To facilitate comparison and to avoid the need to superimpose various peaks, the vertical scales for relative intensities have been moved downwards by 10 per cent for each successive curve. The graph plotted for heterogenic Annealed pearlite is on the same scale as that for the electro-polished sample, but the electro-polished specimen peak has been displaced to the right hand side.

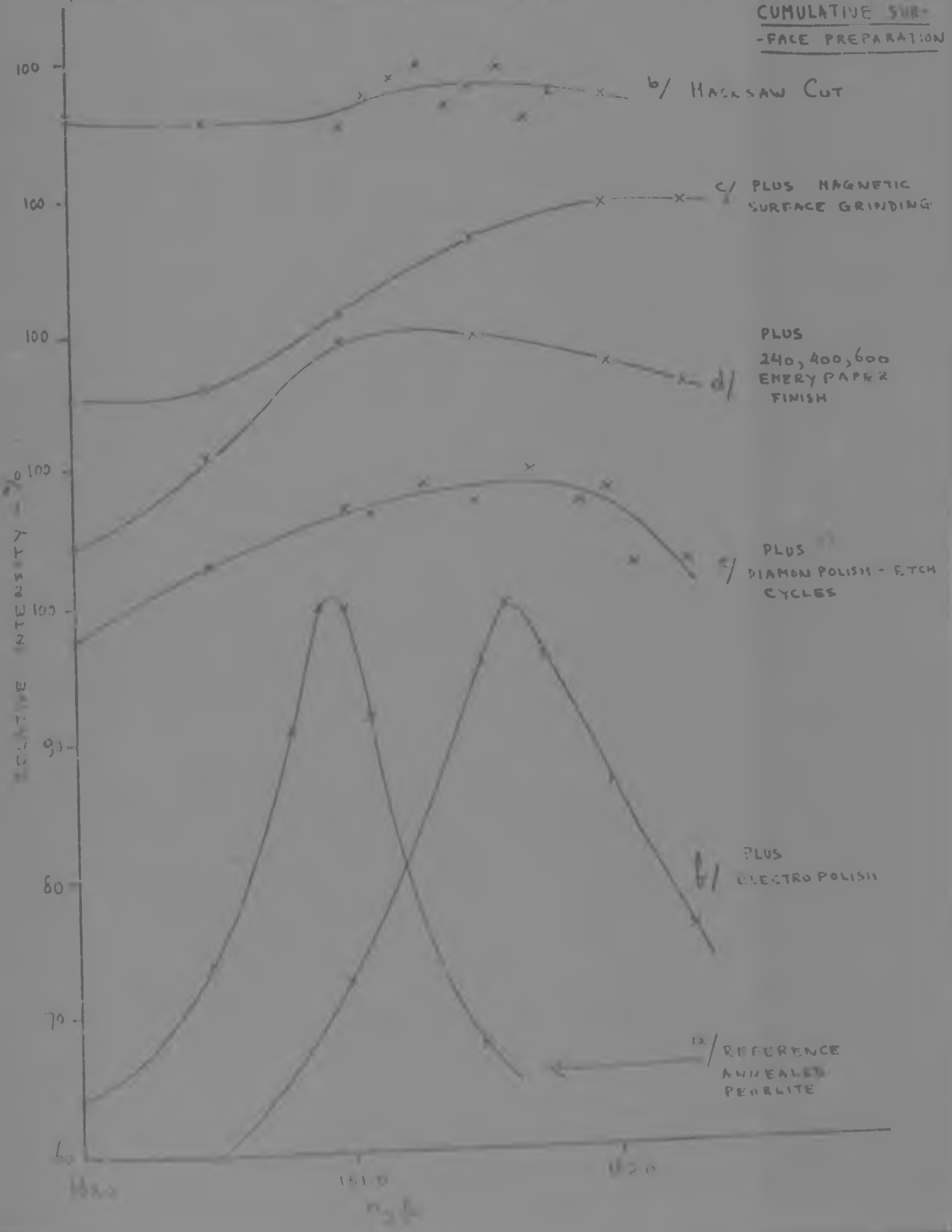

FIGURE 5. [illegible] SPECIMEN UNSTRESSED POSITION

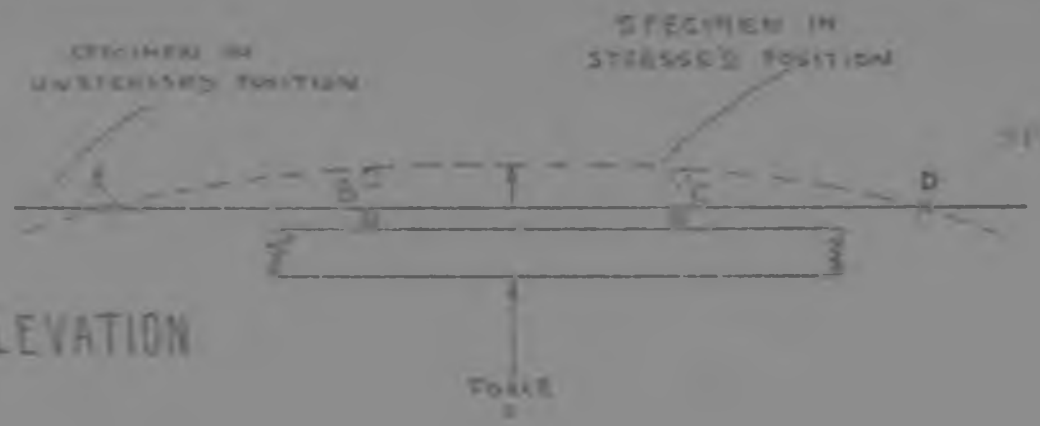

A AND D ARE FIXED POSITIONS AT B AND C 2 STEEL CYLINDERS TRANSMIT FORCE F IN OPPOSITE

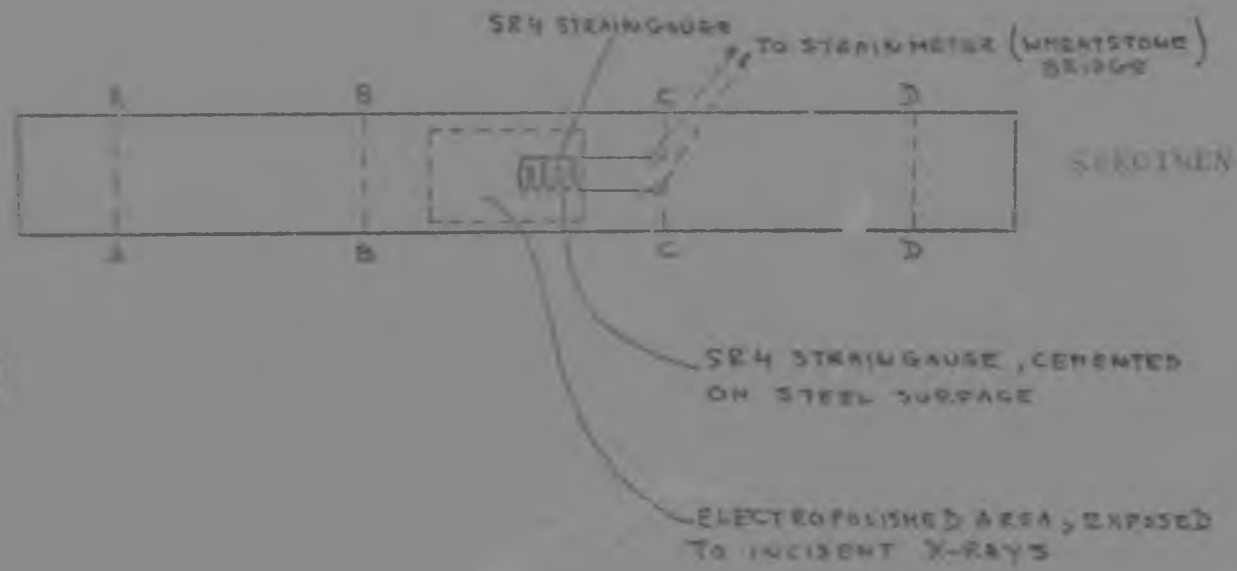

FIGURE 6

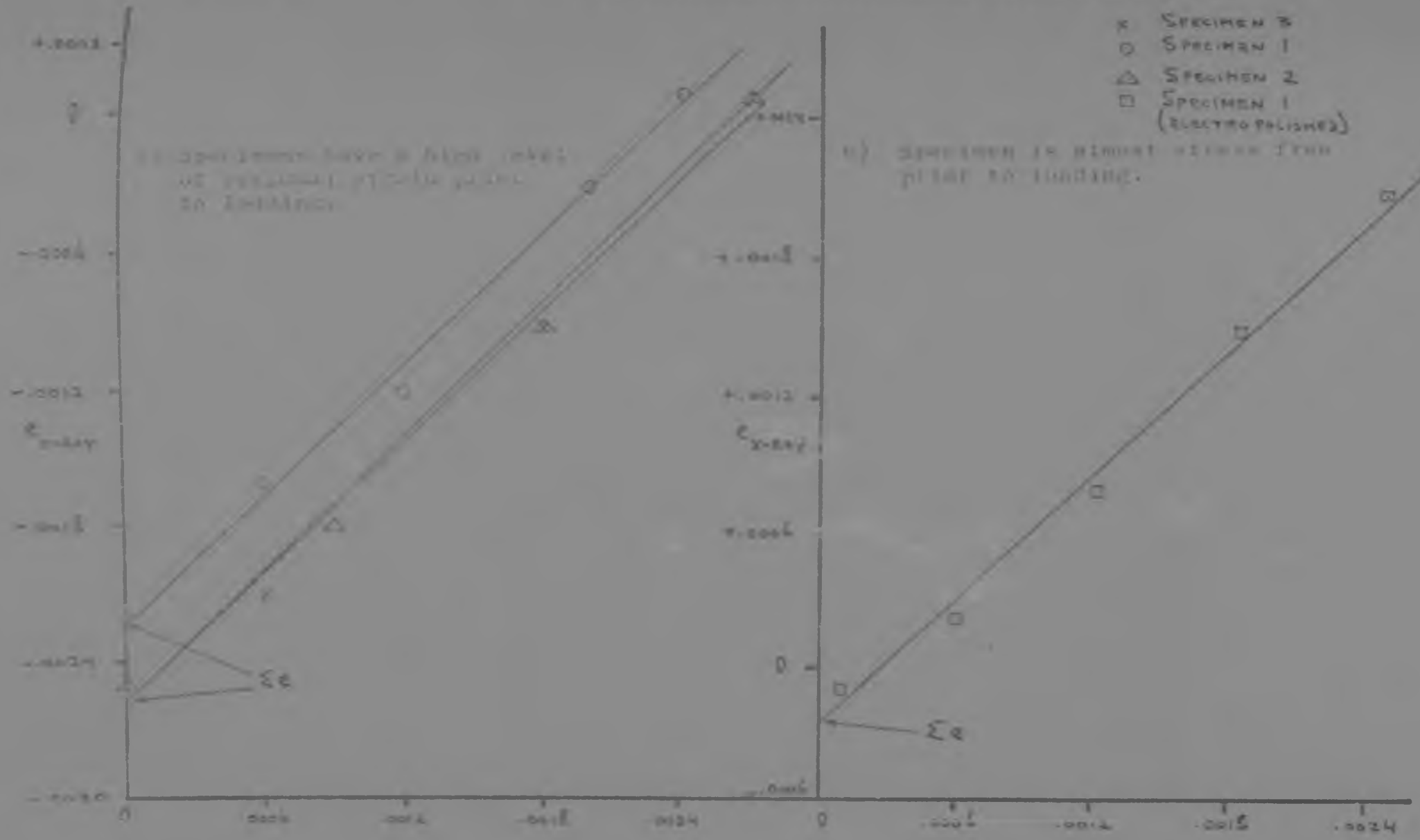
× SPECIMEN 3
○ SPECIMEN 1
△ SPECIMEN 2
□ SPECIMEN 1 (ELECTRO POLISHED)
$\varepsilon_{x\text{-}ray}$
ε_e
EXTERNALLY APPLIED STRAIN (4 POINT BENDING)

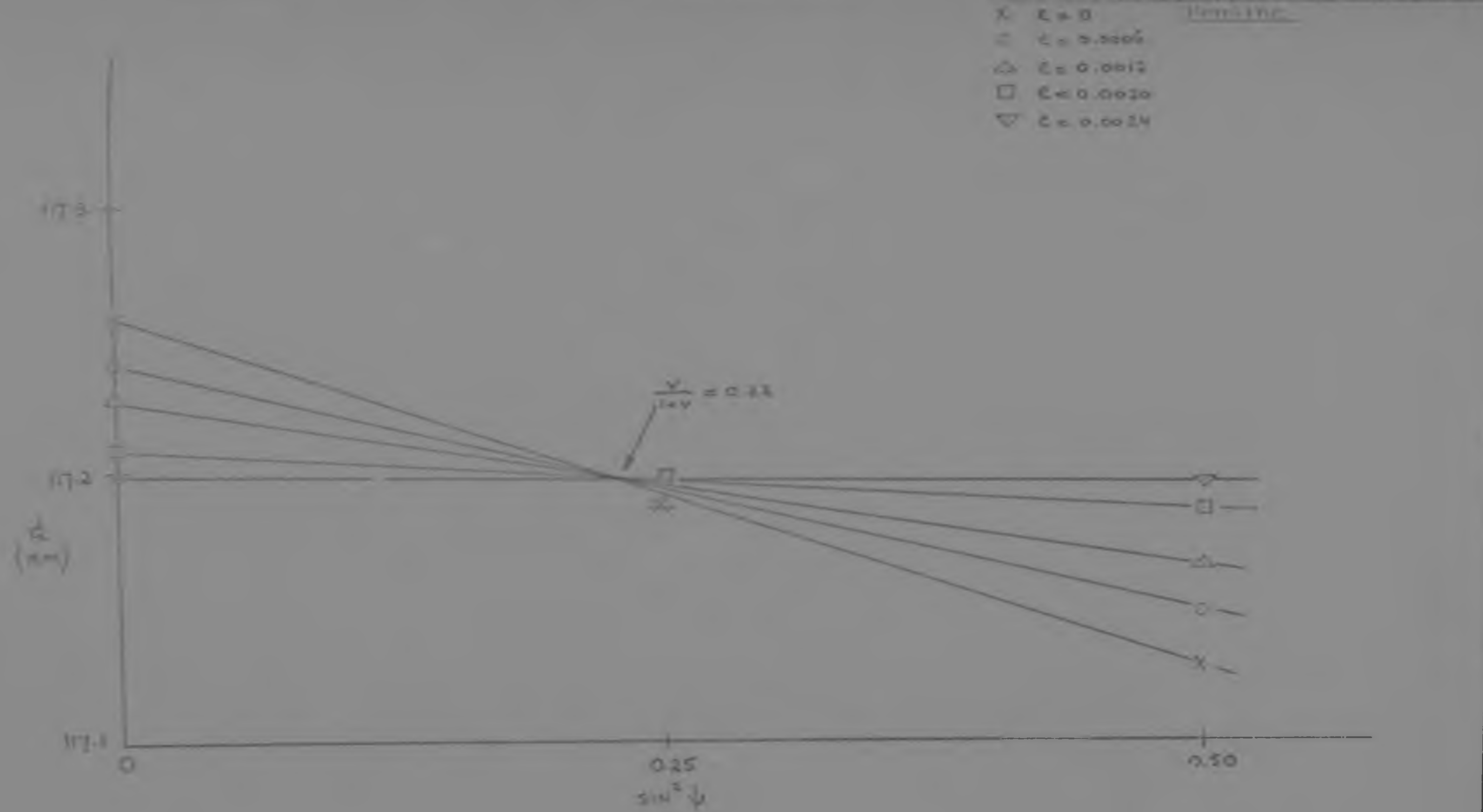

Figure 7: Variation of interplanar spacing versus $\sin^2\psi$ for different levels of EXTERNAL LOADING

FIGURE 8. [illegible] OF THE (220) DIFFRACTION PEAK OF MOLYBDENUM CARBIDE IN COMPACTS AFTER VARIOUS DIFFERENT SURFACE PREPARATION TREATMENTS

1. Tungsten Carbide Powder
2. Sintered Compact
3. Sintered and Tumbled Compact
4. Sintered and Grit Blasted Compact
5. Sintered and Electrolytically Ground Compact
6. Sintered and Ground Compact After All Vacuum Heating Cycles

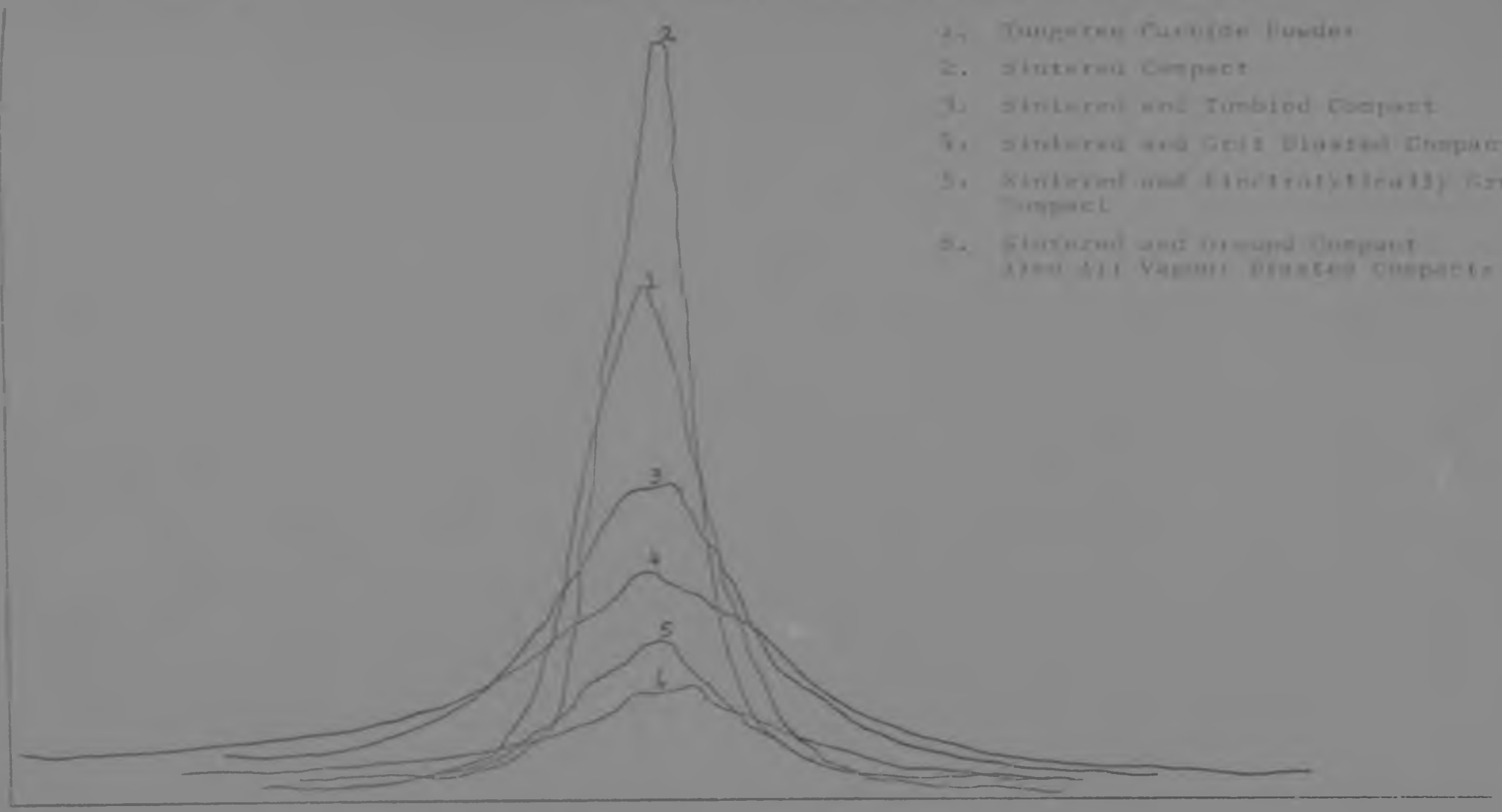

$\Delta 2\theta = 0.5°$

DOUBLE DIFFRACTION ANGLE 2θ

Figure 9 CONTOURS OF THE (100) DIFFRACTION PEAK OF TUNGSTEN CARBIDE IN COMPACTS AFTER SEVERAL DIFFERENT SURFACE PREPARATION TREATMENTS

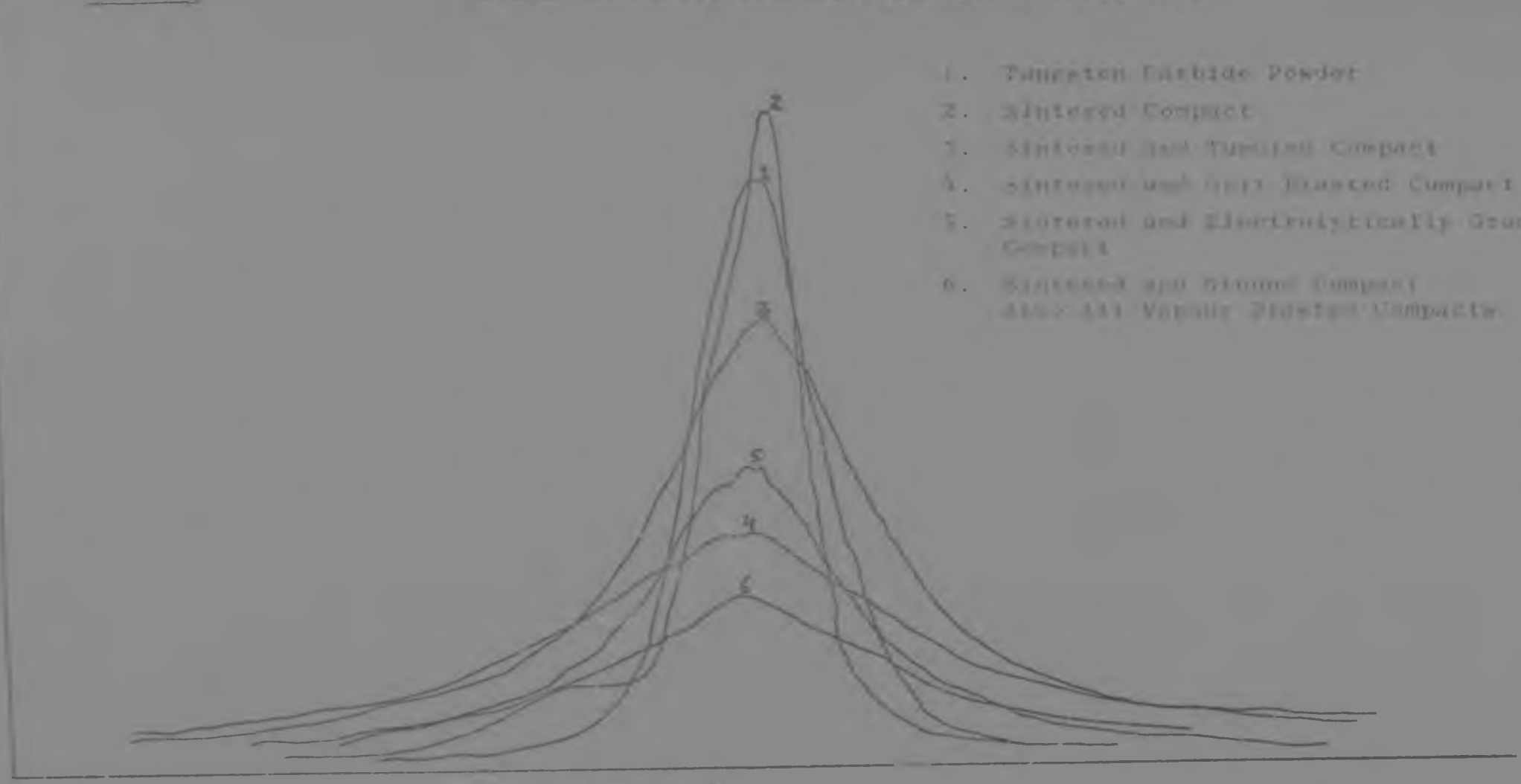

1. Tungsten Carbide Powder
2. Sintered Compact
3. Sintered and Tumbled Compact
4. Sintered and Dry Ground Compact
5. Sintered and Electrolytically Ground Compact
6. Sintered and Ground Compact After All Vacuum Plasma Compacts

FIGURE 10. CONTOUR OF THE (101) DIFFRACTION PEAK OF TUNGSTEN CARBIDE IN COMPACTS AFTER SEVERAL DIFFERENT SURFACE PREPARATION TREATMENTS

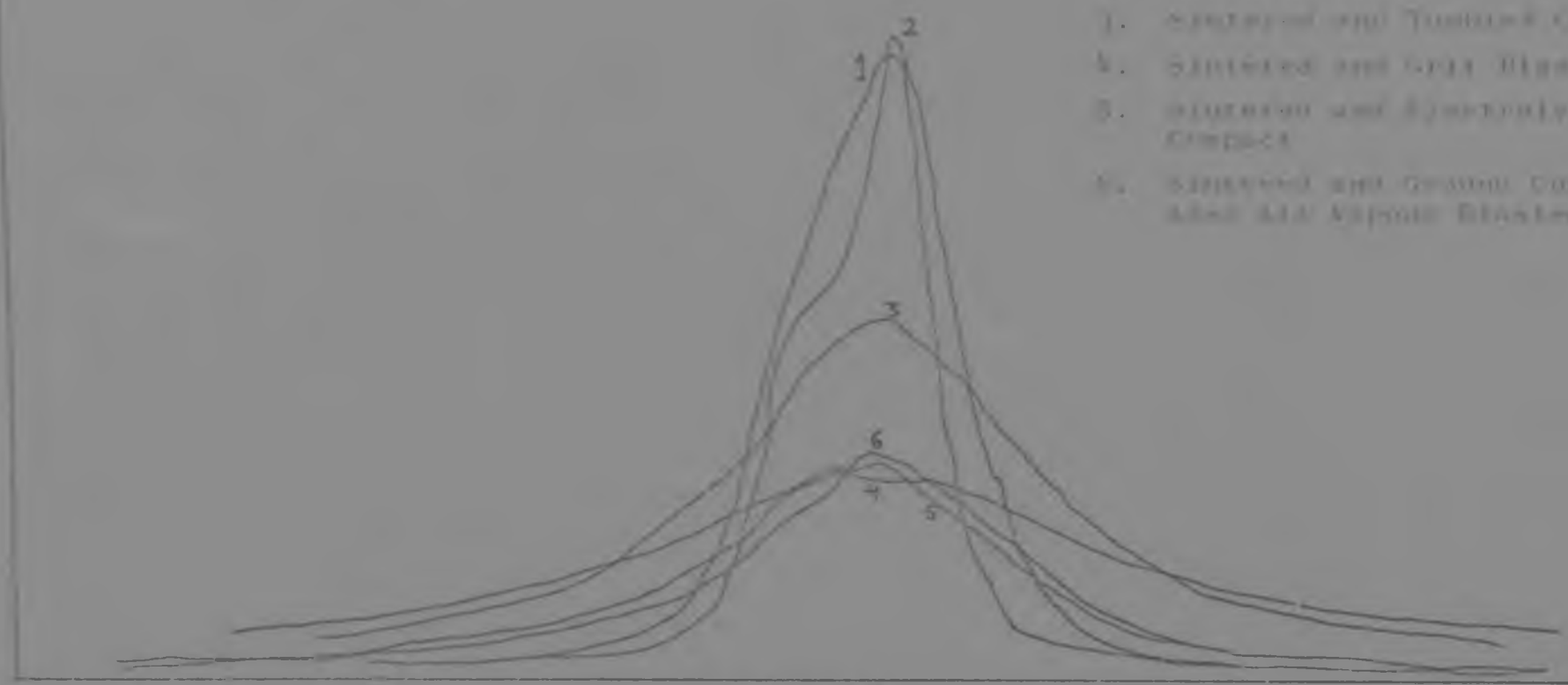

1. Tungsten Carbide Powder
2. Sintered Compact
3. Sintered and Tumbled Compact
4. Sintered and Grit Blasted Compact
5. Sintered and Electrolytically Ground Compact
6. Sintered and Ground Compact After AlO Vapour Blasted Complete

FIGURE 11. CONTOURS OF THE (201) DIFFRACTION PEAK OF TUNGSTEN CARBIDE IN SINTERED COMPACTS AND FRESH WC POWDER

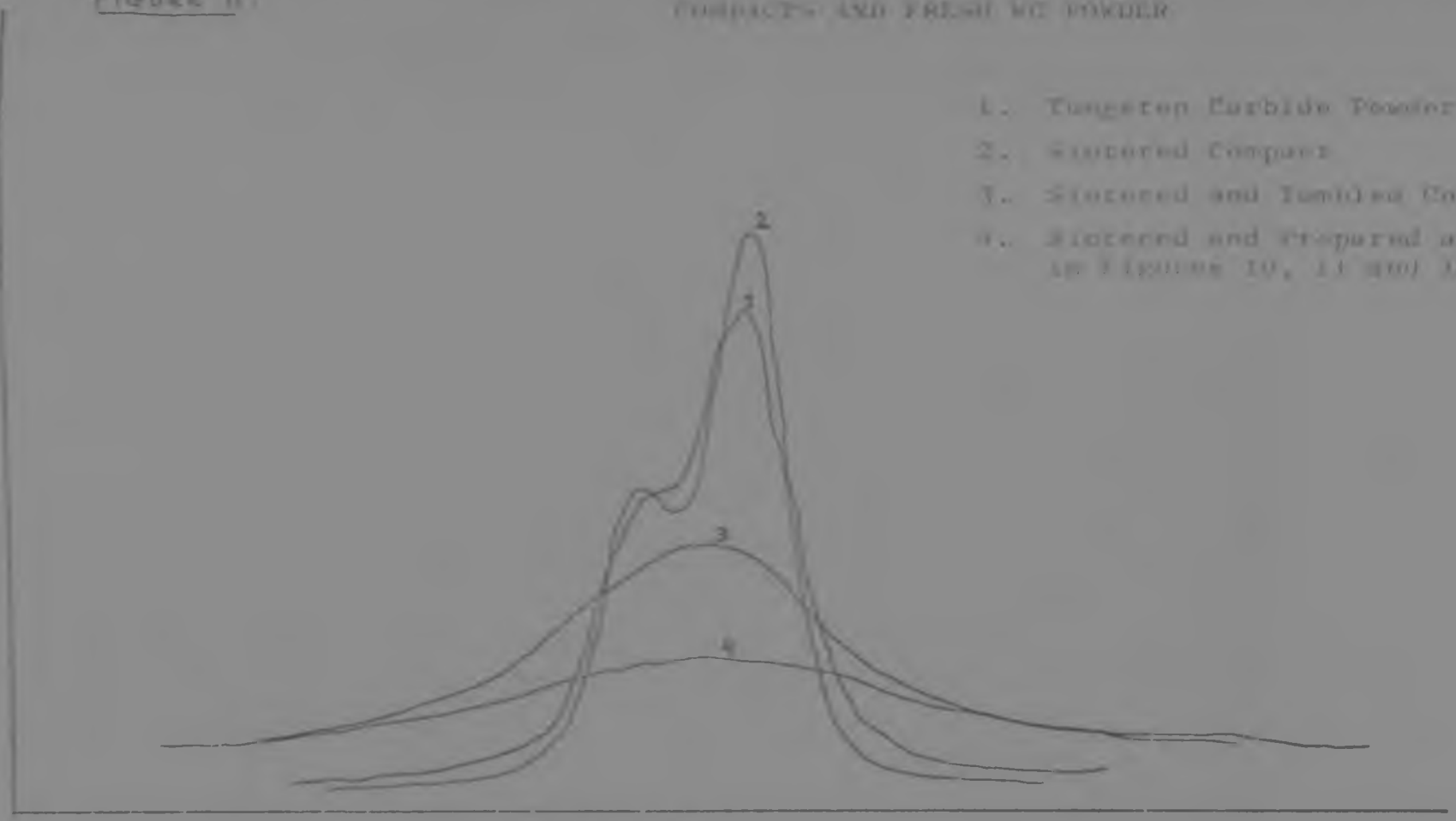

$\Delta 2\theta = 0.5°$

DOUBLE DIFFRACTION ANGLE 2θ

FIGURE 12

PROFILES OF THE (112) DIFFRACTION PEAK OF TUNGSTEN CARBIDE IN COMPACTS AND THESH OF POWDER

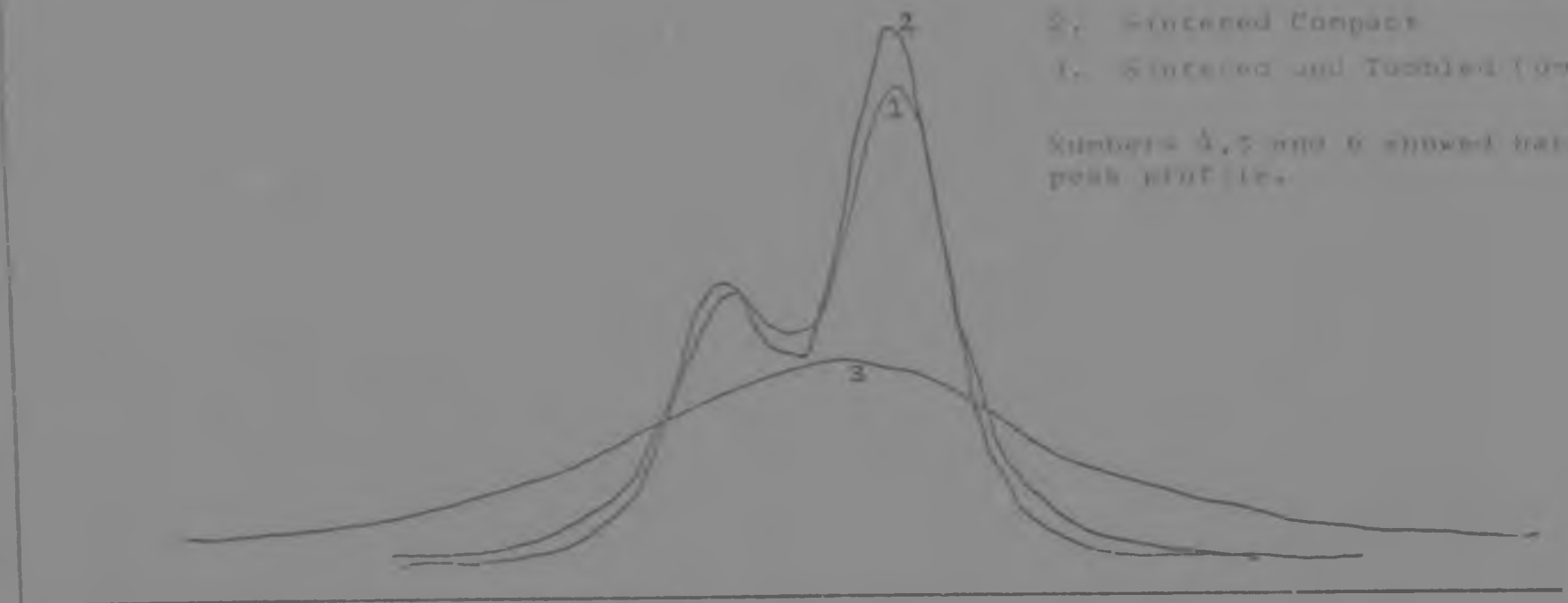

1. Tungsten Carbide Powder
2. Sintered Compact
3. Sintered and Tumbled Compact

Numbers 1, 2 and 3 showed hardly any peak profile.

INTENSITY

$\Delta 2\theta = 0.5°$

DOUBLE DIFFRACTION ANGLE 2θ

FIGURE 13

DETERMINATION OF PARTICLE SIZE AND PLASTIC STRAIN FROM DIFFRACTION PEAK BROADENING

REFERENCE SPECIMEN: ANNEALED AC POWDER

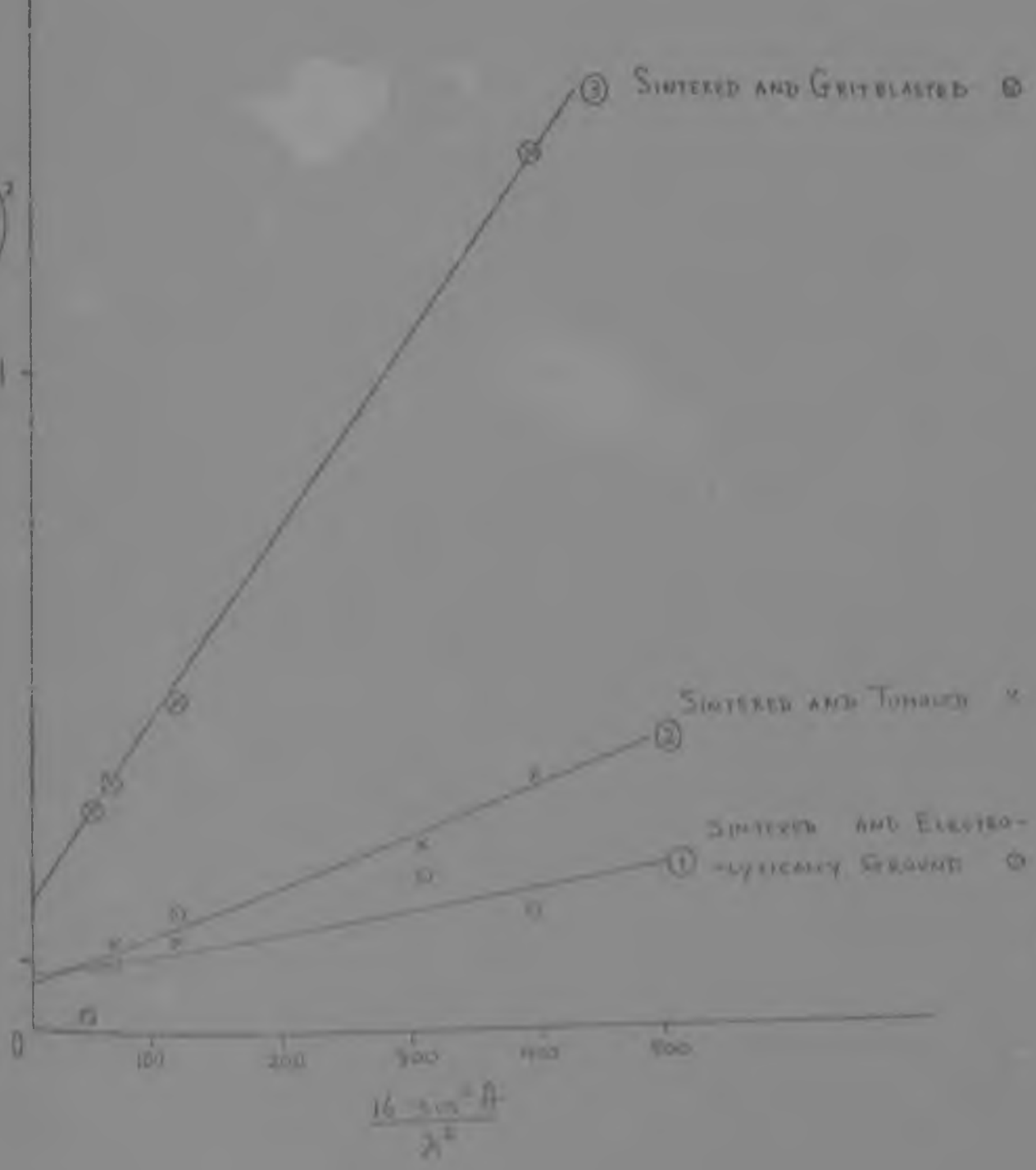

FIGURE 14.

D/II BIT ANALOGUE, PLAN AND ELEVATION.

SCALE: 1 : 1

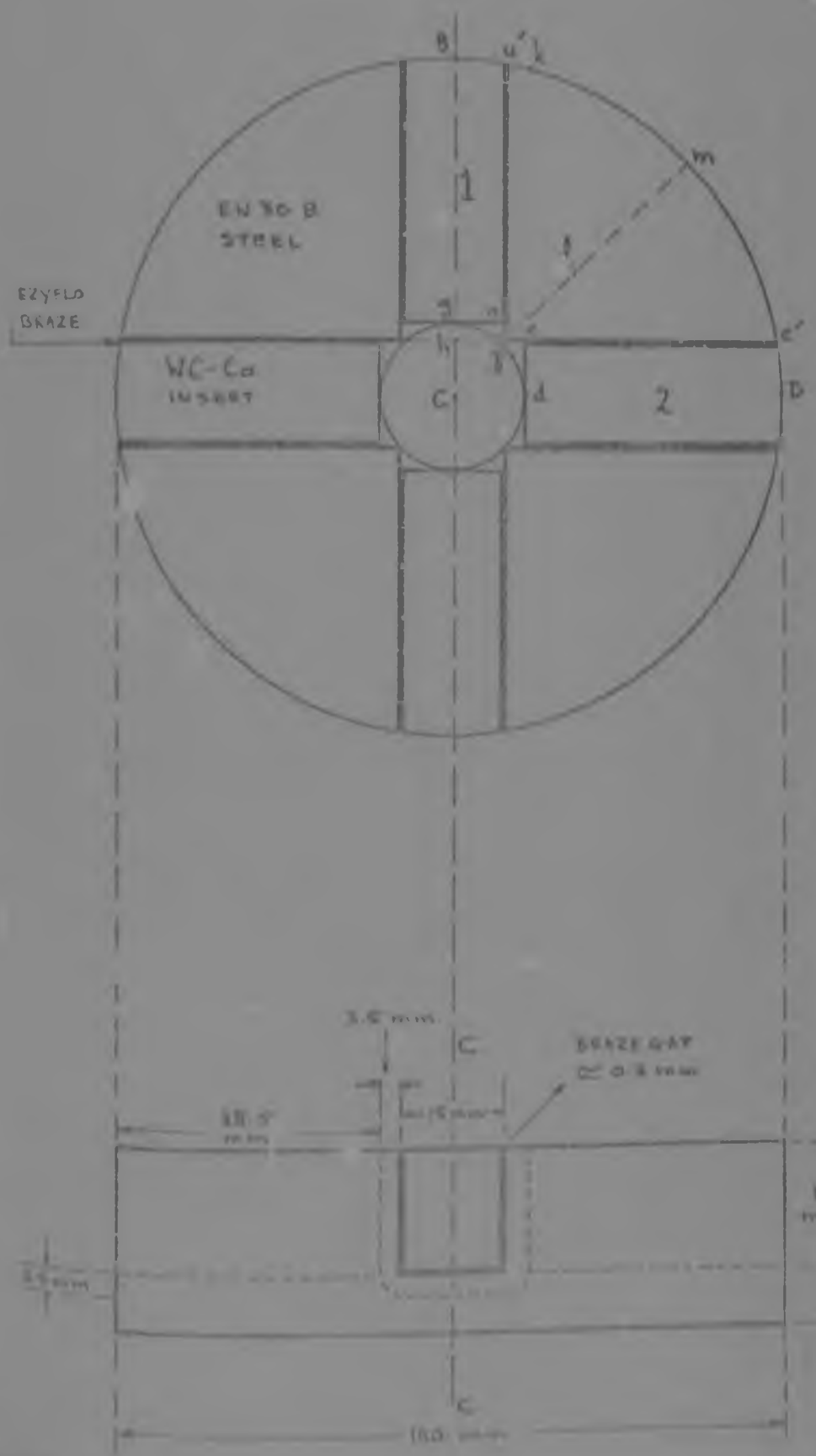

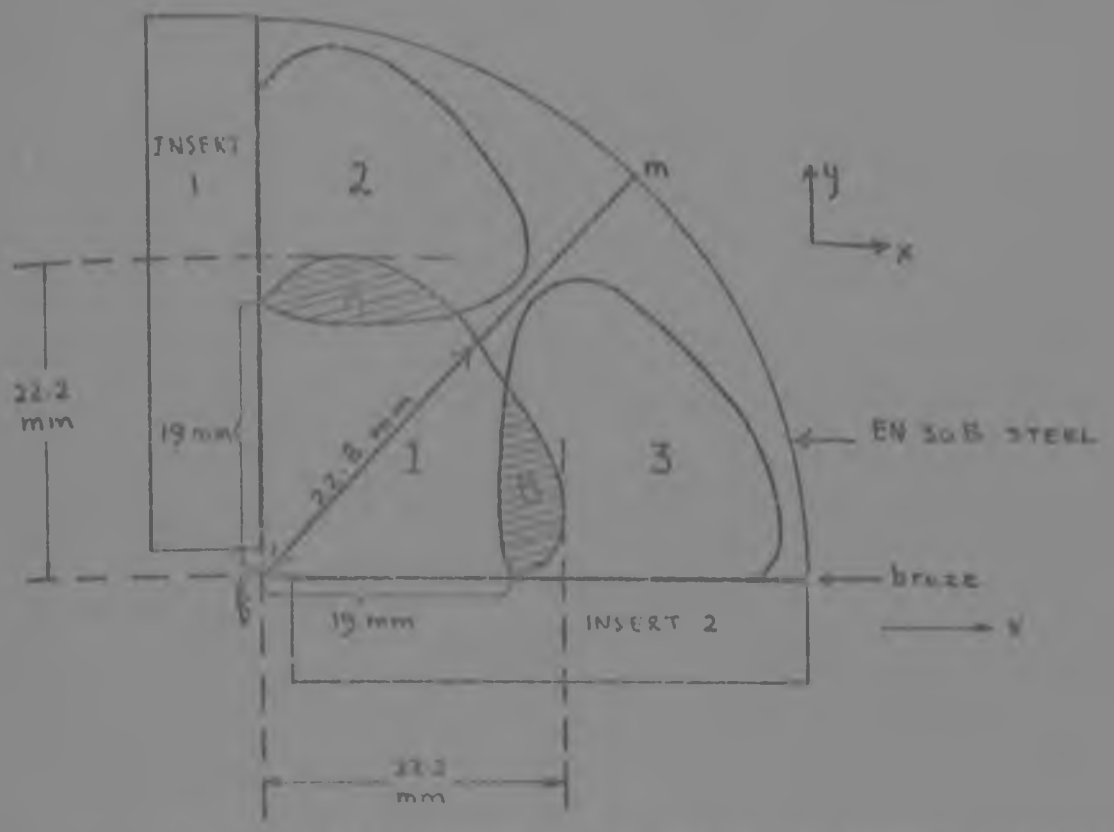

FIGURE 15. ELECTRODEPOSITED AREAS ON SECTOR SURFACES
THE THREE DEPOSITED AREAS ARE designated 1, 2 and 3.

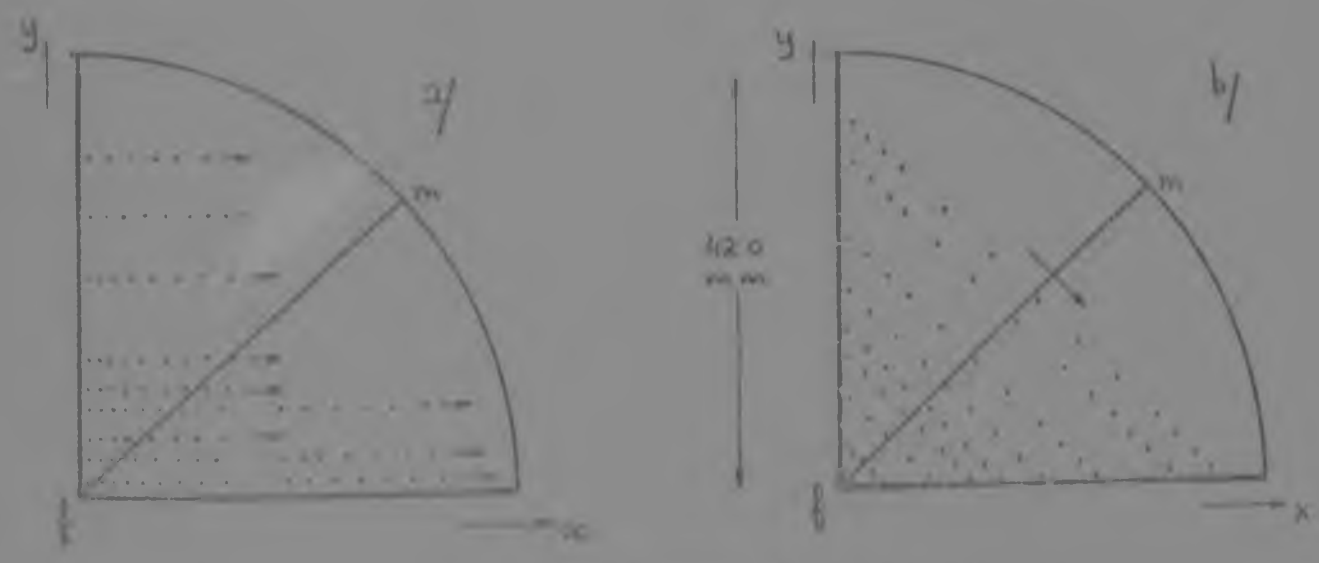

FIGURE 16. a), b), c).
GRID OF DIRECTIONS OF STRAIN MEASUREMENTS ON x, y, 45° AND y TRAVERSES. (a) DIRECTIONS OF STRAIN MEASUREMENT AT $\phi = 0°$, $\phi = 45°$ AND $\phi = 90°$.

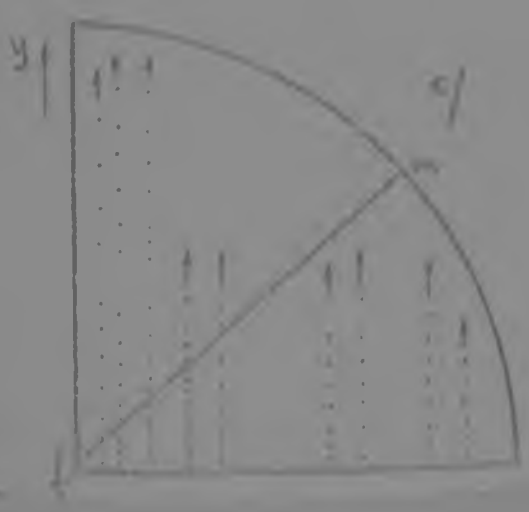

FIGURE 17

STRAIN IN THE X – DIRECTION MEASURED ALONG THE TRANSVERSE $\Delta_3 = 1.27$ mm

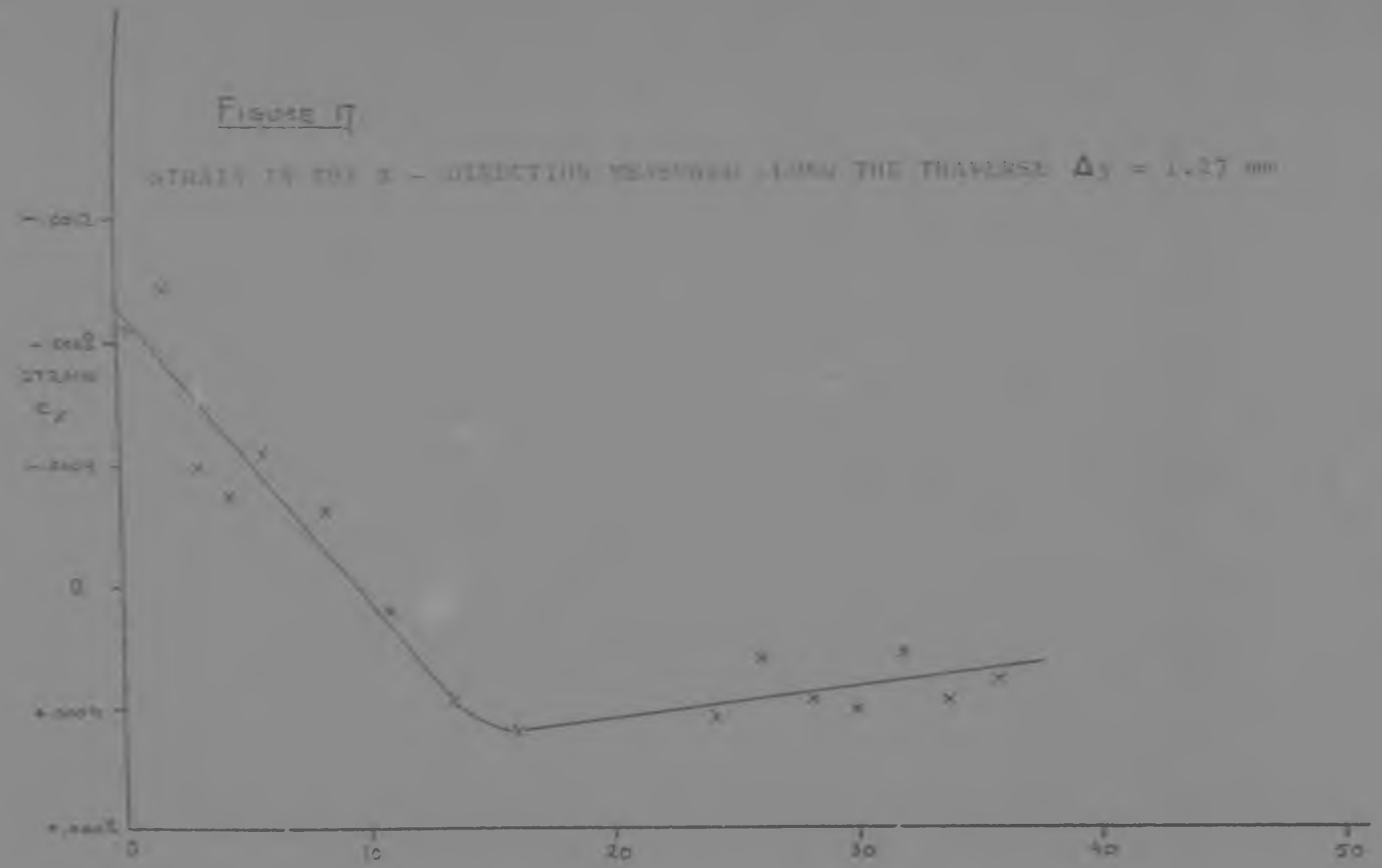

DISTANCE X (mm)

FIGURE 18.

STRAIN IN THE X-DIRECTION MEASURED ALONG THE TRAVERSE Δ_1 = 3.81 mm

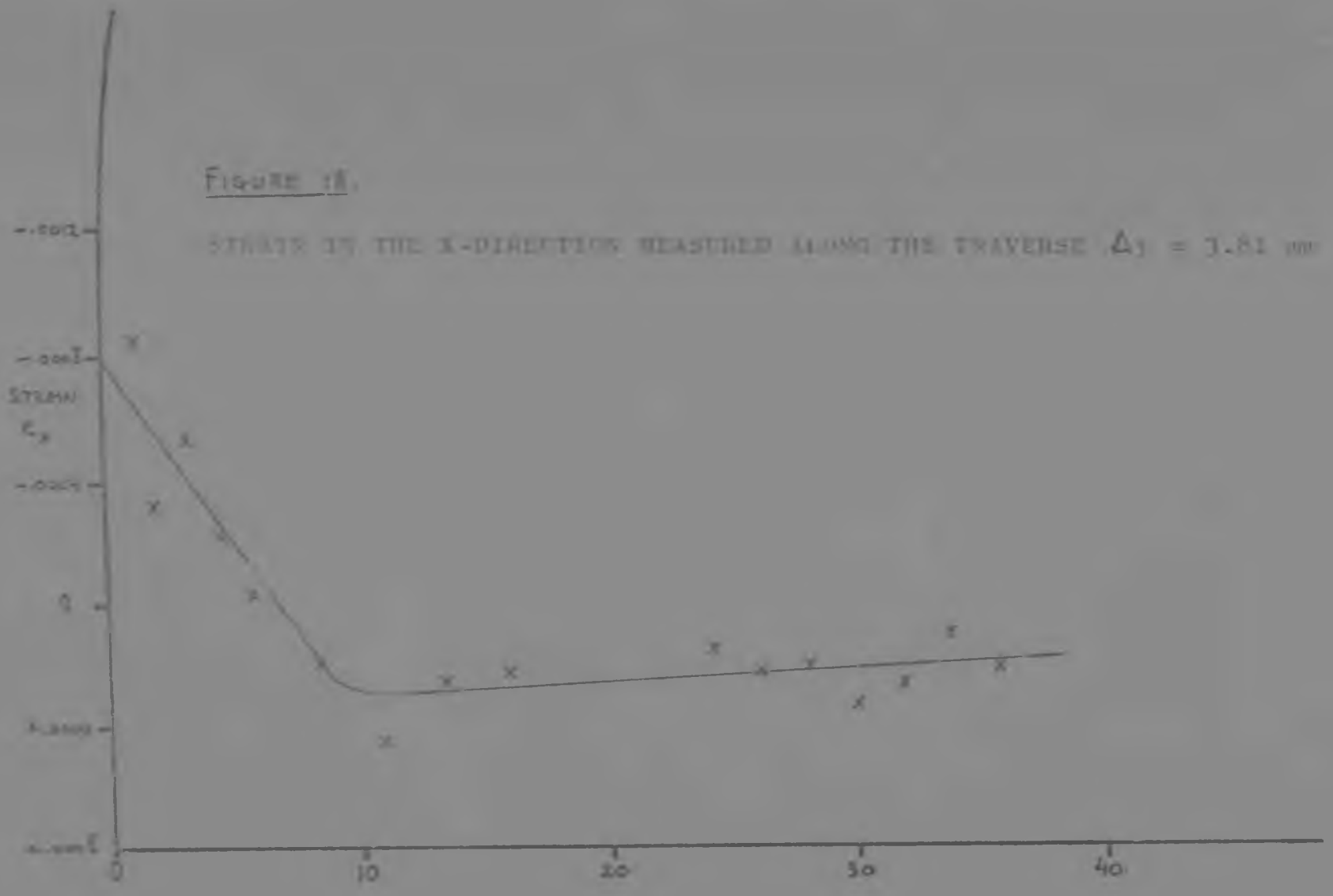

DISTANCE x (mm)

Figure 19.

-1.0/2 IN THE X-DIRECTION MEASURED ALONG THE TRAVERSE $\Delta y = 5.21$ mm

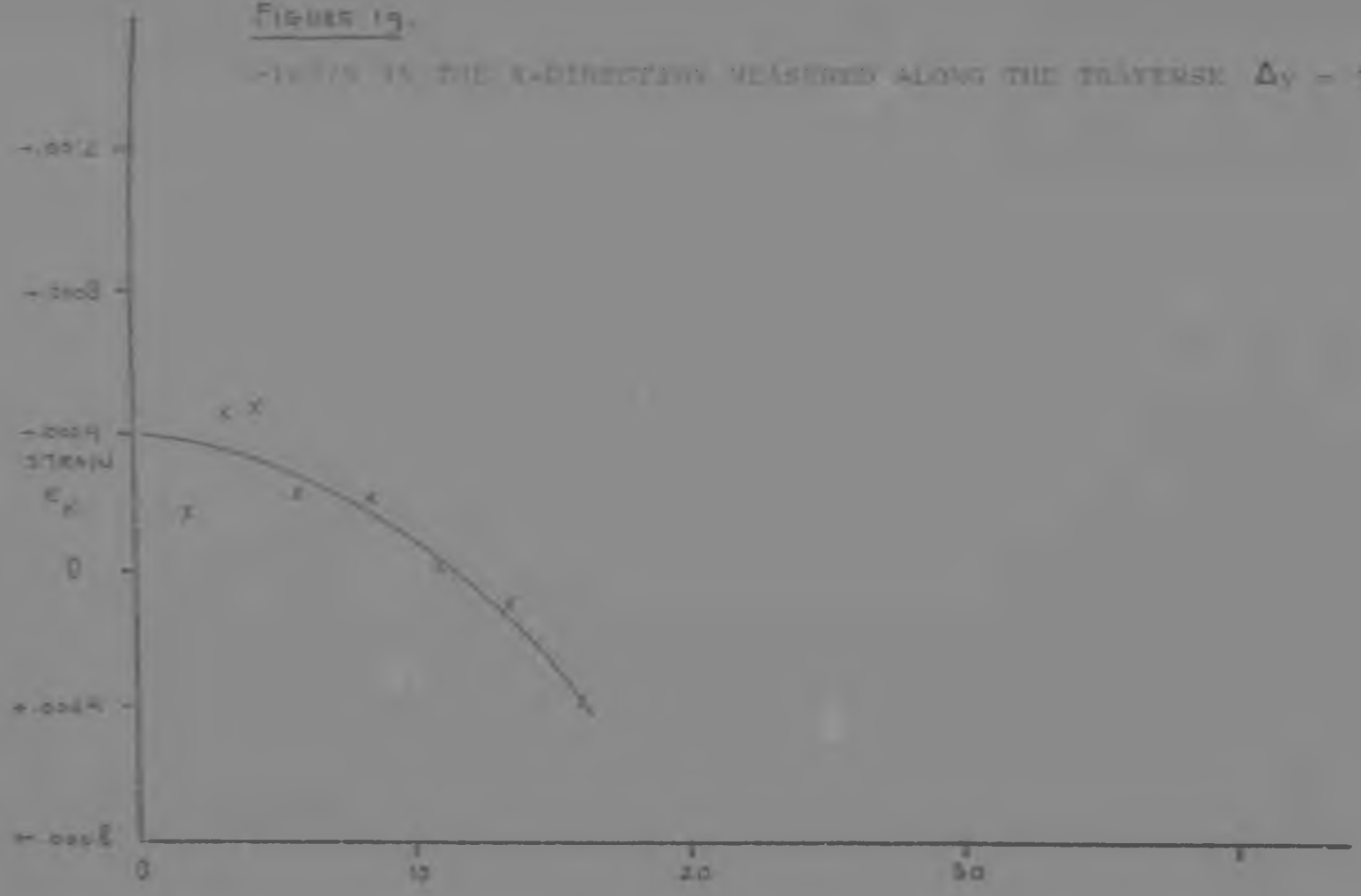

FIGURE 10

STRAIN IN THE X-DIRECTION MEASURED ALONG THE TRAVERSE $\Delta_x = 8.00$ mm

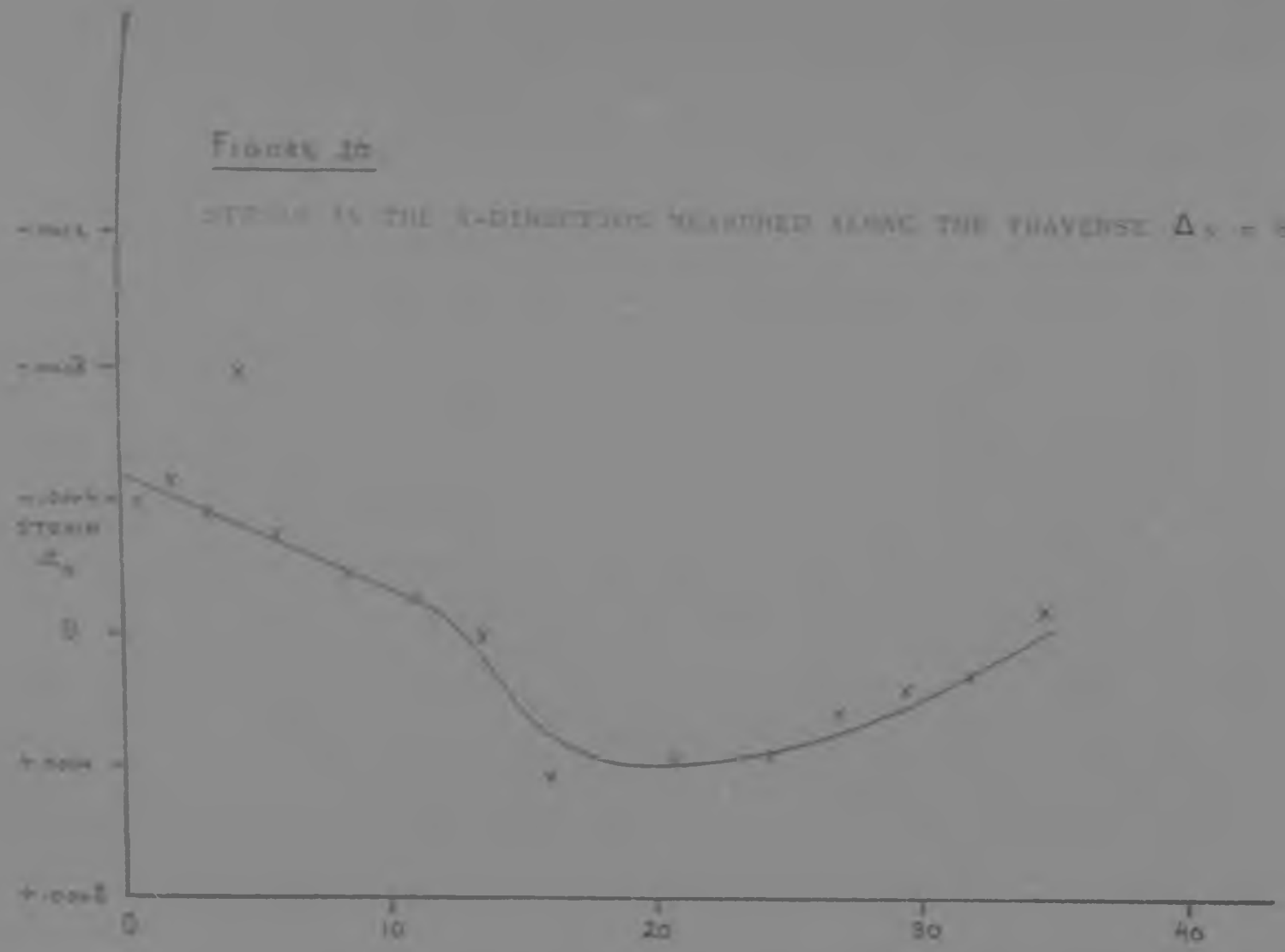

STRAIN IN THE X-DIRECTION MEASURED ALONG Δ_y TRAVERSES

FIGURE 21

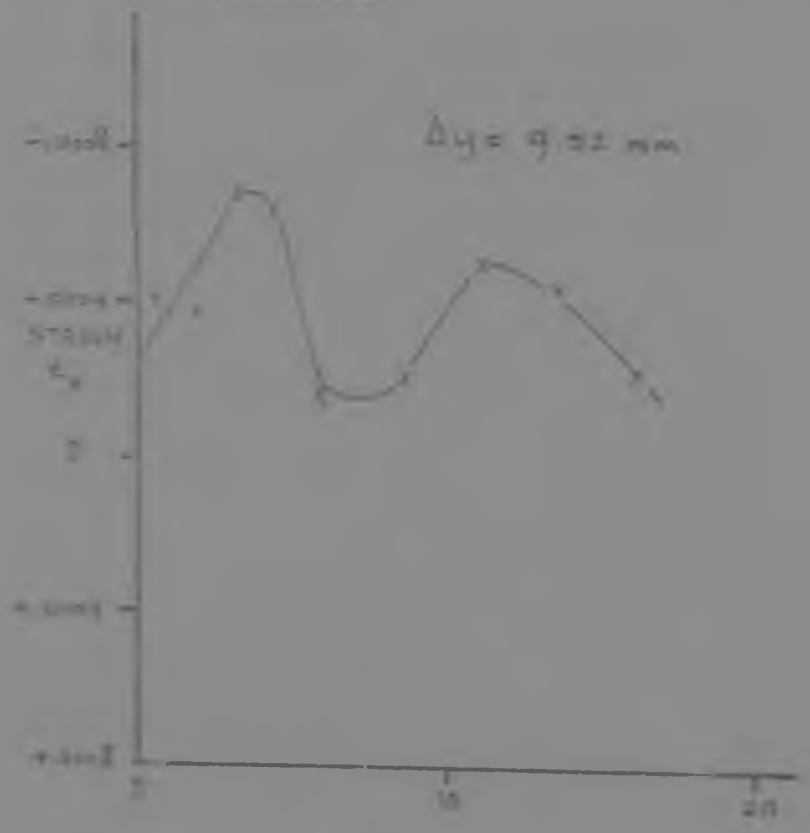

FIGURE 22.

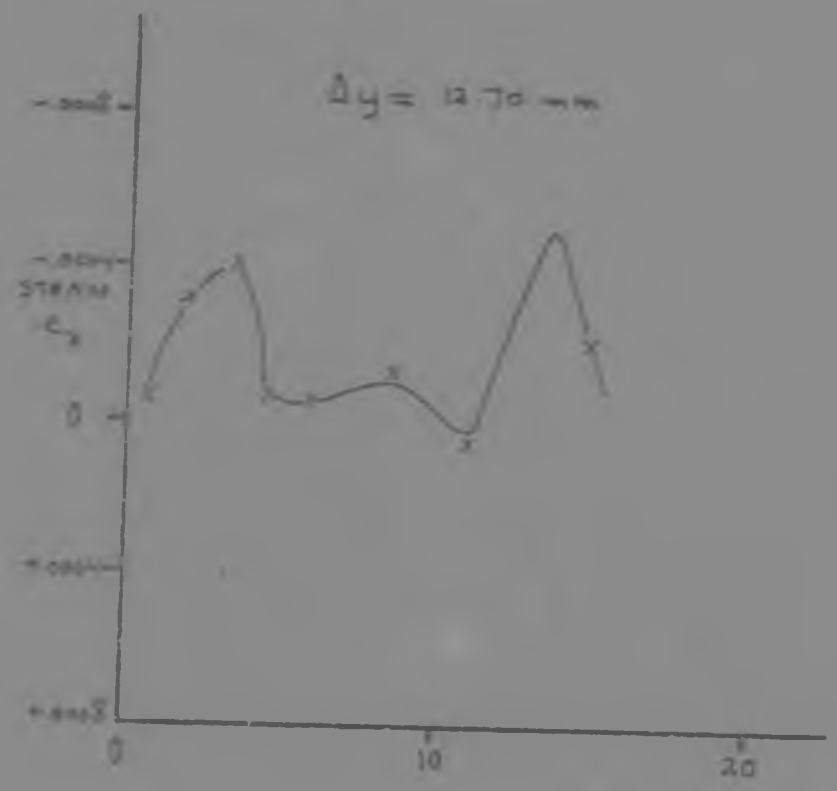

FIGURE 23.

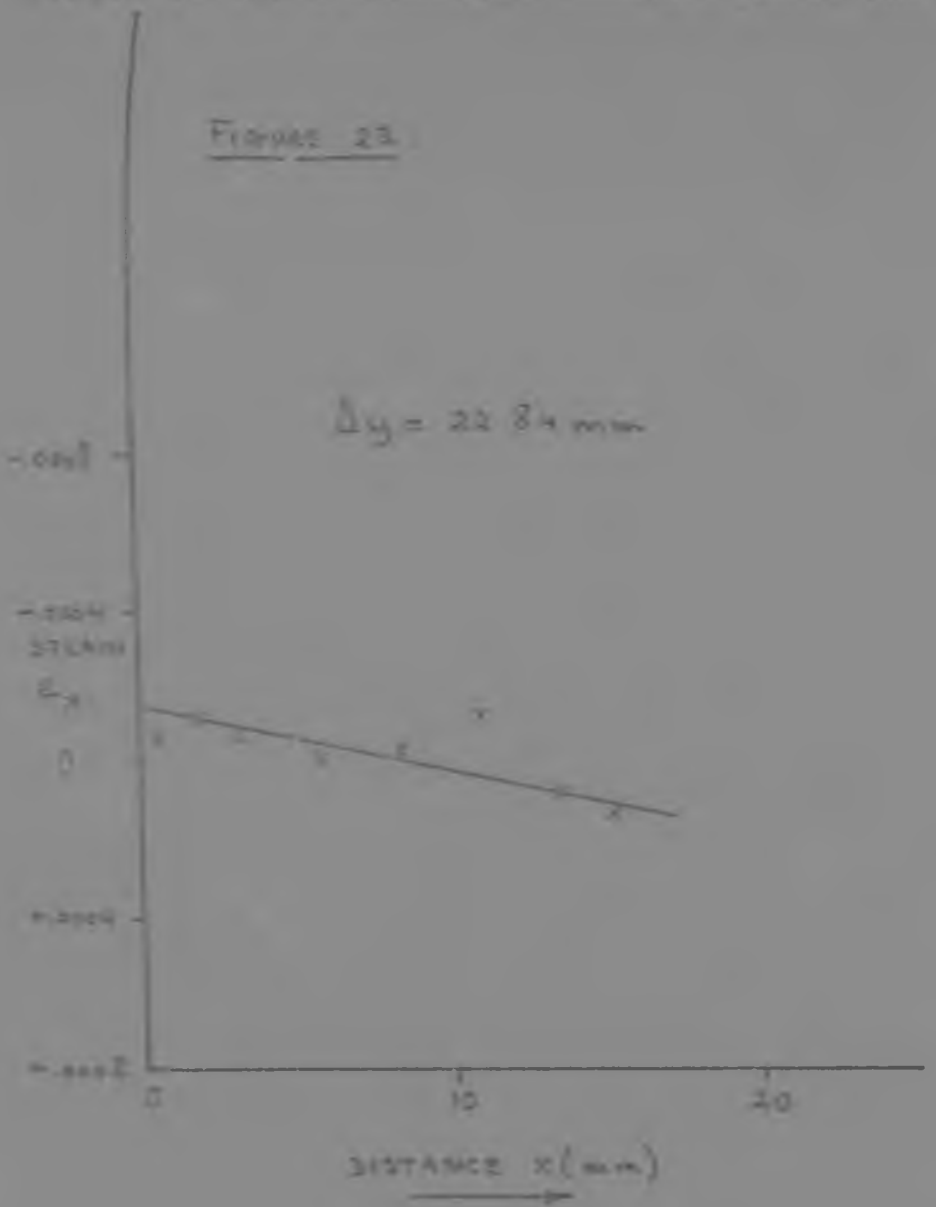

FIGURE 24.

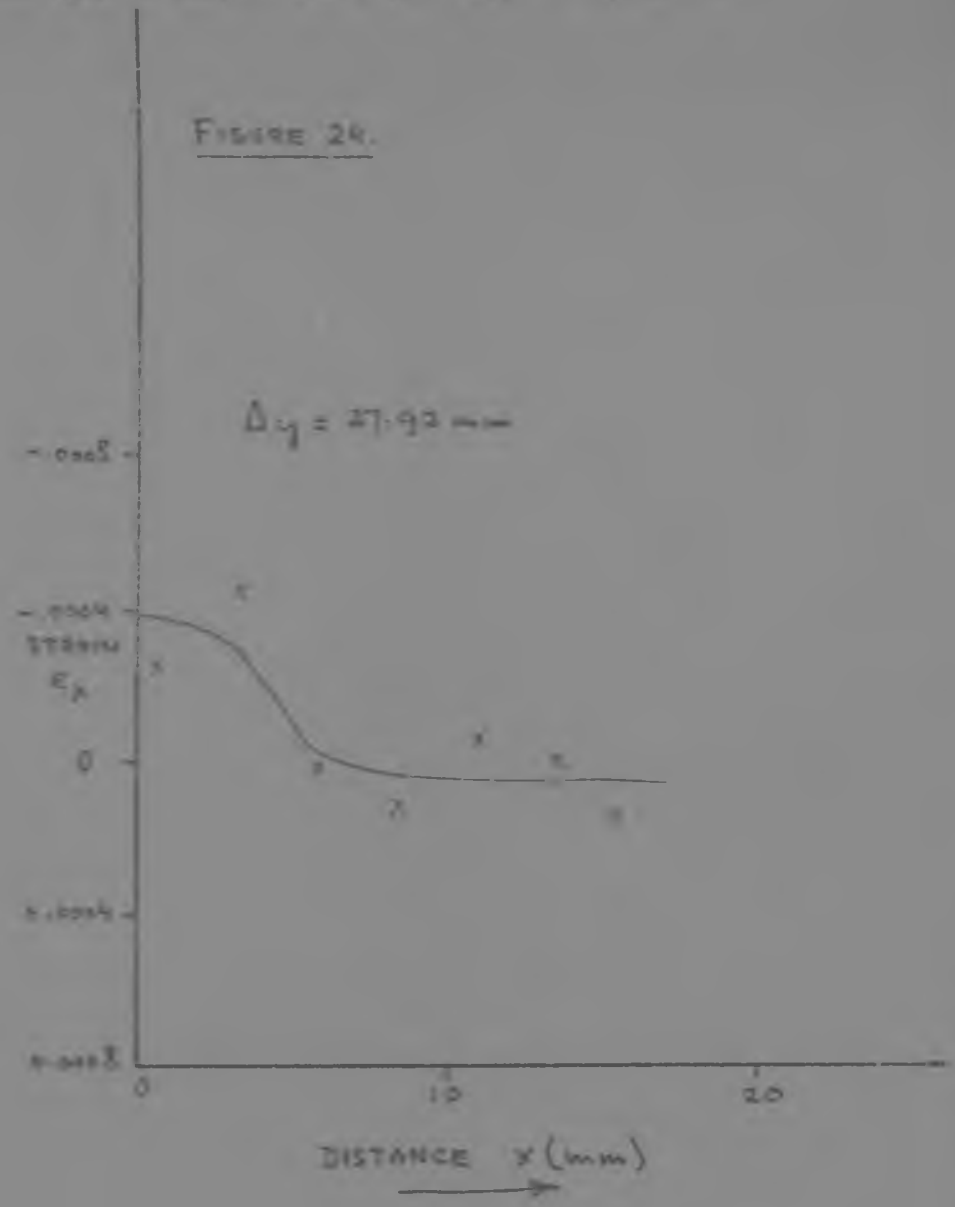

FIGURE 25.

STRAIN IN THE X-DIRECTION MEASURED ALONG THE TRAVERSE Δy = 31.75 mm

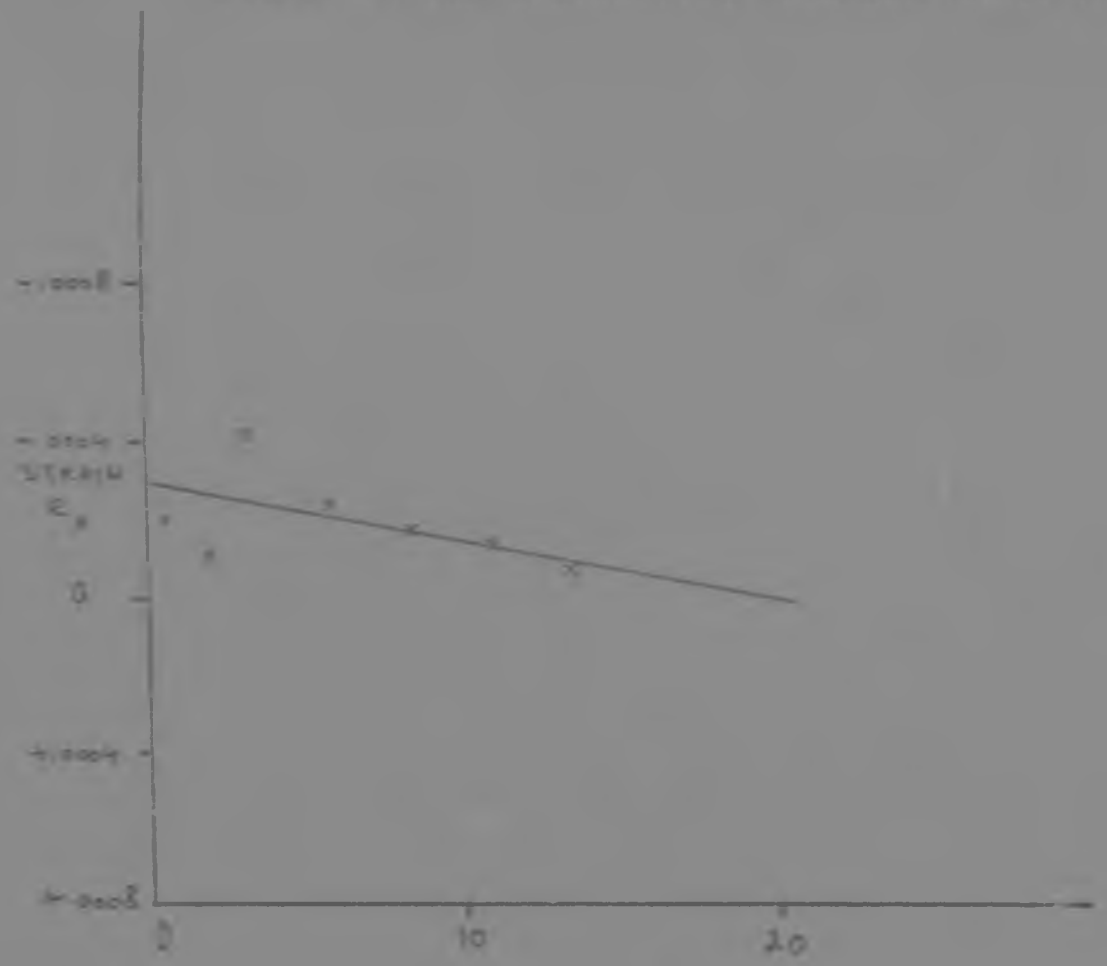

STRAIN $\varepsilon_{45°}$ IN THE 45° DIRECTION MEASURED ALONG THE TRAVERSES
AT S = 1.27 mm, S = 2.54 mm AND S = 5.71 mm FROM POINT A

FIGURE 26.

S = 1.27 mm

FIGURE 27.

S = 2.54 mm

FIGURE 28.

S = 5.71 mm

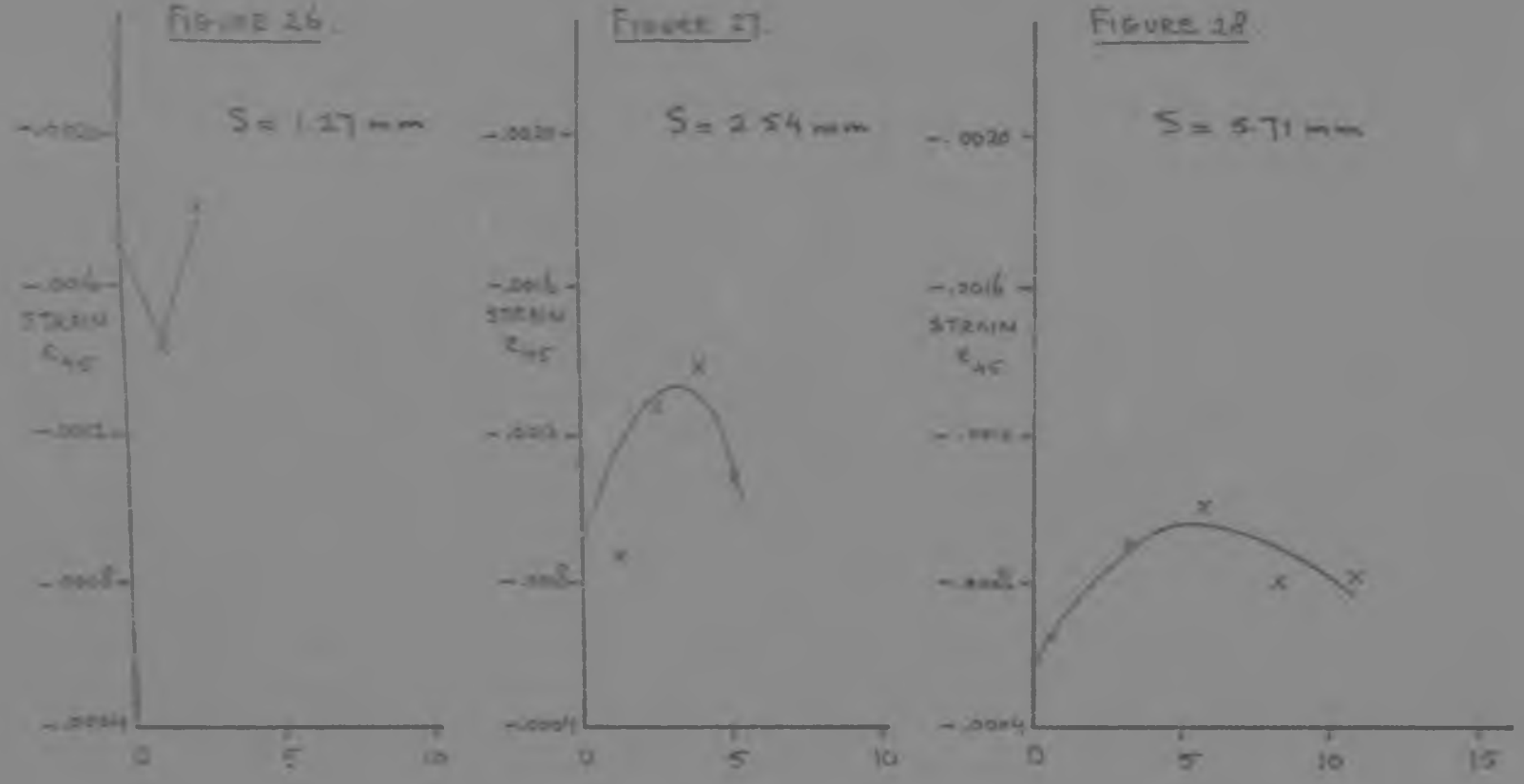

DISTANCE b (mm)

FIGURE 29.

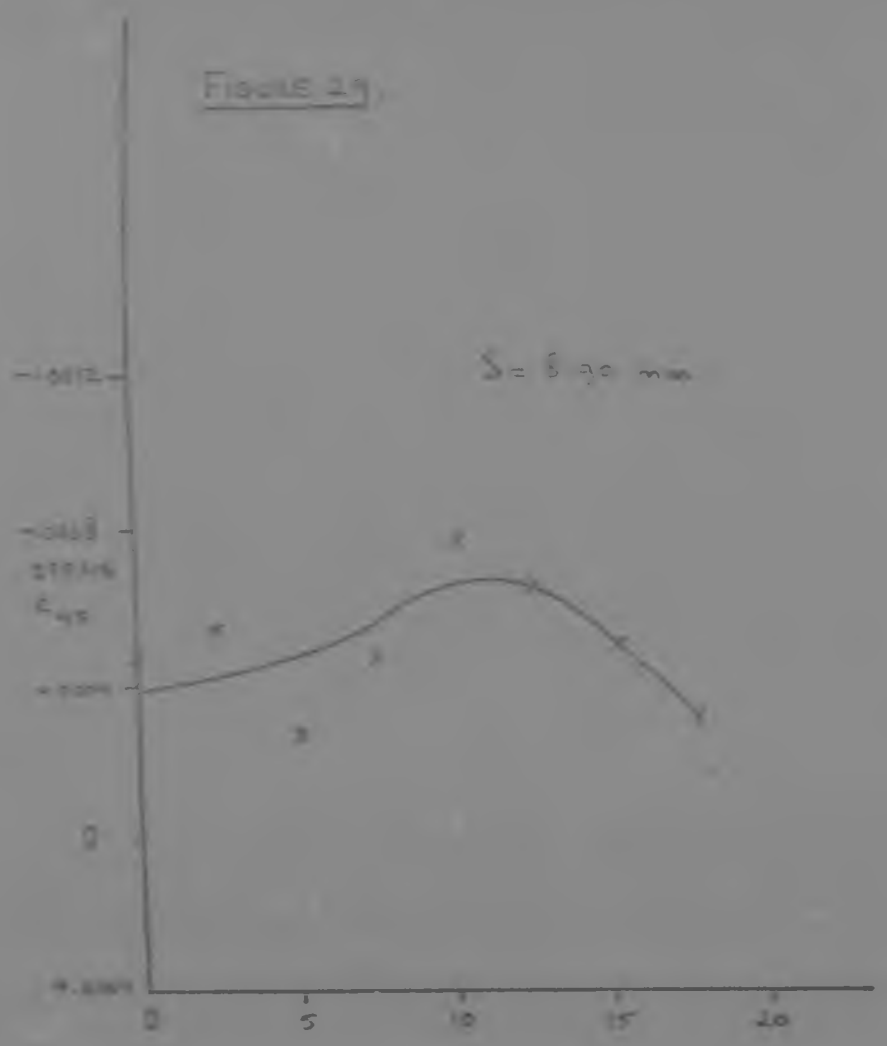

FIGURE 30.

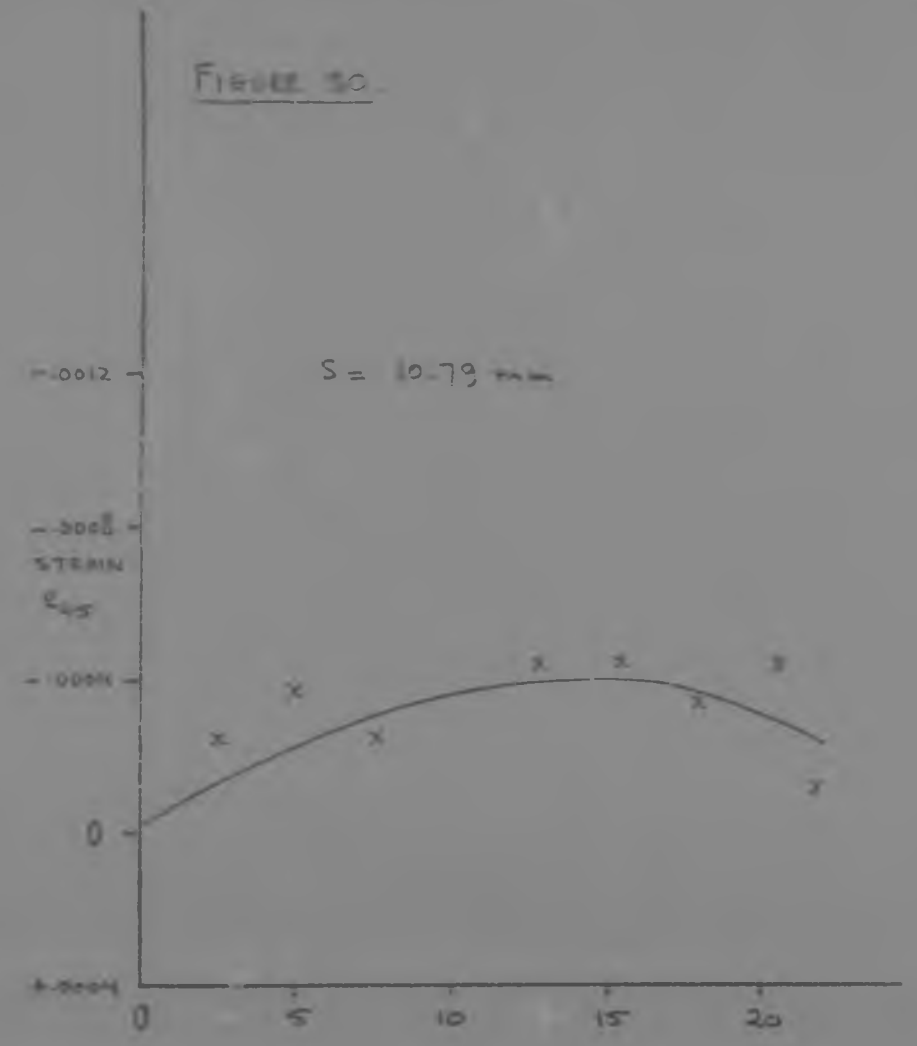

FIGURE 31

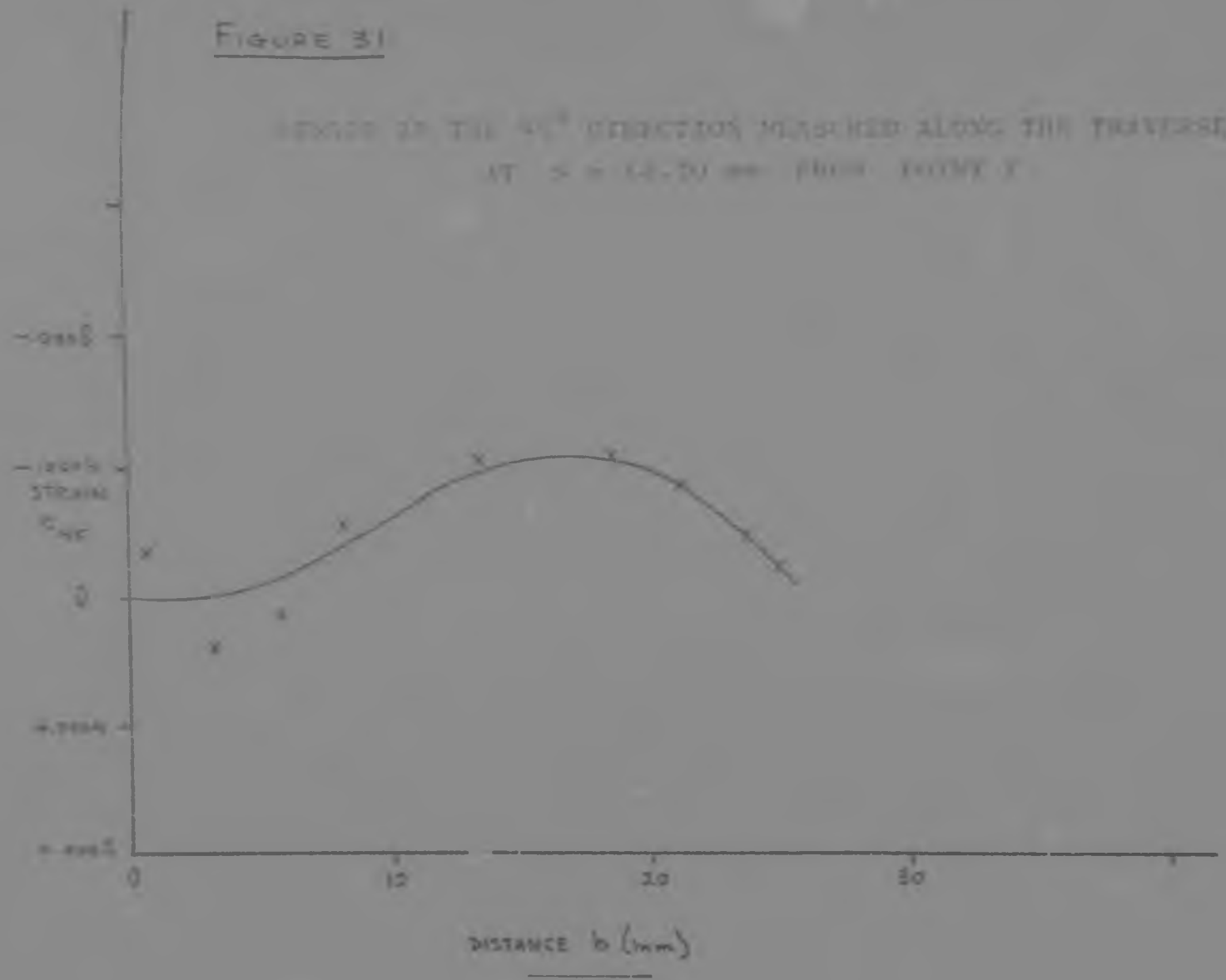

FIGURE 32

STRAIN IN THE 45° DIRECTION MEASURED ALONG 4E TRAVERSE AT S = 17.78 mm FROM POINT 4

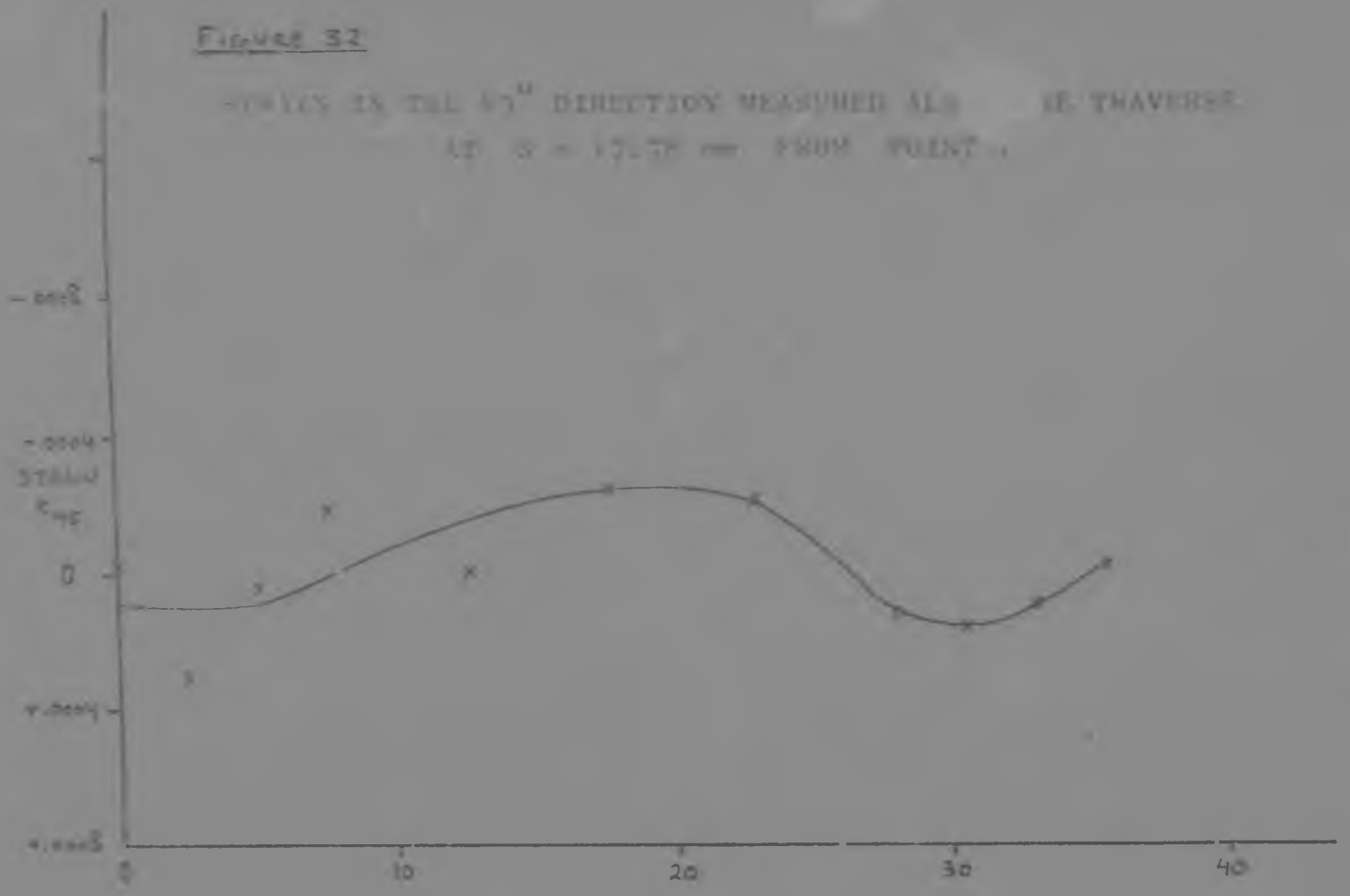

FIGURE 35

STRESS ON THE 45° DIRECTION MEASURED ALONG THE TRAVERSE
AT $\delta = 22.56$ mm FROM POINT 0

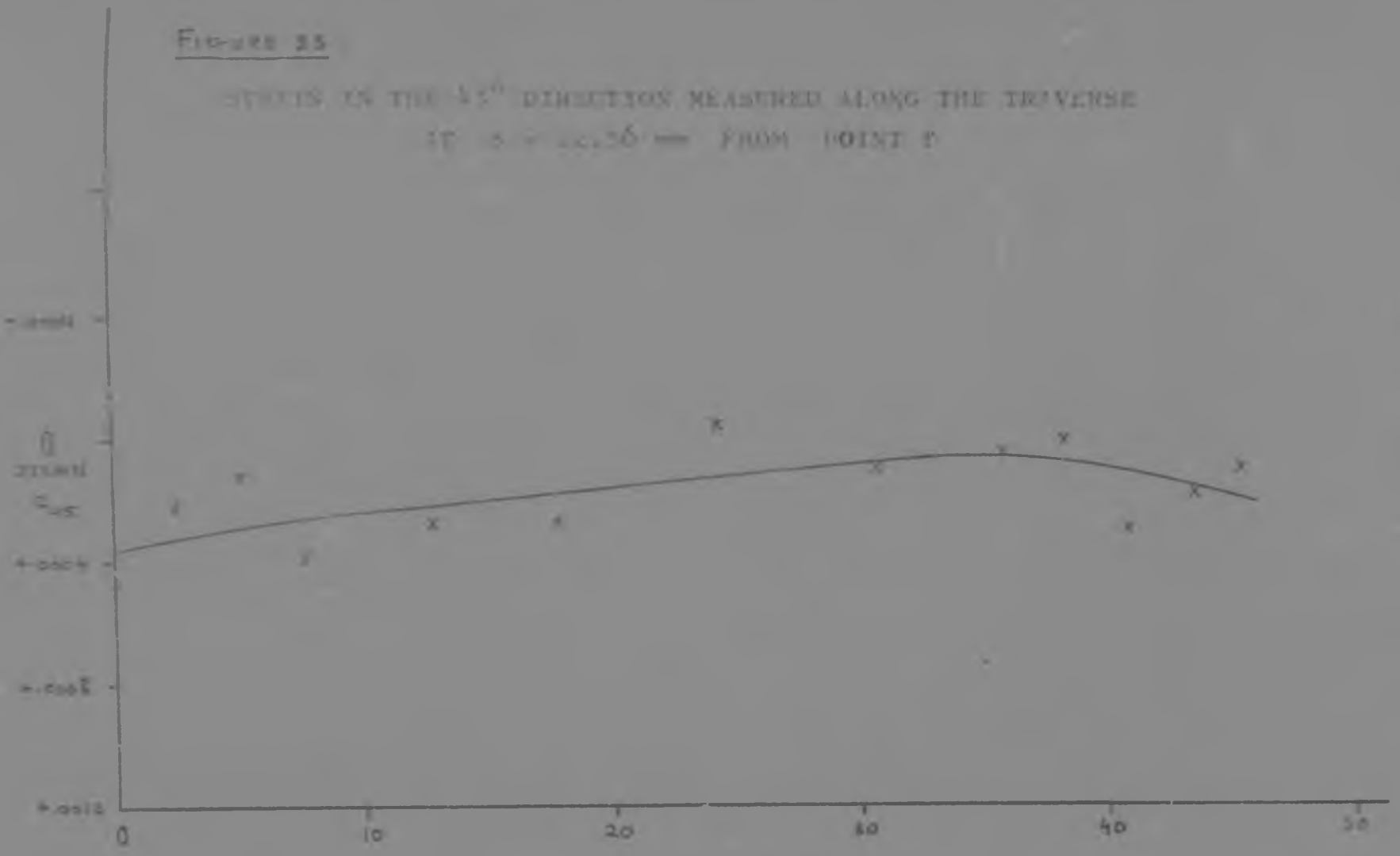

Figure 54.

STRESS IN THE 45° DIRECTION MEASURED ALONG THE TRAVERSE
AT $\sigma = 20{,}04$ mm FROM POINT I

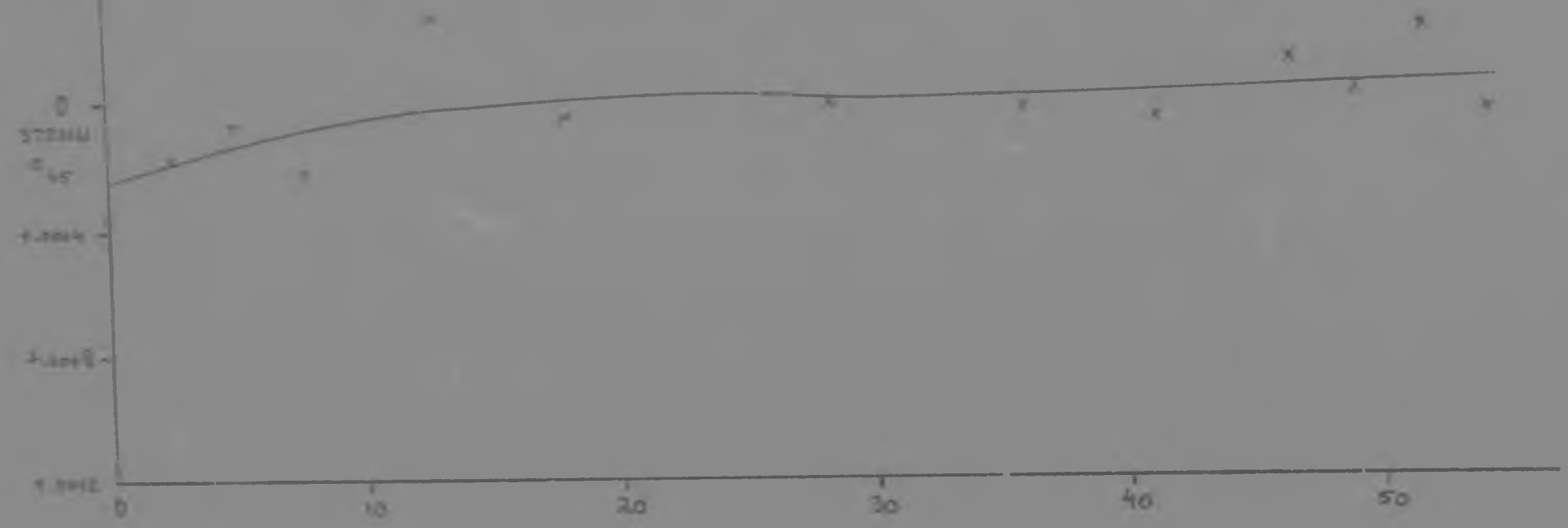

FIGURE 35.

VELOCITY IN THE y-DIRECTION MEASURED ALONG THE TRAVERSE

$\Delta x = 2.5\frac{1}{2}$ mm

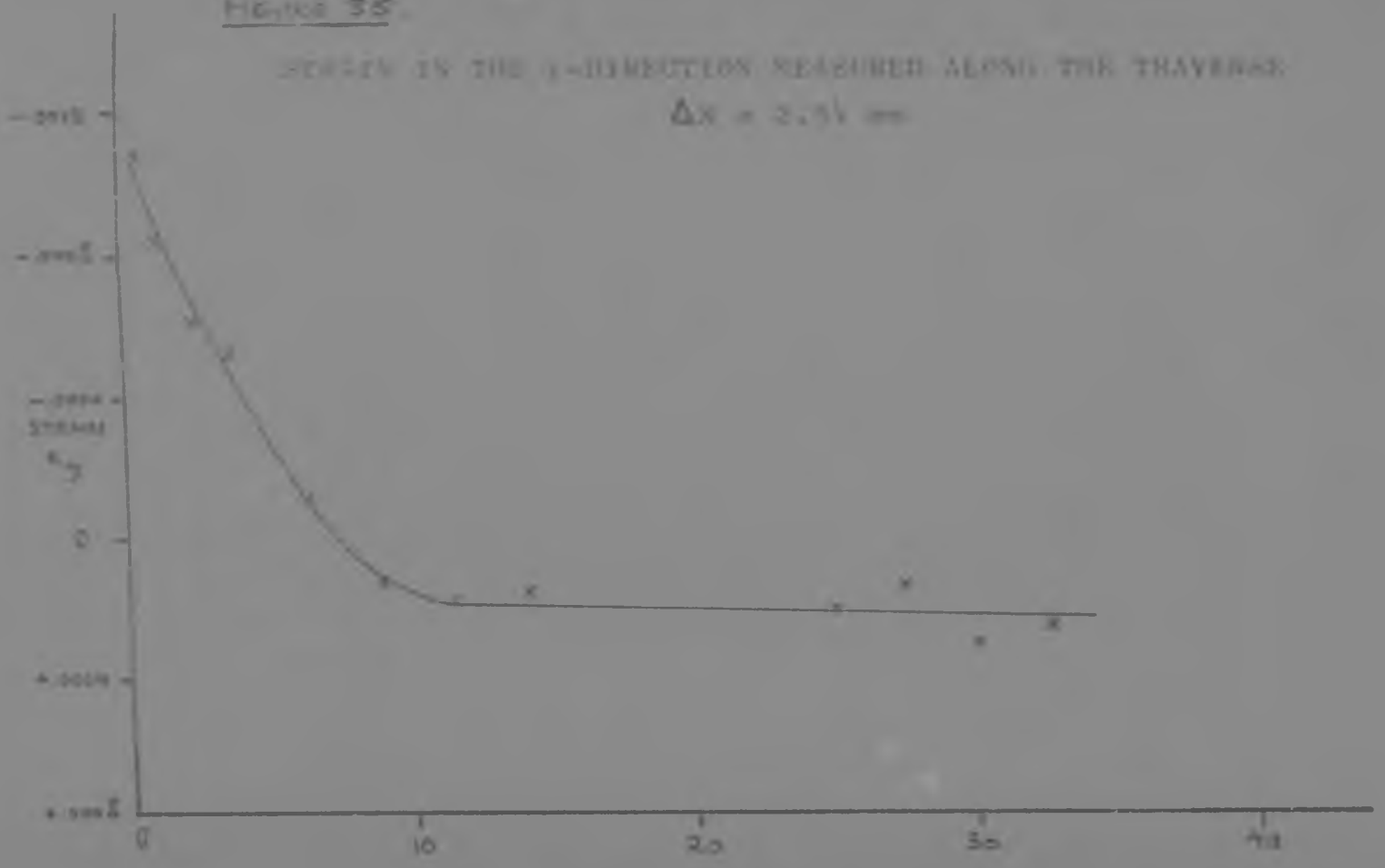

DISTANCE y (mm)

FIGURE 34

SWIRL IN THE z-DIRECTION MEASURED ALONG THE TRAVERSE

$\Delta x = 5.81$ mm

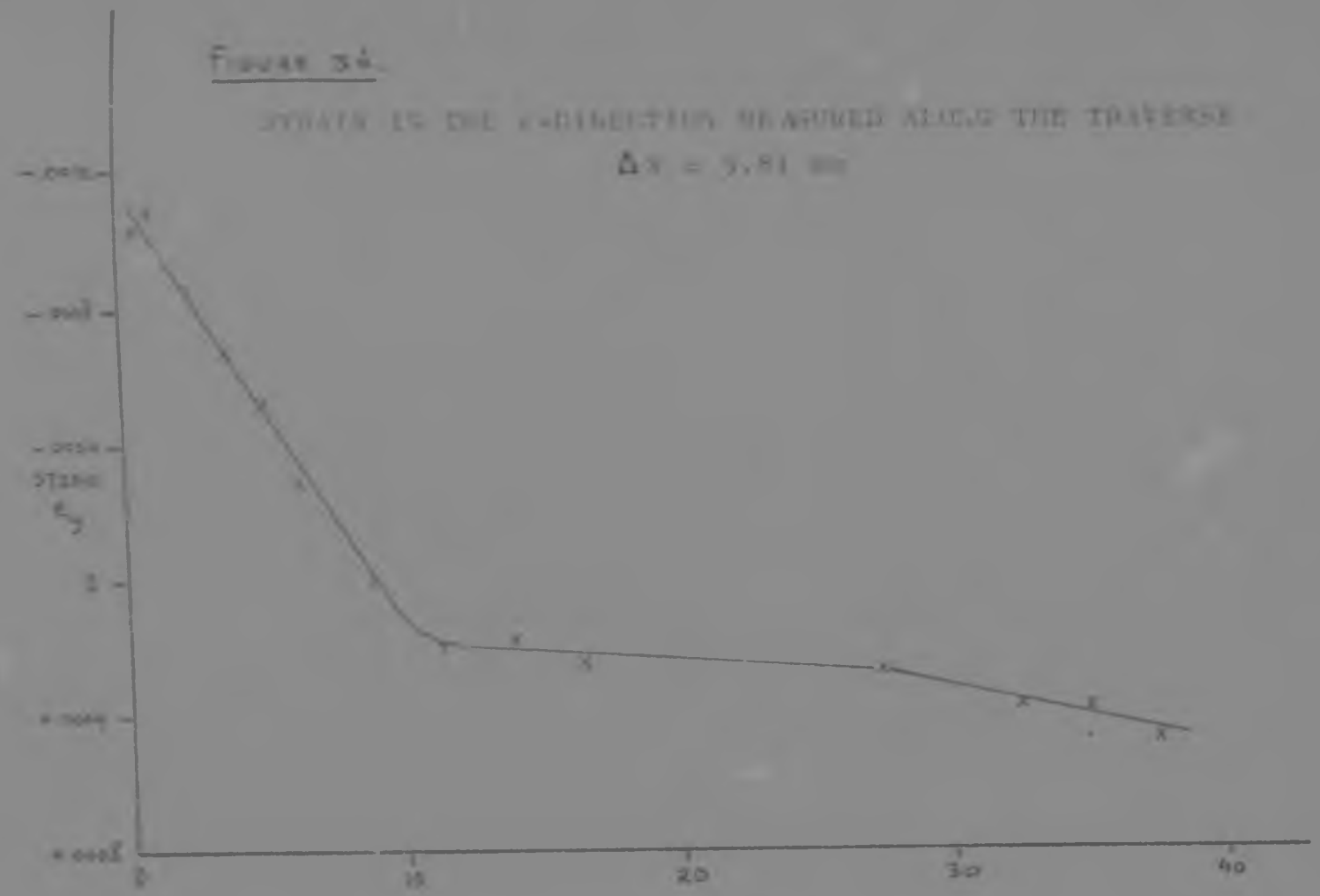

FIGURE 37

$\varepsilon_y = f(y)$ IN THE y-DIRECTION MEASURED ALONG THE TRAVERSE

$\Delta Y = 0.100$ mm

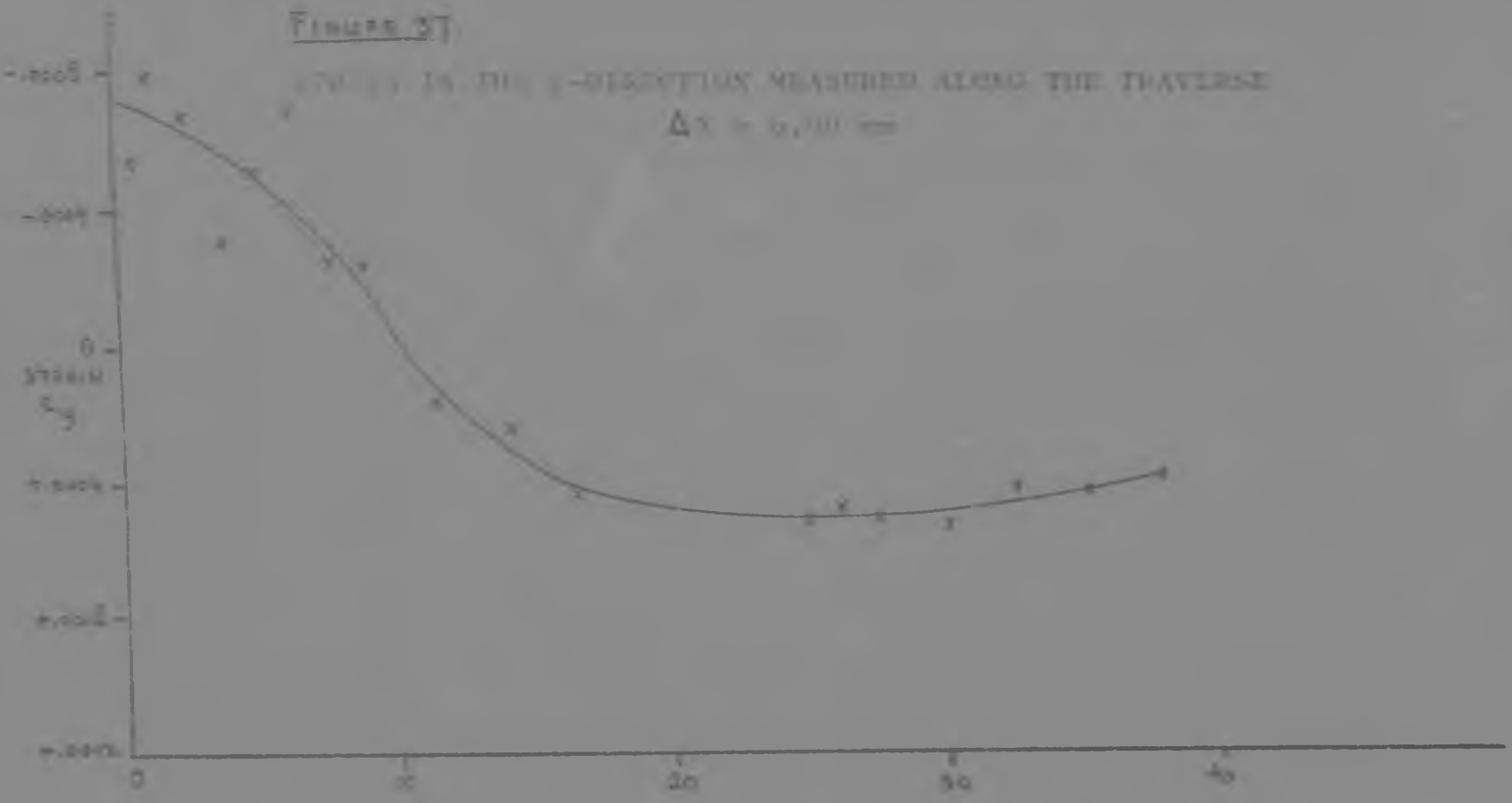

FIGURE 38

FIGURE 39.

FIGURE 40.

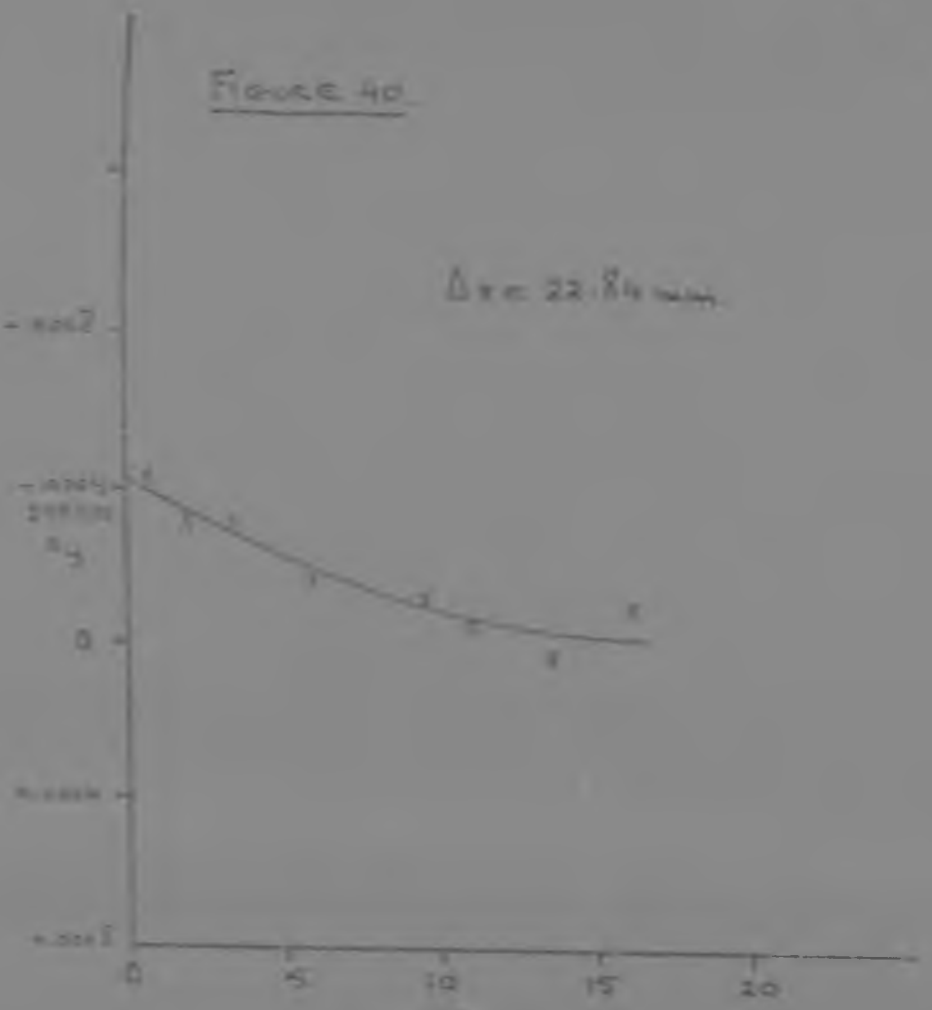

FIGURE 41.

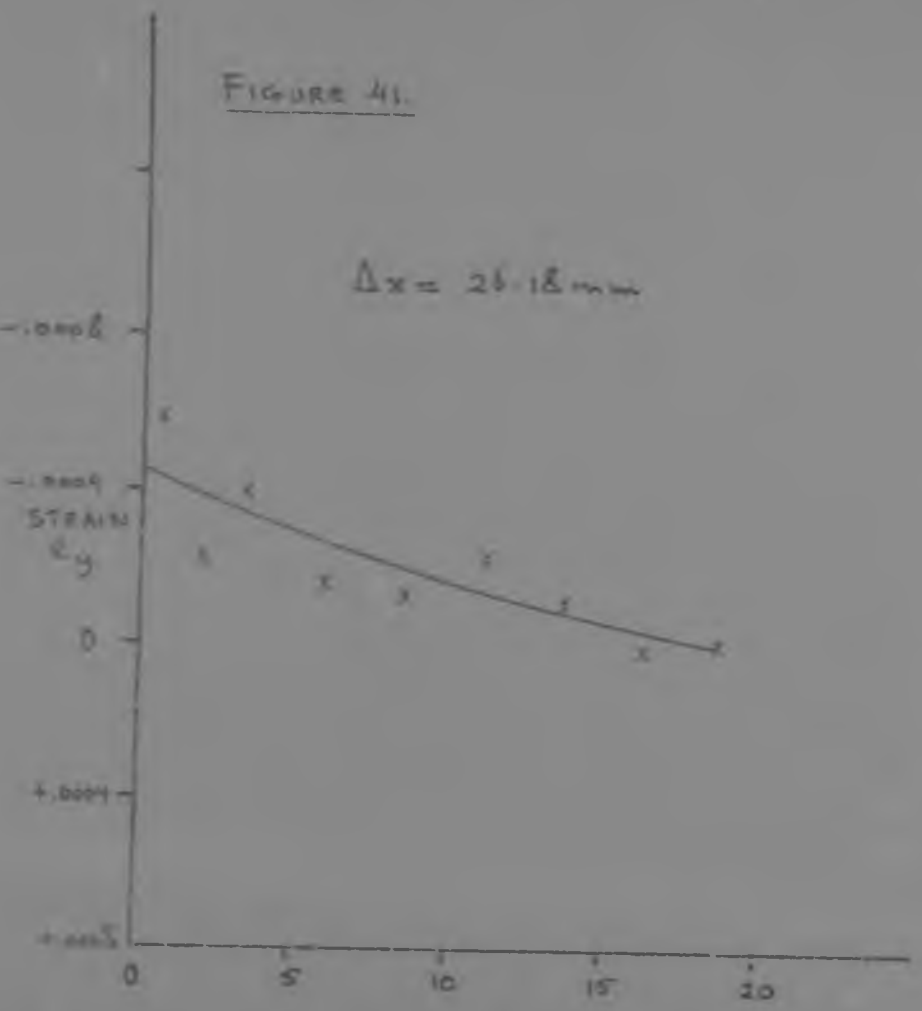

FIGURE 44

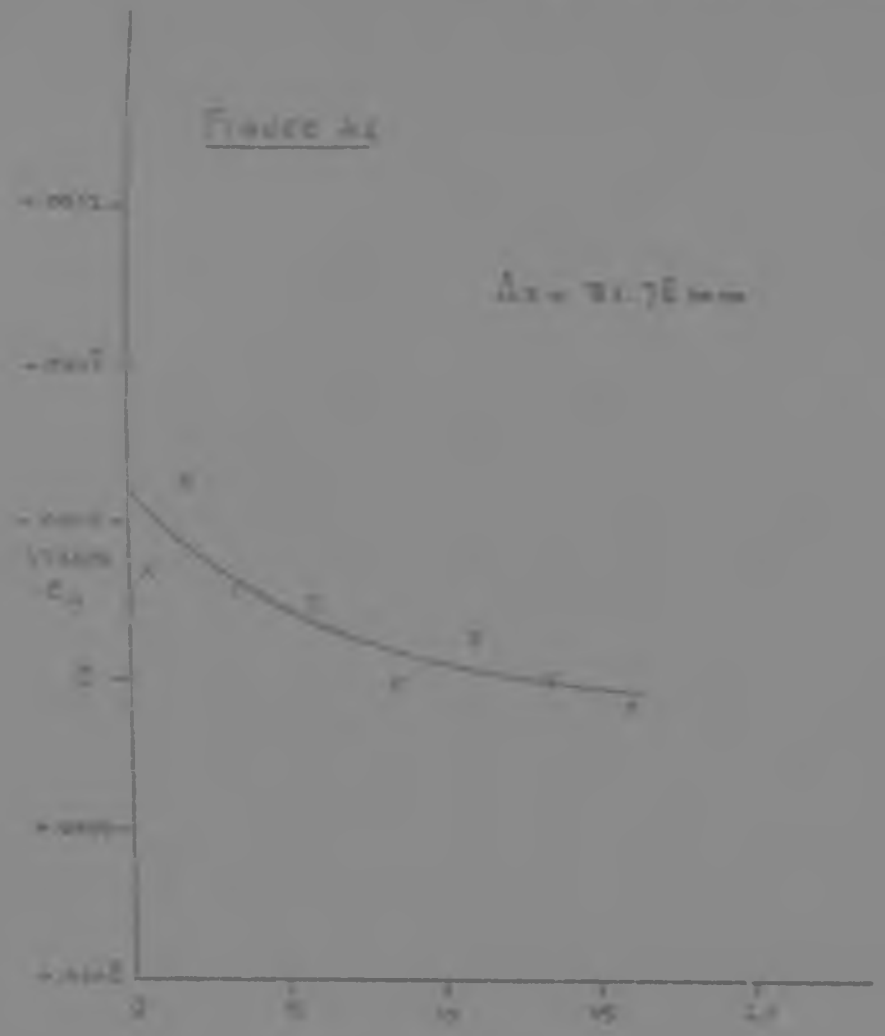

FIGURE 45.

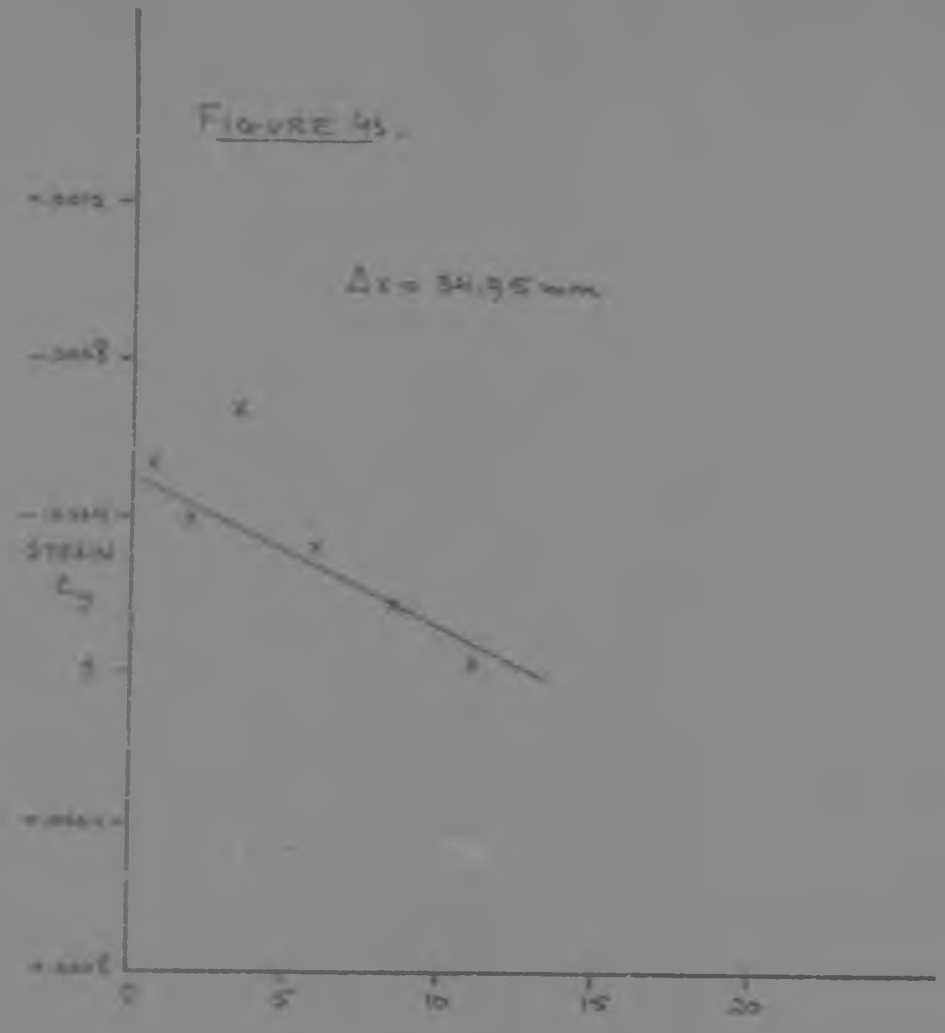

FIGURE 44

STRAIN IN THE y-DIRECTION PLOTTED ALONG Δy TRAVERSES

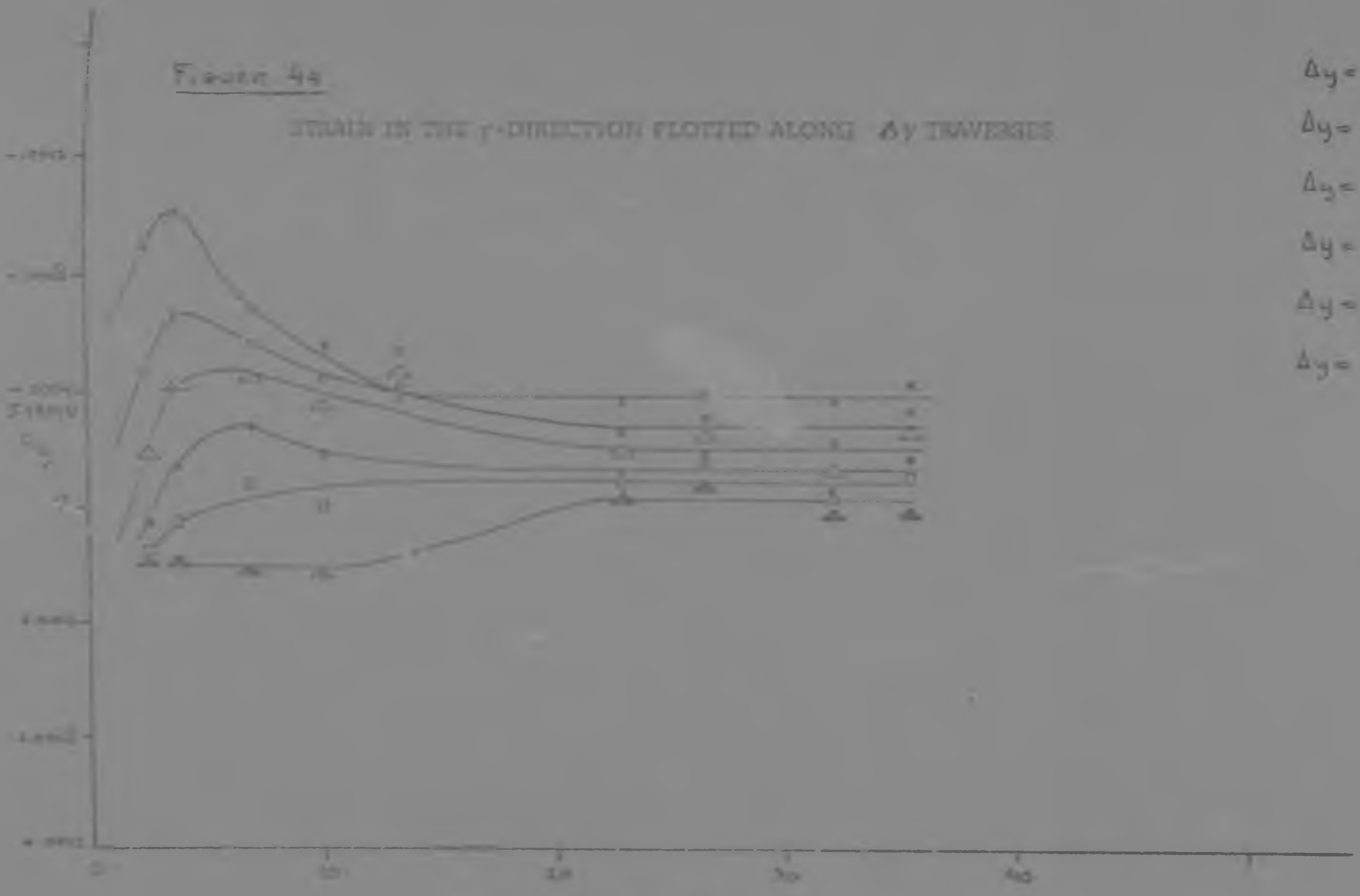

FIGURE 45

$\Delta y = 22.86$ mm

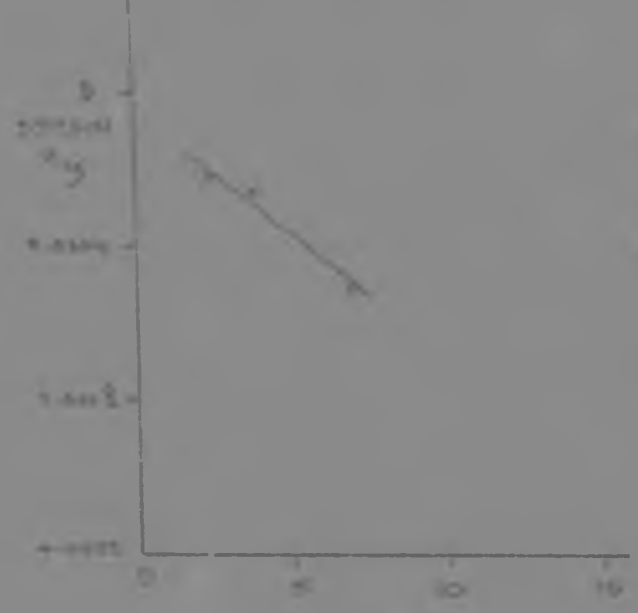

FIGURE 46.

$\Delta y = 27.94$ mm

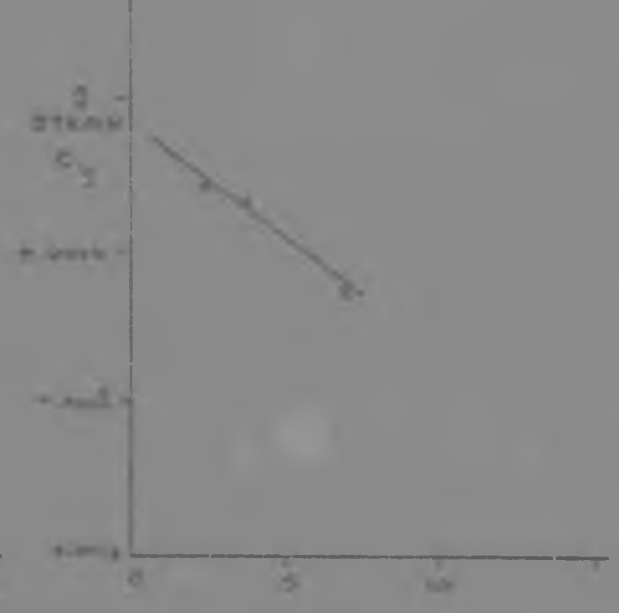

FIGURE 47.

$\Delta y = 31.75$ mm

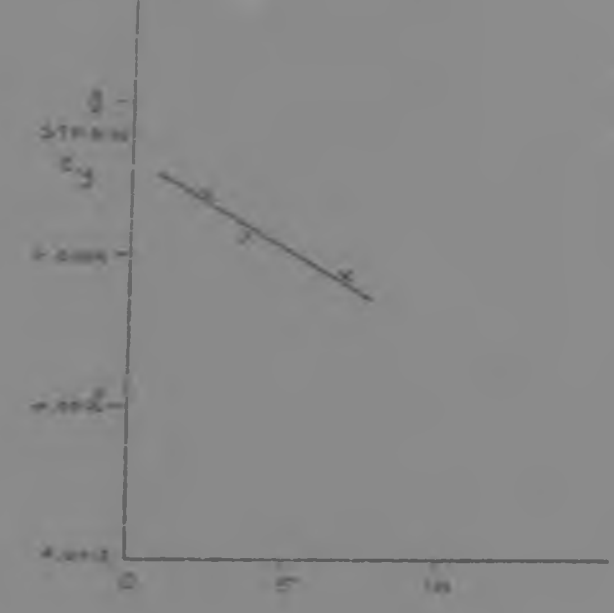

FIGURE A8. STRAIN IN THE x-DIRECTION PLOTTED ALONG Δx TRAVERSES

$\Delta y = 1.27$ mm x

$\Delta y = 3.81$ mm o

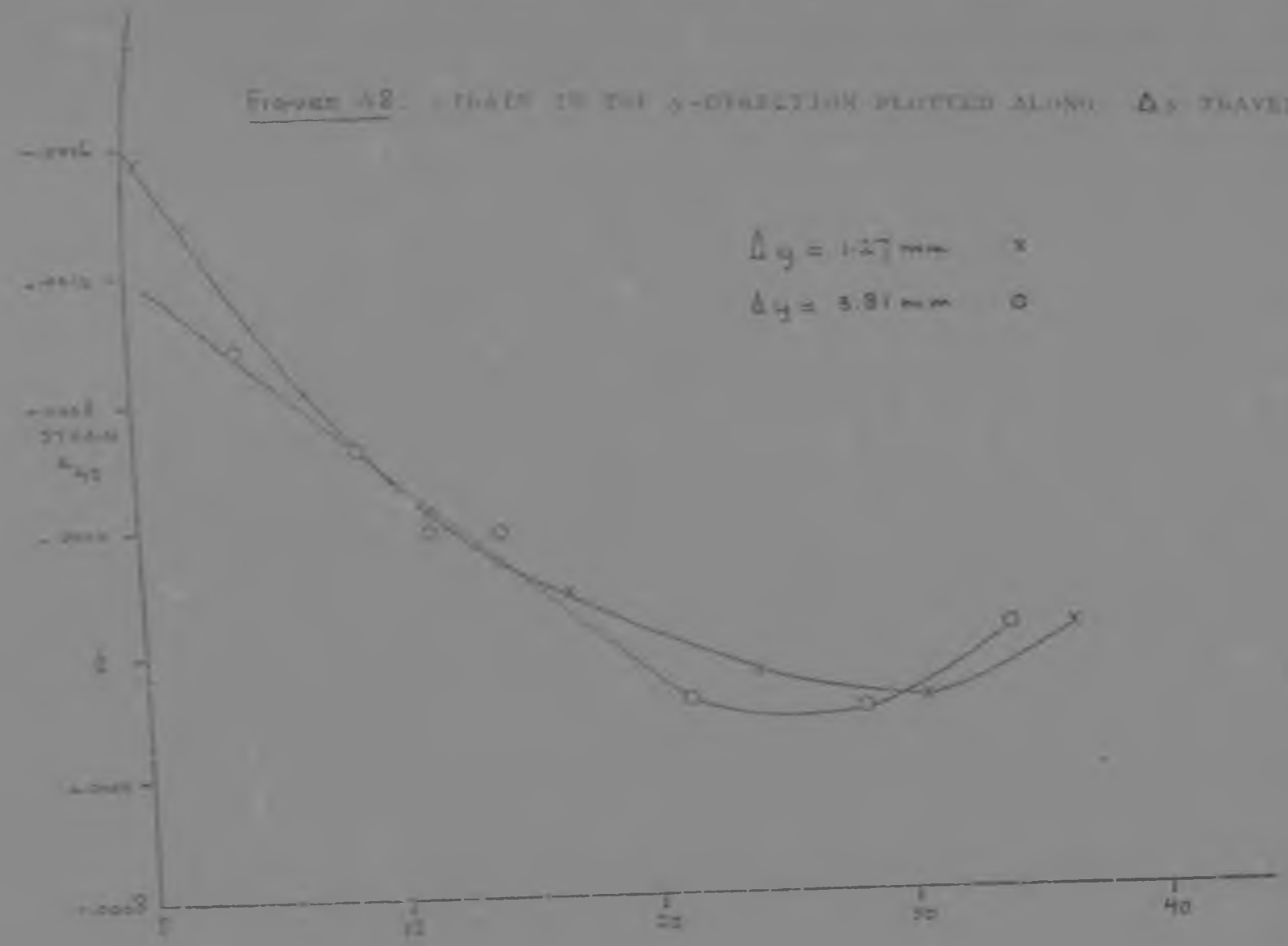

DISTANCE x (mm)

FIGURE 49. STRAIN IN THE "Y" DIRECTION PLOTTED ALONG Δy TRAVERSES

× $\Delta y = 5.71$ mm
○ $\Delta y = 8.00$ mm

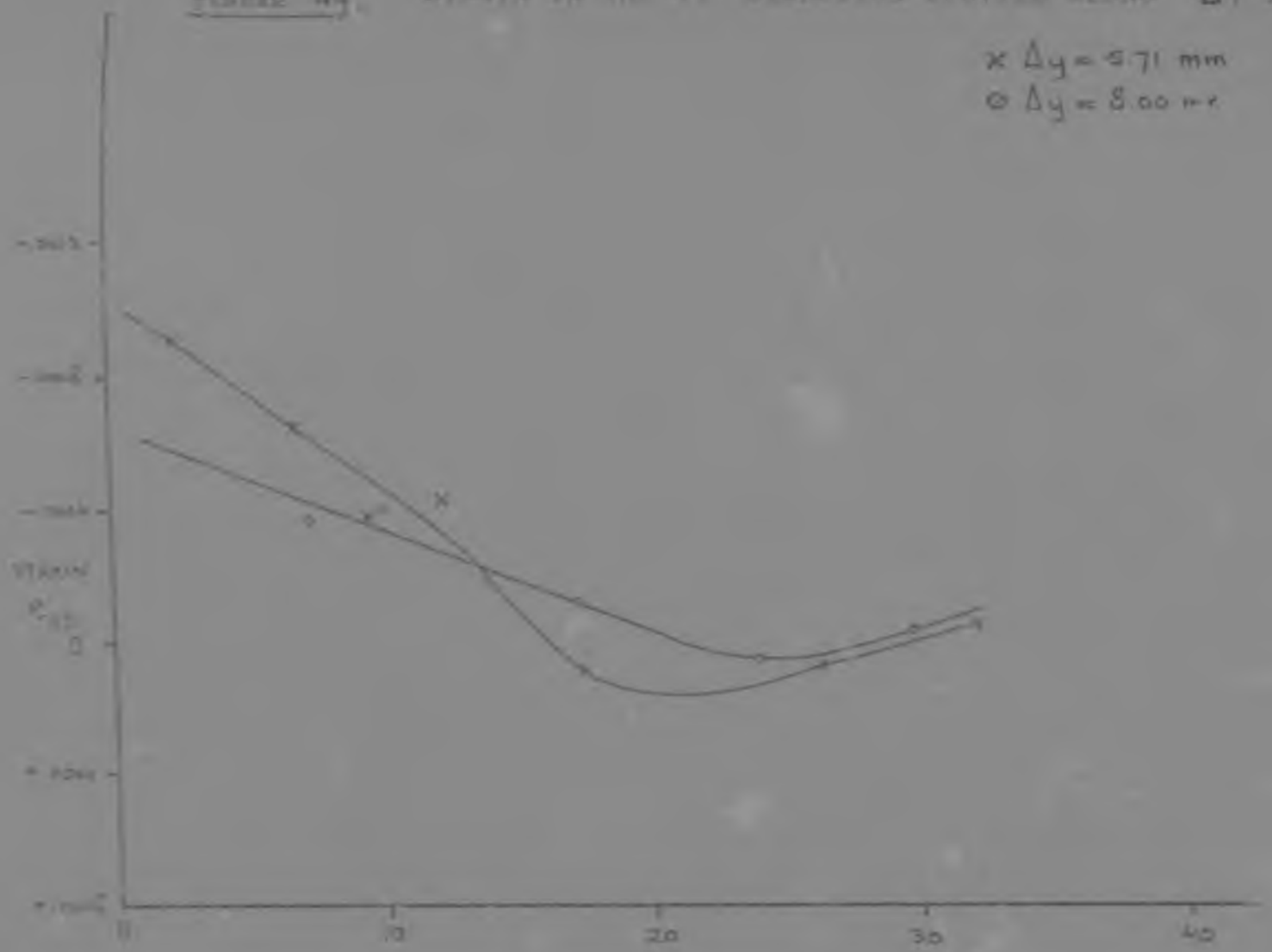

FIGURE 90 - STRAIN IN THE 90° DIRECTION MEASURED ALONG Δy TRAVERSES

$\Delta y = 9.55$ mm ε

$\Delta y = 12.70$ mm ε

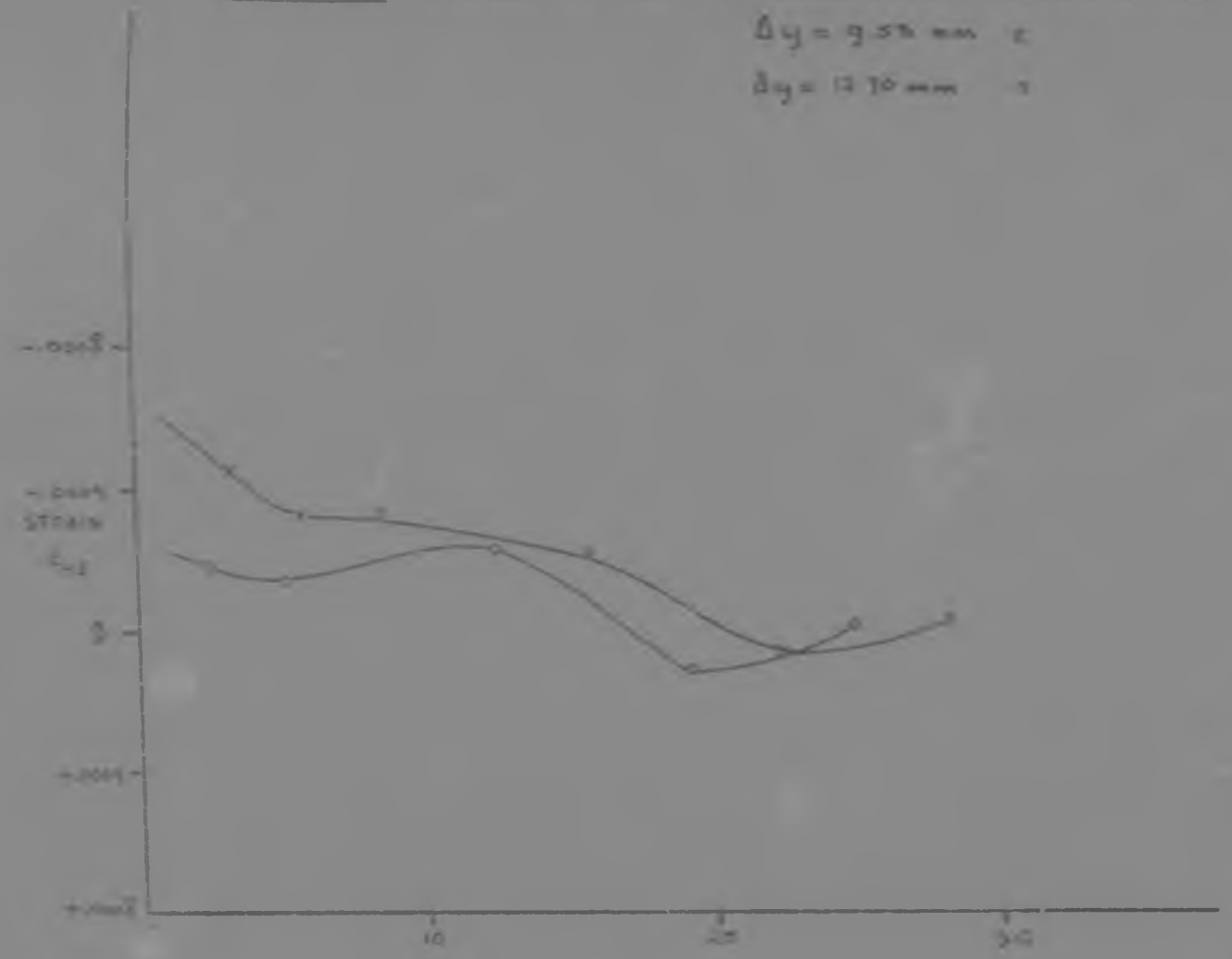

FIGURE 51 STRAIN IN THE 45° DIRECTION PLOTTED ALONG Δy TRAVERSES

$\Delta y = 22.86$ mm x

$\Delta y = 27.94$ mm o

$\Delta y = 31.75$ mm △

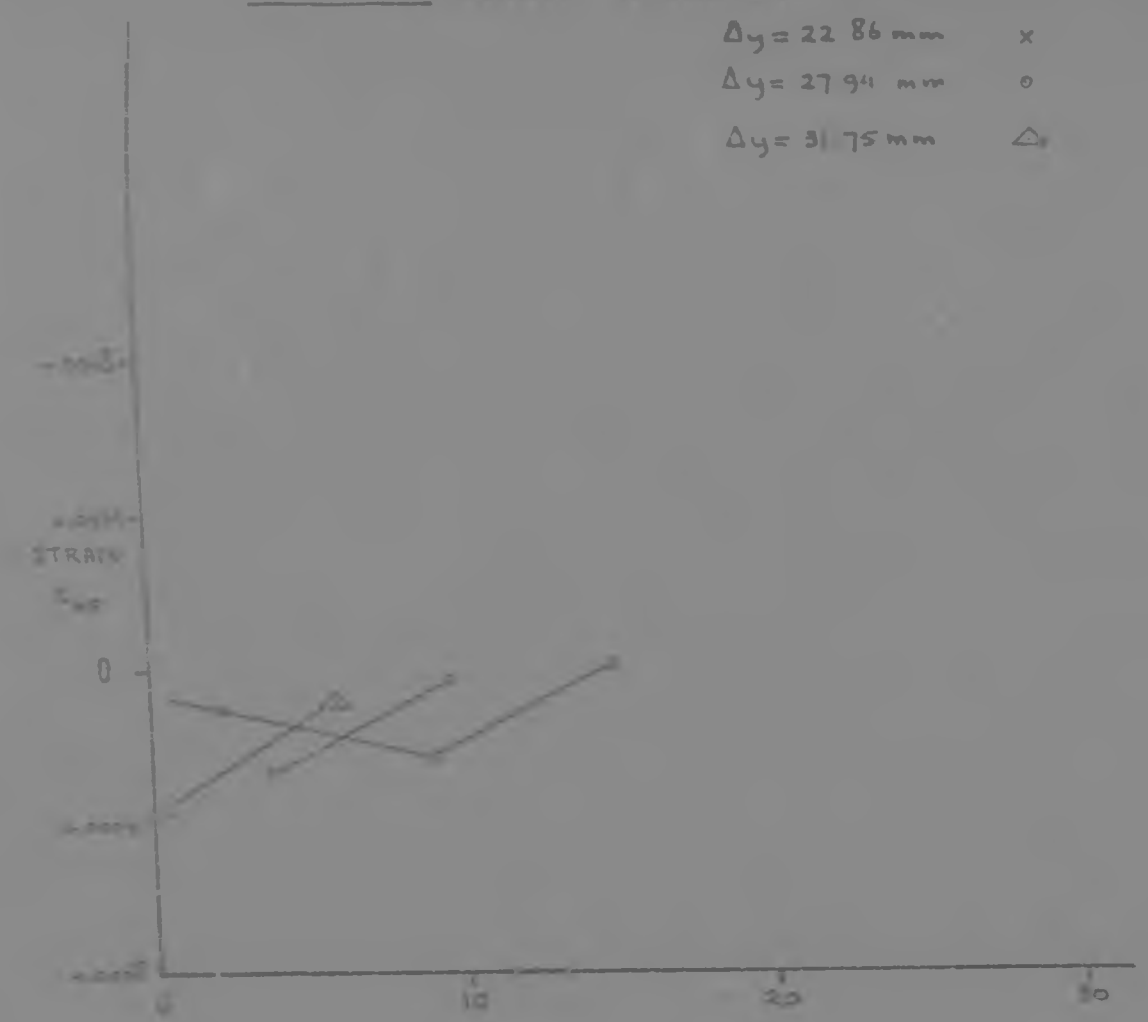

FIGURE 52 STRAIN IN THE ε_x DIRECTION PLOTTED ALONG Δx TRAVERSES

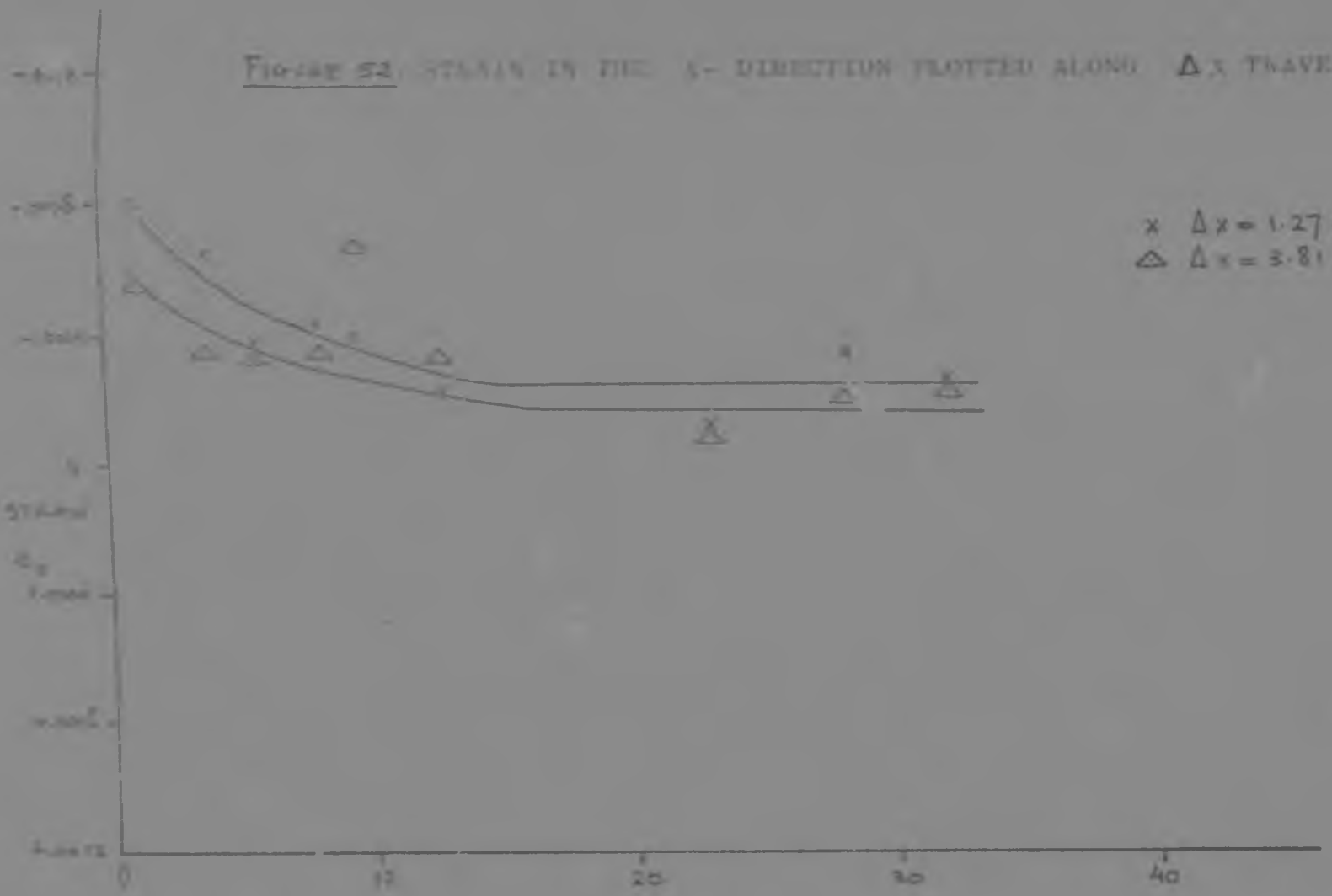

FIGURE 52. STRAIN IN THE X-DIRECTION PLOTTED ALONG Δx TRAVERSES

$\Delta x = 2.54$ mm ×

$\Delta x = 6.99$ mm ○

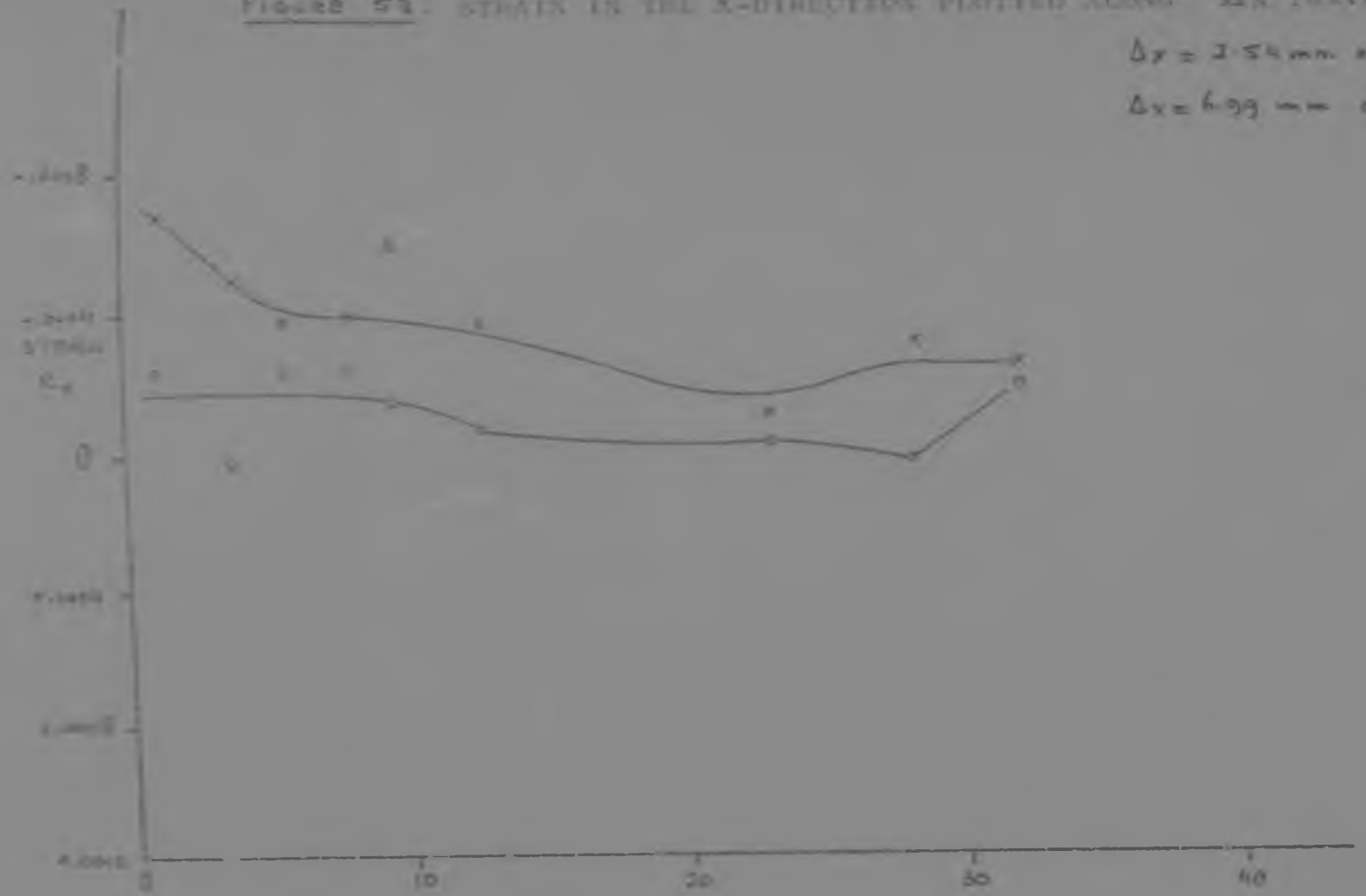

Figure 54. STRAIN IN THE X-DIRECTION PLOTTED ALONG [illegible] X TRAVERSES

$\Delta x = 10.16$ mm x

$\Delta x = 15.33$ mm o

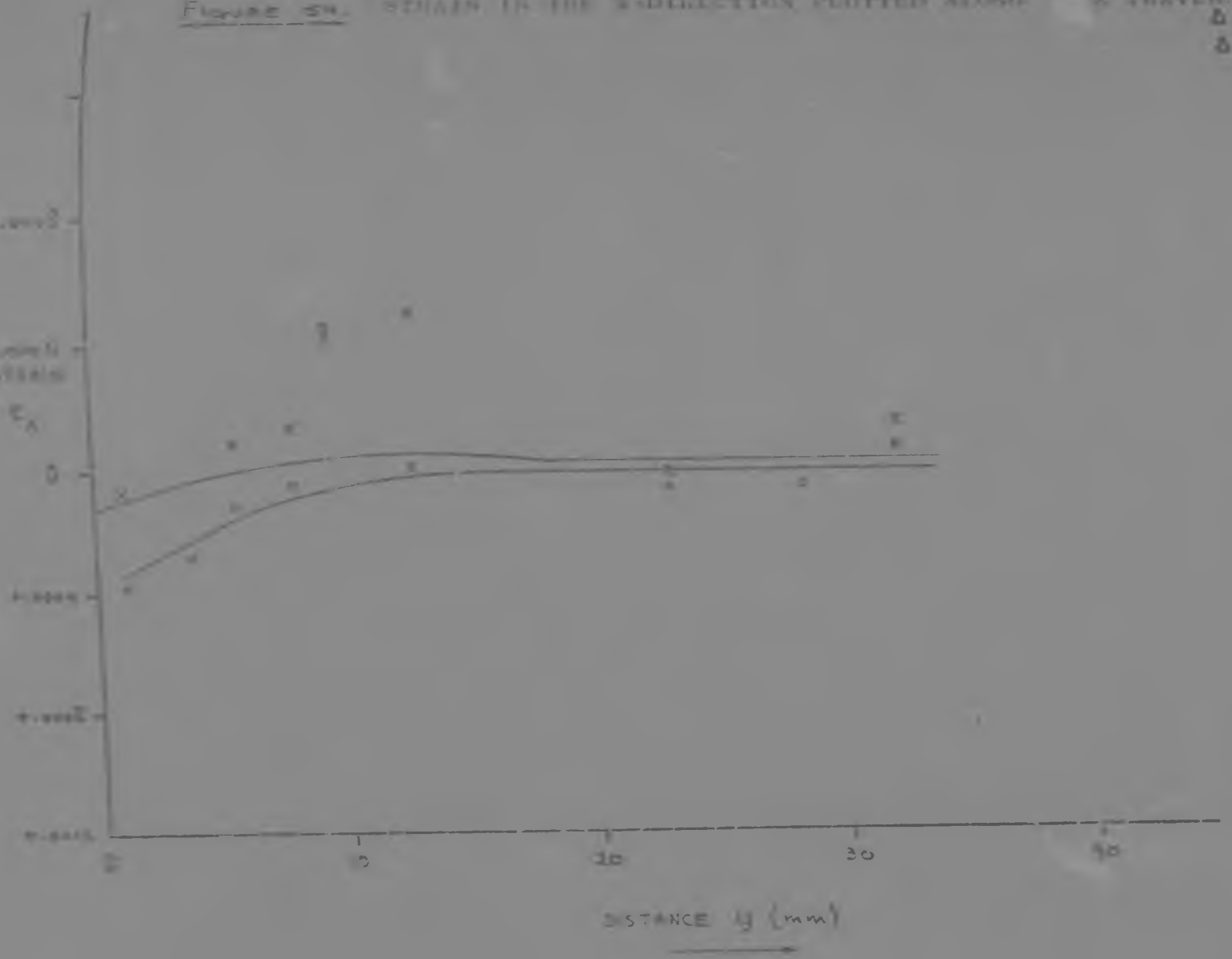

Figure 55.

Figure 56.

FIGURE 57. [illegible] IN THE 1" DIRECTION MEASURED ALONG Δx TRAVERSES

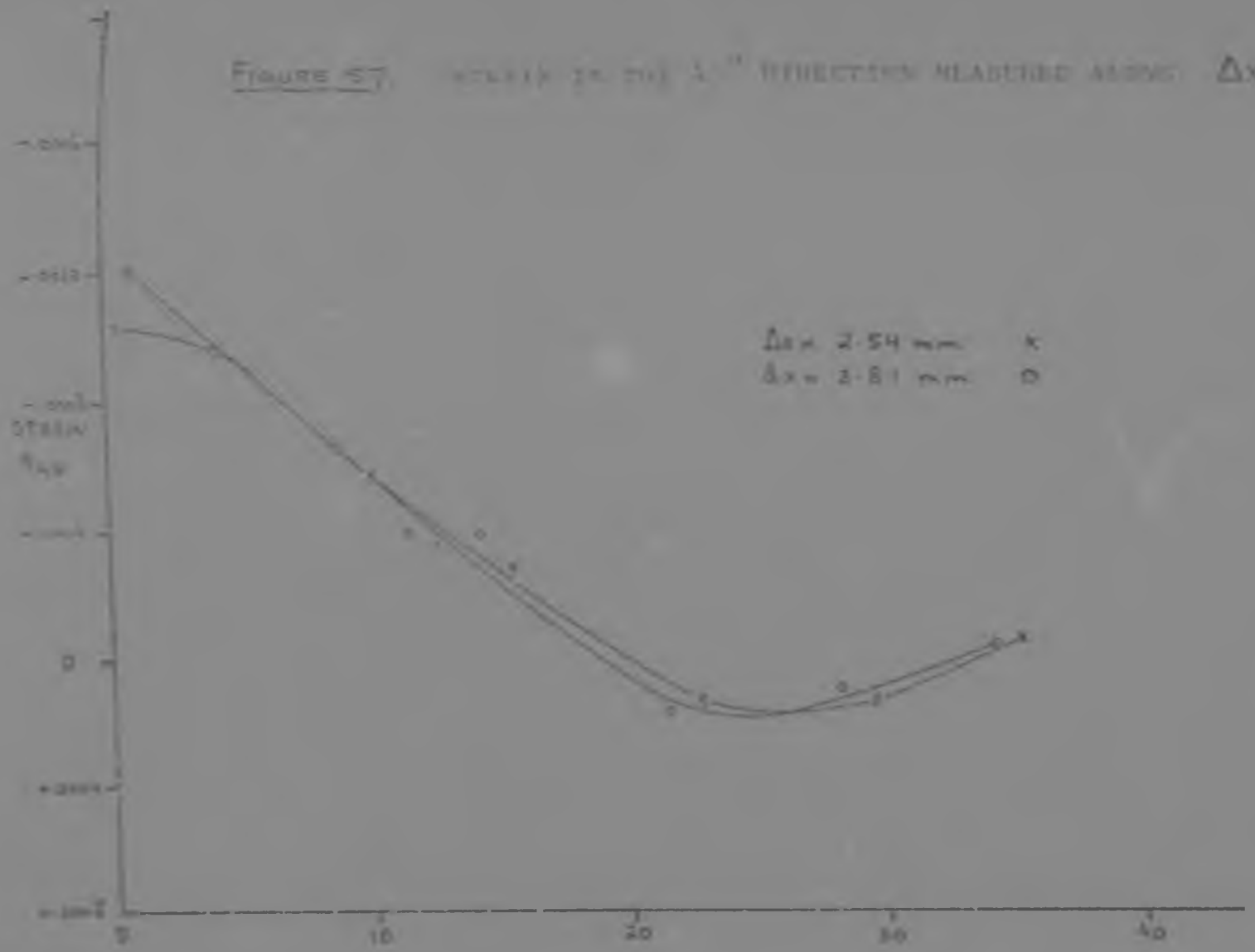

Figure 58 STRAIN IN THE $\theta=0°$ DIRECTION MEASURED ALONG Δx TRAVERSES

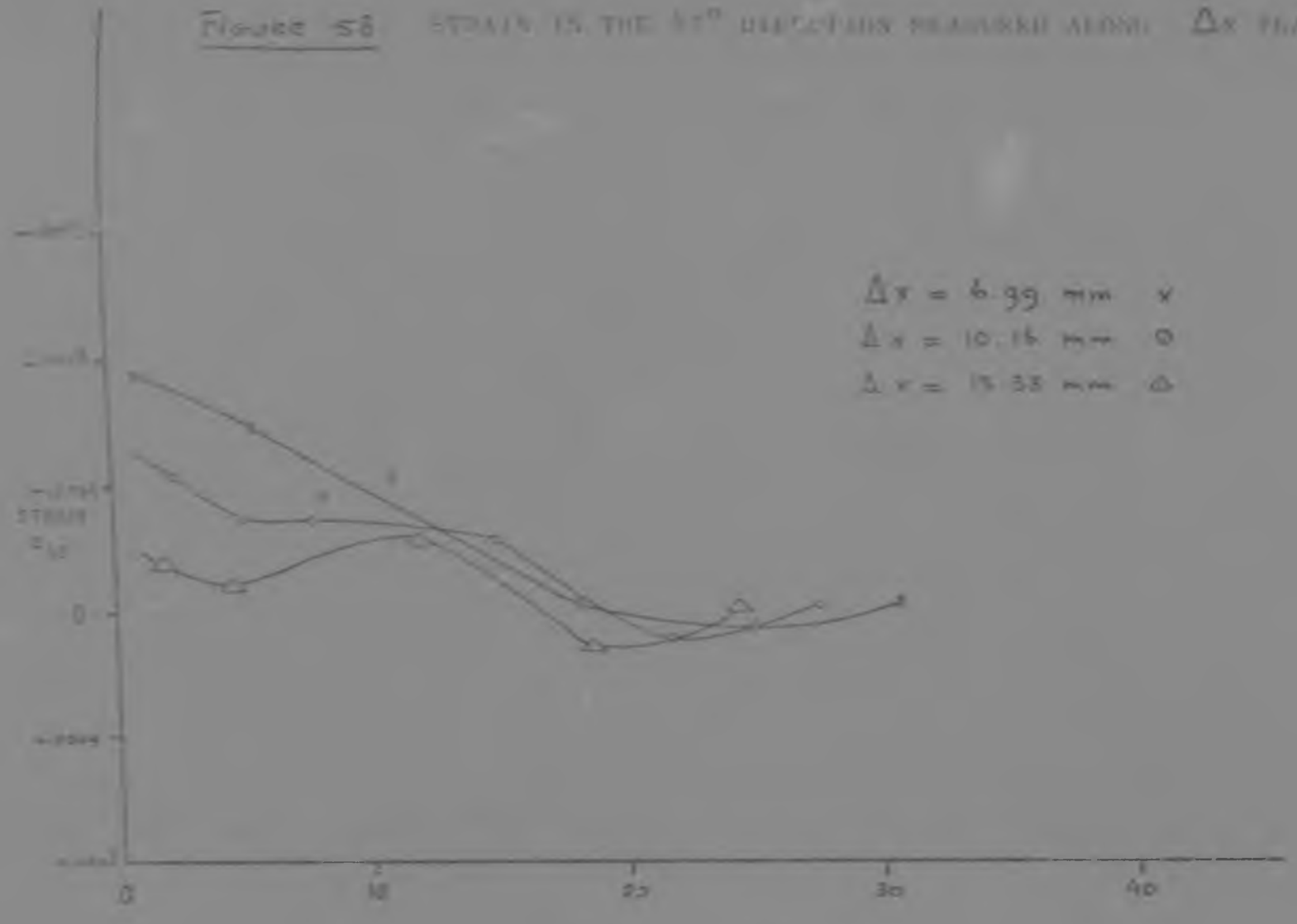

STRAIN IN THE "X" DIRECTION MEASURED ALONG Δ_x TRANSVERSE

FIGURE 59

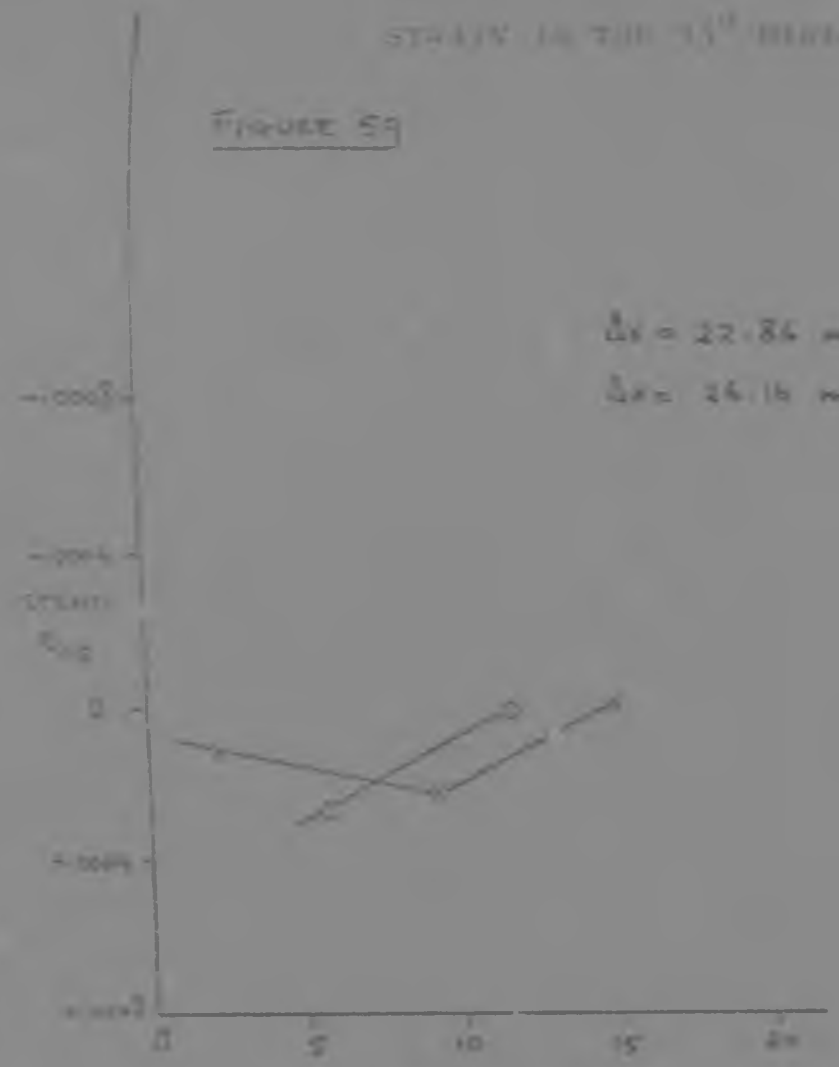

FIGURE 60.

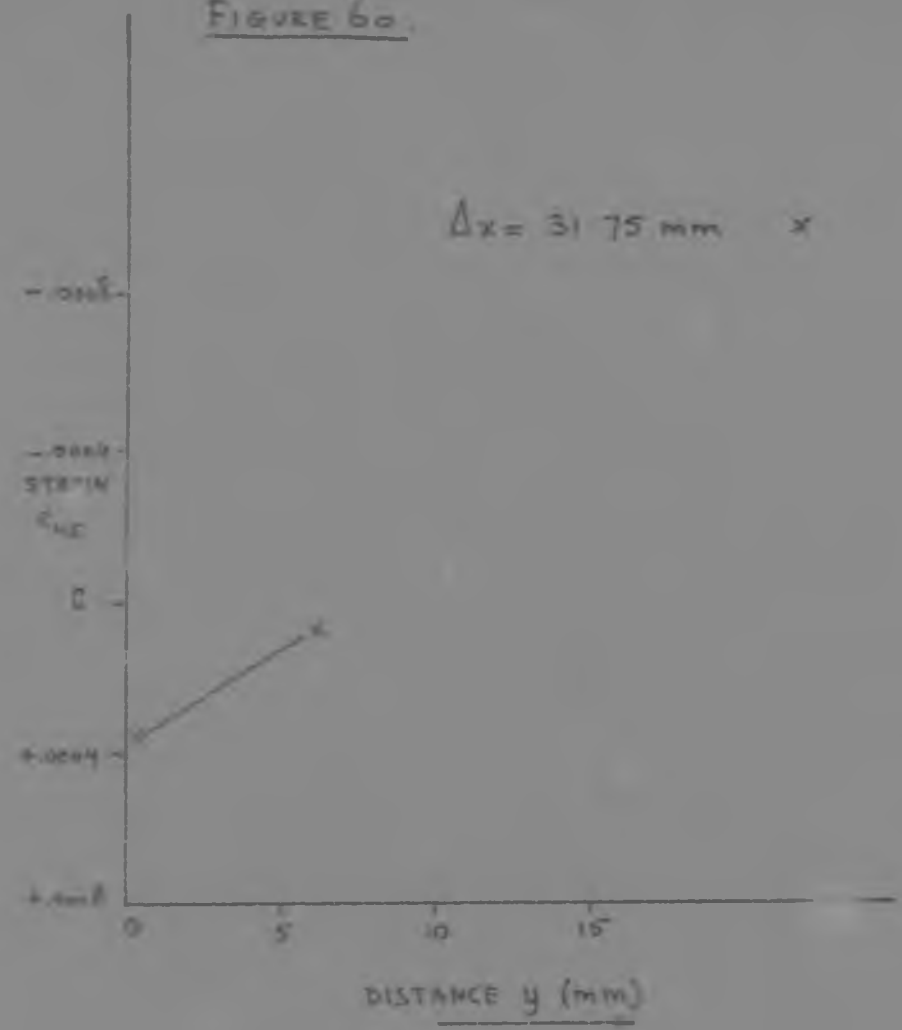

Figure 61.

DISTRIBUTION OF THE σ_1 ISOBARS ACROSS THE STEEL SURFACE OF THE ANALOGUE (X-RAY MEASUREMENT - FROM TABLE XI).

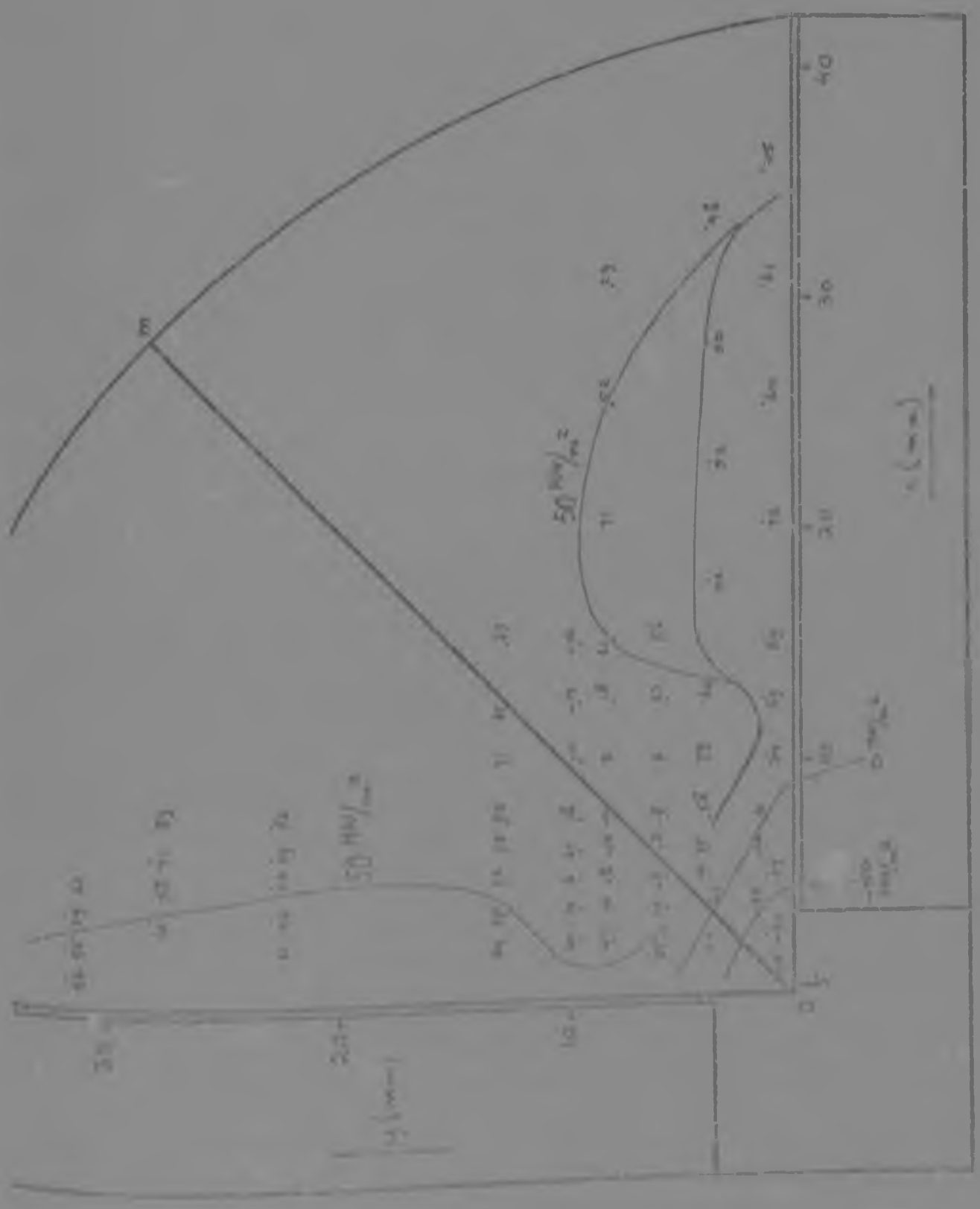

Figure 62.

DISTRIBUTION OF THE σ_1 STRESS ACROSS THE STEEL SURFACE OF THE ANALOG (X-RAY MEASUREMENTS FROM TABLE XLI)

Figure 6a.

DISTRIBUTION OF THE Φ_3 FLUXES ACROSS THE SHELL SURFACE OF THE ANALOGUE X-RAY MEASUREMENTS FROM TABLE XI.

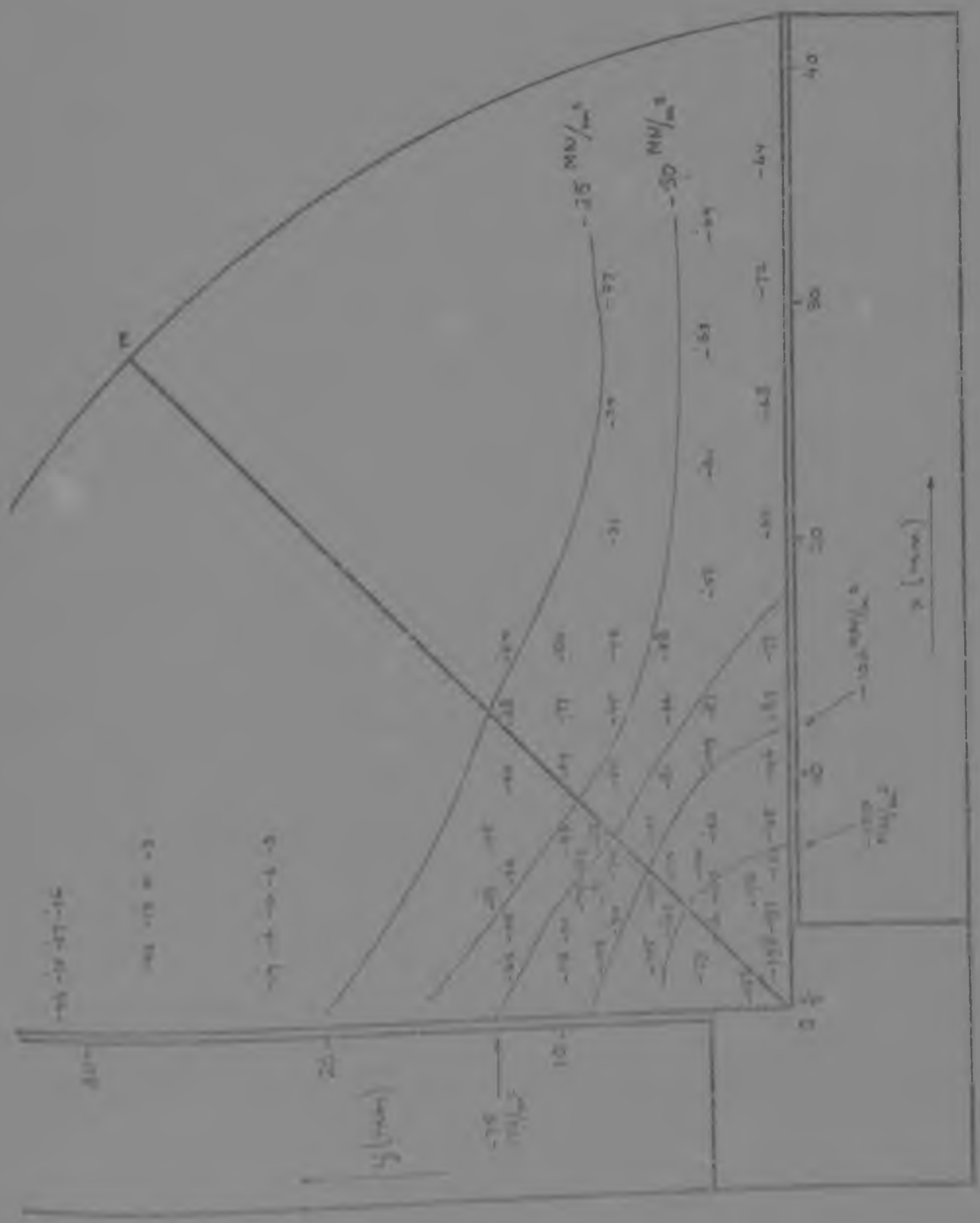

FIGURE 84.

DISTRIBUTION OF THE σ_2 STRESS ACROSS THE FREE SURFACE OF THE ANALOGUE (SEE TABLE XII).

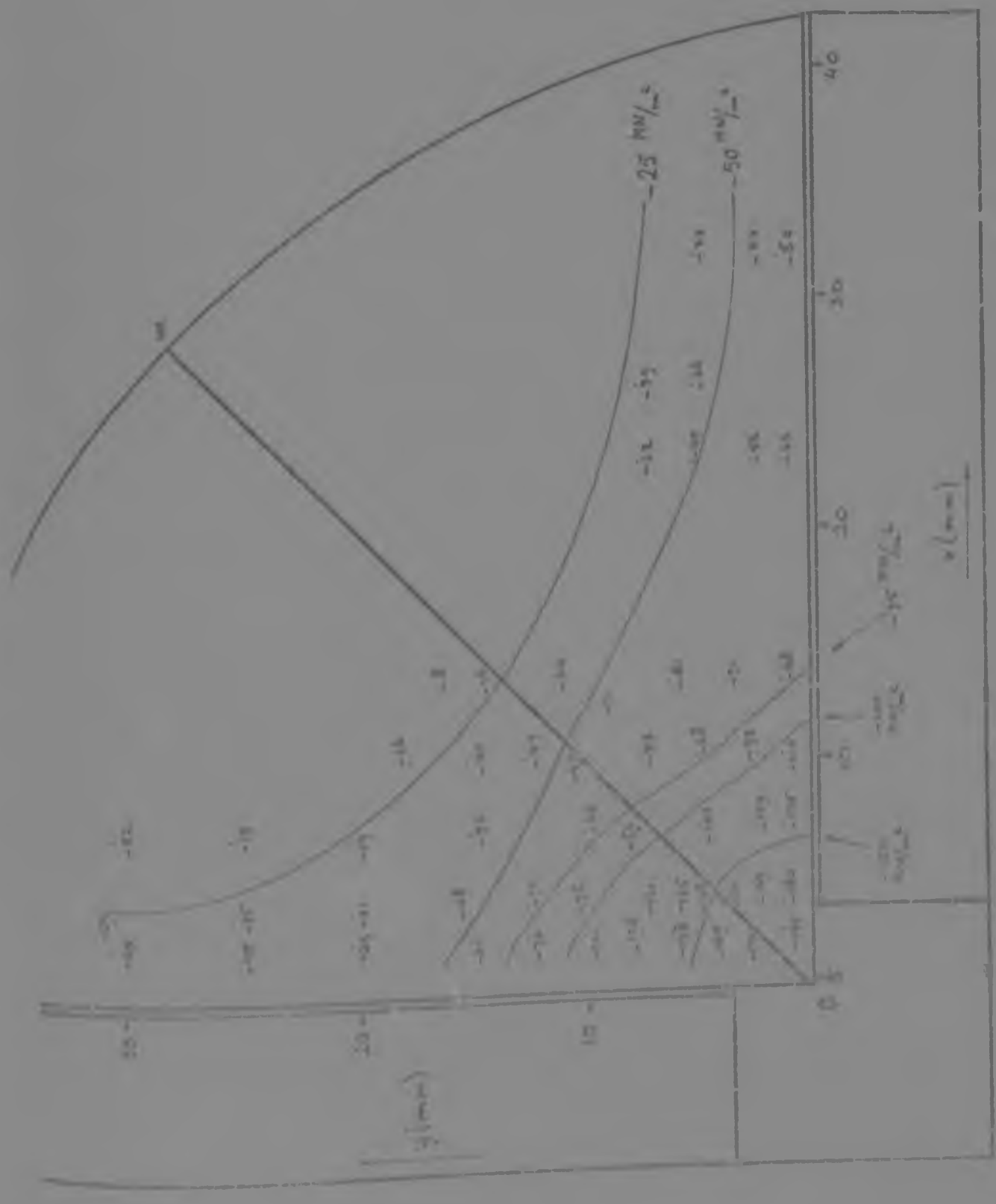

FIGURE 65.

ISOSTATICS OF THE APICAL SURFACE OF THE EXALOSITE
(X-RAY MEASUREMENTS FROM TABLE X).

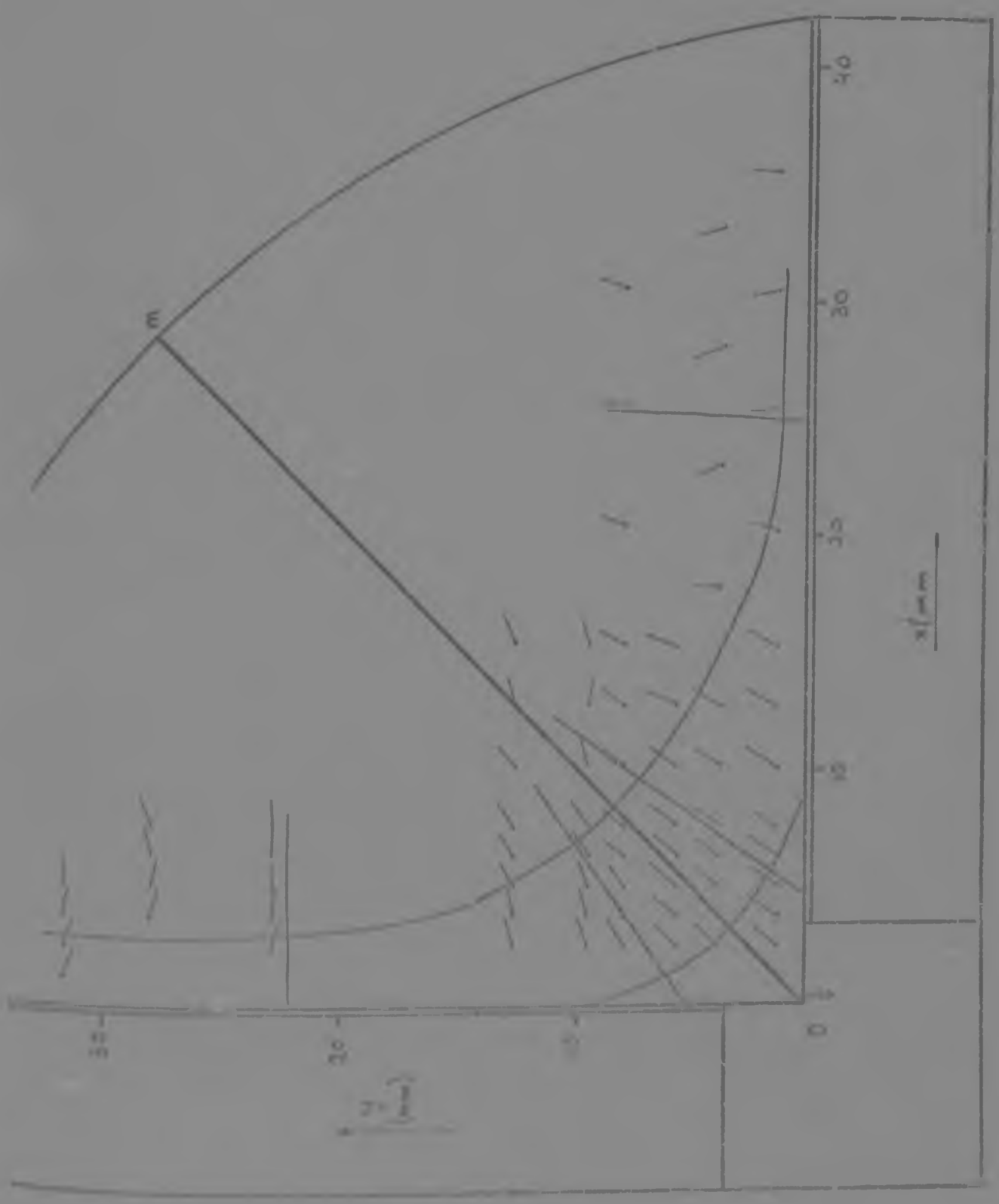

FIGURE 66.

ISOSTATICS IN THE STEEL SURFACE OF THE ANALOGUE
(X-RAY MEASUREMENTS FROM TABLE XI.)

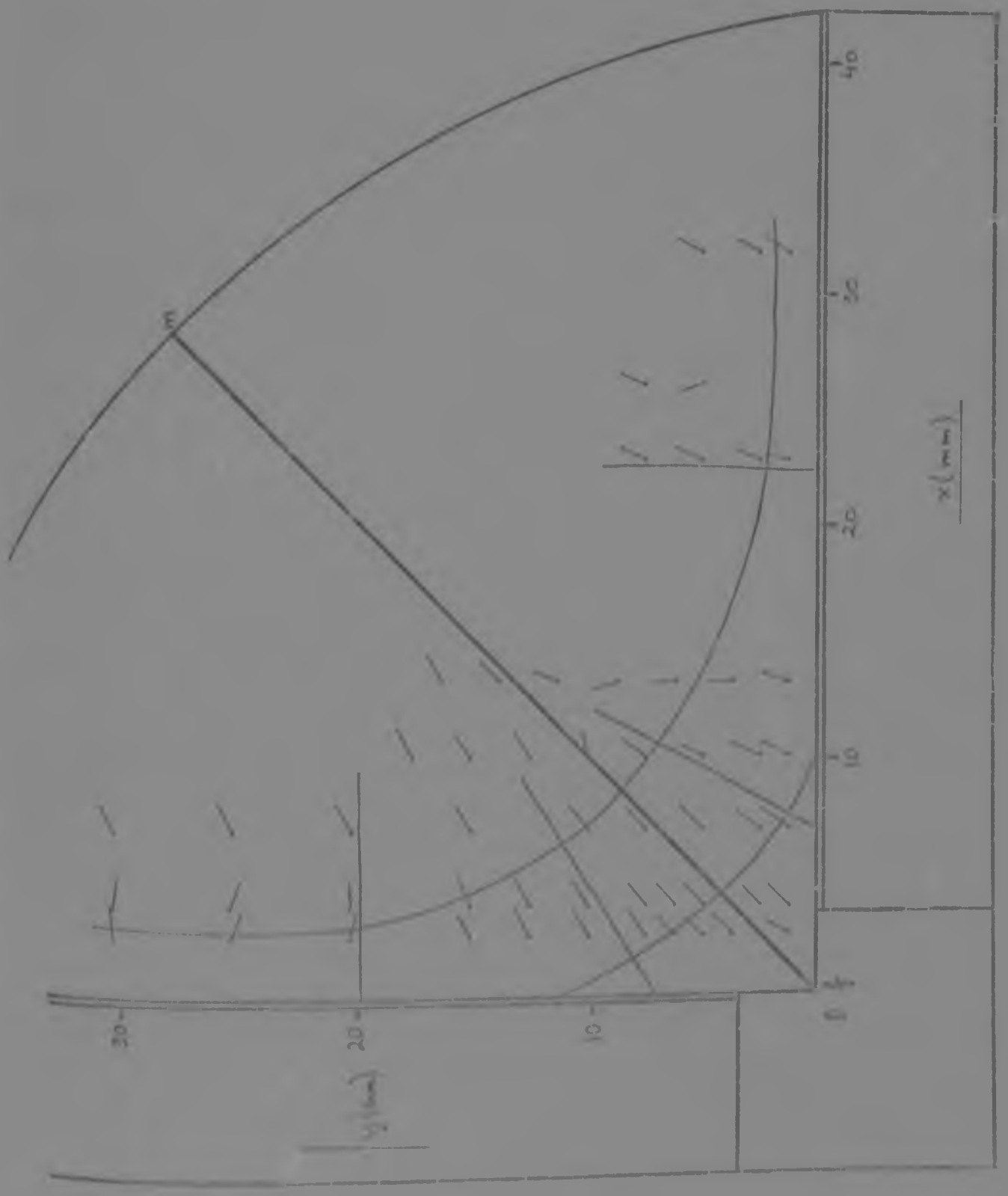

FIGURE 67.

THE STATE OF RESIDUAL STRESS ACROSS THE STEEL SURFACE OF THE ANALOGUE. ($\sigma_A - \sigma_B$) INDICATED FROM X-RAY STRAIN MEASUREMENTS (TABLE X).

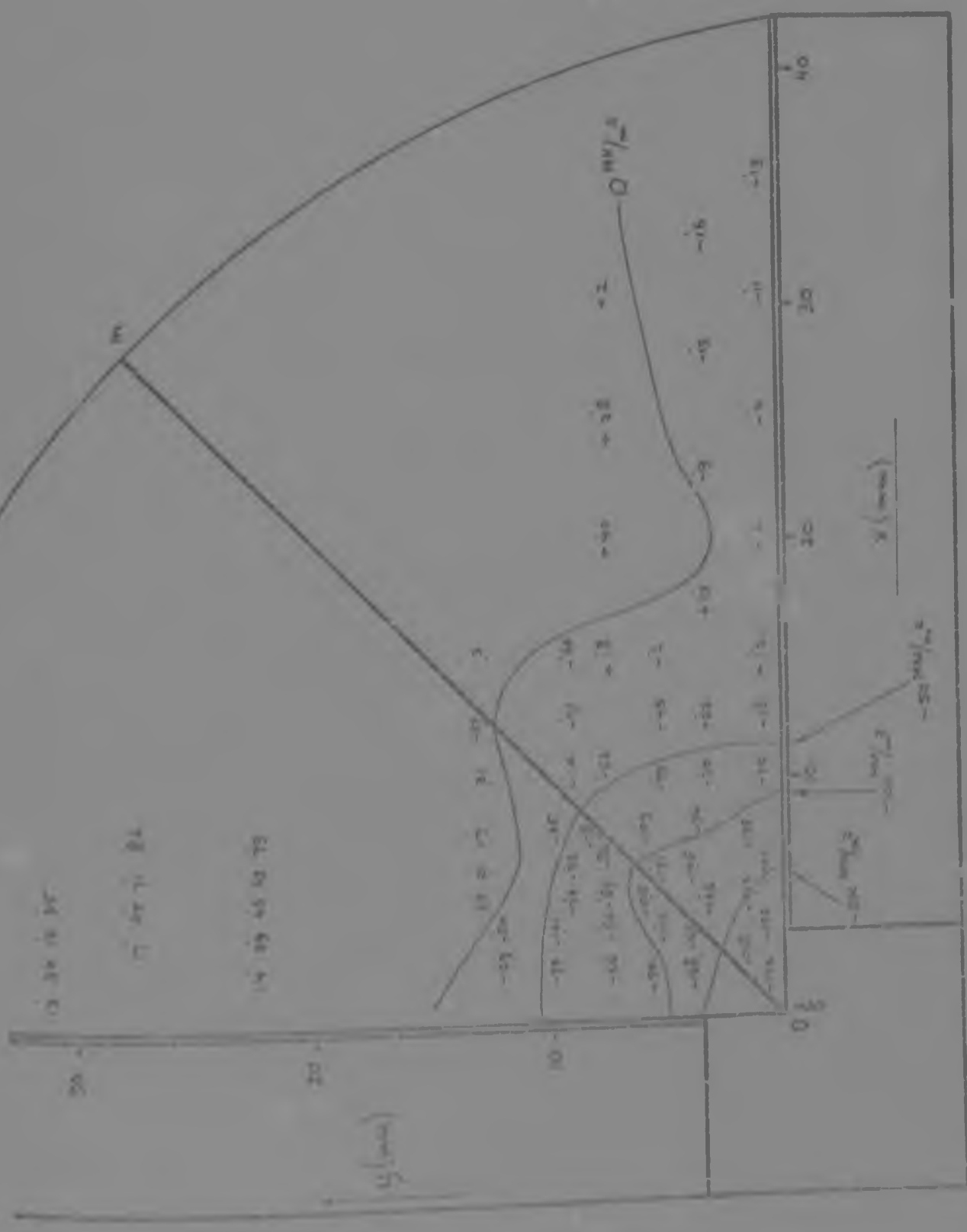

FIGURE 68

THE STATE OF RESIDUAL STRESS ACROSS THE STEEL SURFACE OF THE ANALOGUE. ($\sigma_1 - \sigma_2$) CONTACTICS FROM X-RAY STRAIN MEASUREMENTS (TABLE XI).

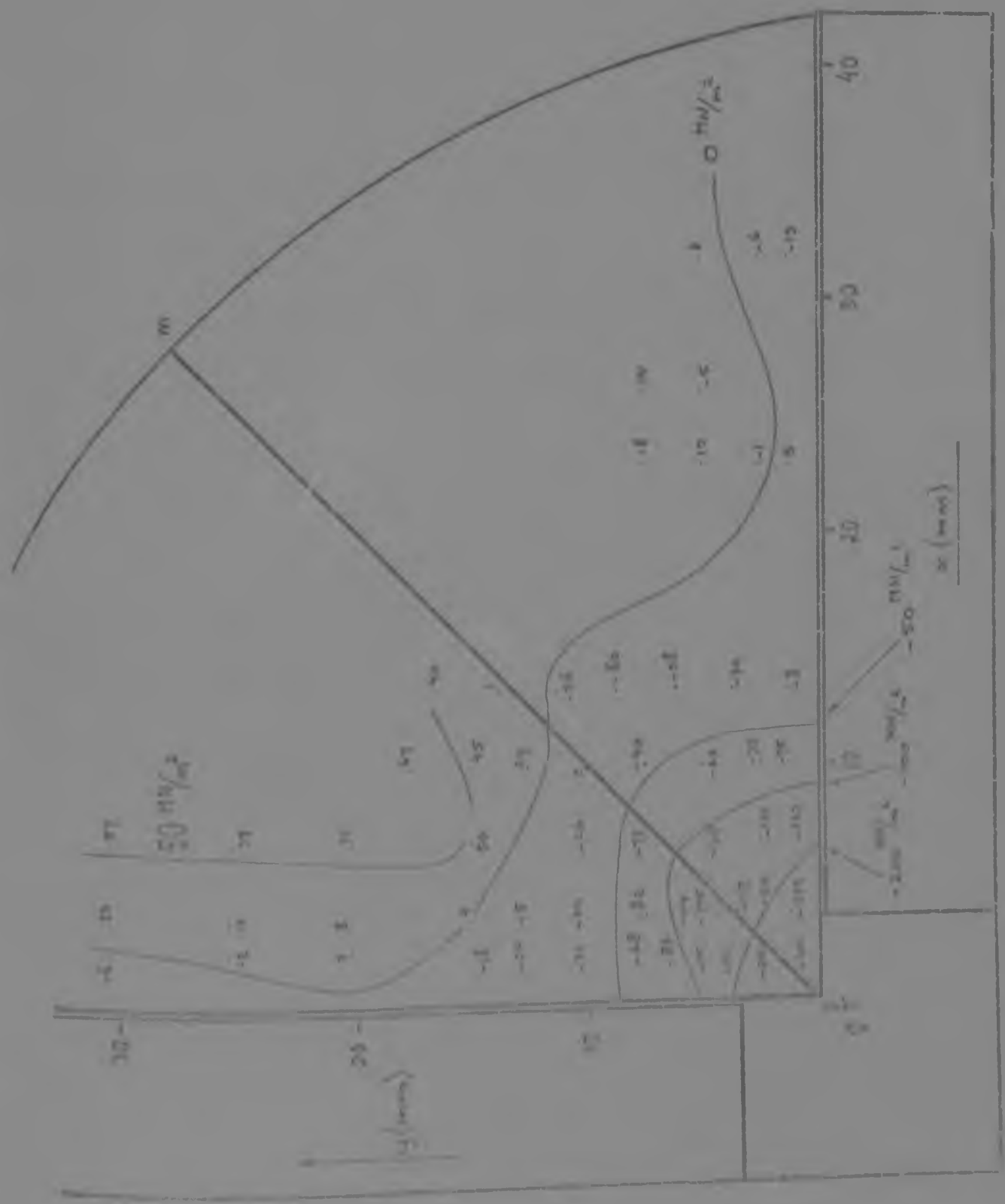

Figure 69.

ISOCLINICS IN THE STEEL SURFACE OF THE ANALOGUE
(X-RAY MEASUREMENTS FROM CALLE 8).

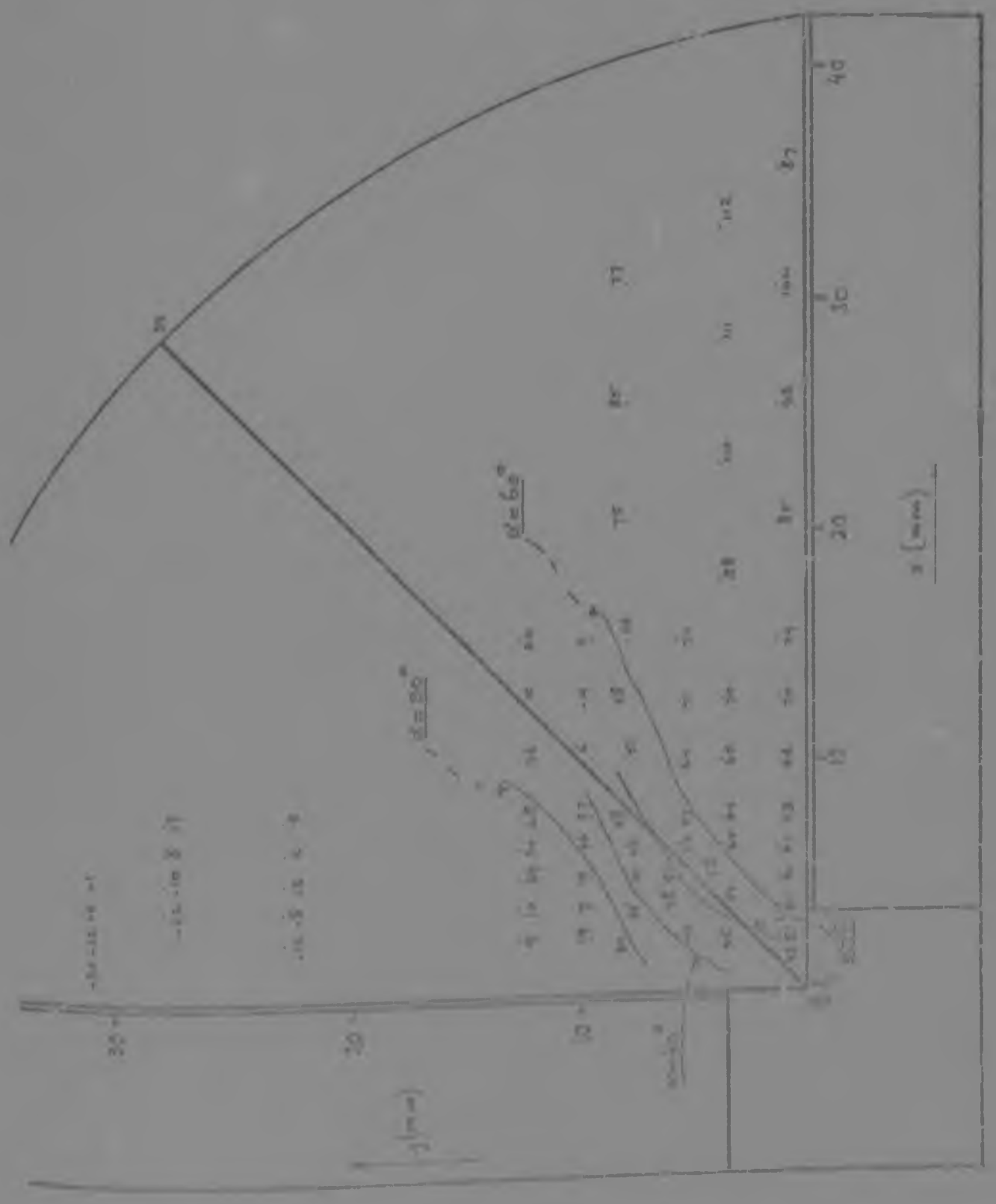

FIGURE 70.

ISOCLINICS IN THE STEEL SURFACE OF THE ANALOGUE
(X-RAY MEASUREMENTS FROM TABLE XI).

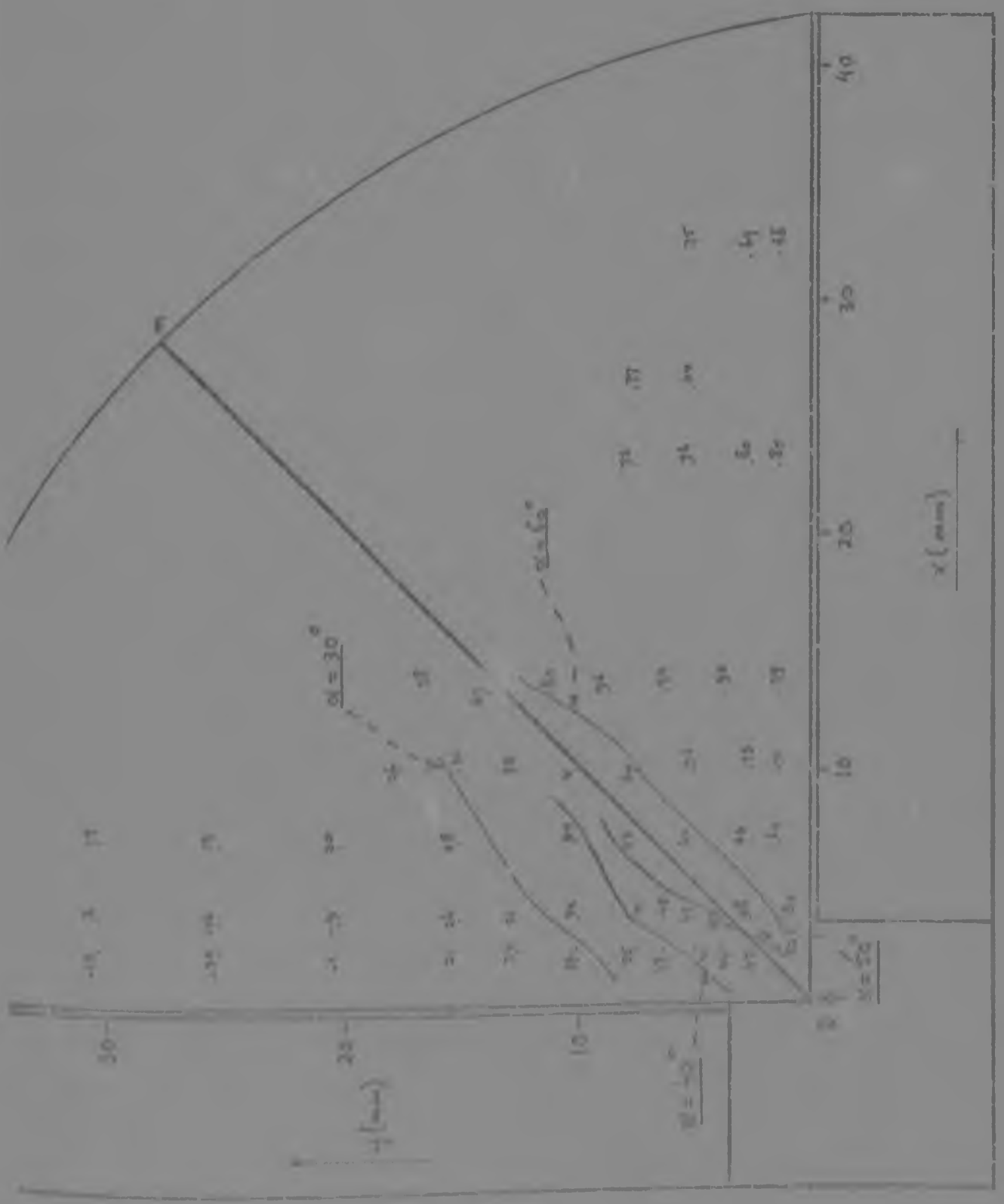

FIGURE 71.

DISTRIBUTION OF ISOCHROMATICS ($\sigma_1 - \sigma_2$) ACROSS THE STEEL SURFACE OF THE ANALOGUE - (X-RAY MEASUREMENTS FROM TABLE X).

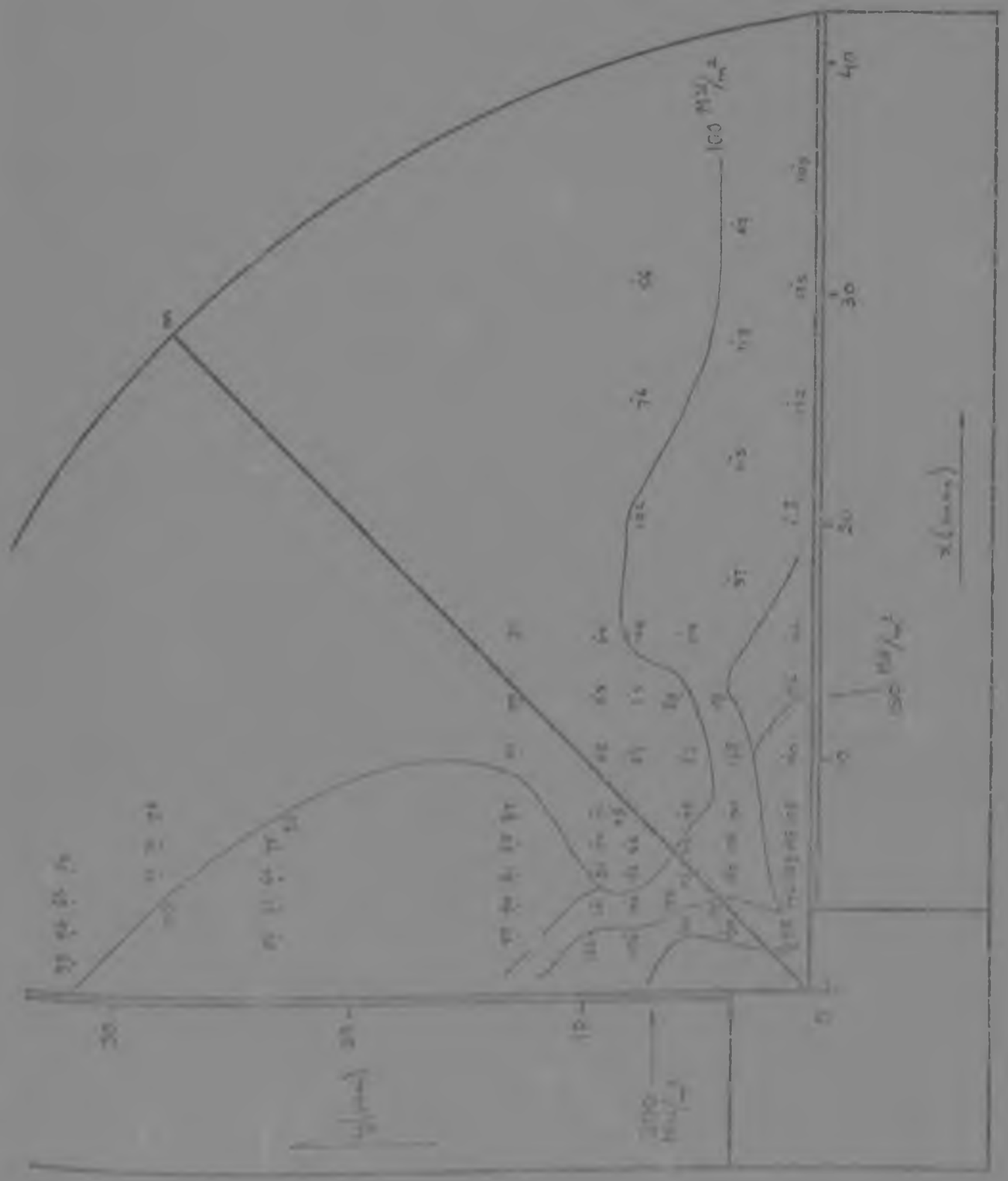

FIGURE 72-

DISTRIBUTION OF ISOCHROMATICS ($\sigma_1 - \sigma_2$) ACROSS THE STEEL SURFACE OF THE ANALOGUE. (X-RAY MEASUREMENTS FROM TABLE XI).

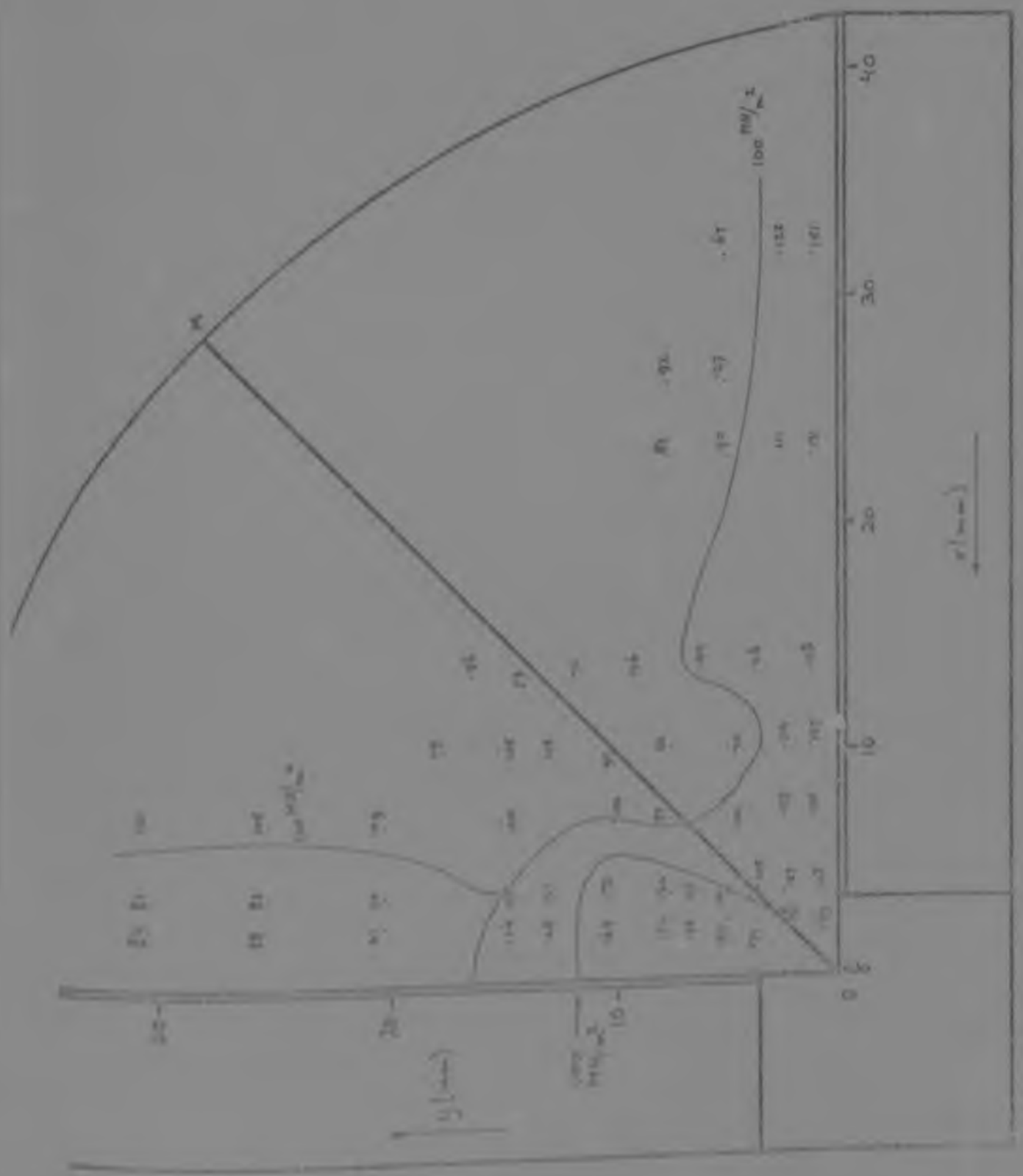

FIGURE 73.

DISTRIBUTION OF MAXIMUM SHEAR STRESS TRAJECTORIES ACROSS THE STEEL SURFACE OF [illegible] ANALOGUE (DATA FROM TABLE X).

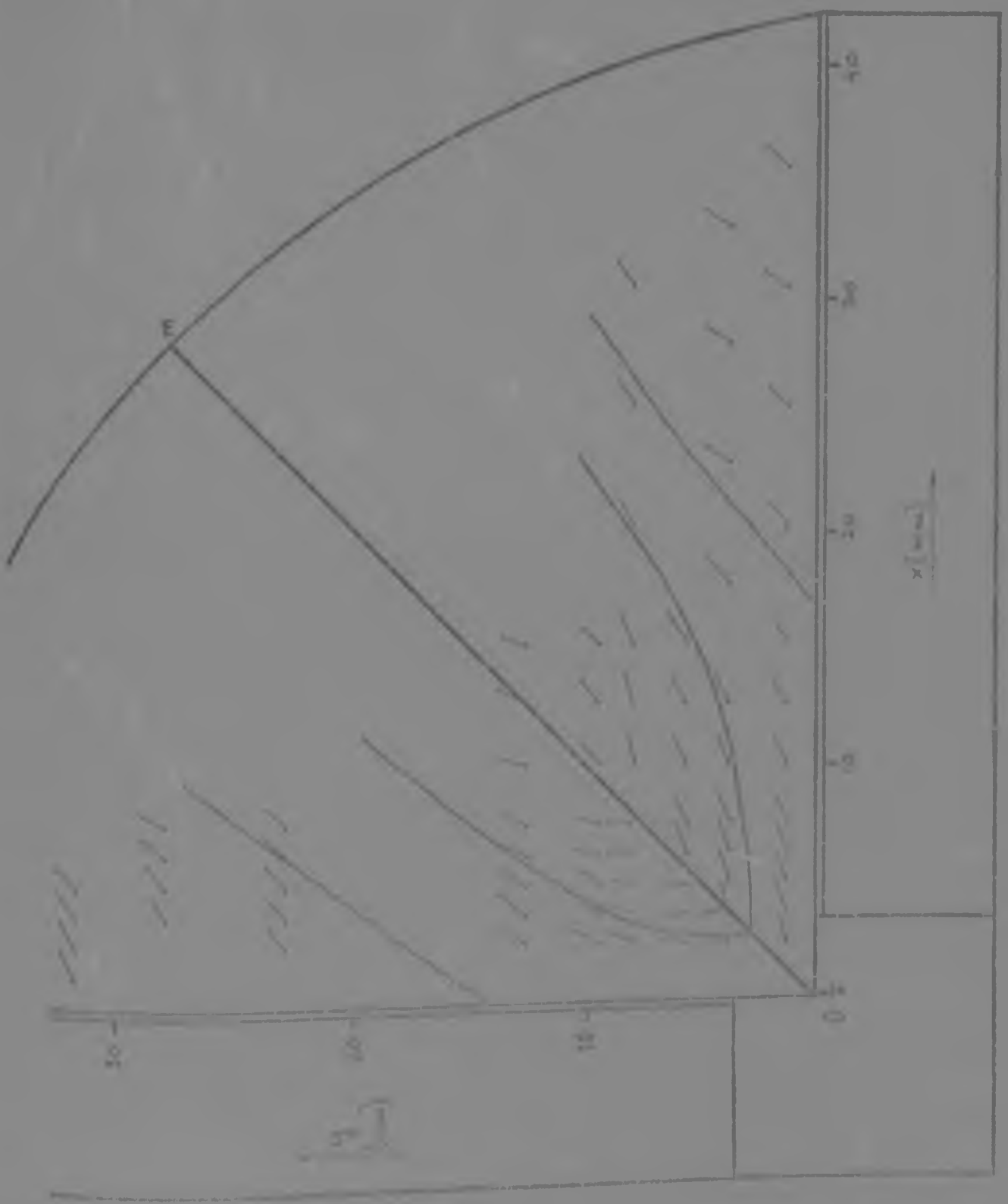

FIGURE 7:

DISTRIBUTION OF MAXIMUM SHEAR STRESS TRAJECTORIES ACROSS THE STEEL SECTION OF ZOT ARMATURE (DATA FROM TABLE XI).

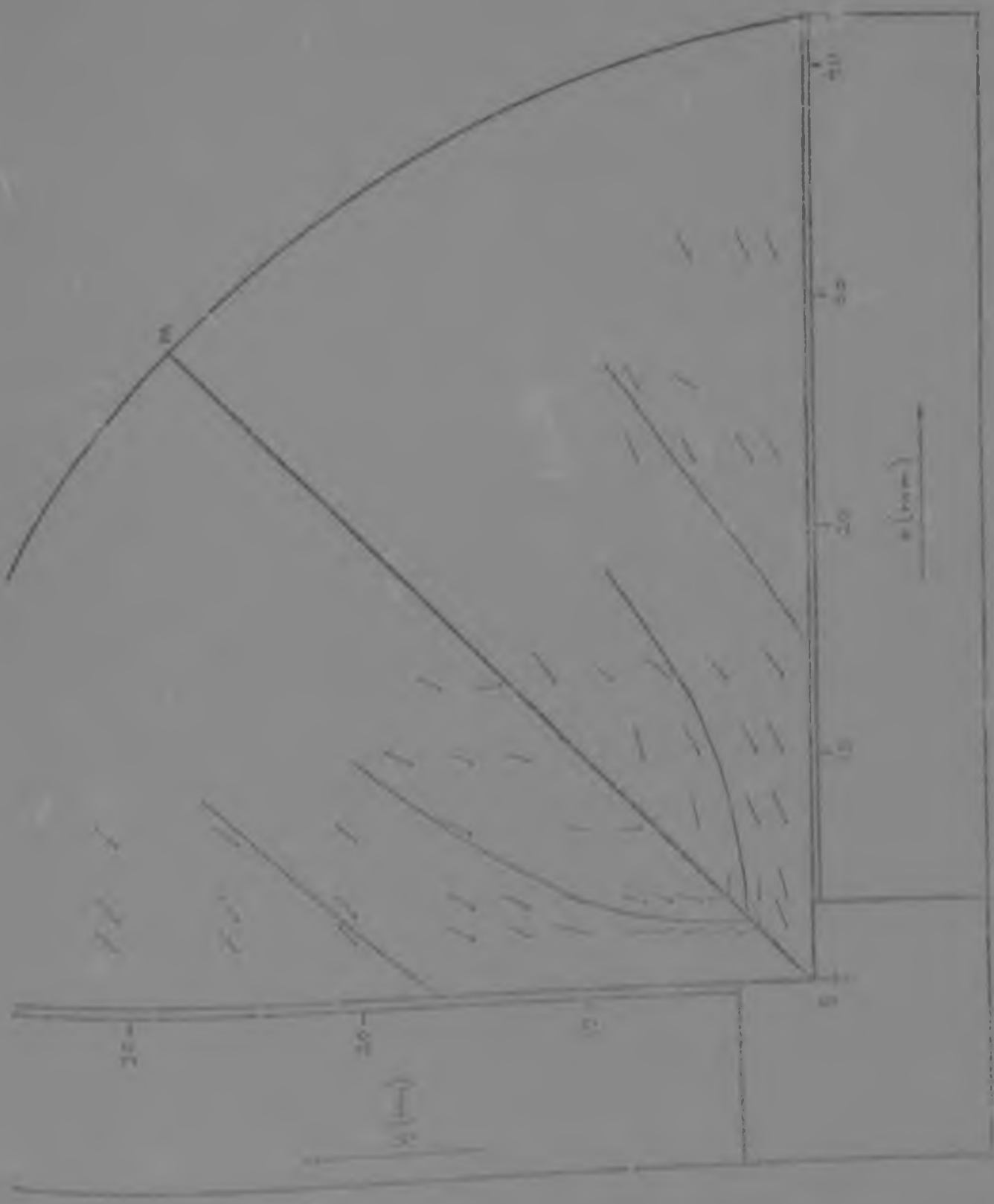

FIG. 75. FINITE ELEMENT ASSEMBLAGE OF A 45° SECTOR OF THE ANALOGUE SURFACE.

FIGURE 76.

RESIDUAL STRESS PATTERN AT 290°C

DISTRIBUTION OF PRINCIPAL STRESS σ_1 (MN/m^2) ACROSS THE SURFACE OF THE ANALOGUE (FINITE ELEMENT ANALYSIS).

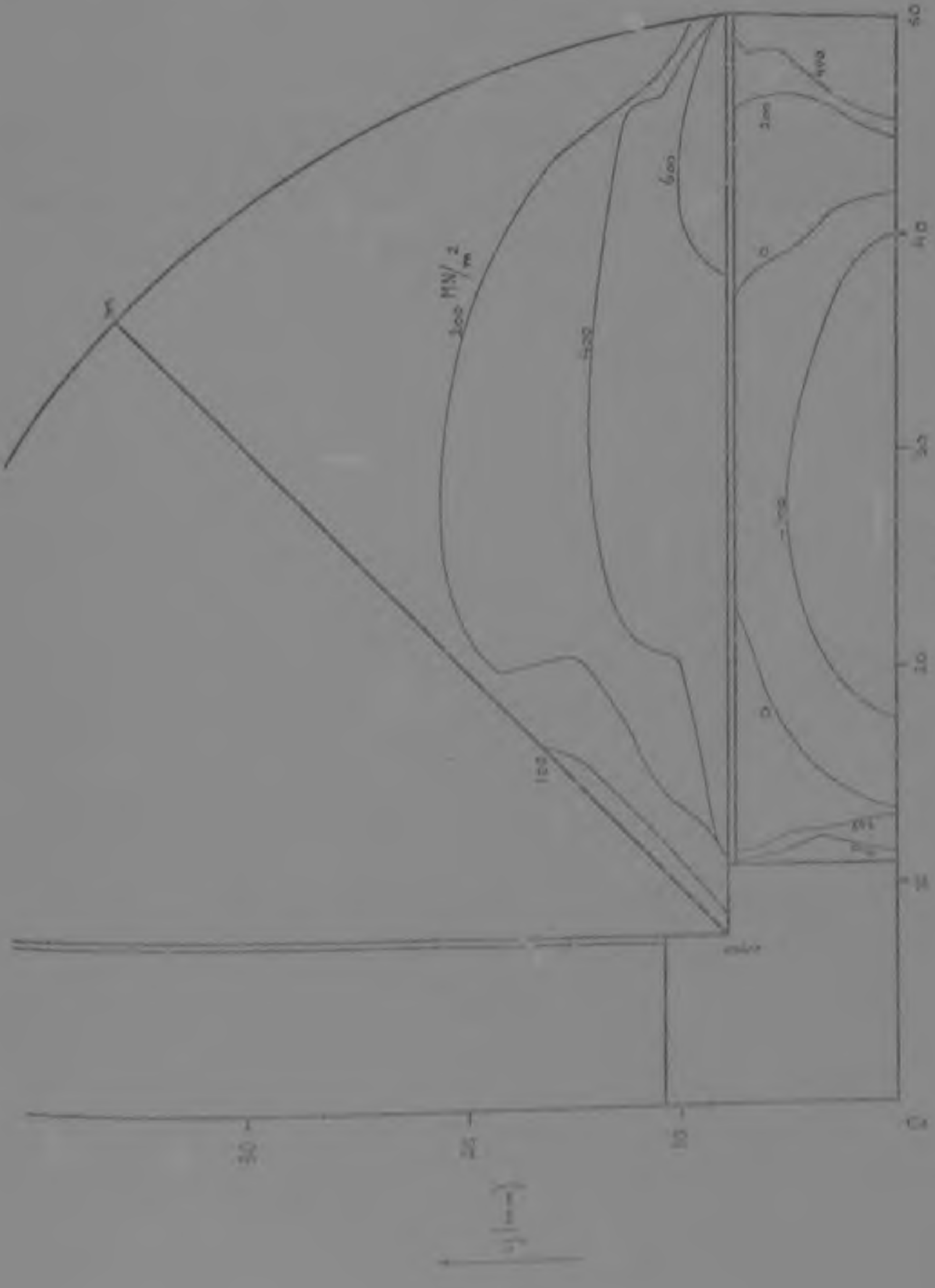

FIGURE 77.

RESIDUAL STRESS PATTERN AT 290°C

DISTRIBUTION OF PRINCIPAL STRESS σ_2 (MN/m^2) ACROSS THE SURFACE OF THE ANALOGUE (FINITE ELEMENT ANALYSIS).

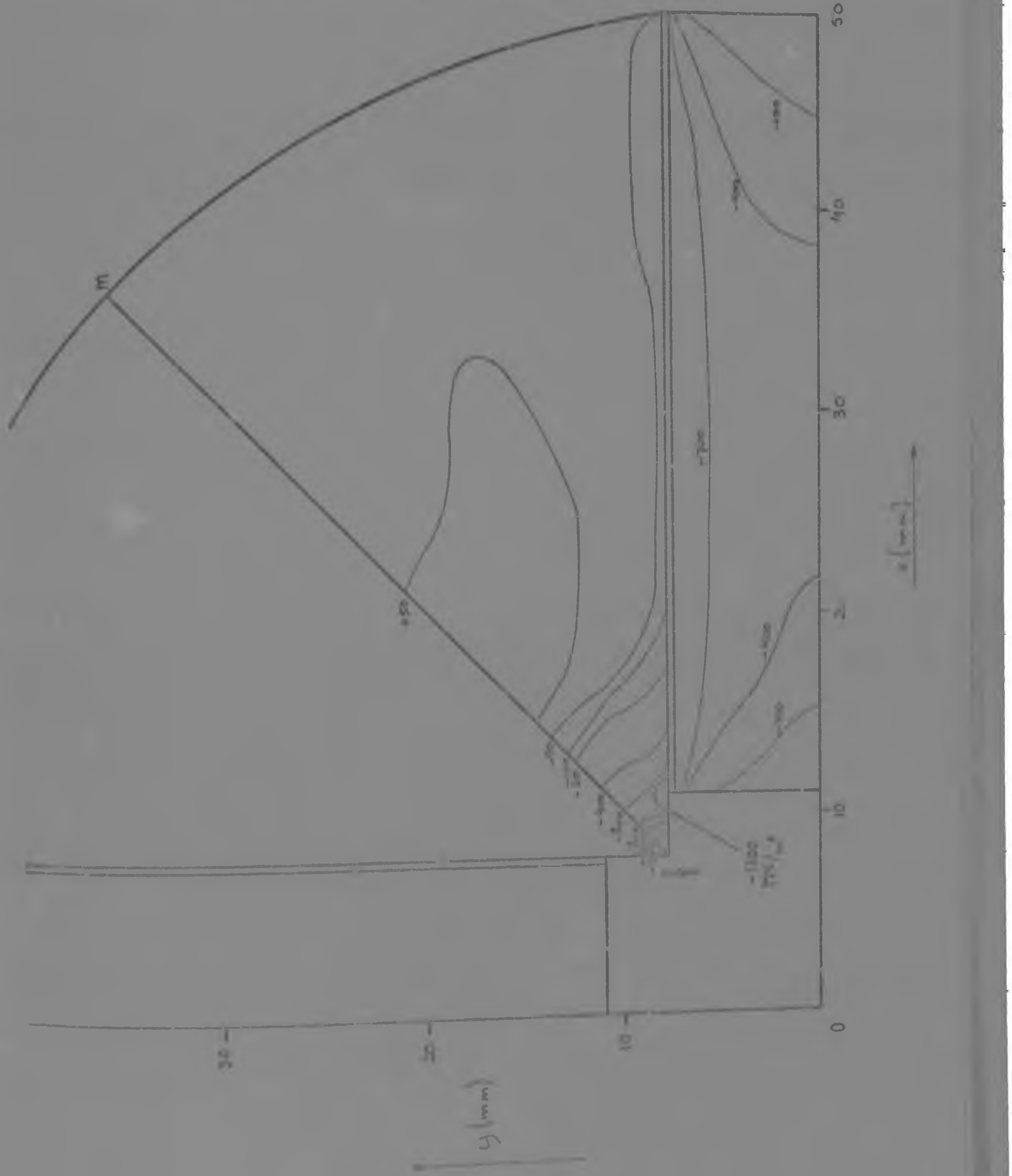

FIGURE 78.

RESIDUAL STRESS PATTERN AT 120°C

DISTRIBUTION OF CIRCUMFERENTIAL STRESS σ_t (MN/m^2) ACROSS THE SURFACE OF THE ANALYSIS (FINITE ELEMENT ANALYSIS)

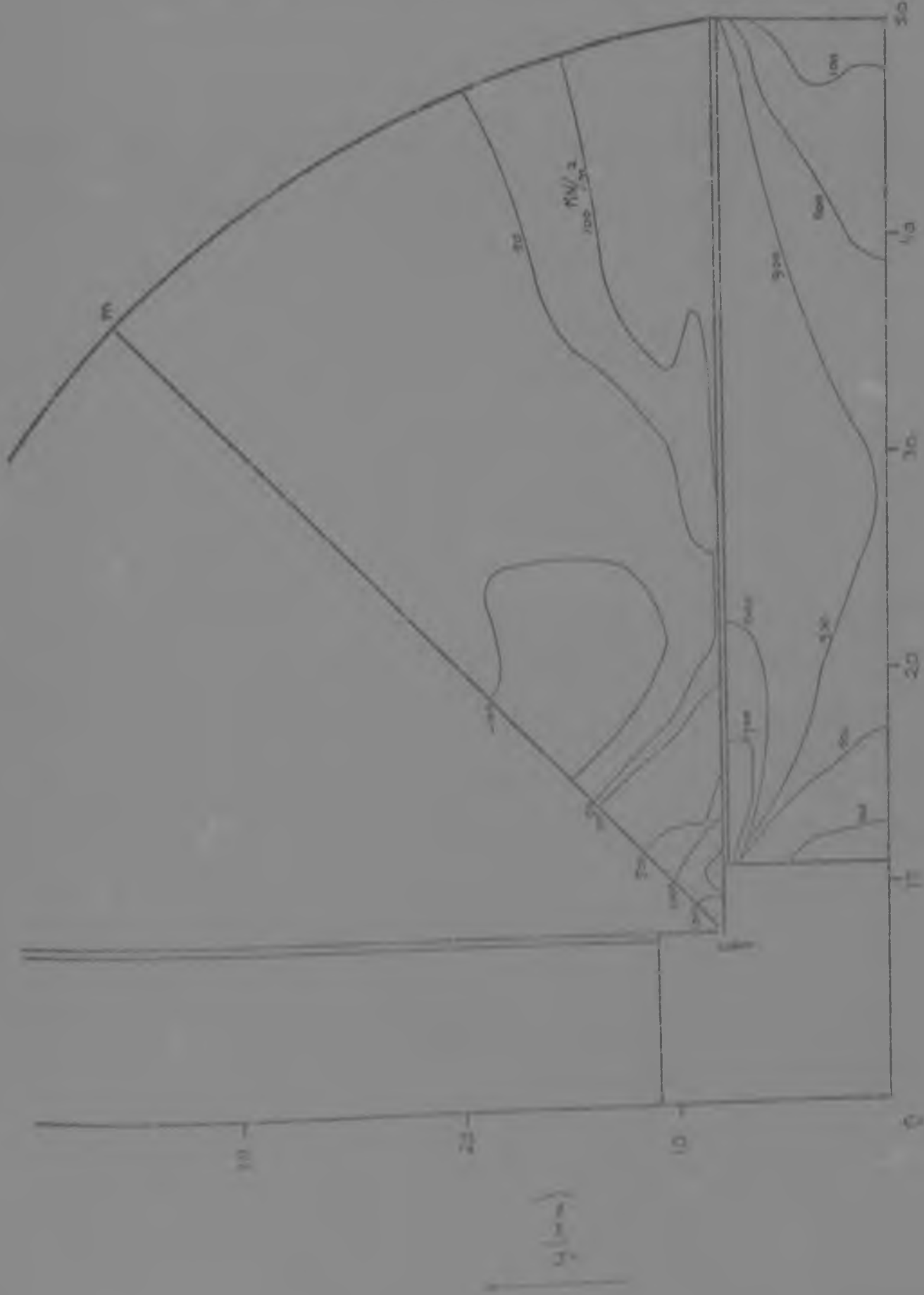

FIGURE 79

RESIDUAL STRESS PATTERN AT 170°C

DISTRIBUTION OF PRINCIPAL STRESS σ_1 ACROSS THE SURFACE OF THE ANALOGUE (FINITE ELEMENT ANALYSIS).

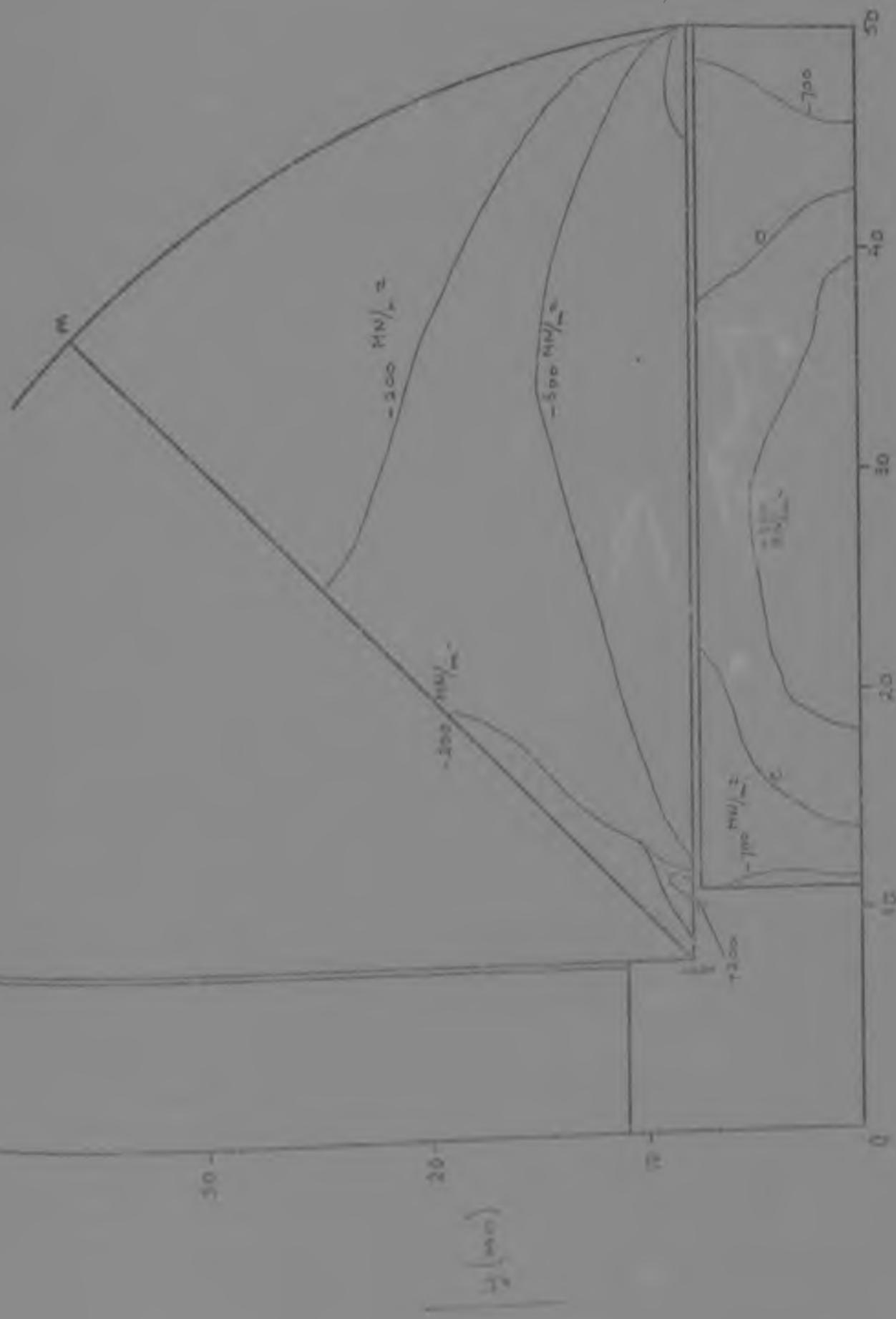

FIGURE 80.

RADIAL STRESS PATTERN AT ROOF PENETRATION
DISTRIBUTION OF MAXIMUM TANGENTIAL STRESS σ_1 ACROSS THE ROOF SURFACE
OF THE ANALOGUE ELASTIC COMPACT ANALYSIS.

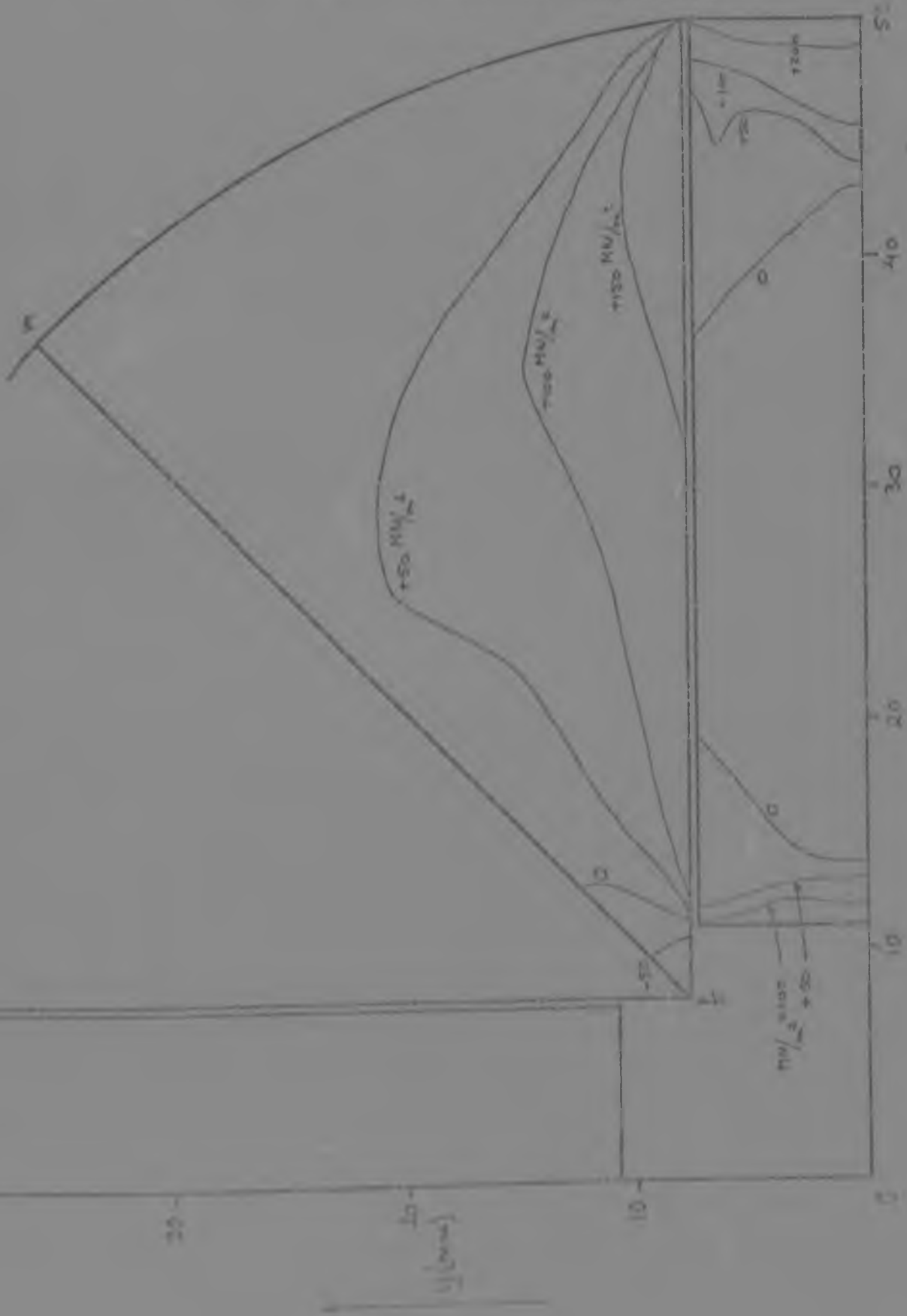

FIGURE 81 :

DISTRIBUTION OF PRINCIPAL STRESS σ_θ ACROSS THE SURFACE OF THE ANALOGUE AT ROOM TEMPERATURE (FROM FINITE ELEMENT ANALYSIS)

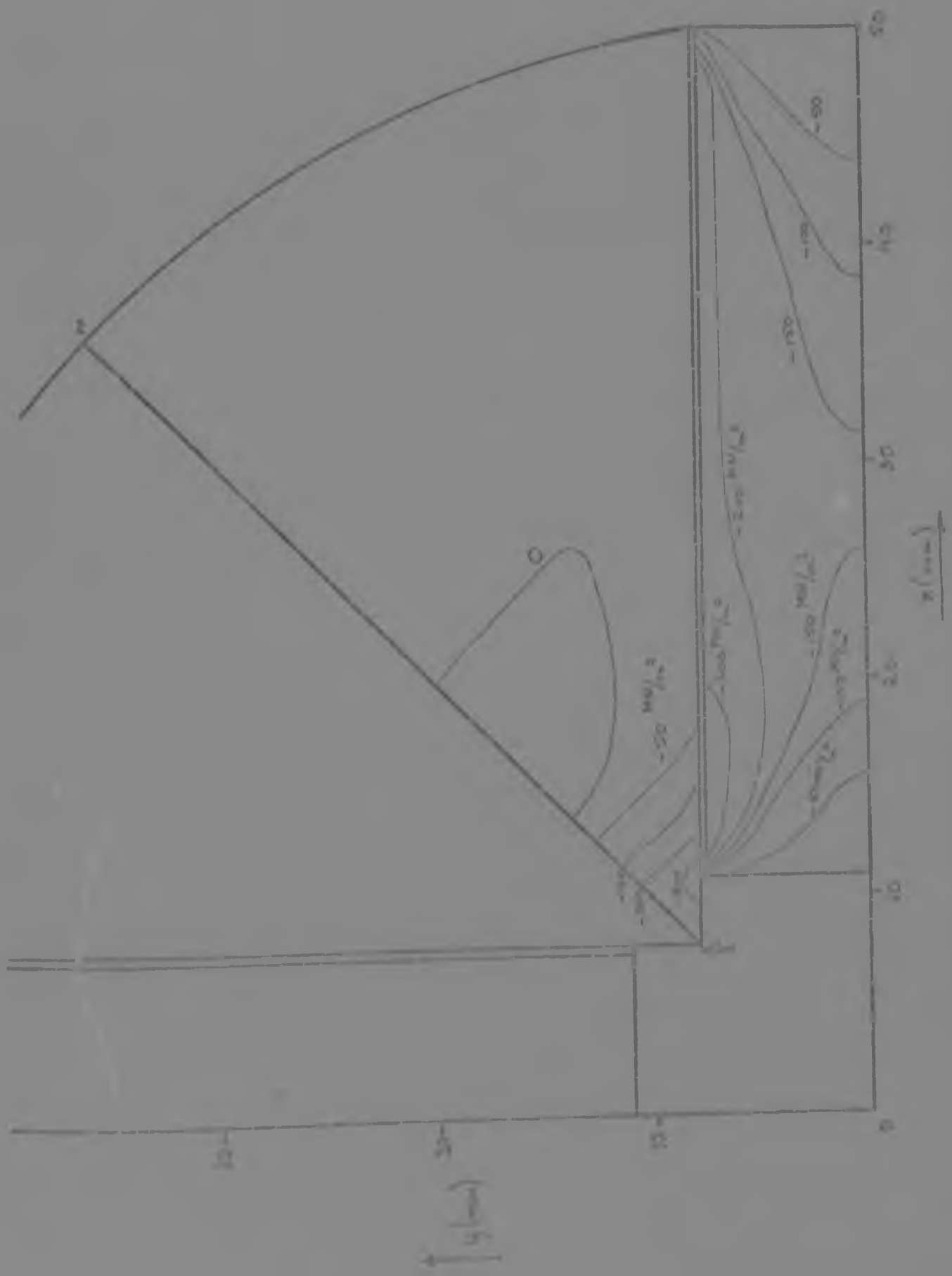

FIGURE 32.

RESIDUAL STRESS PATTERN AT ROOM TEMPERATURE.
DISTRIBUTION OF $(\sigma_1 - \sigma_2)$ PHOTOELASTIC ACROSS THE STEEL SURFACE
OF THE ANALOGUE (FINITE ELEMENT ANALYSIS).

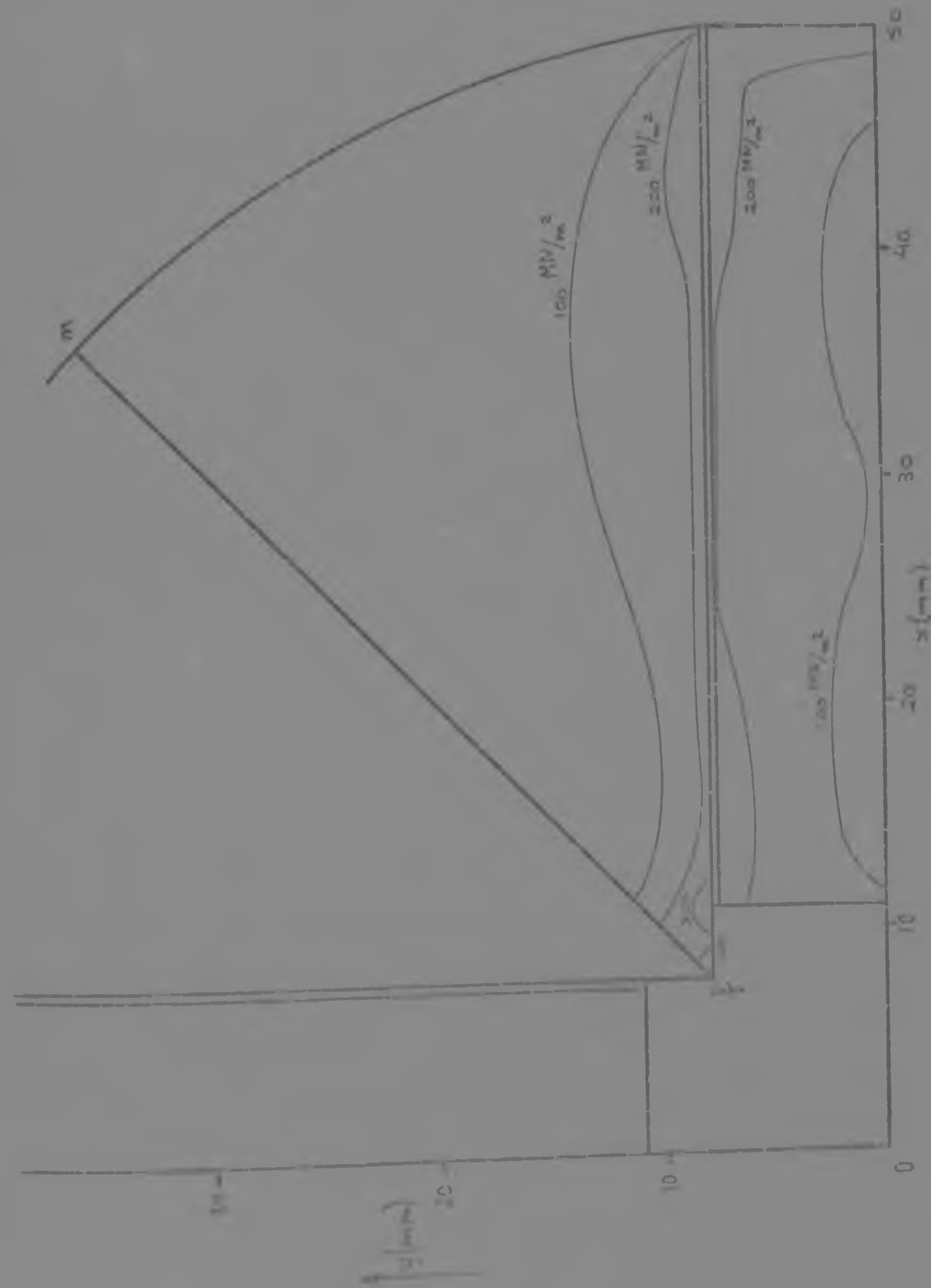

FIGURE 83

DIRECTIONS IN WHICH THE σ_1 PRINCIPAL STRESS ACTS IN THE SURFACE OF THE ANALOGUE AT ROOM TEMPERATURE (FROM FINITE ELEMENT ANALYSIS).